



HAL
open science

Development and validation of quantitative magnetic resonance imaging (MRI) of nonalcoholic fatty liver disease (NAFLD)

Meryem Khalfallah

► **To cite this version:**

Meryem Khalfallah. Development and validation of quantitative magnetic resonance imaging (MRI) of nonalcoholic fatty liver disease (NAFLD). Imaging. Université Paris Cité, 2023. English. NNT : 2023UNIP5031 . tel-04597579

HAL Id: tel-04597579

<https://theses.hal.science/tel-04597579>

Submitted on 3 Jun 2024

HAL is a multi-disciplinary open access archive for the deposit and dissemination of scientific research documents, whether they are published or not. The documents may come from teaching and research institutions in France or abroad, or from public or private research centers.

L'archive ouverte pluridisciplinaire **HAL**, est destinée au dépôt et à la diffusion de documents scientifiques de niveau recherche, publiés ou non, émanant des établissements d'enseignement et de recherche français ou étrangers, des laboratoires publics ou privés.

Université Paris Cité

ED 563 Médicament, Toxicologie, Chimie, Imageries

UMR 1149 Centre de Recherche sur l'Inflammation (CRI)

Laboratoire des biomarqueurs en imagerie (LBI)

Development and validation of quantitative magnetic resonance imaging (MRI) of nonalcoholic fatty liver disease (NAFLD)

Par **Meryem KHALFALLAH**

Thèse de doctorat d'IMAGERIES

Dirigée par Bernard Van Beers

Présentée et soutenue publiquement le 20 février 2023

Devant un jury composé de :

Emmanuel Barbier	Directeur de recherche, Université Grenoble Alpes	Rapporteur
Luis Marti-Bonmati	Professor, University of Valencia	Rapporteur
Najat Salameh	Assistant Professor, University of Basel	Examinatrice
Laura Harsan	Senior Lecturer, University of Strasbourg	Invitée
Philippe Garteiser	Chargé de recherches, Université Paris Cité	Invité/Encadrant
Bernard Van Beers	PU-PH, Université Paris Cité	Directeur de thèse

Title: Development and validation of quantitative magnetic resonance imaging (MRI) of nonalcoholic fatty liver disease (NAFLD)

Abstract

Nonalcoholic fatty liver disease (NAFLD) has emerged as the most common form of chronic liver diseases. Traditionally, NAFLD includes two subgroups, nonalcoholic fatty liver (NAFL) and a progressive inflammatory subgroup, called nonalcoholic steatohepatitis (NASH), which can progress to fibrosis, cirrhosis and hepatocellular carcinoma. Besides this classification, fibrosis is currently recognized as the main prognostic factor of NAFLD. Assessing NAFLD severity requires liver histological analysis, obtained after liver biopsy which is an invasive procedure with sampling variability and moderate inter and intra-operator reproducibility. Quantitative magnetic resonance imaging (MRI) may be used as a non-invasive alternative for assessing NAFLD.

In the first part of this work, the diagnostic value of several quantitative MRI parameters has been assessed in mice models of NAFLD by correlating the MRI data with detailed hepatic histological analysis. The MRI parameters included multifrequency visco-elastic parameters obtained with MR elastography, proton density fat fractions (PDFF) and T1 relaxation times. In the second part of the work, a novel temporal diffusion spectroscopy MRI sequence with oscillating gradient spin echo-echo planar imaging (OGSE-EPI) has been implemented and validated in phantoms and mice to further characterize NAFLD with quantitative MRI.

The results of the first mice study showed that the MRE visco-elastic parameters, and particularly the loss modulus, were highly correlated with hepatic fibrosis, and to a lesser degree with inflammation. None of the visco-elastic parameters was correlated with hepatocyte ballooning, an important histopathological feature of NASH. The diagnostic performance of MRE derived parameters was moderate for diagnosing NASH and high for diagnosing significant fibrosis. The results also confirmed PDFF as biomarker of hepatic steatosis. Moreover, the T1 values correlated with fibrosis and inflammation. However, the T1 measurements were affected by hepatic steatosis. This influence was only partially corrected by using two different two-compartment water-fat no-exchange models. The results of the second part of the work showed that the apparent diffusion coefficients (ADC)

changed with probed spatial scale (i.e with used oscillating frequency). ADC values were mainly influenced by liver steatosis at small spatial scales, by inflammation and ballooning at intermediate scales, and by fibrosis at larger scales.

In conclusion, this work of quantitative multiparametric MRI with MRE, PDFF and T1 mapping in mice models of NAFLD showed the value of quantitative MRI parameters for assessing NAFLD severity. Temporal diffusion spectroscopy might also be a promising tool for assessing the histological features of NAFLD, particularly hepatocyte ballooning.

Keywords:

Liver, Magnetic resonance imaging, Magnetic resonance elastography, Temporal diffusion spectroscopy, Nonalcoholic fatty liver disease, Steatohepatitis.

Titre : Développement et validation de l'imagerie par résonance magnétique quantitative dans la stéatohépatite métabolique chez la souris

Résumé

La stéatose hépatique non-alcoolique (non-alcoholic fatty liver disease, NAFLD) est devenue la forme la plus courante de maladie hépatique chronique. Traditionnellement, on considère que la NAFLD comprend deux sous-groupes, la stéatose hépatique non-alcoolique (non-alcoholic fatty liver, NAFL) et un sous-groupe inflammatoire progressif, appelé stéatohépatite non-alcoolique (non-alcoholic steatohepatitis, NASH), qui peut évoluer vers la fibrose, la cirrhose et le carcinome hépatocellulaire. Outre cette classification, la fibrose est actuellement reconnue comme le principal facteur pronostique de la NAFLD. L'évaluation de la sévérité de la NAFLD nécessite une analyse histopathologique, obtenue après biopsie hépatique qui est une procédure invasive avec une variabilité d'échantillonnage et une reproductibilité inter et intra-opérateur modérée. L'imagerie par résonance magnétique (IRM) quantitative peut être utilisée comme une méthode alternative non-invasive pour évaluer la NAFLD.

Dans la première partie de ce travail de thèse, la valeur diagnostique de plusieurs paramètres IRM quantitatifs a été évaluée dans des modèles murins de NAFLD en corrélant les données d'IRM avec une analyse histologique hépatique détaillée. Les paramètres d'IRM comprenaient des paramètres viscoélastiques multi-fréquentiels obtenus avec l'élastographie par résonance magnétique (ERM), les mesures de fractions de graisse en densité de protons (proton density fat fraction, PDFF) et l'estimation du temps de relaxation T1. Dans la deuxième partie du travail, une nouvelle séquence IRM de spectroscopie de diffusion temporelle avec imagerie écho-planaire à gradients oscillant (OGSE-EPI) a été mise en œuvre et validée dans des fantômes puis appliquée dans des souris pour mieux caractériser la NAFLD.

Les résultats de la première étude chez la souris ont montré que les paramètres viscoélastiques en ERM, particulièrement le module de perte, étaient fortement corrélés à la fibrose hépatique, et dans une moindre mesure à l'inflammation. Aucun paramètre viscoélastique n'était corrélé à la ballonnisation hépatocytaire, une caractéristique

histopathologique importante de la NASH. La performance diagnostique des paramètres d'ERM était modérée pour le diagnostic de la NASH et élevée pour le diagnostic d'une fibrose significative. Les résultats ont également confirmé la PDFF comme biomarqueur de la stéatose hépatique. De plus, les valeurs de T1 étaient corrélées avec la fibrose et l'inflammation. Cependant, les mesures de T1 étaient affectées par la stéatose hépatique. Cette influence n'a été que partiellement corrigée en utilisant deux modèles bi-compartimentaux différents sans échange eau-graisse. Les résultats de la deuxième partie du travail ont montré que les coefficients de diffusion apparents (ADC) changeaient avec l'échelle spatiale explorée (c'est-à-dire avec la fréquence d'oscillation utilisée). Les valeurs de l'ADC étaient principalement influencées par la stéatose hépatique à de petites échelles spatiales, par l'inflammation et le ballonnissement à des échelles intermédiaires et par la fibrose à des échelles plus grandes.

En conclusion, ce travail d'IRM multiparamétrique quantitative avec cartographie hépatique en ERM, PDFF et T1 dans des modèles murins de NAFLD a montré l'intérêt des paramètres quantitatifs d'IRM pour évaluer la sévérité de la NAFLD. La spectroscopie de diffusion temporelle pourrait également être un outil prometteur pour évaluer les caractéristiques histologiques de la NAFLD, en particulier la ballonnisation des hépatocytes.

Mots clefs :

Foie, Imagerie par résonance magnétique, Élastographie par résonance magnétique, Spectroscopie de diffusion temporelle, La stéatose hépatique non-alcoolique, la steatohépatite

Acknowledgment

First of all, I would like to thank my supervisor Bernard Van Beers and my co-advisor Philippe Garteiser for welcoming me into the team during my PhD, for the trust they placed in me, for their guidance, support and patience, but also for always encouraging me to go beyond my limits. I could not have imagined having better mentorship for my PhD work.

I would also like to thank all the members of my thesis jury: Dr. Emmanuel Barbier, Dr. Luis Marti-Bonmati, Dr. Najat Salameh and Dr. Laura Harsan, for accepting to be part of this journey and for their invaluable feedback.

A big thanks to Sabrina Doblas for her advice and help during this thesis and to Mélanie Montabord for the great time we spent performing many experiments together and for her insightful comments and suggestions.

I am also grateful to all my colleagues during this thesis, especially Felicia Julea and Gwenaël Pagé to whom I wish good luck for the future and with whom I hope to be able to work again one day. My gratitude also goes to all the members of the Centre de Recherche sur l'Inflammation (CRI).

Additionally, I would like to thank the QuidNASH and the StediNASH projects members for the generous support and research funding, and to the FRIM platform. This endeavor would not have been possible without them.

Last but not the least, a very special thanks to my family: my parents, my sisters and brothers and to my friends for believing in me and supporting me throughout this process and in my life in general.

To my parents,
Thank you for your love, your support and your trust

À mes parents,
Merci pour votre amour, votre soutien et votre confiance

إلى أبي و أمي،
شكرا لكما على كل الحب و الدعم و الثقة التي غمرتوني بها

Abbreviations

ADC: apparent diffusion coefficient

ALT: alanine aminotransferases

AST: aspartate aminotransferases

BMI: body mass index

CAP: Controlled Attenuation Parameter

CCl₄: carbon tetrachloride

CDAA: choline-deficient, L-amino acid-defined diet

CDA-HFD: choline deficient L-amino acid - high fat diet

DWI: diffusion weighted imaging

HFD: high fat diet

EMA: European Medicines Agency

EPI: echo planar imaging

FAIR: flow-sensitive alternating inversion recovery

FAST: FibroScan-AST

FDA: Food and Drug Administration

FLIP: fatty liver inhibition of progression

FSE: fast spin echo

¹H-MRS : magnetic resonance spectroscopy

ICC: intraclass correlation

IR: inversion recovery

IVIM: intravoxel incoherent motion

MAST: MRI-AST

MEFIB: MRE-Fibros-4

MEGs: motion-encoding gradients

MOLLI: modified Look-Locker pulse sequence

MRI: magnetic resonance imaging

MRE: magnetic resonance elastography

NAFL: nonalcoholic fatty liver

NAFLD: nonalcoholic fatty liver disease

NAS: NAFLD activity score

NASH: nonalcoholic steatohepatitis

NASH CRN: NASH clinical research network

ND: normal diet

OGSE: oscillated gradient spin echo

PDFF: proton density fat fraction

PGSE: pulsed gradient spin echo

ROI: region of interest

SAF: steatosis activity fibrosis score

SE: spin echo

SNR: signal to noise ratio

SR: saturation recovery

TDS: temporal diffusion spectroscopy

TE: echo time

TE: inversion time

TR: repetition time

WD: Western diet

Summary

1. Introduction	14
1.1. Nonalcoholic Fatty Liver Disease	14
1.1.1. NAFL	14
1.1.2. NASH	15
1.1.3. Fibrosis, cirrhosis and hepatocellular carcinoma.....	16
1.1.4. Diagnosis of NAFLD	17
1.1.5. Other definitions of the progressive form of NAFLD	23
1.2. Preclinical models of NAFLD	24
1.2.1. Model design considerations.....	24
1.2.2. Models used in the present work.....	25
1.2.2.1. High Fat Diet (HFD)	25
1.2.2.1. Choline Deficient L-amino acid - High Fat Diet (CDA-HFD).....	26
1.2.2.2. Western Diet (WD) combined with CCl ₄ administration	27
1.3. Quantitative Magnetic Resonance Imaging (MRI) for the diagnosis of NAFLD	31
1.3.1. Proton Density Fat Fraction (PDFF).....	31
1.3.2. Magnetic Resonance Elastography (MRE)	36
1.3.2.1. Mechanical waves generation.....	37
1.3.2.2. MRE sequences	39
1.3.2.3. Inversion algorithms.....	41
1.3.2.4. MRE parameters.....	42
1.3.2.5. Hepatic MRE applications.....	45
1) Diagnostic of hepatic fibrosis	45
2) Diagnostic of hepatic inflammation.....	46
3) Diagnostic of NASH	46
1.3.3. T1 relaxation time mapping.....	47
1.3.4. Diffusion Weighted Imaging (DWI)	49
1.3.5. Temporal Diffusion Spectroscopy (TDS).....	53
2. Aim of the research.....	59
3. Chapter I : Animal models of NAFLD/NASH.....	61
3.1. NASH histological study : WD mouse model.....	61
3.1.1. Methods.....	61
3.1.2. Results.....	63
3.1.3. Discussion	65

3.2.	Second study :	70
3.2.1.	Methods.....	70
3.2.2.	Results.....	72
3.2.3.	Discussion	82
4.	Chapter II : Multi-parametric preclinical MRI of NAFLD	84
4.1.	General elements of the study	85
4.1.1.	Study cohort	85
4.1.2.	MRI experiments.....	86
4.1.3.	Histological analysis.....	86
4.2.	Diagnostic of NAFLD : Magnetic Resonance Elastography.....	87
4.2.1.	Data acquisition	87
4.2.2.	Data processing.....	88
4.2.3.	Statistical analysis	90
4.2.4.	Results.....	90
4.2.5.	Discussion	111
4.3.	Methodology	116
4.3.1.	PDFF mapping.....	116
4.3.1.1.	Data acquisition	116
4.3.1.2.	Data processing.....	116
4.3.1.3.	Statistical analysis	117
4.3.1.1.	Results	118
4.3.1.2.	Discussion	120
4.3.2.	T1 mapping.....	122
4.3.2.1.	Methods.....	123
1)	Data acquisition	123
2)	Data processing.....	123
3)	Statistical analysis	123
4.3.2.2.	Results	124
4.3.2.3.	Discussion	125
4.3.2.4.	T1 data correction: correction model a posteriori on the R1	126
4.3.2.5.	T1 data correction : correction model for the expression of the signal ...	129
4.3.2.6.	Discussion	132
5.	Chapter III : Temporal Diffusion Spectroscopy with oscillating gradients echoplanar imaging	135
5.1.	Introduction.....	135
5.2.	Methods.....	138

5.2.1.	Sequence programming.....	138
5.2.1.1.	Double-sine wave form implementation	138
5.2.1.2.	Sequence optimization : Trapezoidal waveform	140
5.2.2.	Materials and subjects	142
5.2.2.1.	Phantom study.....	142
5.2.2.2.	In vivo repeatability study.....	143
5.2.2.3.	NAFLD mouse models.....	143
5.2.2.4.	Animal procedures.....	144
5.2.3.	Acquisition parameters	145
5.2.3.1.	MRI system.....	145
5.2.3.2.	Conditions assessed in the repeatability study.....	145
5.2.3.3.	Sequence parameters used in the three studies	145
4)	Phantom study.....	145
5)	In vivo repeatability study.....	146
6)	NAFLD mouse models.....	146
5.2.4.	Data processing.....	147
5.2.1.	Statistical analysis	147
5.2.2.	Results.....	149
5.2.2.1.	ADC behavior at multiple frequencies in samples with calibrated characteristic lengths.....	149
5.2.2.2.	In vivo repeatability study.....	155
5.2.2.3.	Sequence application in mouse models of NAFLD	158
5.2.3.	Discussion	169
6.	Discussion and perspectives.....	174
6.1.	Discussion	174
6.2.	Perspectives	177
7.	References	180
8.	Appendix.....	203
8.1.	MRE parametric maps	203
8.2.	Résumé	205
8.3.	List of tables.....	215
8.4.	List of figures	217

1. Introduction

1.1. Nonalcoholic Fatty Liver Disease

Nonalcoholic fatty liver disease (NAFLD) affects approximately 25% of the adult population around the world with the highest prevalence rates found in the Middle East (32%) and South America (31%) and the lowest prevalence in Africa (14%) [1, 2]. NAFLD is defined histologically as hepatic steatosis of at least grade one (i.e. the presence of fat droplets in the cytoplasm of at least 5% of hepatocytes), without any chronic liver disease such as viral or autoimmune hepatitis, hemochromatosis, Wilson's disease, and without any excessive alcohol consumption (current or recent alcohol consumption of more than 21 drinks/week for men and more than 14 drinks/week for women according to the U.S. Guideline for NAFLD) or use of medications that induce liver steatosis [1, 3]. Several metabolic comorbidities are associated with NAFLD including obesity, type 2 diabetes, high blood pressure, dyslipidemia and hypertriglyceridemia which are risk factors for cardiovascular diseases [4-6]. It has been reported that over 75% of patients with type 2 diabetes [7-9] and 90% of severely obese patients undergoing bariatric surgery [1, 3] have NAFLD. In addition to the metabolic comorbidities, age, gender, ethnicity, and genetic polymorphisms can affect NAFLD onset and progression [1, 3, 10]. In clinical practice, liver biopsy remains the most reliable method for diagnosing NAFLD and assessing its severity. However, it is an invasive procedure, limited by cost and sampling variability, and has some morbidity and rare mortality risks [3, 11].

NAFLD is a general term used to describe a spectrum of nonalcoholic fat-related hepatic lesions ranging from non-alcoholic fatty liver (NAFL), the early stage of the disease known as simple isolated steatosis where fat accumulation is observed without significant inflammation or cell injury, to non-alcoholic steatohepatitis (NASH), a progressive form of NAFLD that includes inflammation and hepatocyte injury and can evolve to advanced stages of fibrosis, cirrhosis and hepatocellular carcinoma [3, 11-13].

1.1.1. NAFL

The prevalence of NAFLD is continuously increasing and mirrors the increase in rate of obesity around the world [1, 3]. According to the World Health Organization, the prevalence of

obesity has almost tripled between 1975 and 2016 worldwide. In 2016, more than 1.9 billion adults were considered to be overweight (39% of the world's adult population; 39% of men and 40% of women) and 650 million were estimated to be obese (about 13% of the world's adult population; 11% of men and 15% of women) [14]. Obesity, characterized by excessive accumulation of fat resulting from imbalance in the energy intake-expenditure ratio, is commonly estimated using the body mass index (BMI) where the weight of the individual expressed in kilograms (kg) is divided by the square of its height in meters (m) [15-17]. Based on this estimation, a BMI < 18.5 kg/m² is classified as undernutrition, 18.5 – 24.9 kg/m² as normal weight, 25 – 29.9 kg/m² as overweight, ≥ 30 kg/m² as obesity, and ≥ 40 kg/m² as extreme obesity. Moreover, BMI can be complemented by waist circumference measurement to distinguish subcutaneous obesity from other types of obesity [15, 16].

Several studies have demonstrated that fat location better reflects morbidity/mortality risks than fat quantity. For patients with similar BMI, those who have visceral fat accumulation have a higher risk for adverse events than those with subcutaneous fat accumulation [15, 16]. Subcutaneous fat storage is harmless. In contrast, visceral fat and ectopic fat in the liver, heart, pancreas, kidney and muscle increase the risk for metabolic syndrome, type 2 diabetes, NAFLD and cardiovascular diseases. The precise pathogenesis of NAFLD and its progression from simple steatosis to a more progressive form (i.e. NASH) remains poorly understood. In patients with NAFLD, three sources have been reported to cause hepatic triglyceride accumulation: excess in fatty acids production (accounts for up to 60%), de novo lipogenesis (estimated to be up to 25%) and dietary contribution (approximately 15%) [13, 18-21].

1.1.2. NASH

Although most of NAFLD patients have the early stage noninflammatory form of the disease, approximately one-third of them end up developing nonalcoholic steatohepatitis (NASH). NASH has gained special attention in the last decades due to its risk of evolving to advanced liver fibrosis, cirrhosis, liver failure and even hepatocellular carcinoma. As the diagnosis of NAFLD and NASH requires liver biopsy, establishing the prevalence of NASH is still a complex process especially because the prevalence estimation depends significantly on the diagnostic method and the population included in the study.

A meta-analysis conducted by Younossi et al. included 8,515,431 individuals from all over the world [1]. In this study, the global prevalence of NASH among patients with NAFLD was 59%. Moreover, obesity and type 2 diabetes, two important risk factors for progression to NASH, were identified in 82% and 47% of NASH patients. The prevalence of hepatocellular carcinoma in NAFLD patients was reported to be 0.44 per 1,000 person-years. When analyzing liver-specific mortality and overall mortality among NAFLD and NASH patients, Younossi et al., reported higher liver-specific mortality and overall mortality rates in NASH (15.44 per 1,000 and 25.56 per 1,000 person-years respectively) than in NAFLD (0.77 per 1,000 and 11.77 per 1,000 person-years respectively) which highlights the need for early diagnosis of the disease [1]. Another recent study involving a cohort of military personnel and their dependents reported a NASH prevalence of 12.2% among the whole population and 29.9% among patients with a positive diagnosis of NAFLD [22].

At histology, NASH is defined as hepatic steatosis (at least grade 1 of steatosis) associated with lobular inflammation and hepatocyte injury (cell ballooning) with or without liver fibrosis [3].

1.1.3. Fibrosis, cirrhosis and hepatocellular carcinoma

NASH is typically associated with hepatic fibrogenesis that eventually leads to liver cirrhosis and hepatocellular carcinoma. Although it is mostly associated with NASH, fibrosis may also be observed in NAFL. Fibrosis is described as hepatic tissue scarring caused by a relatively long wound-healing process which involves progressive accumulation of extracellular matrix proteins, mainly collagen. Hepatic stellate cells have a key role in this process [13, 23, 24]. They are activated secondary to an inflammatory reaction triggered by neighboring cells including Kupffer cells, hepatocytes, endothelial cells, lymphocytes and neutrophils. At histology, fibrosis has 4 stages that are defined according to the pattern and quantity of extracellular matrix deposition. Cirrhosis is the terminal stage (i.e. stage 4) and is associated with portal hypertension, alterations of liver functions and a higher risk of liver-related death [25]. Approximately, patients with NASH progress by one stage of fibrosis per 7 years [26].

Cirrhosis is associated with an elevated risk of hepatocellular carcinoma and the classical co-morbidities found in patients with NAFLD including obesity and diabetes increases this risk

[27]. This hepatic cancer is considered to be the second leading cause of cancer-related death [28]. The increased risk of hepatocellular carcinoma in patients with NAFLD is still not fully understood. However, potential causes include increased expression of genes involved in cell proliferation and survival as a consequence of inflammation, hepatocellular injury, and decrease in tumor suppressor factors [13]. The prevalence of hepatocellular carcinoma is much higher in chronic B and C viral infections than in NAFLD. However, NAFLD is the fastest growing cause of hepatocellular carcinoma in the Western world [27, 29]. Currently, the diagnosis of this type of cancer is exclusively recommended in patients with cirrhosis, even though cirrhosis-associated hepatocellular carcinomas represent only half of the NAFLD-associated hepatocellular carcinomas [30].

1.1.4. Diagnosis of NAFLD

NAFLD shows a continuous spectrum of steatosis, hepatocellular injury, inflammation and fibrosis. Dichotomizing NAFLD in two subgroups (NAFL and NASH) may be an oversimplification. To overcome this limitation, semi-quantitative scoring systems have been developed to assess NAFLD. The NAFLD activity score (NAS) has been proposed by the multicenter NASH clinical research network (NASH CRN) sponsored by the American national institute of diabetes & digestive & kidney diseases in 2002 [12, 31, 32]. NAS was developed as a tool to measure changes in NAFLD during therapeutic trials. This scoring system (Table 1.1.1) is defined as the unweighted sum of the scores for steatosis (0–3), lobular inflammation (0–3), and ballooning (0–2); thus ranging from 0 to 8. Steatosis; accumulation of lipidic droplets within hepatocytes (Figure 1.1.1, black circle), is histologically scored as 0: < 5% of hepatocytes with fat droplets, 1: 5 – 33%, 2: > 33–66% and 3: > 66%. Ballooned hepatocytes exhibit a clear, flocculent, non-vacuolar cytoplasm and a balloon-like shape described as the loss of sharp angles in the liver cell (Figure 1.1.1, yellow circle). The size of hepatocytes may or may not increase compared to normal hepatocytes. In the NAFLD scoring system, grading of ballooned cells is based mainly on number of impacted cells; grade 0: none, grade 1: few, and grade 2: many ballooned cells. Lobular inflammation includes small foci of inflammatory cells (lymphocytes and macrophages, sometimes associated with hepatocyte dropout or apoptotic bodies) within the hepatic lobules (Figure 1.1.1, blue ellipse). Based on the NAS

scoring system, lobular inflammation is scored as 0: no foci, 1: < 2 foci per 200× field, 2: 2 – 4 foci per 200× field and 3: > 4 foci per 200× field.

Table 1.1. 1: Scoring systems for evaluating the different histological features of NAFLD based on liver biopsy in NAFLD patients.

NAS (NASH CRN)			SAF (FLIP)		
Components	Score	Description	Components	Score	Description
Steatosis	0	<5%	Steatosis	S0	None
	1	5-33%		S1	5%–33%
	2	>33-66%		S2	34%–66%
	3	>66%		S3	>66%
Ballooning	0	None	Activity:	A0-A4	None Clusters of hepatocytes with rounded shape and pale and/or reticulated cytoplasm Same as score 1 with enlarged hepatocytes (>2_ normal size) 0: None 1: <2 foci per 20/ objective field 2: >2 foci per 20/ objective field mild activity moderate activity severe activity
	1	Few balloon cells	Ballooning	0	
	2	Many cells/ Prominent ballooning		1	
				2	
			Lobular Inflammation	0	
				1	
			2		
			Activity grade*	1	
				2	
				3-4	
Inflammation	0	No foci	Fibrosis	F0	No significant fibrosis
	1	<2 foci/ 200x		F1a	Mild zone 3 perisinusoidal fibrosis
	2	2-4 foci/ 200x		F1b	Moderate zone 3 perisinusoidal fibrosis
	3	>4 foci/ 200x		F1c	Portal fibrosis only
				F2	Zone 3 and periportal perisinusoidal fibrosis
			F3	Bridging fibrosis	
			F4	Cirrhosis	
NAS 0-8			S ₀₋₄ A ₀₋₄ F ₀₋₄		

*Activity grade: The sum of scores for lobular inflammation and ballooning.

NAS: non-alcoholic fatty liver disease activity score; NASH CRN: non-alcoholic steatohepatitis clinical research network; SAF: steatosis activity fibrosis; FLIP: fatty liver inhibition of progression. (from: Papatheodoridi M. et al., *Current Pharmaceutical Design*, 2018 [33])

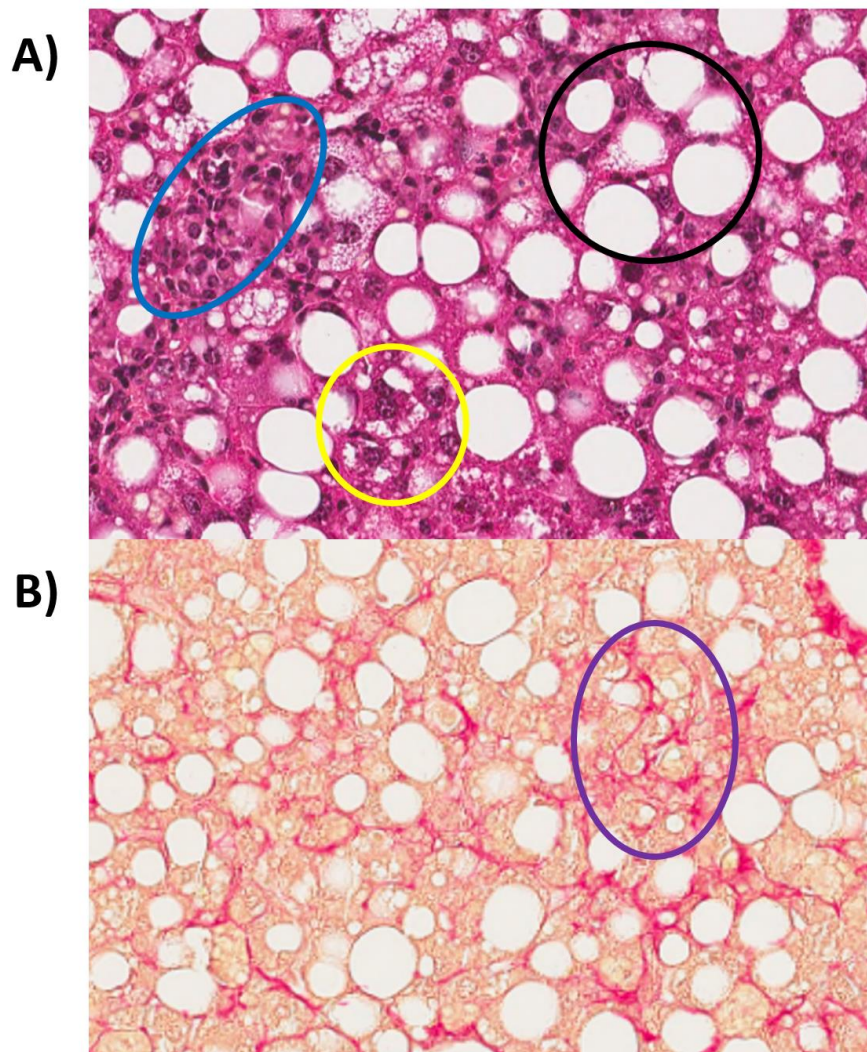


Figure 1.1. 1: Representative histological sections: A) picosirius red stained slice and B) hematoxylin-eosin stained slice. On A), the black circle indicates steatosis, the accumulation of lipids within hepatocytes, the yellow circle indicates ballooned hepatocytes which exhibit a clear, flocculent, non-vacuolar cytoplasm and a balloon-like shape described as the loss of sharp angles in the liver cell, while the blue ellipse shows lobular inflammation which includes small foci of inflammatory cells (lymphocytes and macrophages, sometimes associated with hepatocyte dropout or apoptotic bodies) within the hepatic lobules. On B), the purple ellipse indicates fibrosis described as hepatic tissue scarring caused by a relatively long wound-healing process which involves progressive accumulation of extracellular matrix proteins, mainly collagen.

Fibrosis (not included in the NAS score) has a distinctive pattern in NAFLD compared to other liver diseases (figure 1.1.1, purple ellipse). It is classified as: stage F0 (no fibrosis), stage F1a (mild, zone 3, perisinusoidal fibrosis), stage F1b (moderate, zone 3, perisinusoidal fibrosis), stage F1c (portal/periportal fibrosis), stage F2 (perisinusoidal and portal/ periportal fibrosis), stage F3 (bridging fibrosis) and stage F4 (cirrhosis).

In addition to these histological features observed in NAFLD, it has been reported that during NAFLD pathogenesis macrophages aggregate creating hepatic crown-like structures (hCLS) surrounding hepatocytes with large fat droplets. The number of these inflammatory hCLS was found to correlate positively with hepatic fibrosis. This histological feature of NAFLD was observed in both NAFLD patients and animal models of the disease [34, 35]. However, it is not described as part of the scoring systems of NAFLD.

The NASH CRN system defines NASH by a pattern of injury composed of steatosis, lobular inflammation, and ballooning degeneration [36]. In some studies, threshold values of the NAS, specifically $NAS \geq 5$, has been used as a surrogate for the histologic diagnosis of NASH. This should be avoided as in a clinical cohort only 75% of biopsies with definite NASH had $NAS \geq 5$, whereas 28% of borderline NASH and 7% of no NASH had $NAS \geq 5$ [37]. Indeterminate or borderline NASH, a subclassification only recognized in the NASH CRN scoring system, is defined as non-NASH and characterized by grade ≥ 1 steatosis with mild lobular inflammation and none to rare ballooning [36]. It can be associated with varying amounts of fibrosis and may represent more advanced disease than fatty liver. Hepatic steatosis with varying fibrosis stages short of cirrhosis in the absence of inflammation and ballooning has been observed, but no data link it to clinical outcomes. This entity is classified as steatofibrosis.

The NAS scoring system adds hepatocyte injury / lobular inflammation which are deleterious features, with steatosis for which the pejorative effects has not been clearly depicted [38, 39]. Also, the three components of this scoring system has unequal weights with the lower (0 - 2) for hepatocyte ballooning which is the most prognostic feature [32]. This might affect the diagnosis of NAFL/NASH by giving more weight to steatosis and inflammation than to ballooning.

Another scoring system, named SAF (steatosis, activity, fibrosis) score, has been recently developed in Europe in 2012 [11, 31] (Table 1.1.1). This score evaluates independently the grade of steatosis (S, from S0 to S3), the grade of activity (A, from A0 to A4), and the stage of fibrosis (F, from F0 to F4) [40, 41]. In the SAF system, the activity score is defined as the sum of the semi-quantitative score of lobular inflammation which is defined as 0: none, 1: <2 foci per 20/objective field, and 2: >2 foci per 20/objective field, and hepatocellular ballooning graded as 0: none, 1: clusters of hepatocytes with rounded shape and pale and/or reticulated cytoplasm and 2: same as score 1 with enlarged hepatocytes (>2 the normal size)[40]. Based on the SAF score, the fatty liver inhibition of progression (FLIP) algorithm has been developed by Bedossa P. et al., in 2012 [11, 42] for a reliable diagnosis of NASH with limited inter-operator variation. According to the FLIP algorithm, a grade of 1 or higher for steatosis, lobular inflammation, and ballooning is needed for the diagnosis of NASH (figure 1.1.2). SAF score can be applied for any association of steatosis, fibrosis and activity, particularly the cases that are difficult to classify as NAFLD or NASH including steato-inflammation (i.e. steatosis with lobular inflammation alone) and steato-fibrosis (i.e. steatosis with fibrosis but without lobular inflammation or hepatocyte ballooning).

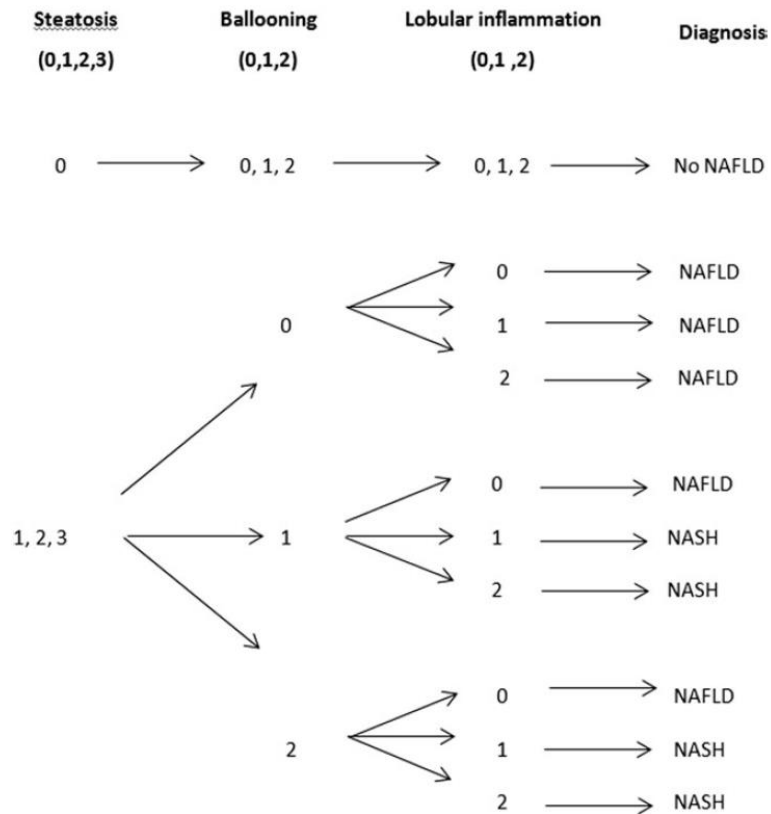


Figure 1.1. 2 : The FLIP algorithm used for diagnosing NAFLD and NASH. This algorithm is only a classification method and does not necessarily denote the order in which the lesions appear in the course of disease progression. (from: Bedossa P. et al., HEPATOLOGY, 2012[11])

Both the NAS and SAF scores have similar histological definitions of steatosis grading. However, lobular inflammation has 4 grades in the NAS score and only three in the SAF score. Also, in contrast to NAS, the SAF score dissociates steatosis from activity as these lesions have different pathogenesis and prognosis. In addition, hepatocyte ballooning grading in NAS is based on number of ballooned cells (none, few, many), while in the SAF score, it is based on size of ballooned hepatocytes. Moreover, the SAF score takes into consideration fibrosis stages in contrast to the NAS scoring system.

1.1.5. Other definitions of the progressive form of NAFLD

It is increasingly recognized that fibrosis rather than activity is the main prognostic factor of NAFLD [43-45]. Poynard T. et al. have proposed a simplified definition of NASH as activity grade $A \geq 2$ without the requirement of steatosis and without the requirement of both lobular inflammation and hepatocyte ballooning [46]. Moreover, they qualify progressive NAFLD as significant metabolic liver disease (MLD), defined as fibrosis stage $F \geq 2$ or activity grade $A \geq 2$.

Another definition of the progressive form of NAFLD that has been recently proposed is NASH-related fibrosis, also called NAFLD with significant fibrosis [47] or fibro-NAFL. NASH-related fibrosis is defined among the patients with NAFLD as fibrosis stage $F \geq 2$ with no consideration for presence or absence of NASH [48, 49].

In contrast, fibro-NASH is defined by the presence of NASH with a NAS value ≥ 4 and fibrosis stage $F \geq 2$ [50]. This definition is based on the guidance by the Food and Drug Administration (FDA) and the European Medicines Agency (EMA) on the requirements for inclusion of patients in clinical trials. These inclusion criteria comprise a diagnosis of non-cirrhotic NASH, defined as a NAS score of ≥ 4 , with 1 point each for lobular inflammation and ballooning, and a NASH CRN fibrosis stage of 2 or 3 [51].

NASH-related fibrosis definition was used for assessing the diagnostic accuracy of the MEFIB score that combines magnetic resonance elastography (MRE) with fibrosis-4 (FIB-4; a serum test based on aspartate aminotransferases (AST), alanine aminotransferases (ALT) and platelet count) in candidates for pharmacological therapies [47, 48]. Fibro-NASH classification has been used in the FAST (FibroScan-AST) score that combines liver stiffness measurements with Fibroscan and AST:ALT ratio. Fibro-NASH classification has also been used in the MAST score (magnetic resonance imaging (MRI)-AST score) that combines MRI-PDFF (proton density fat fraction measurements) and MRE [47, 50, 52].

Differentiating the progressive form of NAFLD defined as NASH, significant MLD, NASH-related fibrosis or fibro-NASH from the early stage (NAFL) still relies on histologic analysis which requires liver biopsy. However, this method has multiple limitations since it is an

invasive and expensive procedure and has high sampling variability. Moreover, NAFLD histopathologic features, particularly hepatocyte ballooning can be hard to assess even by expert liver pathologists [42, 53]. To investigate other possible noninvasive and reliable methods for diagnosing NAFLD, the use of animal models of the disease is required.

1.2. Preclinical models of NAFLD

1.2.1. Model design considerations

Although much has been elucidated about the molecular and cellular mechanisms involved in the pathophysiology of NAFLD since its first description few decades ago, there is still a lot to clarify regarding its diagnosis, prognosis, prevention, and treatment. Studying NAFLD in human subjects has many challenges especially with the slow, variable and nonlinear progression of the disease and the limitations to access liver tissue and perform experimental drug studies in NAFLD patients. Therefore, preclinical models that mimic human histopathology of this disease are needed. The use of animal models allows for controlled experiments on multiple levels including diet, exercise, study duration, tissue sampling at defined intervals, association of multiple measured endpoints (neuro-endocrine, metabolic, immune, etc.), potential genetic manipulations and the possibility of tracking physiological mechanisms during disease progression or reversal [54, 55].

Animal models cannot display pathological features that are strictly identical to those in humans. However, they enable studying specific pathogenic pathways or specific histopathological features. An ideal animal NAFLD model should display similar risk factors as in humans, including obesity, type 2 diabetes and metabolic syndrome. Moreover, it should be induced with a diet close to human diets. The reproducibility of the model and its robustness regarding the sensitivity to light-dark cycles, housing conditions and ambient temperature [54-58], as well as its cost and availability, should be considered when selecting an animal model.

The severity of NAFLD/NASH depends on the duration of the diet and the animal species. Rodents (mice and rats mainly) are most frequently used in NAFLD modeling. These species,

especially mice, are typically preferred because of their small size, low-cost, short lifespan and simplicity in genetic manipulation. The gender of the animal has also an impact on the development and progress of the disease since hormones, particularly estrogens, are protective against NASH [59-61]. Moreover, animal strain has been shown to influence disease progression [56, 62]. The C57BL/6 mouse strain and Wistar and Sprague Dawley rat strains are widely used because they develop obesity, type 2 diabetes and the progressive forms of NAFLD [56, 59, 63].

Preclinical models of NAFLD are typically classified as dietary-based, genetically altered or chemically induced models and many of them are a combination of these different factors. Dietary-based animal models of NAFLD are typically based on overnutrition using high amounts of nutrients such as fat, glucose, sucrose and fructose. However, most of these models relying only on overnutrition require diet induction over long durations to progress to severe stages of NASH or NASH with significant fibrosis. Hence, to promote the progression of the disease, dietary-based models can be associated with methionine and choline deficiency which causes hepatic fat accumulation with inflammatory response and fibrogenesis. High fat diet (HFD), high fat, glucose, sucrose, fructose, methionine and choline deficient (MCD) diet, choline-deficient L-amino-defined (CDAA) diet, high cholesterol diet (HCD), Western diet and cholesterol and cholate are among the commonly used dietary-based models. To induce the progressive stages of NAFLD from isolated hepatic steatosis to NASH and NASH with significant fibrosis, these diets can be used separately or combined.

The three preclinical models of NAFLD that were used in this project and are most relevant to studying hepatic steatosis as well as NASH, advanced stages of fibrosis, cirrhosis and hepatocellular carcinoma are described in the following section.

1.2.2. Models used in the present work

1.2.2.1. High Fat Diet (HFD)

High fat diet was first described as a liquid form of diet and has been used for decades to study metabolic syndrome characteristics and pathophysiology. There are several high fat – based diets (see Table 1.2.1) but the standard HFD is composed of 71% fat, 11%

carbohydrates, and 18% proteins [54, 56, 61]. With 45–75% of total caloric intake derived from fat, this diet allows to replicate both the histopathology and pathogenesis of human NAFLD with the risk factors observed in human patients including obesity and insulin resistance. The pathological outcome, however, is not as severe as NASH and advanced fibrosis but mostly limited to hepatic steatosis and early stages of inflammation and fibrosis with no ballooning [55, 61, 64]. Also, the effects of this diet seem to be dependent on multiple factors including the species, strain, sex, duration and fat content of the diet, and composition of gut microbiota which limits its use in NASH studies [54, 61, 65]. It has been reported that rats fed with HFD for 3 weeks developed insulin resistance with marked panlobular steatosis, inflammation and fibrosis [66] while mice fed with HFD displayed similar results after 16 weeks of diet [67].

1.2.2.1. Choline Deficient L-amino acid - High Fat Diet (CDA-HFD)

Choline is an important nutrient for both humans and animals and is stored and metabolized in the liver. A deficiency in choline alters fatty acid oxidation in liver cells and promotes lipid synthesis, oxidative stress, and inflammation, leading to liver fibrosis [54, 56, 68]. The choline-deficient, L-amino acid-defined (CDAA) dietary model, a model with a deficiency in choline and with proteins replaced with an equivalent and corresponding mixture of semisynthetic L-amino acids [69], has been reported to develop hepatic steatosis, inflammation and hepatocyte injury resulting in NASH, advanced liver fibrosis and hepatocellular carcinoma [69-71]. But these histological features require a long time frame to develop (20–22 weeks) [68, 72]. Also, animals with CDAA diet do not display a metabolic phenotype like that of humans as the animals do not gain weight and do not display insulin resistance or any changes in peripheral insulin sensitivity [54, 56, 73, 74]. Combined with a HFD, the choline-deficient, L-amino acid-defined, high-fat diet (CDA-HFD) results in early development of NASH with fibrosis (6–9 weeks of diet). Multiple versions of the CDA-HFD model have been developed recently [73, 75-78] (see table 1.2.2). However, even with the high-fat component, this model still fails to generate the metabolic syndrome features seen in human NAFLD such as obesity and IR [56, 73]. Hence, this animal model should not be considered when studying the metabolic profile of the disease.

Table 1.2. 1: Examples of high fat diets used to induce NAFLD/NASH with diet composition and the resulting NAFLD histological features, displayed according to diet duration.

Reference	Model	Diet composition	Duration	Histological features
Park S. et al., Nutrients. 2016 [79]	HFD	45% of the energy from fat with 35% from lard and 10% from soybean oil	12 weeks	Mild steatosis, inflammation and ballooning
Eccleston H. B. Antioxid Redox Signal. 2011 [67]	HFD	71% total calories as fat, 11% as carbohydrate, and 18% as protein	16 weeks	hepatic steatosis (verified by the increase in liver triglyceride levels) and multiple ballooned hepatocytes
Tetri L. H. et al., Am J Physiol Gastrointest Liver Physiol. 2008 [80]	HFD	45 kcal% rich in trans fats (30% of fat content) + Fructose in drinking water	16 weeks	substantial steatosis with necroinflammatory lesions
Charlton M. et al., Am J Physiol Gastrointest Liver Physiol., 2011 [58]	HFD	60% of energy as fat (milk fat, 0.8% saturated), + drinking water with high-fructose corn syrup (HFCS, 42 g/l final concentration)	25 weeks	Significant steatosis, with early inflammation and ballooning, No fibrosis
Nakamura A. et al., Diabetologia (2012) [81]	HFD	22% saturated fatty acid (12.6% palmitic acid, 7.5% stearic acid) + 77% unsaturated fatty acid (64.3% oleic acid, 10.2% linoleic acid)	60 weeks	NASH with steatosis, Inflammation, hepatocellular ballooning and fibrosis with hepatic tumors (dysplastic nodules, adenomas or well-differentiated carcinomas)

1.2.2.2. Western Diet (WD) combined with CCl₄ administration

Western style diets are high-fat diets mimicking typical human high-fat diets in North America and Europe [82, 83]. Composed of high-fat, high-fructose (or sucrose), and high-cholesterol levels (the composition of the diet may vary but it is usually composed of 21% fat, 41% sucrose, and 1.25% cholesterol with high sugar solution for drinking (23.1g/L d-fructose and 18.9 g/L d-glucose); see Table 1.2.3). Western diets (WD) have been widely used to generate mouse NASH models because of their capacity to develop hepatic steatosis and progress to

NASH and fibrosis along with key phenotypes of human NAFLD including obesity, insulin resistance, hypercholesterolemia, and hypertriglyceridemia [10, 54, 57, 58, 65, 83]. It has been reported that mice fed with WD for 9.5 months developed both NASH and significant fibrosis [83]. However, the major limitation of this animal model is that it does not completely evolve to acute NASH and advanced fibrosis even with long-term feeding which makes it unsuitable for drug testing because of the cost and duration of diet feeding and drug treatment [56, 58, 65]. It has been demonstrated that combining WD with low weekly intraperitoneal CCl₄ administration (typically 0.2 µl (0.32 µg)/g of body weight) provides a preclinical NASH model that rapidly produces key histological and transcriptomic characteristics of human NASH (within 12 weeks), and progress to advanced fibrosis and hepatocellular carcinoma (in about 24 weeks) as the pro-inflammatory properties of CCl₄ serve to speed up the pathologic evolution [10]. Hence, this preclinical model can be suitable for investigating pathophysiology and progression of NAFLD from hepatic steatosis to NASH and hepatocellular carcinoma.

Table 1.2. 2: Examples of CDA-HFD models used to induce NAFLD/NASH with diet composition and the resulting NAFLD histological features, displayed according to diet duration.

Reference	Model	Diet composition	Duration	Histological features
Chiba T. et al., PLOS ONE 2016 [75]	CDA-HFD	46 kcal % Fat, 36 kcal % carbohydrate, 18 kcal % protein and 0.1 or 0.2 or 0.4 or 0.6 methionine	12 weeks	Higher steatosis, inflammation and fibrosis in 0.1% and 0.2% methionine groups than in 0.4% and 0.6% groups with low ballooning grades in all the groups. 0.1% and 0.2% methionine induced NASH, whereas 0.4% and 0.6% attenuated the induction of NASH by CDA-HFD
Matsumoto M. et al., International Journal of Experimental Pathology 2013 [73]	CDA-HFD	60 kcal % fat and 0.1% methionine	14 weeks	Advanced steatosis with mild inflammation and ballooning and significant fibrosis
Yasud D. et al., Biological and Pharmaceutical Bulletin 2020 [77]	CDA-HFD	62% kcal fat and 0.1% methionine	14 weeks	Remarkable accumulation of lipid droplets and leukocytes, as well as fibrosis and significant inflammation factors
Suzuki-Kemuriyama N. et al., FEBS Open Bio 2021 [78]	CDA-HFD-0.1	45 kcal % fat and 0.1% methionine	26 weeks	Severe NASH with marked steatosis, inflammation, ballooning and fibrosis
	CDA-HFD-0.6	45 kcal % fat and 0.6% methionine	26 weeks	Mild NAFL with little to no inflammation or fibrosis
Ikawa-Yoshida A. et al., International Journal of Experimental Pathology 2017 [76]	CDA-HFD	60 kcal % fat and 0.1% methionine	36 weeks	Severe NASH with steatosis, inflammation and hepatocyte injury with advanced hepatic fibrosis and progression towards hepatocellular carcinoma

Table 1.2. 3: Examples of Western diets used to induce NAFLD/NASH with diet composition and the resulting NAFLD histological features, displayed according to diet duration.

Reference	Model	Diet composition	Duration	Histological features
Ishimoto T. et al., Hepatology. 2013 [84]	Western diet	36% calories from fat (9% corn oil and 27% butter), + 43.2% calories from carbohydrate with sucrose (30% sucrose calories)	15 weeks	Early NASH with severe steatosis with mild inflammation and fibrosis
Machado M. V. et al., PLoS ONE, 2015 [57]	Western diet	45% energy from fat with 0.2% cholesterol + drinking water with High-fructose syrup (42 g/L, 55% glucose and 45% fructose)	16 weeks	Early NASH with severe steatosis, mild inflammation, ballooning and fibrosis
Tsuchida T. et al., J Hepatol. 2018 [10]	Western diet	21.1% fat, 41% sucrose, and 1.25% cholesterol + high sugar solution (23.1g/L fructose and 18.9 g/L glucose.	24 weeks	Early NASH with advanced steatosis, mild inflammation, ballooning and fibrosis
	Western diet + CCl ₄	The same Western diet + CCl ₄ at the dose of 0.2 µl (0.32 µg)/g of body weight	24 weeks	Advanced NASH with severe steatosis, inflammation, ballooning and fibrosis
Charlton M. et al., Am J Physiol Gastrointest Liver Physiol., 2011 [58]	Western diet (Fast food)	40% of energy as fat (milk fat) with 2% cholesterol + drinking water with High-fructose corn syrup (HFCS, 42 g/l final concentration)	25 weeks	NASH with pronounced steatosis, inflammation and ballooning, and advanced fibrosis
Asgharpour A. et al., J Hepatol. 2016 [65]	Western diet (DIAMOND)	42% kcal from fat with 0.1% cholesterol + a high fructose-glucose drinking water (23.1 g/L fructose +18.9 g/L glucose)	52 weeks	NASH with prominent steatosis, inflammation and cell ballooning, severe bridging fibrosis and spontaneous hepatocellular carcinoma
DeLeve L. D. et al., The American Journal of Pathology, 2008 [83]	Western diet	41% of calories from fat, 43% calories from carbohydrate, and 17% of calories from protein	9.5 months	NASH with Marked steatosis, inflammation, ballooning and significant fibrosis

1.3. Quantitative Magnetic Resonance Imaging (MRI) for the diagnosis of NAFLD

Currently, the gold standard for performing the diagnosis, assessing the prognosis and the treatment efficacy in NAFLD is histopathological scoring after liver biopsy. However, this method is invasive, costly and has high sampling variability. Moreover, the assessment of NAFLD histopathologic features in liver tissue is a subjective procedure. Liver histology for the assessment of NAFLD has been reported to have a modest inter-observer agreement [42, 85-90]. Therefore, reliable, precise, and non- or, at least, minimally invasive biomarkers need to be investigated.

Magnetic resonance imaging (MRI) is a non-invasive, non-ionizing imaging modality that offers many applications in preclinical imaging research and clinical assessment. Based on the principles of nuclear magnetic resonance first described by Isidor Rabi in 1938, it allows to explore multiple types of soft tissue contrast throughout the whole body and provides extremely useful information on many biological, biochemical, and medical features. MRI has many advantages among which the possibility of imaging whole organs, eliminating sampling variability, the safety of the method as compared to other imaging methods, and the multiparametric in vivo assessment.

Multi-parametric MRI has emerged as a useful tool to diagnose NAFLD and assess its severity. The MRI-based proton density fat fraction (PDFF) method has been reported to be useful in assessing hepatic steatosis. Magnetic resonance elastography (MRE) has been proven very effective for diagnosing hepatic fibrosis by measuring liver tissue stiffness in addition to other biomechanical parameters. T1-relaxation time mapping has been used to detect liver inflammation and fibrosis. Moreover, diffusion weighted imaging (DWI) has been investigated for the identification of multiple changes in hepatocytes including accumulation of fat droplets and cell ballooning.

1.3.1. Proton Density Fat Fraction (PDFF)

MRI can detect the signal from protons in molecules such as water and triglycerides. Because of the relative electronegativity of the O and C elements, the electronic density of protons in

water (O-H bond) is less than in triglycerides (C-H bond), which results in a slightly higher resonance frequency for the water protons [91]. This difference between water and fat proton resonances, known as the “chemical shift”, is very small (~1000 Hz at 7T [92]) and is measured in parts per million (ppm; dimensionless unit) .

The chemical shift phenomenon can be used to quantify the amount of water and triglyceride signal within the tissue allowing for accurate measurement of PDFF [93, 94]. PDFF is a characteristic of the tissue that indicates the concentration of triglycerides and is expressed as the ratio between proton density from triglycerides and the total proton density from both triglycerides and water. Protons bound in the lipid bilayer of cells such as in cholesterols are imperceptible by standard MRI. Two methods exist for the measurement of PDFF: magnetic resonance spectroscopy (^1H -MRS) and MRI-PDFF. In ^1H -MRS, chemical shift between water and fat-based chemical species is used to obtain direct noninvasive quantification of hepatic fat concentrations [91, 95, 96]. However, this method is limited by its measurements of small volume tissue samples, cost, long acquisition time and complex post-processing methods with potential errors [97, 98].

For the MRI-PDFF method, a gradient-echo sequence is used to measure the signal at multiple echo times. As the water and fat protons precess at different frequencies, a phase interference occurs between their signals measured at different echo times. The signals of water and fat protons add when they are measured with in-phase echo time and cancel when they are measured with opposed-phase echo time. Thus, the total signal from water and fat protons is assessed with in-phase echoes, and the signal from the protons of water from which the fat signal is subtracted is acquired separately with opposed-phase echoes [99, 100]. Furthermore, the signal is fitted into an algorithm that calculates fat and water proton concentrations, resulting in a liver fat percentage ranging between 0% and 100%. PDFF estimation can be performed with two approaches: either with the complex value of the MRI signal including both the phase and the magnitude or with only the magnitude of the signal. Complex-based PDFF methods include a full PDFF range of fat concentration (0 - 100%) and have an enhanced signal to noise ratio (SNR) values, whereas magnitude-based approaches have a limited fat concentration range of 0 – 50%, lower values of SNR and low sensitive to system instabilities. Both approaches can estimate hepatic fat concentration of the entire

liver, which is within the dynamic range of magnitude-based method ($\leq 50\%$ typically in the liver) with excellent accuracy and precision. A large number of studies have been performed to validate both approaches of MRI-PDFF quantification including phantom [101, 102] and animal studies [103, 104], as well as studies in ex-vivo human liver tissue [105].

MRI-PDFF is easily amenable to automatic reconstruction of parametric maps without user input other than the selection of the region of interest for the measurement [94]. MRI gradient-echo based measurements have the advantage that they can yield maps of the PDFF and can be used to analyze liver fat in a spatially resolved fashion at the acquisition resolution, whereas $^1\text{H-MRS}$ results are limited to a box-shaped volume determined at acquisition. Several studies have compared the performances of MRI-PDFF and $^1\text{H-MRS}$ [106-109], in some cases with liver histology as the reference standard [110-112]. These studies have reported a similar accuracy in quantifying steatosis for both MRI and MRS PDFF methods with MRI-PDFF being slightly better in some of these studies.

The measurement of PDFF by MRI provides accurate, repeatable and reliable quantitative estimation of hepatic steatosis throughout the whole liver with high intra- and inter-observer agreement [100, 113-116]. Although several studies have confirmed the high correlation between PDFF quantification of liver fat and histological grades of steatosis, these two evaluations of hepatic fat accumulation are not equivalent [117, 118]. Among all the non-invasive imaging methods, MRI-based PDFF is currently recognized as the most accurate method for quantitative assessment of hepatic fat content as it showed the highest diagnostic accuracy for hepatic steatosis in patients with NAFLD.

Multiple studies have reported that this method can accurately distinguish small amounts of microscopic liver fat (even 5%) [119-122]. Tang et al. reported a sensitivity of 68% and specificity of 98% in detecting histologic steatosis grade 0 versus 1 with MRI-PDFF [123]. In a two-center prospective validation study performed on 161 adult patients with liver diseases who underwent liver histology, MRI-PDFF demonstrated high accuracy for hepatic steatosis grades (AUC = 0.90 - 0.94) [124]. A cross-sectional study carried out by Imajo K. et al. in Japan including 142 patients with NAFLD (identified by liver biopsy) showed that MRI-PDFF is significantly superior to transient echography-based Controlled Attenuation Parameter (CAP) in the diagnosis of each steatosis grade (steatosis ≥ 1 : PDFF AUC = 0.96, CAP AUC = 0.88,

steatosis ≥ 2 : PDFF AUC = 0.90, CAP AUC = 0.73, steatosis ≥ 3 : PDFF AUC = 0.79, CAP AUC = 0.70) [125]. In a study performed by Garteiser P. et al. in morbidly obese patients undergoing bariatric surgery, MRI-PDFF performed better than CAP for grading steatosis ($S > 33\%$, AUC 0.97 versus 0.78; and $S > 66\%$, AUC 0.93 versus 0.75; $p = 0.0015$) and diagnosing NASH (AUC 0.82 versus 0.68) [126]. A meta-analysis was conducted by Qu Y. et al. in 1,100 patients with chronic liver disease to evaluate the diagnostic accuracy of MRI-PDFF for the assessment of hepatic steatosis with liver histology as reference standard. In this study, high diagnostic performance of MRI-PDFF was shown to differentiate between steatosis grades ≥ 1 , ≥ 2 and ≥ 3 with AUCs of 0.98, 0.91 and 0.92 respectively [127]. In another recent meta-analysis including a total of six studies (635 patients), it was concluded that MRI-PDFF has excellent diagnostic value for the assessment of liver fat accumulation and classification of histologic steatosis in patients with NAFLD [128].

In a recent study conducted by Kim M. et al., MRI-PDFF was used as a reference to evaluate the diagnostic performance of conventional ultrasonography in assessing hepatic steatosis [129]. PDFF has a better performance in quantifying hepatic steatosis in patients with morbid obesity than ultrasonography and transient elastography. However, morbid obesity can be a limitation of this method depending on the weight of the patient as the MRI scanner has a maximum weight application factor. Also, this method have been used by Loomba R. et al. as the diagnostic reference of liver fat concentration when studying the effects of GS-0976 on hepatic steatosis in a treatment study [130].

Multiple studies also have investigated MRI-PDFF to quantify hepatic fat content in mice models [103, 104, 131, 132]. In a study performed by Hines C. et al., [103] in an ob/ob mouse model of hepatic steatosis, MRI-PDFF measurements were highly correlated with lipid extraction and qualitative and quantitative steatosis histologic analysis ($r^2 = 0.92, 0.87, 0.82$, respectively). Another study was conducted by Runge G. et al. [131] to compare three non-invasive MRI methods and two histopathological approaches against the reference standard of biochemically determined liver triglyceride content. The results showed a high correlation between MRI-PDFF values and liver fat content. Ryu J. E. et al. [132] performed a study for the assessment of NAFLD in a mouse model with histological analysis as gold standard and

the results showed that MRI-PDFF can effectively diagnose severe from mild hepatic steatosis, with an AUC of 0.92.

Multiple factors may confound PDFF measurements including T1 bias, noise bias, T2* decay, spectral complexity of fat, and eddy currents [94, 95, 108]. Fat and water have different T1 relaxation times which causes a relative signal amplification of fat compared to water. Thus, the value of fat concentration can be overestimated if T1 weighting is present but not accounted for. This T1 relaxation effect can be diminished with low flip angle [95, 133, 134].

Noise can influence the PDFF measurements. The calculation of fat-fraction is, for most of PDFF estimation methods, based on magnitude images which can create a noise bias in areas with low signal because of skewed noise distribution. Clinically, this effect can lead to imprecise PDFF estimation in regions with low fat content and or low SNR, which may result in difficulties in the diagnosis of mild steatosis. Multiple methods and algorithms have been developed to reduce this noise bias [108, 133].

T2* decay causes signal loss among echoes, and is magnified in the presence of iron deposition, which leads to a significant bias in the estimation of fat [134, 135]. Disturbed levels of iron displayed by elevated serum ferritin has been reported in approximately one third of NAFLD patients. This excessive iron deposition is essentially caused by the inhibition of iron mobilization from hepatocytes and Kupffer cells [136]. The T2* effect can be accounted for with triple or multiple echo acquisitions and signal models in which a T2* decay term is incorporated [95].

Fat chemical spectrum covers several different spectral components (CH₃, CH₂, CH₂COOR and CH=CH groups at 0.9, 1.2, 2.2 and 5.3 ppm respectively). The phase interaction between these fat components can lead to inaccurate quantification of steatosis [134]. Several algorithms have been recently developed to obtain an accurate spectral modeling of fat signal and therefore obtain an accurate estimation of fat fraction [95, 134, 135, 137]. Moreover, in multi-echo acquisitions, eddy currents can have an impact on the relative phase of the acquired echoes resulting in errors in water-fat separation especially at low (~0%) and high (~100%) fat concentrations. These errors can be minimized with a magnitude-based method where the phase of all echoes is suppressed, but at the expense of a significantly degraded

signal-to-noise ratio. In the last decade, multiple algorithms and reconstruction methods have been developed to correct the phase errors caused by eddy currents [138-140].

Of note, complex-based MRI-PDFF methods are FDA approved, have been successfully implemented in multiple MRI scanners including GE Healthcare, Siemens and Philips, and has been successfully applied in several clinical studies [112, 122, 141, 142]. These methods were also implemented in preclinical MRI system Bruker and performed in multiple preclinical studies [103, 104, 143, 144]. This non-invasive, quantitative, precise and reproducible method is emerging as one of the leading biomarkers to assess hepatic fat, particularly in NAFLD studies. As such, it is an important tool in the assessment of NASH with imaging, because hepatic steatosis is an important marker for NASH diagnosis. However, hepatic steatosis is not the only marker required for diagnosis of NASH, in which ballooning and inflammation also play a constitutive role, and hepatic steatosis is not linked to fibrosis, which is an important component of NASH-related disease. Hence the specificity of PDFF measurement towards steatosis makes it necessary to use multi-modality assessment for the diagnosis of NAFLD, NASH and liver fibrosis.

1.3.2. Magnetic Resonance Elastography (MRE)

It is known that many diseases can be associated with changes in the tissue mechanical properties. For centuries these changes have been assessed with palpation. Although palpation can be effective, it is qualitative, subjective and can only be applied on accessible parts of the body [145]. MRE is a kind of “palpation by imaging” based on a phase contrast MRI method that allows for non-invasive quantitative measurements of the tissue mechanical by assessing the displacements generated by the propagation of mechanical waves into tissues [145-147]. As described by Muthupillai R. et al. [148], MRE is becoming increasingly important for the assessment of hepatic diseases as it has been reported to accurately differentiate the early stages of fibrosis from advanced stages [113, 146, 149, 150].

The dynamic MRE approach has three main steps: (1) application of mechanical waves into the body, (2) measurement of tissue displacements caused by the mechanical wave with a phase encoding MRE acquisition, and (3) estimation of the mechanical parameters from the displacement data with an inversion algorithm [145, 146, 151].

1.3.2.1. Mechanical waves generation

An external driver generates the mechanical waves at specific amplitude, frequency, phase and in an operating mode that is dynamically and precisely synchronized with the operation of the MRI system. The transducers include electromagnetic, piezoelectric, pneumatic and electromechanical acoustic transducers [152-156]. The pneumatic driver design is the most widely used in clinical practice because it is simple and appears comfortable for the patients (figure 1.3.1). The source of the mechanical excitation can also be an internal by using the cardiovascular activity for example [152].

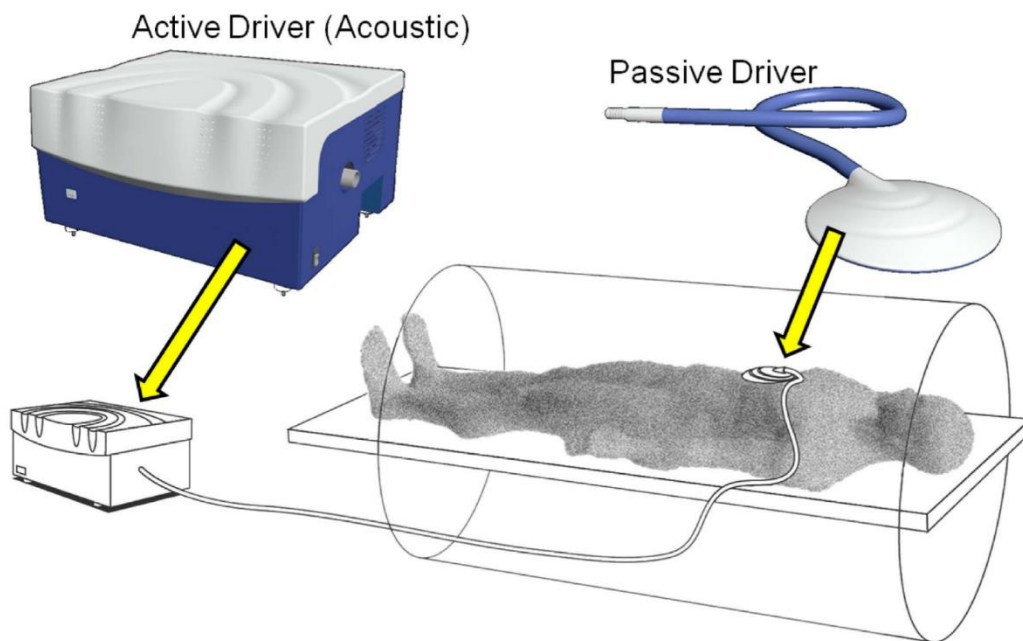


Figure 1.3. 1: Illustration of the pneumatic driver design used in clinical hepatic MRE. Mechanical waves are transmitted from the active driver system placed outside the scanner room to the passive driver placed on the liver via a flexible plastic tube. (Venkatesh S. K., et al., J Magn Reson Imaging 2014 [157])

In rats and mice, the actuators need to be small, compatible with small bore scanners and capable of generating high frequency waves. Small piezoelectric actuators are typically used

directly inside the magnet bore [158]. These actuators can generate mechanical waves at high frequencies with good penetration and high resolution.

External electromechanical acoustic transducers also have been introduced as mechanical wave generators. In this model, a carbon fiber rod is used to transmit the waves from the wave generator to a piston positioned against the studied organ [159, 160]. This type of actuators has been successfully used to generate mechanical waves for the quantification of liver fibrosis with three dimensional MRE in thin liver rat slices [160], to assess rapid changes in the structure of individual neurons in rat brain after cannabinoid induction [159] and to diagnose NASH in mice liver [161]. Of note, when imaging small animals, artifacts caused by respiratory motion should be taken into consideration because breath holding is not feasible and acquisitions are typically performed under anesthesia with variable respiratory rate. Respiratory gating can be used to limit this type of artifact but this may increase the acquisitions time.

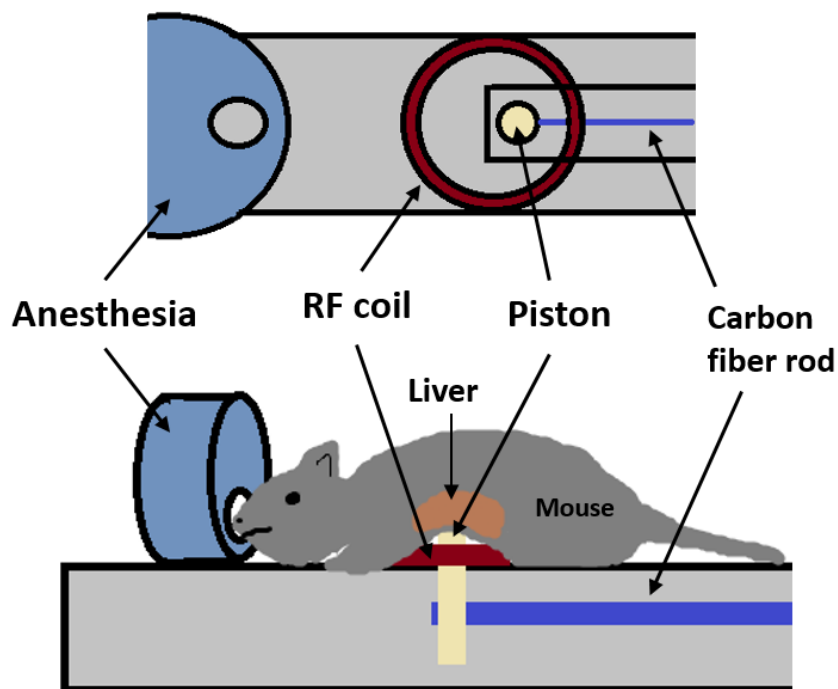


Figure 1.3. 2: Illustration of the external electromechanical acoustic transducer (this type of transducers has been used in MRE experiments in this PhD project). Mechanical waves are transmitted by a carbon fiber rod from a remote vibration generator to a piston in contact to the liver of the animal placed in the prone position.

1.3.2.2. MRE sequences

To image the propagation of the mechanical waves, multiple phase-contrast MRE sequences including gradient-recalled echo [148, 162-165], spin-echo [166, 167] and spin-echo imaging with echo-planar imaging (EPI) readout [168-171] can be used, with added cyclic motion-encoding gradients (MEGs) at the same frequency as the mechanical excitation frequency or not [165, 172]. These added MEGs are typically composed of two or more opposite gradient lobes with identical amplitude and duration. The MEGs are synchronized with the applied vibration [173]. With these MEGs, the cyclic motion of the spins develops phase shifts that can be determined on the resulting wave images providing information on the propagation of the mechanical waves within the tissue. The MEGs may be applied in one specific direction (often orthogonal to the imaged plane) or in the three directions of space.

The gradient-echo based MRE sequence was developed by Muthupillai R. et al. in 1995 [148] at the Mayo Clinic. In this method, successive phase offset values (θ) between the mechanical excitation and the trapezoidal bipolar MEGs are imposed to acquire the displacement field at different moments of the mechanical excitation period. This method has a major limitation related to its sensitivity to the magnetic field inhomogeneity, which may provoke detrimental phase shifts affecting the phase accumulation originating from spin motion. This bias can be suppressed by reconstructing a final phase difference image from two phase images with opposite MEG polarities. However, this increases the acquisition time.

The spin-echo based MRE sequence was developed by Sinkus R. et al. in 2000 [174] using sinusoidal bipolar MEGs synchronized with the external vibration and applied on either side of the refocusing pulse along each of the encoding axis to encode the three-dimensional displacement field. Again, the displacement field is acquired at different moments of the excitation period by shifting the mechanical excitation from a phase offset (θ) with respect to the onset of the bipolar gradient. The refocusing pulse used in this method provides a relative immunity to field inhomogeneity. However, the refocusing pulse increases the echo time and thus the total acquisition time. Increasing TE can be particularly critical when studying tissues with short T_2 , such as the liver.

Several methods have been proposed to decrease the acquisition time including EPI. In EPI, the whole k-space can be acquired with a single radiofrequency excitation (single shot) or a few radiofrequency excitations (multi-shots), accelerating the standard gradient-echo or spin-echo imaging sequences. With this method, acquisition time can be decreased substantially. Huwart et al., reported an acceleration factor of 10 when using SE-EPI MRE instead of standard spin-echo MRE [170]. However, EPI MRE is limited by magnetic field inhomogeneities, T2* blurring and off-resonance artifacts. Therefore, partial k-space coverage (against T2* blurring) and fat-suppression preparation modules (to limit the influence of off-resonance artifacts) are often used.

Fractional encoding method may be used to reduce the MRE acquisition time. Fractional encoding consists of using only one bipolar gradient with a frequency higher than the frequency of the mechanical excitation resulting in encoding only a fraction of one vibration cycle per repetition time (TR) and so reducing TE and TR. A gradient-echo fractional encoding MRE sequence has been developed by Garteiser P. et al. [165]. The sequence is composed of multiple imaging blocks. Each block contains multiple shots, which have a duration of an integer number of vibration cycles. During each shot, a gradient-echo based MRE sequence with fractional encoding is performed. With this method, a multi-frequency excitation can also be encoded in only one acquisition. The limitation of fractional encoding is the reduced sensitivity for motion encoding, which can limit the assessment of displacement fields with low amplitudes.

In the clinics, gradient-echo MRE is currently the most commonly method for hepatic applications with MEG imposed along the longitudinal axis of the body (z direction). Of note, hepatic MRE may be limited in patients with moderate to severe levels of iron overload because of low SNR. Moreover, MRE measurements have been reported to be dependent on the magnetic field strength. The technical failure rate of with gradient-echo MRE was found to be low at 1.5 T but higher at 3.0 T [175, 176]. MRE measurements performed on systems from different manufacturers are reported to be highly comparable [147].

1.3.2.3. Inversion algorithms

Several inversion algorithms have been introduced to obtain biomechanical properties of the material from the acquired data based on the equation of motion (the Helmholtz equation) that is typically simplified with multiple assumptions and approaches [145, 152, 153]. Usually, the studied tissue/material is assumed to be linear, and either elastic with a fast response to the applied mechanical excitation (no energy dissipation) or viscoelastic with a temporal response to the applied strain (with energy dissipation) [177]. Moreover, the material is typically assumed to be homogeneous and to have the same properties in all directions (i.e. isotropic). The assumption of tissue isotropy reduces the number of parameters in the equation of motion to two: the Lamé constants λ and G (also denoted as μ) that refer to the longitudinal and shear strains, respectively. Soft tissue has a Poisson's ratio nearly equal to 0.5 which makes it almost incompressible. In this type of tissues, Lamé constant λ is usually much larger than G making their calculation simultaneously a complex, numerically ill-conditioned process. However, the impact of the longitudinal strain λ can be simply neglected when the excitation is mainly shear or can be eliminated by filtering out longitudinal wave motion with bandpass filtering since the effect of longitudinal wave is at very low (near zero) spatial frequency or curl filtering as the displacement field corresponding to the longitudinal wave is curl free [177]. Curl processing approach was proposed by Sinkus R. et al. to eliminate the effects of λ from the equation of motion by applying curl operator to the acquired MRE displacement data [178]. Subsequently, the complex biomechanical parameter shear modulus G^* can be deduced from the Helmholtz equation with:

$$G^* = -\rho\omega^2 \frac{u}{\nabla^2 u} \quad (1)$$

Where \mathbf{u} is the complex harmonic shear displacement field, ρ is the density and ω is the angular frequency of the mechanical oscillation and ∇^2 is the Laplacian operator. The complex shear modulus $G^* = G' + iG''$ with G' being the storage modulus; the elasticity-related parameter, and G'' the loss modulus; the-viscosity related parameter. Several MRE inversion algorithms used in practice are based on this equation including direct inversion, algebraic Helmholtz inversion and algebraic inversion of the differential equation (AIDE) [179].

However, such algorithms are sensitive to noise. Data smoothing or regularization of the inversion to remove the effect of the noise is usually required [180, 181].

1.3.2.4. MRE parameters

The shear modulus G , a complex biomechanical quantity defined as $G^* = G' + iG''$ with units of kPa, is the most frequently reported MRE parameter. Measured at a given frequency, this complex quantity has a real part known as the storage modulus and commonly denoted as G' , and an imaginary part known as the loss modulus and usually referred to as G'' . The magnitude of the shear modulus ($|G^*|$) reflects the stiffness of a given material and thus is known as shear stiffness. Storage modulus G' represents the elastic behavior of the medium (i.e. its spring constant) and is sometimes called elastic modulus or elasticity. Loss modulus G'' represents the viscous behavior related to the attenuation of mechanical energy and is sometimes called viscosity [145]. These parameters are usually expressed in units of kilopascal (kPa; $1 \text{ Pa} = 1 \text{ N m}^{-2} = 1 \text{ kg m}^{-1} \text{ s}^{-2}$).

Energy dissipation related to viscosity can be represented by other parameters which are easily converted to each other. For instance, Loss tangent or loss factor (G''/G') is a direct estimation of the relative magnitude of the loss and storage moduli. Damping ratio ($\zeta = G''/2G'$) is a standard quantity in mechanics and it represents simply half of the loss tangent. A damping ratio of 1 is “critical damping” for a simple harmonic oscillator (i.e. the damping at which the displacement dies out as quickly as possible) [145]. Shear modulus phase angle ($\arctan[G''/G']$) refers to the phase lag between stress and strain (equals to 0° when the material is purely elastic, and to 90° when it is purely viscous)[145, 182].

MRE data can be expressed in terms of G^* as described above, which is based on the material behavior. These data can also be expressed in terms of the wavenumber k , which is a quantity describing the wave as it travels through the medium under consideration. The wavenumber k is a complex quantity ($k = \beta + i\alpha$) which real part β is the propagation coefficient, expressed in m^{-1} and which imaginary part α is the attenuation coefficient (m^{-1}). β can be understood as the inverse of the wavelength, while α describes the loss of the wave energy in a viscoelastic medium. The two representations of the material properties (in terms of properties of the medium through G^* or in terms of properties of the wave k) are interconvertible when

considering a monochromatic wave of angular frequency ω with: $k = \omega\sqrt{(\rho/G^*)}$. They also have different noise sensitivities [183].

Finally, wave speed (m/s) in MRE is a phase velocity that depends on both the storage and loss modulus (or, alternatively, on both the propagation and the attenuation coefficients). Reporting this quantity alone does not allow for separate description of the effects of these two quantities. It can be calculated as $c_s = \sqrt{|G^*|/\rho}$ (or alternatively, as $c_s = \omega/\beta$). Of note, the wave speed is defined as a phase velocity in MRE measurements, whereas in transient ultrasound measurements, it is defined as a group velocity that combines the behavior of a range of frequencies [145].

In MRE applications at a single frequency, it is recommended that two parameters be reported to capture the full tissue viscoelastic behavior. Pairs such as storage and loss moduli or shear modulus magnitude $|G^*|$ and phase angle or damping ratio are commonly used. Of note, these mechanical parameters are frequency dependent in soft tissues. Therefore, the frequency at which the value is measured should be clearly reported and carefully selected.

When performing MRE at different frequencies, a material that has purely elastic properties will display the same mechanical properties at all the studied frequencies. However, when the material has viscoelastic properties, it will exhibit frequency dispersion. G' and G'' will have frequency dependent behavior in viscoelastic materials. These changes in the viscoelastic parameters with frequency are increasingly being investigated as additional useful biomarkers [165, 168, 184]. MRE applications at multiple frequencies can be performed either separately with multiple acquisitions [184, 185] or simultaneously [186].

The measurements of mechanical parameters, particularly storage and loss moduli, at a single frequency are not based on any specific assumptions regarding rheological models. However, when examining data at multiple frequencies, different rheological models are commonly used, each assuming different behavior with frequency.

The spring-pot model (hierarchical organization of springs and dashpots) simulates the materials response to mechanical excitation as a powerlaw in time and frequency with an exponent (γ) [187-190]. The dimensionless power-law exponent or multifrequency dispersion

coefficient, γ represents the solid-liquid duality of biological soft tissues within the boundaries of 0 and 1 for pure elastic materials or viscous liquids [190-192]. In the spring-pot model, the measured dynamics of the complex shear modulus (i.e. G' and G'') are connected to the fractal geometry of complex structures in hierarchical systems. With only two parameters, usually noted k and γ , this model predicts the monotonic increase of the storage (G') and the loss moduli (G'') over frequency ω . The organization of springs and dashpots to a fractal ladder in this model emerges into parallel linear functions of $\log G'(\log \omega)$ and $\log G''(\log \omega)$ with identical slope (γ). Based on this, the ratio G''/G' is estimated to be a constant given by $\tan(\gamma \times \pi/2)$. The typical simple notation of the springpot powerlaw is given by: $G^* = \kappa(i\omega)^\gamma$ (with κ is the second springpot variable and can be converted to a shear modulus μ by assuming a specific viscosity η using $\kappa = \mu^{1-\gamma} \eta^\gamma$). Of note, the loss tangent or loss factor G''/G' mentioned above is typically frequency dependent and thus not comparable to γ of the springpot model. This model offers a better representation of soft tissue behavior in the frequency range of MRE than the Voigt or the Maxwell models. However, most multifrequency MRE applications are performed within a narrow frequency range, which can be a limitation when estimating the multifrequency dispersion coefficient [187].

The repeatability and reproducibility of MRE have been investigated [193-201] and the reported intraclass correlation coefficients (ICCs) for MRE repeatability are typically of the order of 0.9. Also, studies have been performed to assess hepatic MRE reproducibility with different scanners and reconstruction algorithms. The dependence of MRE reproducibility on field strength, pulse sequence and MRI vendor has been explored [193, 202-204]. These studies have agreed on the reliability of MRE for assessing liver stiffness, with some variability reported between image manufacturers, field strengths, and pulse sequences. Hepatic MRE reproducibility has also been assessed regarding the positioning of regions of interest (ROIs). Very good reproducibility results have been reported for manual drawing of large ROIs avoiding vessels and organ edges as well as for positioning of several circular ROIs interspersed among liver segments with ICCs typically above 0.9 [194, 195, 198, 200, 201, 205, 206]. Good reproducibility of MRE has been also reported in phantoms [204], in mice [207] and in rats [158] at 7T.

1.3.2.5. Hepatic MRE applications

1) *Diagnostic of hepatic fibrosis*

NAFLD comprises simple steatosis, the early stage of the disease, and NASH, the progressive form, which is histologically characterized by steatosis, lobular inflammation and hepatocellular injury with or without fibrosis. However, from a prognostic perspective, diagnosing fibrosis in patients with NAFLD is important because fibrosis is associated with overall and liver - related mortality, apart from other histological features [43].

The diagnostic performance of MRE in hepatic fibrosis has been assessed [164, 208-210]. Hepatic stiffness has been shown to increase with fibrosis stage. The increase in fibrillary collagen deposition, especially collagens I and III, caused by fibrogenesis process increases the stiffness of the hepatic tissue [211]. Indeed, MRE has shown good performance in differentiating patients with clinically significant hepatic fibrosis (F2–F4) from patients with early stages of fibrosis (< F2) [48, 167, 168, 170, 208, 209, 212-218].

Liver MRE has shown better diagnostic performance compared to other diagnostic approaches for staging liver fibrosis including conventional MRI markers [219, 220], gadoxetic acid-enhanced MRI [221], diffusion-weighted MRI [212, 222-226], serum biomarkers [157, 167, 219, 227, 228] and ultrasonography [47, 49, 209, 229-233]. In a head-to-head comparison study between MEFIB, MAST, and FAST for detecting significant fibrosis ($F \geq 2$) in 563 patients with biopsy proven NAFLD, MEFIB was better than MAST and FAST in diagnosing significant fibrosis [47].

Hepatic stiffness IG^* and storage modulus G' are the most reported MRE mechanical parameters for diagnosing liver fibrosis. Other MRE parameters related to viscosity or to viscosity/elasticity ratio (loss modulus G'' , phase angle α , damping ratio, and frequency dispersion coefficient) have a lower correlation with fibrosis [160, 167, 234, 235]. In several studies, it has been reported that the frequency dispersion coefficient decreases with increasing fibrosis stage [160, 168, 188, 234].

In preclinical studies of MRE with animal models, biomechanical parameters are reported to be very well correlated with quantitative measurements of fibrosis as well as with mechanical properties estimated with oscillatory rheometry [160, 236-244].

2) *Diagnostic of hepatic inflammation*

Inflammation and fibrosis are generally correlated in patients with chronic liver disease. Therefore, the changes in the biomechanical properties of the tissue because of inflammation can be hard to differentiate from those of fibrosis. Inflammation has been reported to either have an influence or not on hepatic stiffness measurement [173, 245-247]. These contradictory reports may at least be partially explained by the smaller influence of inflammation compared to fibrosis on liver stiffness [222]. It has been reported in several studies that patients with inflammation and fibrosis tend to have higher stiffness compared to those with fibrosis alone, which may lead to overestimation of fibrosis stage [158, 212, 248-250]. Moreover, it has been suggested in some MRE studies that viscosity-related mechanical parameters can be used to detect inflammation before the onset of fibrosis [235].

3) *Diagnostic of NASH*

The diagnosis of NASH with hepatic stiffness measurements was reported to have a moderate accuracy with AUCs of 0.73 [251], 0.74-0.76 [216], and 0.70 [252], which indicates the necessity of developing more advanced MRE methods to accurately diagnose of NASH in a NAFLD population. Preclinical and clinical showed that hepatic stiffness measurements increased in NASH before the development of hepatic fibrosis [158, 253]. This increase was found to be related to the development of inflammation and the activation of the stellate cells [158]. However, this increase associated with “inflammatory” NASH is lower than the increase associated with NASH and fibrosis. Loomba et al. reported AUCs of 0.74 and 0.98 respectively for MRE staging of NASH and NASH with advanced fibrosis [216].

With all the reported results from the different published MRE studies, investigating and identifying which MRE-derived biomechanical parameters should be used to diagnose NAFLD progressive forms from the early stage of the disease, and detect the different histopathological features of NAFLD is required.

1.3.3. T1 relaxation time mapping

T1 relaxation time represents the time needed for the longitudinal spin magnetization to reach 63% of its original state after the application of a radiofrequency pulse [254, 255]. This measure is a fundamental characteristic of soft tissue contrast in MRI. T1 relaxation time is also referred to as “spin-lattice” relaxation since it involves the loss of energy put into the spin system by the radiofrequency pulse to the surrounding macromolecules, i.e. the “lattice”. The concept of measuring the T1 relaxation time to distinguish between normal and diseased liver tissue was already used in the 1980s [256, 257] and has recently gained renewed interest. T1 mapping has been used in several medical research areas including cardiac imaging to detect myocardial edema, iron overload, myocardial infarcts and scarring [258]. Also, it has recently been used to detect hepatic inflammation and fibrosis. Several studies have reported that T1 values of the liver increases with the increase of the extracellular water and protein concentration observed in inflammation and fibrosis [259, 260].

Two approaches have been introduced to acquire T1 maps, either with inversion recovery (IR) or saturation recovery (SR) sequences [261]. For the IR sequence, a 180° radiofrequency pulse is applied to invert the z-magnetization, which then recovers with relaxation time T1, and at specific inversion times along the relaxation process, k-space lines are acquired either via spin or gradient echoes. Acceleration schemes such as fast spin echoes [262], or EPI [263] can be used to acquire several k-space lines during a single regrowth period. The sequence is repeated N times with variable TIs to produce N images along the T1 recovery curve. These N images are fitted and T1 measurements are retrieved. For the SR sequence, no inversion pulse is used. In this sequence, T1 regrowth is sampled by acquiring sequentially several images at different repetition times, and exploiting the saturation effect when $TR \sim T1$. This signal reflects T1 differences in tissues because of different amounts of longitudinal recovery during the TR period.

With both methods, the acquisition sequence is performed several times to appropriately sample the recovery curve which is then fitted to an exponential model. This exponential fitting model, which is typically an equation of the form $(A-B \cdot \exp(-t/T1))$, where A and B are fitting constants related to the equilibrium magnetization and type of preparation and t is the time after the preparation (i.e., either the inversion time (TI) or the time after saturation

pulse), is considered to be accurate only under the assumptions of perfect pulse, constant temperature, or where necessary, recovery times much larger than the T1 relaxation time. While both methods provide accurate and precise T1 measurements, their acquisition times are too long for clinical applications [264].

In this work, inversion recovery was used, exploiting the "flow-sensitive alternating inversion recovery (FAIR)" method [265, 266] but with only the nonselective inversion pulse. In this case the exponential fitting model is: $S = S_0 (1 - \beta \exp(-TI / T1))$, where S_0 is the equilibrium magnetization and β is an inversion efficiency term.

T1 mapping has been reported to have lower variability than MRE which makes it more reliable for longitudinal monitoring of patients with NASH [267-269].

Inflammation and fibrosis have been reported to increase T1 relaxation time values because of the excessive accumulation of extracellular fluids [267, 270, 271]. Also, several studies have shown that T1 values increases significantly in diseased and cirrhotic livers compared to healthy controls in both animal models and humans [124, 270, 272, 273]. However, T1 measurements are affected by histological confounding factors including fat and iron. Different results for the influence of hepatic steatosis on T1 mapping measurements have been reported [272, 274-276]. Multiple reasons have been considered for this variability in T1 results regarding liver fat content including the used T1 mapping method, the influence of MRI field strength, the used fitting model and the difference in the fat fraction of the assessed tissues [274]. Moreover, most of the T1 mapping methods currently used assume a single measured species (e.g., water or fat) and thus for the estimation of T1 values a mono-exponential curve fit is usually performed. However, this assumption is not completely true as in hepatic steatosis water and fat coexist in the tissue. In this case, the curve fit need to include both species and thus be a bi-exponential rather than mono-exponential. With the mono-exponential curve fit, only a single T1 value is measured which results in an error called the partial volume effect [275, 277].

To eliminate the confounding effect of steatosis on the T1 measurements of liver fibro-inflammation, an algorithm that provides fat suppressed T1 measurements have been proposed by Mozes F. E. et al. [276]. Also, water only T1 values can be calculated after MRI

acquisition [278]. Recently, fat-water separated T1 mapping sequences have been introduced as new methods to measure T1 values without fat confounding effect but no methods have been commercialized yet [279-281]. A fat suppression pulse could also be helpful in avoiding this fat effect on T1.

In addition to hepatic steatosis, excessive accumulation of iron in liver tissue have been shown to decrease the measured T1 relaxation time values which may result in an underestimation of the effects of inflammation and fibrosis on T1 [282, 283]. The correction of this potential bias requires an iron quantification which can be performed with a parallel acquisition of T2* in the same slice as T1. The combination of the acquired T1 and T2* data in one algorithm allows to obtain iron corrected T1 mapping (cT1) values [269]. cT1 has been used to evaluate diffuse liver diseases and monitor response to treatment [124, 284-286]. A NAFLD study performed in 50 patients undergoing liver biopsy reported that cT1 could accurately differentiate between patients with simple steatosis and those with NASH. This biomarker, however, could not significantly distinguish between individual stages of fibrosis in comparison with histological scorings in this same cohort of patients [287]. Other studies have shown that cT1 measurements increased in patients with advanced fibrosis or cirrhosis and that this quantitative parameter could be used as a standardized continuous score to predict liver-related outcomes in patients with chronic liver disease [267, 288].

1.3.4. Diffusion Weighted Imaging (DWI)

Diffusion reflects the physical mechanism of Brownian movement of water molecules caused by thermal energy. When the environment surrounding the water molecules is unrestricted, the water molecules movement is random. In biological tissues, the diffusion mechanism is typically observed in intracellular, extracellular and intravascular spaces and is affected by the biophysical properties of tissue (cell membranes, fibers and macromolecules, cell density), microstructure and microcirculation [289-294]. The diffusion of water molecules can be affected by diseases that lead to changes in the volume or structure of intra- and extracellular spaces. Restricted diffusion has been observed in tissues with high cellularity such as tumors, abscesses, fibrosis and cytotoxic edema while unrestricted diffusion has been described in tissues with low cellularity or tissues with disrupted cell membranes including cysts and necrotic tissues [289, 295-297] Diffusion is considered to be isotropic when the displacement

of water molecules is restricted in all spatial directions, while it is described as anisotropic when water molecules can move in a preferred direction, along a white matter tract in the brain for example. In the liver, tissue is considered isotropic and diffusion weighted imaging (DWI) focuses on the differences in water molecules movement without taking into consideration the direction of their movement [290, 298-300].

When water molecules experience a static, homogeneous magnetic field, their hydrogen nuclei precess with the Larmor frequency. However, in a temporary magnetic field (gradient), this homogeneity can be disturbed because static and moving water molecules react differently to the magnetic field. DWI captures the sensitivity of MRI to water molecules motion. DW imaging [301] is based on a T2-weighted spin-echo sequence with pulsed diffusion gradients added symmetrically before and after the 180° refocusing pulse. With the application of the first gradient, spins located at different positions in the scanner undergo different magnetic fields which leads to the accumulation of different phase shifts. When the second gradient is applied, the static spins accumulate the same phase as the phase accumulated during the first gradient application. However, with the first phase shift reversed by the 180° pulse of the spin-echo sequence, the final phase shift accumulation is null. Spins moving randomly experience a different gradient field during the application of the two gradients and their final phase shift accumulation is randomly distributed which results in signal attenuation. In a gradient-echo sequence, no refocusing 180° pulse is applied. Thus, the two dephasing and rephasing gradients are applied with opposite polarity [294, 301-303]. The contrast of DW images is based on the difference in water molecules position between the dephasing and rephasing gradients. A tissue where the motion of water molecules is unrestricted displays low signal, while a tissue with restricted motion of water molecules displays high signal [292, 302]. The degree of diffusion weighting, termed the b-value and measured in units of s/mm^2 , depend on the gradient amplitude (strength), duration and the time separating the application of the dephasing and rephasing gradients. The higher the b value, the stronger the diffusion weighting [292]. The diffusion gradients used to sensitize the MRI signal to water molecules motion have the same area and polarity (for the spin-echo sequence, while for the gradient-echo sequence the diffusion gradient must have the same area and opposite polarity), and they affect directly the degree of diffusion weighting (as explained above), the TE and TR.

DWI can be implemented with different acquisition sequences, including SE, FSE, and EPI. Currently, the most used DWI sequence for body imaging is a single-shot spin-echo echo-planar (SE-EPI) sequence. This sequence can be acquired with free breathing, breath holding or respiratory gating. However, this method has some limitations [289, 295-297, 304, 305]. First, SNR and the spatial resolution are low because of hardware limitations and high bandwidth (i.e. frequency range allowed in the signal). SNR can be improved, but at the cost of spatial resolution [295, 304-307]. The SNR is particularly important in DWI because with the attenuation of the diffusion signal with the increase of the b-values, a low SNR value can lead to inaccurate estimation of the diffusion coefficient. Of note, using strong gradients and high slew rates in DWI can decrease the diffusion encoding time, which enhances SNR by decreasing the TE.

Moreover, ghosting artifacts and image blurring can occur because of respiratory, cardiac or patient movements. Breath holding and respiratory gating can decrease image artifacts. Breath hold acquisitions are performed in very short times (~ 20-30 s) which makes them theoretically less likely to be altered by motion-related artifact. However, breath-holding may be difficult for patients and is obviously not achievable in small animals. Respiratory gating increases the acquisition time, particularly if the patient has irregular or slow breathing [306, 308-310]. Motion artifact caused by heart beating can degrade ADC measurements in the left lobe of the liver. To overcome this type of artifact, electrocardiographic triggering can be used. However, cardiac gating increases scan duration substantially [305, 306, 311].

Another limitation of DWI is susceptibility artifact caused by magnetic field inhomogeneity which appear as bright spots, spatial distortion or signal drop out. This type of artifact is mainly found in fast imaging methods like EPI [304-306]. Also, some artifacts can occur at the edge of an anatomical structure because of air-tissue or fat-water interfaces. These artifacts appear as black or bright bands. Eddy current is another type of artifact. It arises because of the rapid cycling of the gradients required to generate the diffusion-encoding gradient lobes, leading to geometrical distortion and image smearing artifacts [304-306].

Water molecules diffusion in tissue is reflected in the apparent diffusion coefficient (ADC, expressed in mm^2/s). This coefficient represents the degree of molecular mobility of water molecules and is modulated by tissue properties such as extracellular space size, viscosity and

cellularity. ADC estimation is usually automated and available on most MRI scanners. ADC is calculated at each voxel (volumetric pixel) of an image by considering the signal intensity, S , at different b-values, and introducing an ADC-dependent diffusion-weighting term which attenuates the signal relative to the maximum available magnetization in the absence of diffusion encoding, S_0 [293, 301]:

$$S(b) = S_0 e^{-b \text{ADC}} \quad (2)$$

ADC measurements can be displayed as a parametric map and the mean ADC for a given region of interest can be used for further analysis. The b-value is in fact a compact representation of the effect of the time-dependent diffusion gradient $g(t)$ on the signal, and it can be estimated as:

$$b = \gamma^2 \int_0^T dt \left[\int_0^t dt' g(t') \right]^2 \quad (3)$$

With γ , the gyromagnetic ratio of hydrogen protons ($2.68 \times 10^8 \text{ rad}\cdot\text{Hz}\cdot\text{T}^{-1}$) and T , the gradient duration. For the DWI pulsed-gradient spin-echo (PGSE) sequence, the integration of this equation gives [312]:

$$b = \gamma^2 G^2 \delta^2 \left(\Delta - \frac{\delta}{3} \right) \quad (4)$$

where δ is the duration of the application of each of the diffusion gradients and Δ is the time separating the application of these two gradients, with the assumption that gradient ramp time (t_r : the minimum time needed for the gradient to ramp up to its full strength) is very small compared to δ ($t_r \ll \delta$). The term $\left(\Delta - \frac{\delta}{3} \right)$ corresponds to the effective diffusion time (Δ_{eff}); the time allowed for diffusing water molecules to probe the local microstructure.

Liver fibrosis and cirrhosis have been shown to affect the hepatic parenchymal structure because of excessive extracellular matrix deposition which results in diffusion decrease. Several studies [212, 293, 313, 314] have reported that ADC measurements in the liver correlates with histological stages of fibrosis. Most of these studies observed a decrease in ADC values with increasing fibrosis stage and in cirrhosis. In a study performed by Lewin et al [314], AUCs of 0.79 and 0.92 were obtained for detection of advanced to severe fibrosis stages

(F2–F4 and F3–F4) using ADC cutoff values of 1.24 and $1.21 \times 10^{-3} \text{ mm}^2/\text{s}$, respectively. Another study conducted by Taouli et al [313] reported AUCs of 0.90 for detection of fibrosis stages of F2–F4 and F3–F4, with cutoff values of 1.54 and $1.53 \times 10^{-3} \text{ mm}^2/\text{s}$. Wang et al [212] performed a study comparing DWI and MRE for diagnosing liver fibrosis, the AUCs obtained were 0.78–0.88 for ADC versus 0.92–0.99 for MRE for diagnosing any stage of fibrosis. In addition to fibrosis, the influence of inflammation on ADC has been studied in focal lesions [315, 316] and in the liver [317]. The results have shown restricted diffusion with inflammation, possibly because of viscosity increase. The increase of hepatic steatosis has also been reported to cause ADC decrease [318]. DWI was investigated for diagnosing NAFLD, however the early results showed that ADC values were not associated with any histological feature of NAFLD [319].

Moreover, DWI has been performed to evaluate ADC measurements in animal models of NAFLD, hepatic fibrosis, diffuse liver disease and liver tumors [320-326]. In an ex-vivo study performed by Anderson S. W. et al. [320] to assess liver ADC values in a mouse model of NAFLD, ADC values significantly correlated with steatosis and inflammation. In rats with liver fibrosis, Annet L. et al. [321] reported decreased ADC correlated with increased liver fibrosis in living rats, but not after death. They concluded that restricted water diffusion could not be assessed with DWI in liver fibrosis. Other factors, such as a decrease of perfusion, might explain the decrease of ADC in rats with liver fibrosis.

1.3.5. Temporal Diffusion Spectroscopy (TDS)

Temporal diffusion spectroscopy (TDS) is a DWI method that provides an approach to characterize tissue microstructure at various spatial scales ranging from sub-cellular to cellular levels [327-332]. With this approach shorter diffusion times than those used in conventional DWI can be obtained by replacing the standard diffusion gradients in the conventional pulsed gradient spin echo (PGSE) sequence by oscillating gradients with an oscillation frequency (f). The oscillation frequency corresponds to a given diffusion time. With multiple oscillating frequencies, the ADC values obtained at each frequency are sensitive to different diffusion times, and thus different length scales. TDS with oscillating gradient spin

echo (OGSE) sequence has been successfully implemented and used to study spatial heterogeneity in brain tumors [333], to assess the impact of organelle changes in malignant tumor cells [334], to determine the alterations in different phases of cancer cell division cycle [335] and to monitor tumor early response to treatment [336].

OGSE methods have been implemented with several sequences including SE [337] fast spin FSE [338] or EPI [339]. SE sequence provides good image resolution but has long acquisition time which is not adequate for clinical practice. FSE can be used to shorten the acquisition time by acquiring multiple echoes per repetition time, but it can be influenced by magnetic field inhomogeneity and has limited spatial resolution. EPI is the fastest MRI sequence with the opportunity of acquiring the total k-space in a single shot with several possible trajectories to fill k-space. However, it is sensitive to gradient susceptibility and motion and has limited spatial resolution.

To reduce diffusion times and selectively sample a narrow frequency domain, multiple oscillating gradients waveforms have been proposed including sine-, cosine and double-sine-modulated waveforms with their mathematical formula expressed in terms of gradient amplitude G and oscillating angular frequency ω_0 ($\omega_0 = 2\pi f$ with f the frequency) respectively [327]:

$$g_{sine}(t) = G\sin(\omega_0 t) \quad (6)$$

$$g_{cosine}(t) = G\cos(\omega_0 t) \quad (7)$$

$$g_{double-sine}(t) = G\sin(\omega_0 t)\text{sgn}\left[\sin\left(\frac{\omega_0 t}{2}\right)\right] \quad (8)$$

where sgn is the signum function. The sine-modulated waveform has a narrow frequency content at the principal oscillation frequency, but also has an undesirable zero-frequency component, similar as the PGSE sequence. The cosine waveform would be ideal as it does not present the PGSE-like zero frequency peak. However, true cosine-modulated function cannot be implemented because of the finite gradient rise times. To overcome this limitation, the modulation function can be apodised, for instance by prepending and appending the waveform with a sine function of twice the frequency. The mathematical expression of this apodised waveform is [327]:

$$g_{\text{cosine-apodised}}(t) = \begin{cases} G \sin(2\omega_0 t) & 0 \leq t < \frac{\tau}{4} \\ G \cos(\omega_0 t) & \frac{\tau}{4} \leq t < T - \frac{\tau}{4} \\ G \sin(2\omega_0 t) & T - \frac{\tau}{4} \leq t \leq T \end{cases} \quad (9)$$

With τ , the waveform period and T , the wave duration ($T = N \times \tau$, where N is the number of periods). The double-sine modulated waveform is similar to the sine-modulated waveform, but with the polarity of every other period reversed. This waveform is suitable for oscillating gradient spin-echo echo planar (OGSE-EPI) imaging as it combines the narrow frequency content at the main frequency with only 4% energy as side-lobes, absence of zero-frequency content, and low duty cycle requirements. These gradient waveforms and their corresponding power spectra are presented in figure 1.3.1. Of note, the waveforms are typically implemented with a duration that includes a number of oscillation periods (N) that is as large as possible to ensure that the spectral content of the encoding is sharply defined at the oscillation frequency. The b-values corresponding to these gradient waveforms are thus expressed in terms of G , N and T and obtained via the integration of the square of the time integral of the gradient waveshape as described generally in equation (3). For the sine and double-sine modulated waveforms, the corresponding b-values formula and the effective diffusion time are expressed as [327] :

$$b = \frac{3}{8} \left(\frac{\gamma G}{\pi N} \right)^2 T^3 \quad (10)$$

$$\Delta_{eff} = \frac{3T}{8N} = \frac{3}{8f} \quad (11)$$

For the cosine-apodised modulated waveform, the corresponding b-values formula and the effective diffusion time are expressed as [327]:

$$b = \frac{1}{8} \left(\frac{\gamma G}{\pi N} \right)^2 T^3 \left(1 - \frac{1}{8N} \right) \quad (12)$$

$$\Delta_{eff} = \frac{T}{4N} = \frac{1}{4f} \quad (13)$$

ADC measurements from the cosine-apodized waveform acquisitions have been reported to be similar to those from the double-sine waveform [327].

In addition to the oscillating gradient waveforms mentioned above, a trapezoidal-modulated waveform has been recently proposed as an improvement of the cosine waveform [330, 340-342]. This “trapezoid cosine” waveform (represented in Figure 1.3.1 E) allows for increase in the maximum achievable b-value by 67% over the sinusoidal variant at any given gradient strength with minimal degradation of the encoding spectrum. At a maximum slew rate and gradient amplitude, trapezoid lobes have at least $(\pi-1)/2$ times higher gradient-time integrals than sine/cosine lobes with the same duration which leads to higher b-values. The mathematical formula corresponding to the trapezoidal gradient waveform is [341]:

$$g(x) = (-1)^{\lfloor x \rfloor} \cdot \begin{cases} \frac{1}{2ft_r}(x - \lfloor x \rfloor) & \text{if } \lfloor x \rfloor \leq x < \lfloor x \rfloor + 2ft_r \\ 1 & \text{if } \lfloor x \rfloor + 2ft_r \leq x < \lfloor x \rfloor + 1 - 2ft_r \\ \frac{1}{2ft_r}(\lfloor x \rfloor + 1 - x) & \text{if } \lfloor x \rfloor + 1 - 2ft_r \leq x < \lfloor x \rfloor + 1 \end{cases} \quad (15)$$

Where $\lfloor \cdot \rfloor$ denotes the integer part and t_r is the gradient rise time. The associated b-value and effective diffusion time are [330]:

$$b = 2N\gamma^2 G^2 \left(\frac{1}{4f} - \frac{t_r}{2} \right)^2 \Delta_{eff} \quad (15)$$

$$\Delta_{eff} = \frac{1}{6f} + \frac{2}{3}(t_r - (t_r^2 \times f)) \quad (16)$$

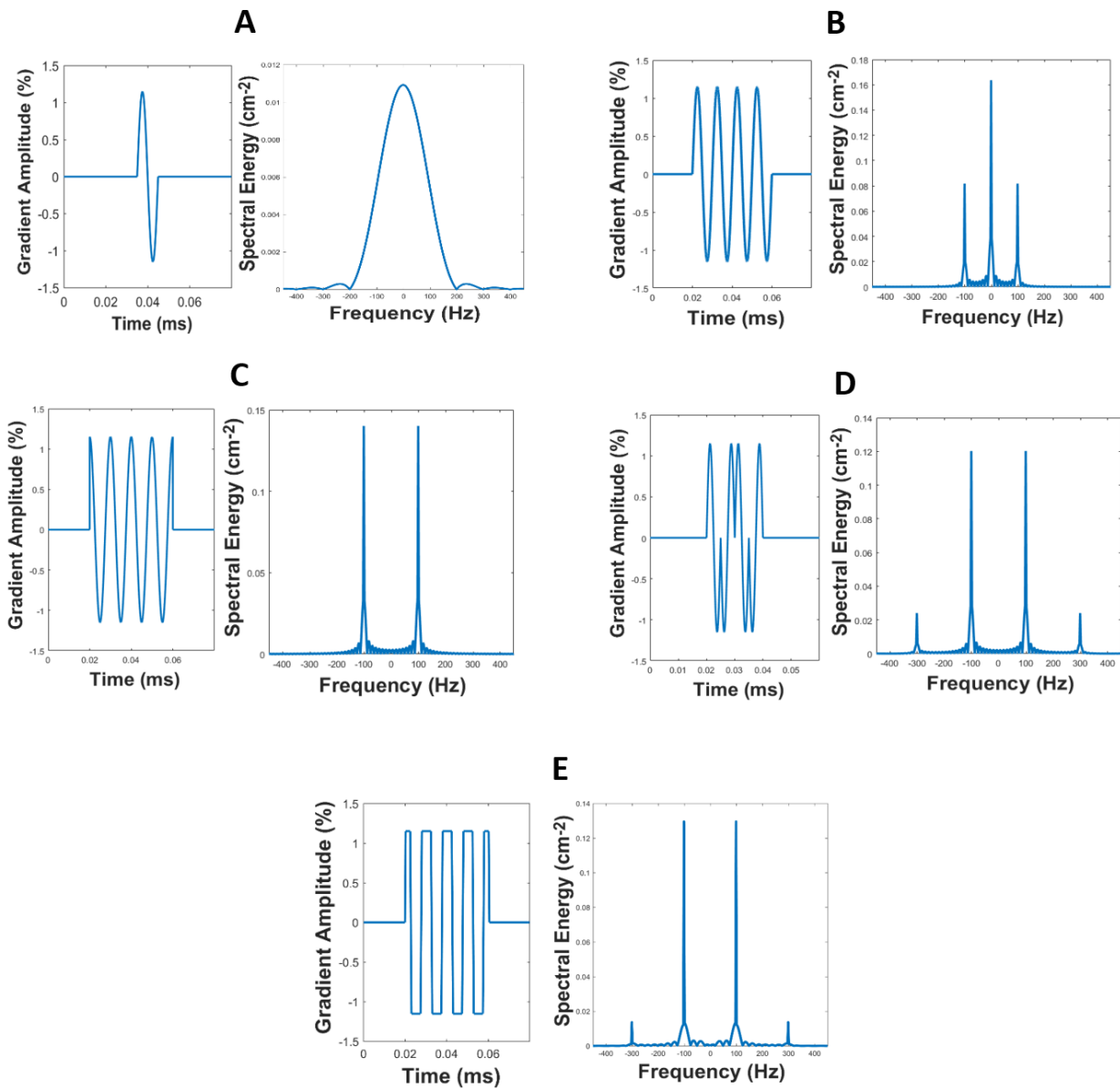


Figure 1.3. 3: Representation of A) a single period sine waveform similar to a standard PGSE approach B) sine-, C) cosine- D) double-sine- and E) trapezoid modulated oscillating gradient waveforms and their corresponding gradient modulation power spectra. The spectra were numerically determined which explains the truncation/apodisation effects that broaden the components from their ideal spectral form.

The time separating the application of the two gradients applied before and after the refocusing pulse has been reported to influence the diffusion frequency spectra. A perfect frequency spectra requires an infinite encoding waveform. This requires an infinite echo time

which is experimentally unfeasible. The truncation of the waveform results in an inaccurate spectra. Narrower spectral shape can be obtained when using an optimal gradient separation time where a continuous unbroken waveform can be drawn across the two gradient waveforms in a way that these two gradients are connected as one waveform [330].

Applications

TDS with OGSE-EPI has been applied in several studies. In a study performed by Does M. D. et al., in 2003 [327] in vivo in a rat model of global brain ischemia, the three modulated gradient waveforms sine, double-sine and cosine were implemented and used to probe the diffusion-time/frequency dependence of water diffusion in the gray matter in normal versus globally ischemic rat brain. The results showed that ADCs were higher at shorter diffusion times. This increase was more pronounced in the double-sine and cosine measurements, and slightly more pronounced in the postmortem data compared to the normal in vivo data. Recently, OGSE-EPI has been used to assess treatment induced apoptosis in vivo in a mice model and in vitro. The results showed that TDS-derived parameters detected cell size decrease during apoptosis in responsive tumors that occurred earlier than gross tumor volume regression [343]. Moreover, tumor response to chemotherapy was investigated with TDS in a rat gliomas. Parameters derived from TDS measurements including mean cell size successfully separated 90% of irradiated tumors from non-irradiated cases [344]. Finally, TDS was also performed in the liver to characterize hepatocellular carcinomas [345] and to quantify hepatocyte size [332].

2. Aim of the research

This PhD project is part of the Quantitative Imaging in Diabetes (Quid-NASH) consortium; a research program co-funded by Inserm, Assistance Publique-Hôpitaux de Paris (AP-HP), Université de Paris (Descartes and Diderot), Commissariat à l’Energie Atomique (CEA), Laboratoires Servier, BioPredictive in addition to the French State, that aims to develop a virtual (noninvasive) liver biopsy for the diagnosis and staging of NASH in patients with type 2 diabetes and increasing our knowledge of the NASH pathophysiology with the identification of new metabolic pathways, drug targets as well as predictive animal models (mouse and mini pig). A part of this PhD project is also involved in the temporal diffusion spectroscopy in nonalcoholic steatohepatitis (STEDI-NASH) consortium; a research program funded by l’Agence Nationale de la Recherche (ANR), that aims to develop temporal diffusion spectroscopy (TDS-MRI) sequences for non-invasive characterization and diagnosis of NASH.

The main purpose of this preclinical study was to identify reliable noninvasive methods for the assessment of NAFLD severity by investigating quantitative MRI and MRE methods in mouse models of the disease and developing alternative MRI sequences to improve temporal diffusion spectroscopy. This PhD program consisted of three main projects:

- In the first project “Animal models of NAFLD/NASH”, the aim was to develop and study the reproducibility and effectiveness of the recently introduced Western diet mouse model of NASH.
- In the second project “Multi-parametric preclinical MRI of NAFLD”, the purpose was to perform a preclinical MRI study on mouse models of NAFLD/NASH to investigate whether or not magnetic resonance elastography derived parameters, T1 relaxation time and PDFF measurements are biomarkers of NAFLD, NASH or its histological features, i.e. steatosis, inflammation, ballooning and fibrosis.
- In the third project “Temporal diffusion spectroscopy”, we aimed to implement a temporal diffusion spectroscopy method with a spin echo oscillating gradient – echo-planar imaging (OGSE-EPI) sequence. Once the sequence was implemented we improved and validated this sequence with phantoms and in vivo, then applied it in a

mouse model of NAFLD/NASH to assess the pathological alterations of this disease on a subcellular level.

3. Chapter I : Animal models of NAFLD/NASH

Understanding the pathophysiology of NASH is still challenging. Hence, preclinical models of this disease are needed. Several mouse models of NASH have been reported, each having different utility and clinical translation [346, 347]. However, no current model can fully replicate all the pathogenic determinants of human NASH. Thus, it might be advantageous to compare results in more than one model. The Western diet model has been reported to replicate the progressive stages of human fatty liver disease, from simple steatosis, to inflammation, fibrosis and NASH with key phenotypes of human NAFLD including obesity, insulin resistance, hypercholesterolemia, and hypertriglyceridemia [10, 54, 58, 65]. This simple diet- and chemical-induced murine NASH model was established using a Western diet (WD), which is a high-fat, high-fructose and high-cholesterol diet, combined with low weekly dose of intraperitoneal carbon tetrachloride (CCl₄), which pro-inflammatory properties serve to speed up the pathologic evolution. In this project, I performed a histological study of NAFLD/NASH using a WD combined with a low dose of CCl₄, in mice, to investigate the effectiveness and reproducibility of this model. The induction of this model was based on the WD + CCl₄ murine model established by Tsuchida T. et al.,[10] where this model was applied using C57BL/6J mice for 12 weeks and 24 weeks and resulted in rapid progression of advanced fibrosis (F3 bridging fibrosis) and severe steatohepatitis after 12 weeks of induction, and hepatocellular carcinoma in 24 weeks, with histological, immunological and transcriptomic features similar to the human NASH.

3.1. NASH histological study : WD mouse model

3.1.1. Methods

Animal experiments in this study were done in accordance with local ethical regulations (CEEA-121, Apafis: #19705). To study the effectiveness and reproducibility of the WD model, four groups of male C57BL/6JRj (Janvier Labs, Genest-Saint-Isle, France) mice (8 weeks old) were used:

- A normal diet group : injected only with olive oil (ND + oil)
- A ND + CCl₄ group: injected with a mixt of olive oil and a CCl₄ dose

- A Western diet group : injected only with olive oil (WD + oil)
- And a WD + CCl₄ group : injected with olive oil and a CCl₄ dose.

The WD used in this study consists of 21.1% fat, 41% sucrose, and 1.25% cholesterol (TD. 120528, Envigo, Gannat, France) with a high sugar solution for drinking (23.1 g/L d-fructose and 18.9 g/L d-glucose). This diet was combined with low weekly intraperitoneal CCl₄ administration (0.2 µl (0.32 µg)/g of mouse body weight) to accelerate disease progression. The mice were housed for 6 and 12 weeks (n = 6 mice per time point subgroup) (Figure 3.1.1). For each mice cage (group of 4 mice), 130 g of diet (4-5 g / mouse / day) were provided weekly with 330 ml of drinking solution changed twice per week. The injected solution (CCl₄ + olive oil or olive oil only) was prepared based on mice weight, weekly, just before the intraperitoneal injections. All the injections were performed under anesthesia induced with isoflurane in a 70% air / 30% O₂ mixture at a concentration of 3% for a duration of about 5 minutes. At each time point, mice were euthanized. Their liver samples were analyzed by an expert liver pathologist blinded to the treatment received, to assess NASH characteristics.

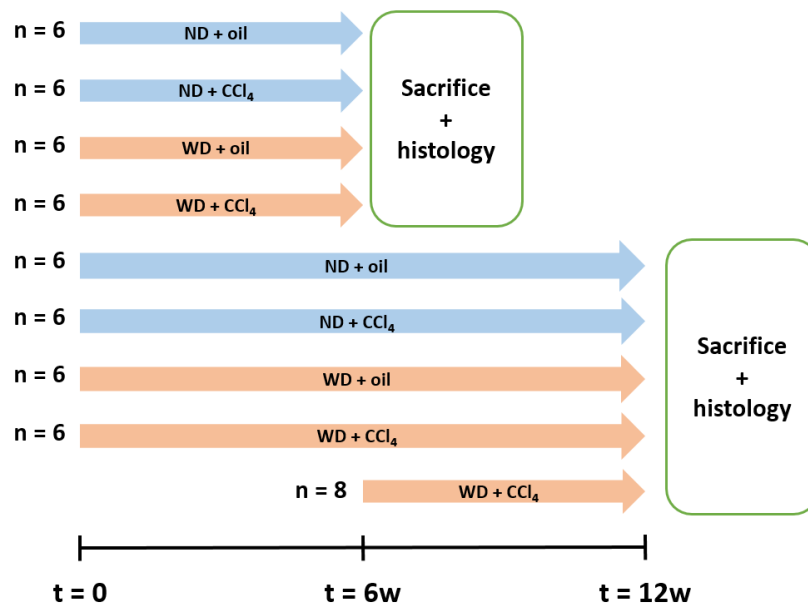


Figure 3.1. 1: Study timeline with the groups and subgroups included

Injections preparation

The mean weekly dose injected per mouse was 300 μ l of CCl₄ + olive oil or olive oil only. As mentioned before, the injection dose of CCl₄ is 0.2 μ l/g of mouse body weight. For the groups ND + CCl₄ and WD + CCl₄ (24 mice), all mice were weighed, and the average value of their weight was defined and used to calculate a common dose to inject. For example, if the average weight of the mice was 25 g, the injected dose was $0.2 \times 25 = 5 \mu$ l of CCl₄ + 295 μ l of olive oil = 300 μ l of the mixture.

Once the main injection solution was prepared, the injection volume for each mouse was calculated based on its weight, for example a mouse that weighed 24 g was injected with a volume of $24 \times 300 / 25 = 288 \mu$ l \approx 280 μ l (rounding up the values as the syringes were not precise enough).

For the ND + oil and WD + oil groups (also 24 mice) injected with olive oil only, the volume of olive oil injected was calculated using the weight of each mouse. Hence, if the average weight of the mice was 25 g the volume injected was 300 μ l and a mouse weighing 24 g was injected with 280 μ l of olive oil ($V = 24 \times 300 / 25 = 288 \mu$ l \approx 280 μ l).

3.1.2. Results

Forty-eight mice were first enrolled in this study, divided in four groups with two time points (6 weeks and 12 weeks). Out of these 48 mice, 11 were excluded (2 ND + oil, 1 ND + CCl₄, 2 WD + oil, and 6 WD + CCl₄; the mice excluded died either directly after injection or were found dead in their cages). As most of the lost mice were from the group WD + CCl₄, 8 mice (WD + CCl₄) were added to the cohort for 6 weeks of diet (Figure 3.1.1). Of the 8 added mice, 2 died after injection. The final cohort included 43 mice (Table 3.1.1).

All mice were weighed weekly before injections and the results (Figure 3.1.2) showed that the WD + oil mice group gained more weight than the ND + oil mice group. However, this difference was not substantial except for the last two weeks (11 and 12). The weight of the WD + CCl₄ mice group dropped between week 2 and week 5 and increased after 5 weeks. However, this weight increase was lower than that in the other three groups. For the ND + CCl₄ mice group, their weight increased similarly to the ND + oil mice group.

Table 3.1. 1: Mice number per group after 6 and 12 weeks of induction

Mice groups	Induction duration	
	6 weeks	12 weeks
ND + oil	5	5
ND + CCl ₄	6	5
WD + oil	5	5
WD + CCl ₄	6	6

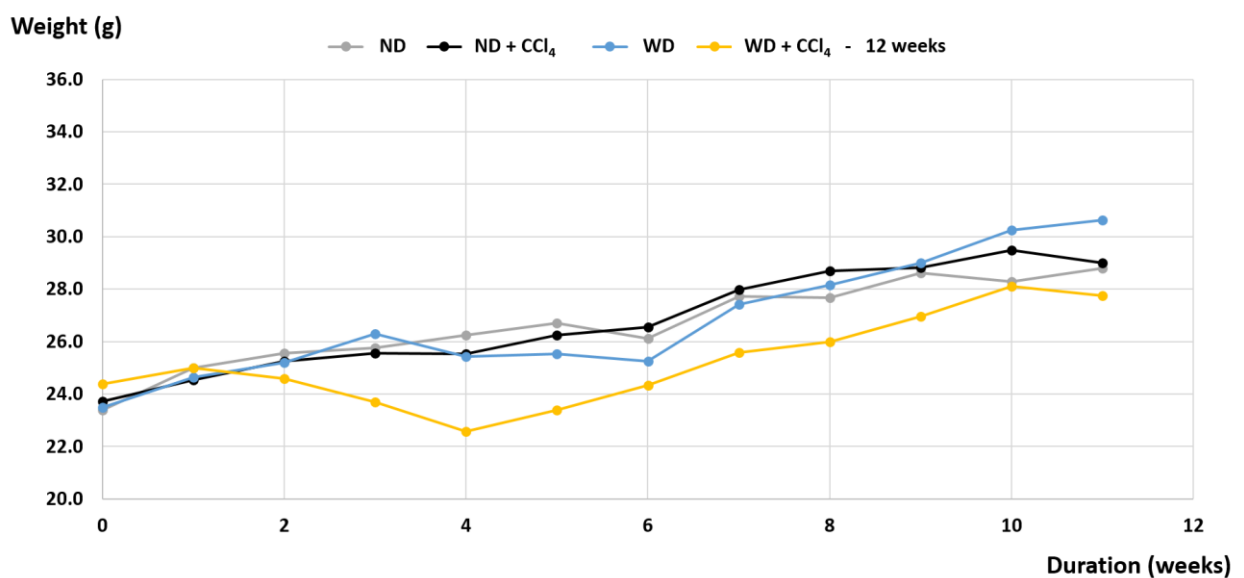


Figure 3.1. 2: Mice mean weight per group measured weekly for the 12 weeks of model induction.

The histological results of this study reported based on the NAS scoring system are shown in Figure 3.1.3 and representative images of the histologic analysis results are shown in Figure 3.1.4. The results showed that after six weeks of diet, the ND + CCl₄ group developed very modest inflammation (I0-I1), modest fibrosis (F1-F2) with no steatosis nor hepatocyte ballooning. The WD group developed low scores of steatosis (S0-S1) without inflammation, ballooning or fibrosis. While the WD + CCl₄ group had low to advanced steatosis (S1-S3), none to early inflammation (I0-I1), low to moderate fibrosis (F1-F2) with no ballooning. After twelve

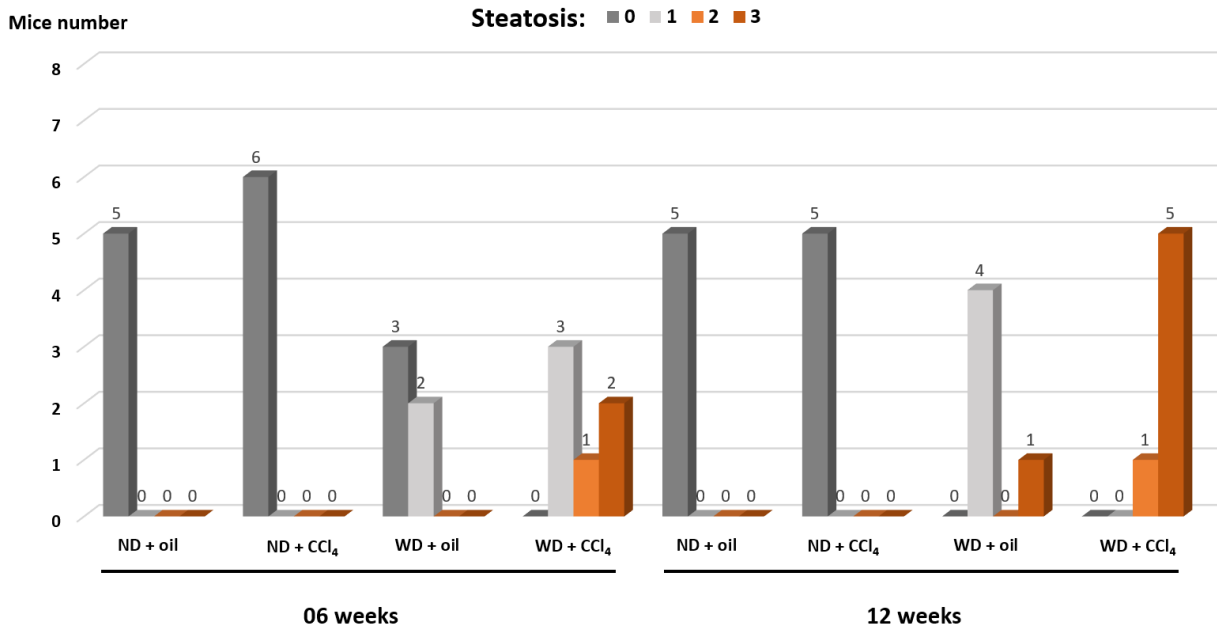
weeks of induction, the ND + CCl₄ group showed moderate to advanced levels of fibrosis (F2-F3) with no steatosis, no inflammation, nor ballooning. The WD group displayed early to advanced steatosis scores (S1-S3), none to moderate inflammation (I0-I2) with no ballooning nor fibrosis. Moreover, the WD + CCl₄ group had advanced stages of steatosis (S2-S3), moderate inflammation (I1-I2) and moderate to advanced fibrosis (F2-F3) with no hepatocellular ballooning.

3.1.3. Discussion

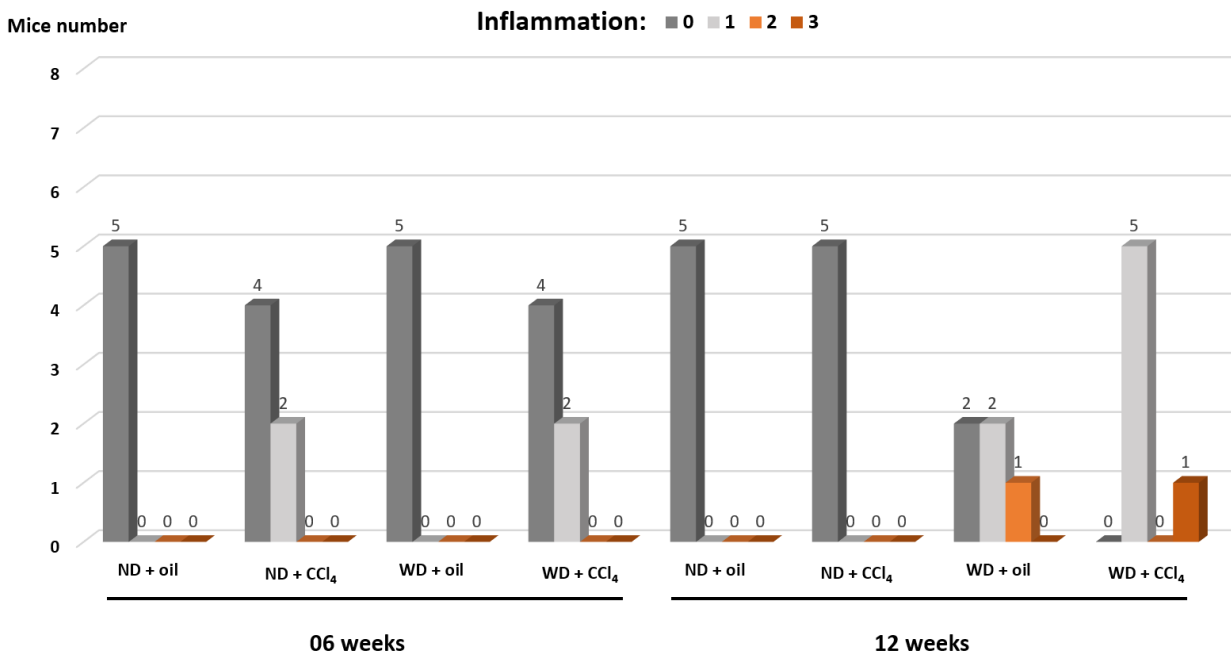
In this study, I investigated the efficacy and reproducibility of the WD combined with CCl₄ murine NASH model in C57/bl6 male mice. The data of mice body weight measured weekly, showed a decrease of the WD + CCl₄ group weight between the second week and the fifth week of induction then a monotone, but limited, increase till week twelve. This decrease is probably caused by CCl₄ treatment that decreased mice food intake and attenuated the body weight gain induced by WD feeding.

Our histological results showed less severe NAFLD than that reported by Tsuchida T. et al.[10]. In that study, stage 3 bridging fibrosis and severe NASH developed as early as 12 weeks using the same mice strain (C57BL/6J), the same sex (male mice) and the same diet. Western diets based on high-fat, high-fructose (or sucrose), and high-cholesterol have been widely used to produce mouse NASH models as such dietary features can induce not only steatohepatitis, but also obesity and insulin resistance in mice which are key features associated with human NASH [58, 65, 348-350]. However, the WD-based NASH models do not typically progress to severe steatohepatitis and advanced fibrosis even after long-term induction [58, 348]. CCl₄ is a standard tool for inducing liver injury and fibrosis in mice and has been used for decades [351]. It has also been reported that CCl₄ induces hepatocyte ballooning in mice [352], which is a typical key feature of NASH.

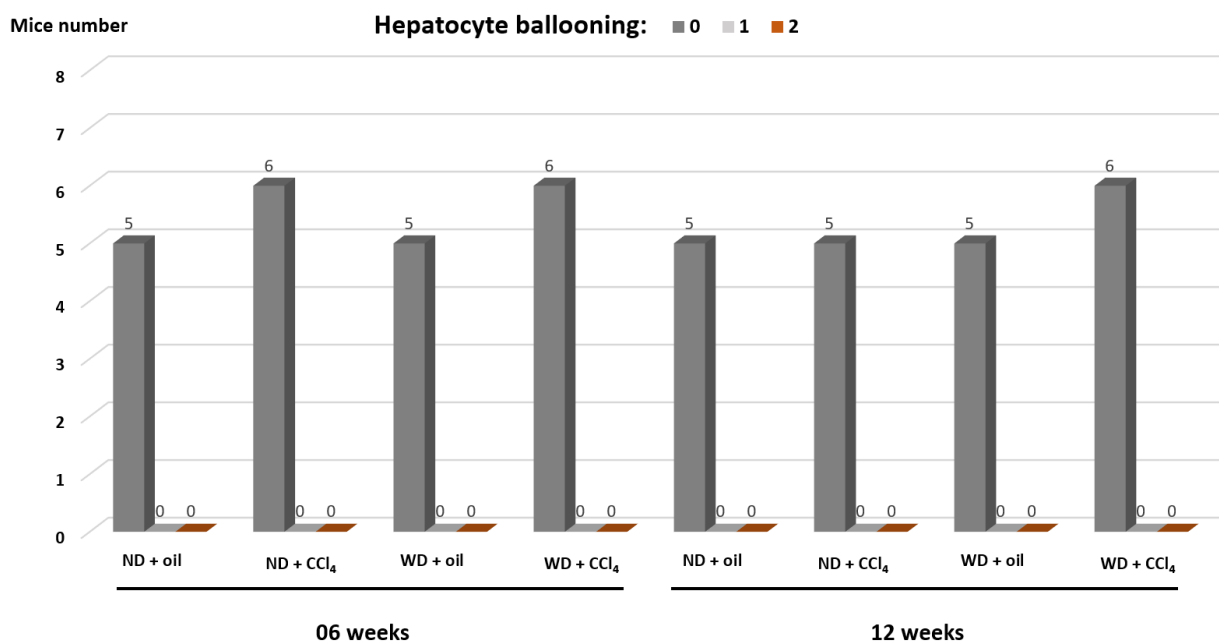
a)



b)



c)



d)

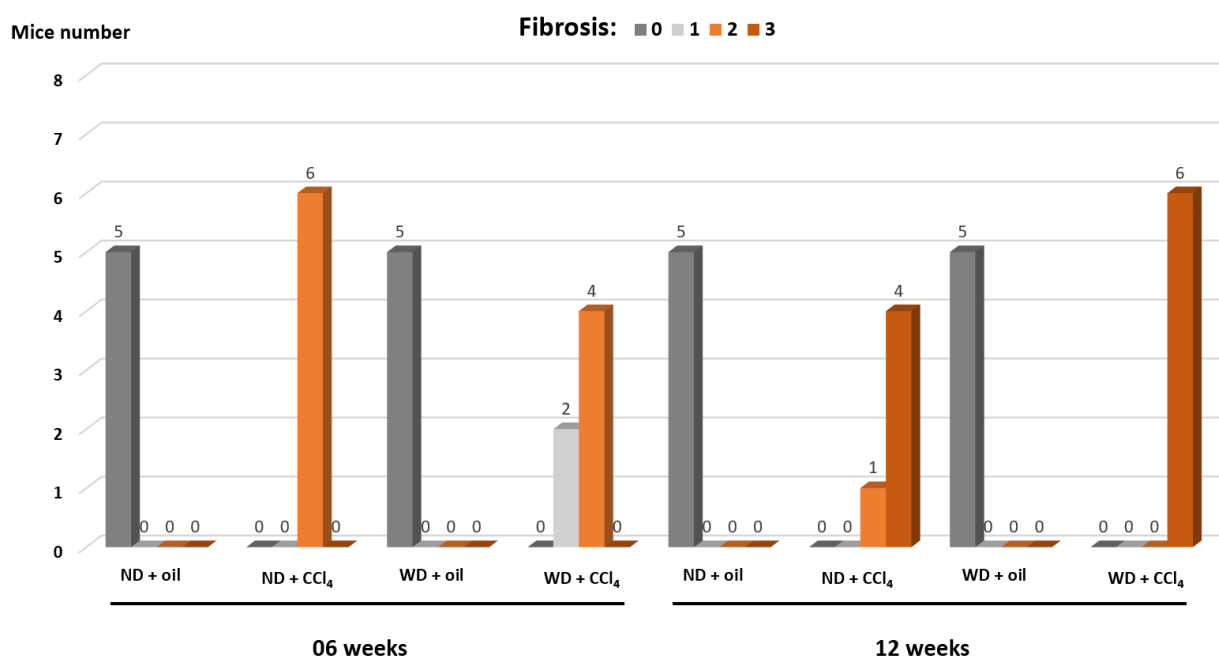


Figure 3.1. 3: Histological results of our NASH mice model study presented per group (ND + oil, ND + CCl₄, WD + oil and WD + CCl₄) at 6 weeks versus 12 weeks for each histological feature of NAFLD; a) steatosis, b) inflammation, c) hepatocyte ballooning and d) fibrosis.

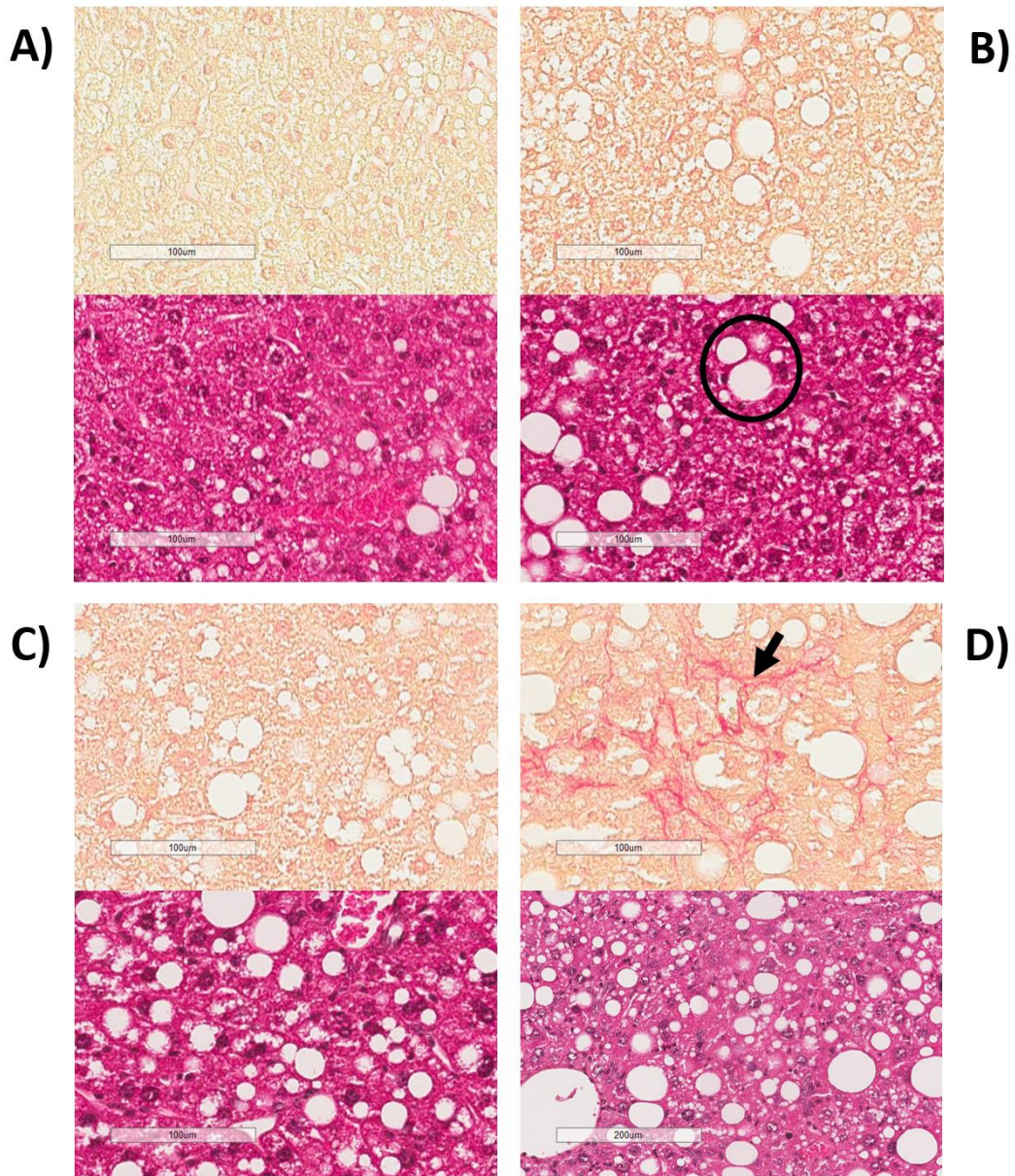


Figure 3.1. 4: Histological sections (upper row: picosirius red stained slices; second row: hematoxylin-eosin stained slices) with x20 image magnification. A) Mouse fed WD for 6 weeks (grade 1 for steatosis with no inflammation, ballooning nor fibrosis). B) Mouse fed WD for 12 weeks (grade 1 for steatosis (circle) and inflammation with no ballooning nor fibrosis). C) Mouse fed WD + CCL₄ for 6 weeks (grade 3 for steatosis with no inflammation nor ballooning and with stage 1 for fibrosis). D) Mouse fed WD + CCL₄ for 12 weeks (grade 3 for steatosis, grade 1 for inflammation with no ballooning and with stage 3 for fibrosis (arrow)).

In our study, CCl₄ was combined with the WD to accelerate inflammation, ballooning and fibrosis. However, no hepatocyte ballooning was detected after 6 weeks or after 12 weeks of induction. This may be explained by several reasons. First, the induction (diet change + CCl₄ injections) was started when the mice were 8 weeks old. We made the assumption that the mice had difficulties to adapt to the new diet, affecting their food intake. We postulated that starting the diet earlier (in 4 week-old mice) might have changed the outcomes of the study. Second, the stress that might have been caused by intraperitoneal injections of CCl₄ (even though they were performed under anesthesia) might also have affected the mice diet intake and sleep routine. Moreover, the animal housing room temperature might have been a co-factor. The room temperature was not monitored during this study and as the experiments took place from October to December 2020, there might have been a decrease in the room temperature. Moreover, we postulated that 12 weeks of diet might have been insufficient to reproduce all the stages of NASH.

3.2. Second study :

3.2.1. Methods

To further investigate the WD/NASH mice model, a second study was performed with better animal housing conditions using two models:

- A WD combined with CCl₄ model: 36 C57/bl6 male mice (diet provided in 4 week-old mice and injections started in 8 week-old mice) were enrolled in the study divided in four groups with 12 and 16 weeks as time points, two WD + oil groups (n = 8 mice per time point) and two WD + CCl₄ groups (n = 10 mice per time point) (Figure 3.2.1 a).
- A choline deficient L-amino acid - high fat diet (CDA-HFD) model with diet reversal as treatment for NAFLD/NASH: 48 male C57/bl6 mice (8 week-old) were included divided in six groups (n = 8 mice per group) with 10 and 16 weeks as time points followed by 0, 1 or 4 weeks with normal diet (Figure 3.2.1 b).
- And 3 control groups (normal diet, n = 4 mice per group) with 10, 12 and 16 weeks as time points (Figure 3.2.1 c).

The WD combined with a low weekly dose of CCl₄ model of NASH used in this study was the same diet as the one used in the previous histological study. However, some changes to improve the outcomes were performed:

- The mice were enrolled in the study at four weeks old (and not eight weeks) where they were fed the WD (for WD + oil and WD + CCl₄ groups) or ND (for the ND + oil and ND + CCl₄ groups) so they could quickly and easily adapt to the new diet. However, the intraperitoneal injections (CCl₄ or oil) were started at 8 weeks.

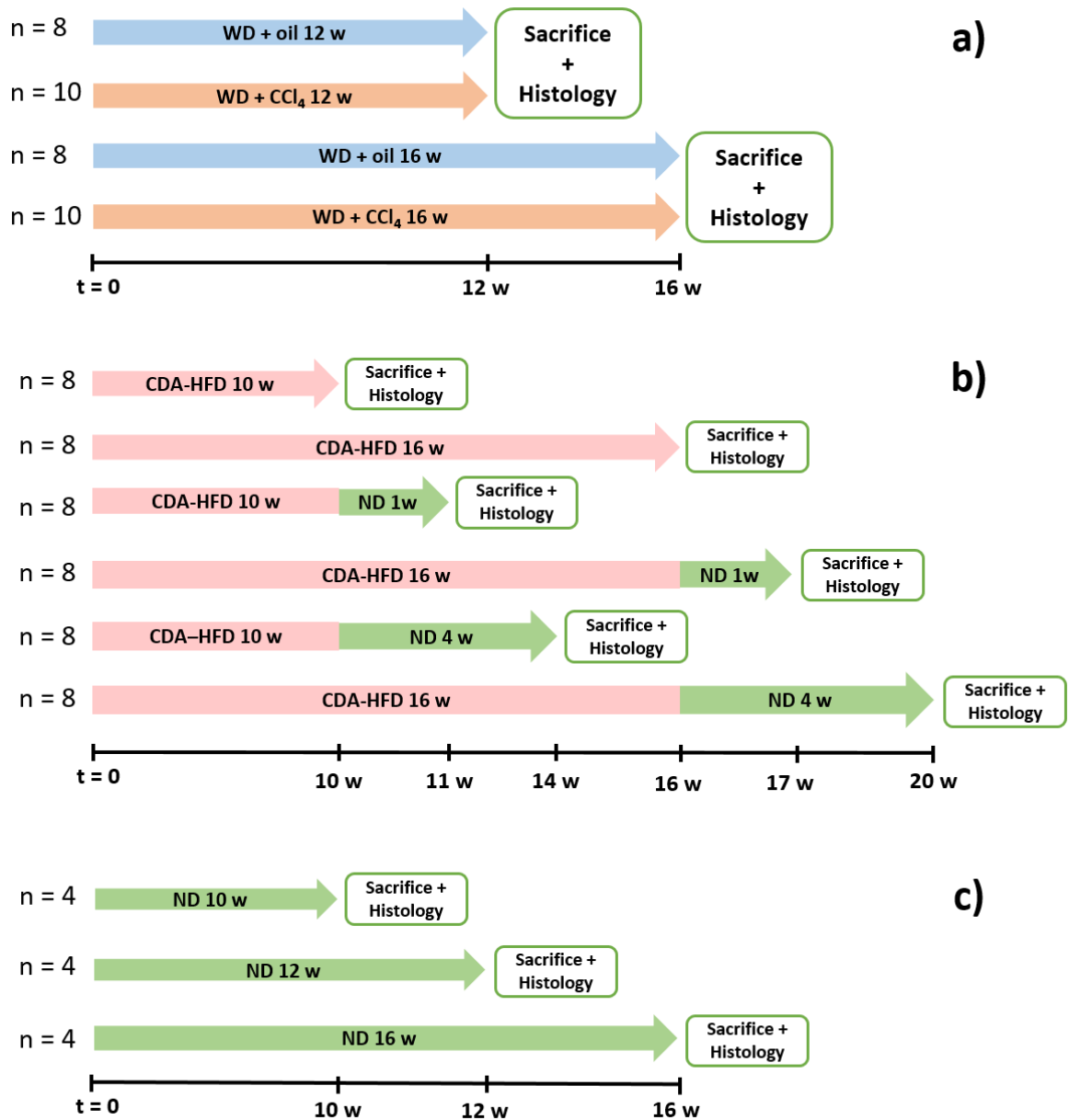


Figure 3.2. 1: Study timeline with the groups and subgroups included. a) the WD combined with a low dose CCl₄ mice model of NASH (12 or 16 weeks of induction). b) the CDA-HFD mice model (10 or 16 weeks of diet) with diet reversal (normal diet) as treatment of NASH (0, 1 or 4 weeks of reversed diet, i.e. normal diet). C) Control groups (normal diet, n = 4 mice per group) with 10, 12 and 16 weeks as time points.

- The induction duration was increased (12 and 16 weeks instead of 6 and 12 weeks) to have a more progressive form of the disease.
- Diet and drinking water were changed twice a week and mice were weighed weekly and observed twice a week for better monitoring. Cut off conditions were set up based on the mouse appearance, its natural behavior, its provoked behavior, the amount of weight loss and abdominal palpation. Mice were euthanized when 2 cut off conditions or more were critical.
- Moreover, the housing conditions were improved, and room temperature was monitored and kept at 22°.

The mice of the CDA-HFD NASH model were fed CDA-HFD diet with normal drinking water, they were weighed weekly and monitored twice a week and their diet and drinking water were changed twice a week. At each time point, mice were euthanized, and their liver samples were analyzed by an expert liver pathologist blinded to the treatment received, to assess the presence of steatosis, inflammation, hepatocyte ballooning and fibrosis stages based on the NAS scoring system.

3.2.2. Results

Ninety-six mice were included, 36 in the WD NASH model, 48 in the CDA-HFD model and 12 as control subjects. Out of the 36 WD mice, 5 mice were excluded (2 WD + oil and 3 WD + CCl₄; euthanized as they were in a critical state). Out of the 48 CDA-HFD mice, 2 mice were also excluded (1 CDA-HFD + 1w ND and 1 CDA-HFD + 4w ND). The final cohort included in this study is summarized in Table 3.2.1.

The results (Figure 3.2.2) showed that for the WD NASH mice model, before starting the CCl₄ or oil peritoneal injections (the first four weeks), both WD + CCl₄ and WD + oil mice groups gained weight in a similar way. This weight increase was higher than the weight increase of the ND mice group. Once the injections started, the WD + oil mice weight increased monotonously while the increase in the WD + CCl₄ mice weight was less marked and close to the ND mice weight increase. For the CDA-HFD NASH mice model, the mice weight increased

during the 16 weeks of CDA-HFD diet, but the increase was less marked than the ND mice weight increase. Once the diet was reversed their weight increased distinctly.

Table 3.2. 1: The final mice cohort included in this study.

Mice groups	Induction duration (weeks)	Mice number
WD + oil	12	8
	16	6
WD + CCl₄	12	7
	16	10
CDA-HFD	10	8
	16	8
CDA-HFD + ND (Diet reversal as treatment)	10 + 1	7
	10 + 4	7
	16 + 1	8
	16 + 4	8
ND	10	4
	12	4
	16	4

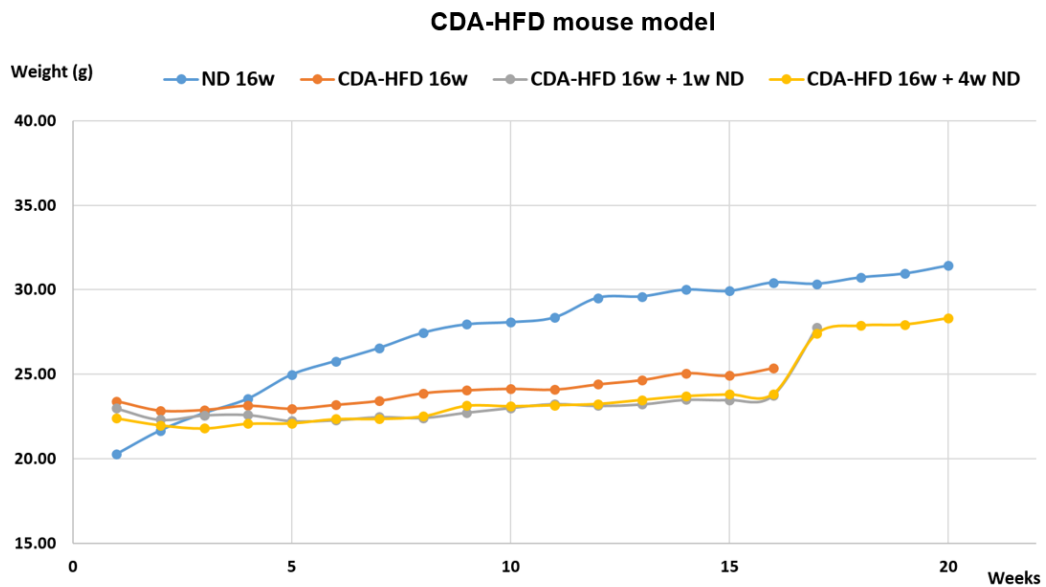


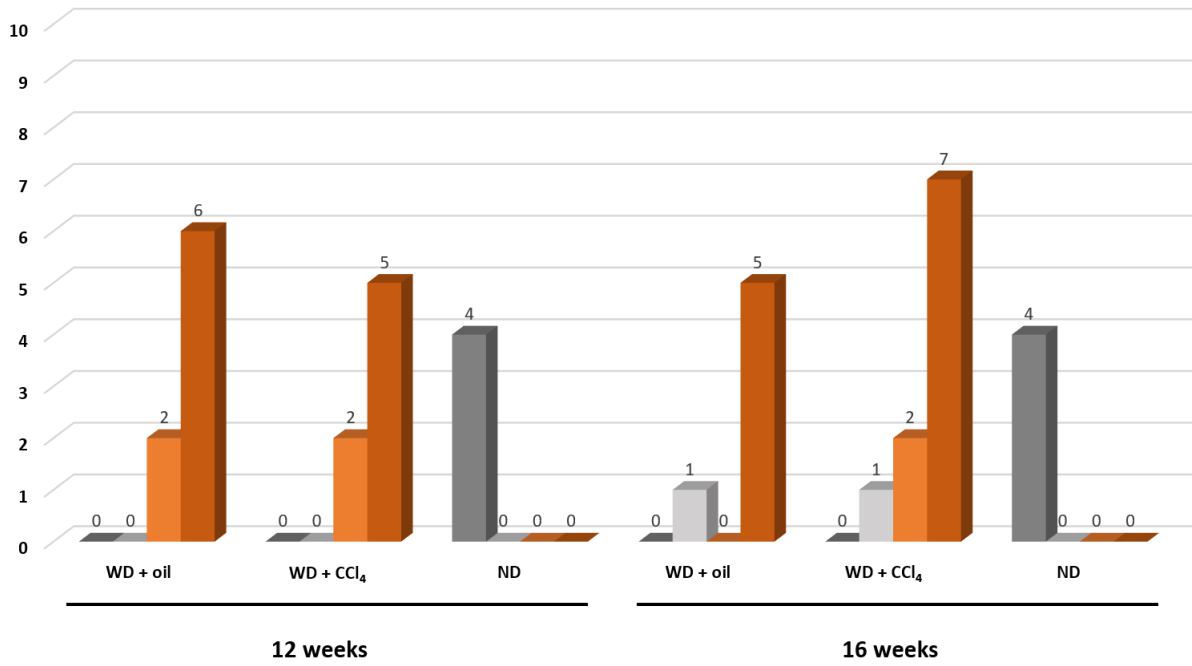
Figure 3.2. 2: Mice mean weight per group measured weekly for a) WD NASH mice model from 4 weeks until 20 weeks and b) CDA-HFD NASH mice model (the results presented here are those of the 16 weeks of diet, 16 weeks of diet + 1 weeks of reversed diet (ND) and 16 weeks of diet + 4 weeks of reversed diet (ND) in addition to the control group (16 weeks of ND)).

The histological results are reported in Figure 3.2.3 (for the WD NASH mice model) and Figure 3.2.4 (for the CDA-HFD NASH mice model) and summarized in table 3.2.2. Representative images of the histologic analysis results are shown in Figure 3.2.5. For the WD NASH mice model, after 12 weeks of induction, moderate to advanced steatosis (S2-S3) was reported in the WD + oil group with no inflammation, hepatocellular ballooning or fibrosis, while the WD + CCl₄ group developed moderate to advanced steatosis (S2-S3), low to moderate inflammation (I1-I2), low to advanced fibrosis (F1-F3) with no hepatocyte ballooning. After 16 weeks of induction, the WD + oil mice group displayed low to advanced steatosis (S1-S3), none to moderate inflammation (I0-I2), minor stages of fibrosis (F0-F1) with no ballooning, whereas the WD + CCl₄ mice group showed mostly advanced steatosis (S3), severe inflammation (I3), moderate to advanced fibrosis (F1-F3) and 3 out of the 10 mice of this group developed early ballooning (B1).

For the CDA-HFD NASH model, mice had severe stages of steatosis (S3), inflammation (I3), fibrosis (F3) ≥ 10 weeks. No hepatocyte ballooning was detected after 10 weeks of induction nor after 16 weeks. After one week of reversed diet (ND), steatosis decreased from severe (S3) to low (S1) for both 10w-CDA-HFD and 16w-CDAHFD groups, inflammation and fibrosis decreased as well for some mice of the 10w-CDA-HFD group. However, these two histological features did not regress within the 16w-CDA-HFD group. After four weeks of reversed diet (ND), steatosis disappeared in both 10w-CDA-HFD and 16w-CDA-HFD groups, while inflammation and fibrosis regressed for some mice of the 10w-CDA-HFD group and did not change at all within the 16w-CDA-HFD group.

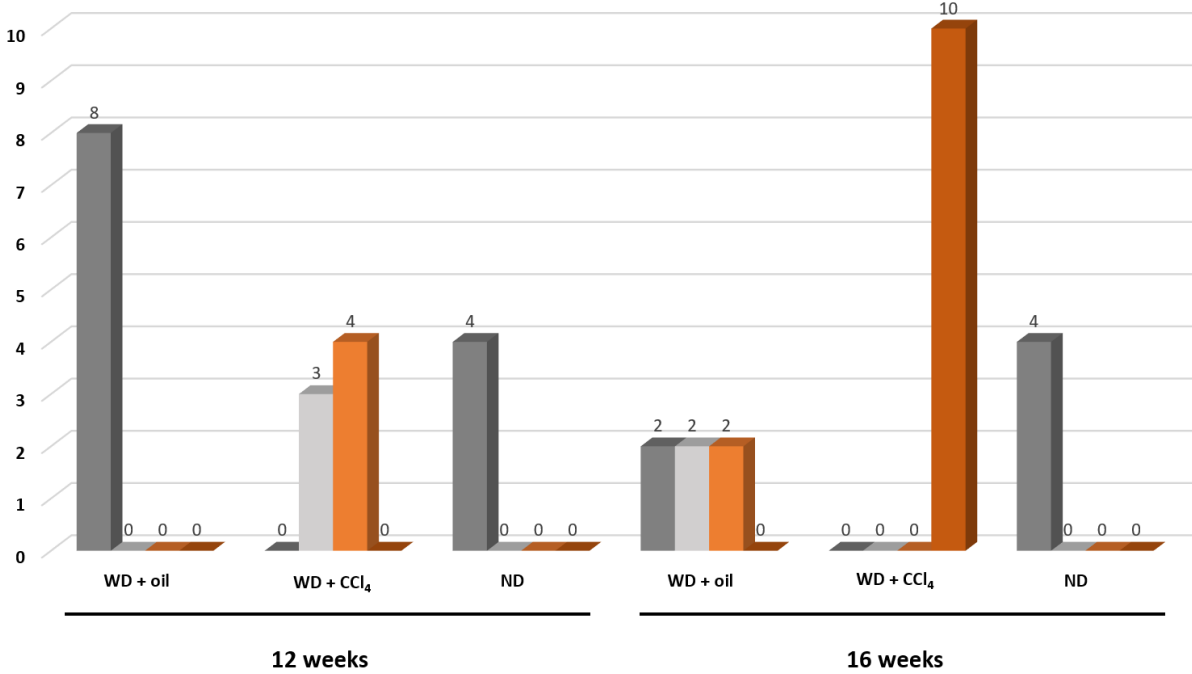
Mice number

Steatosis: 0 1 2 3



Mice number

Inflammation: 0 1 2 3



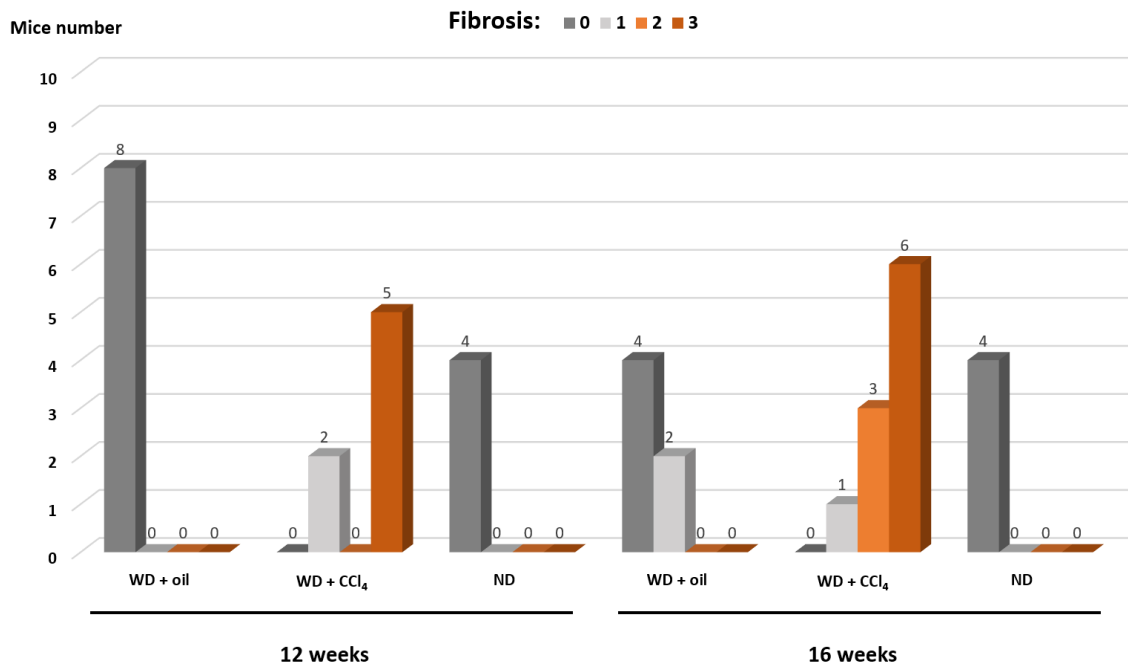
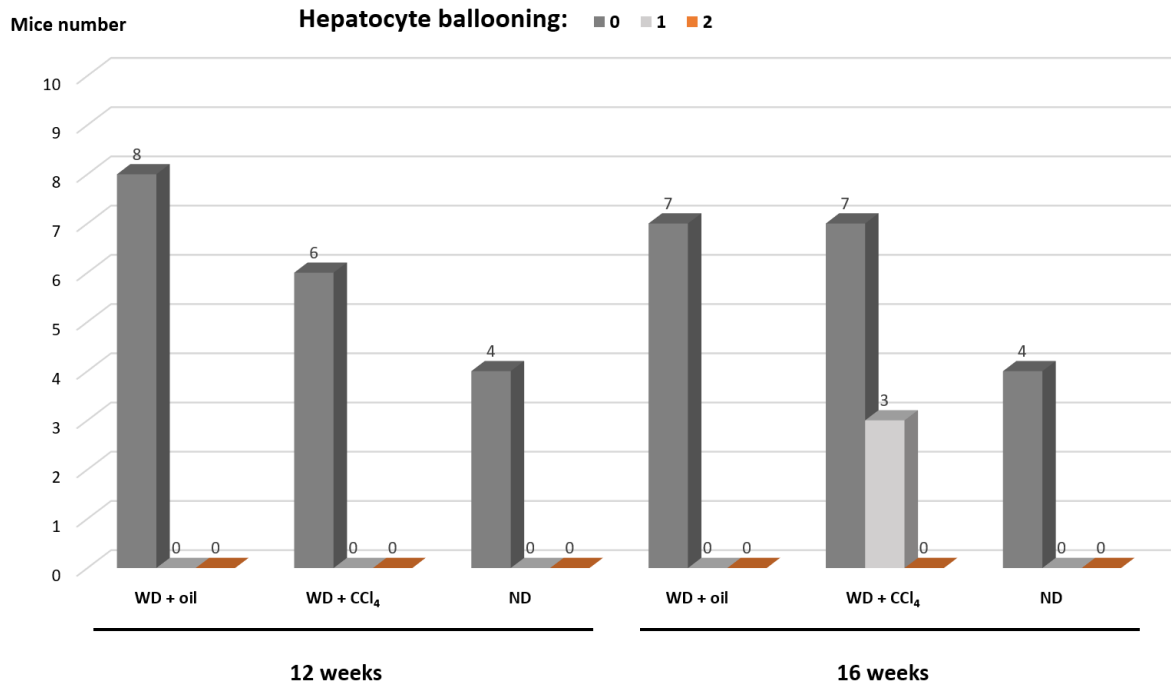
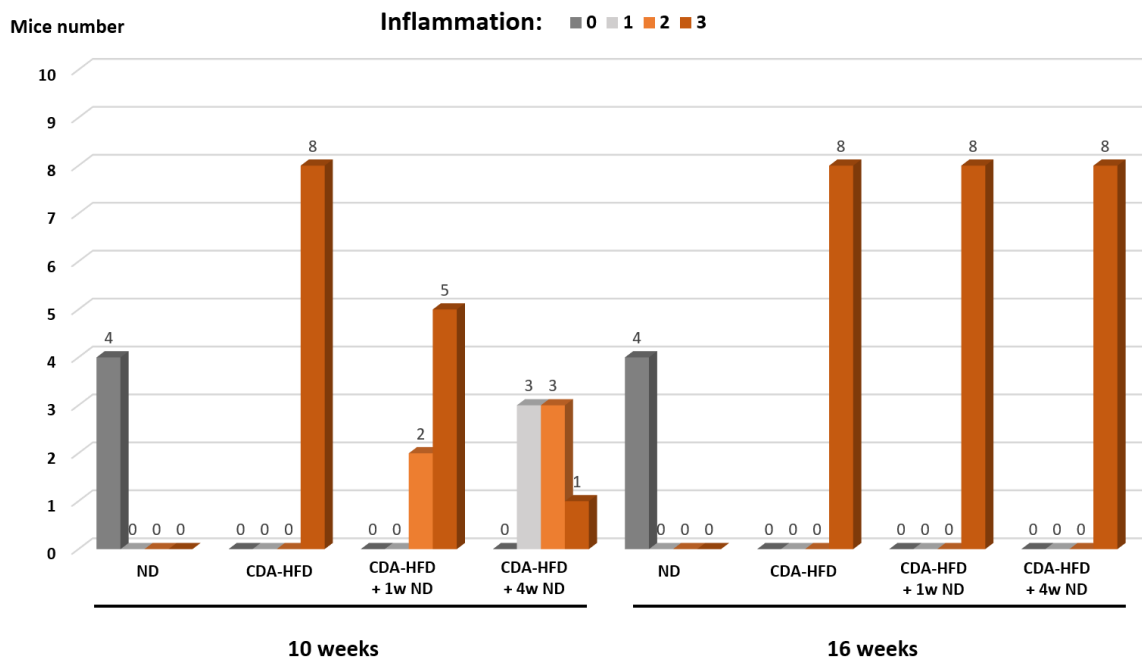
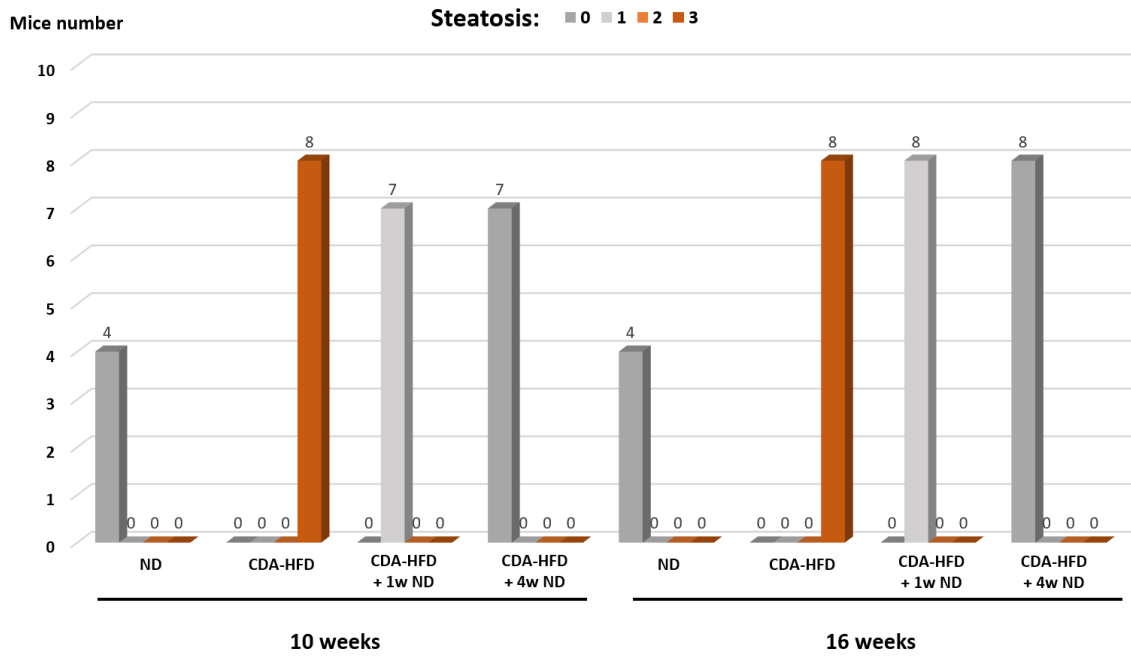


Figure 3.2. 3: Histological analysis of our WD NASH mice model study presented for each histological feature of NAFLD; a) steatosis, b) inflammation, c) hepatocyte ballooning and d) fibrosis, per group (WD + oil and WD + CCl₄ groups versus the control group (ND)) at 12 weeks versus 16 weeks.



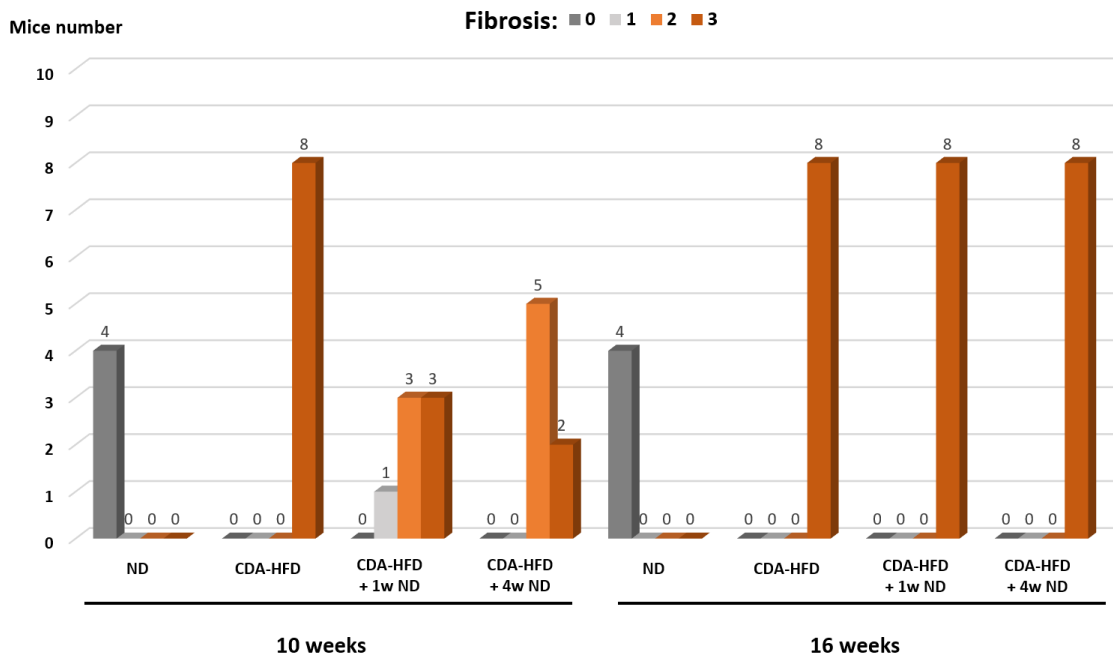
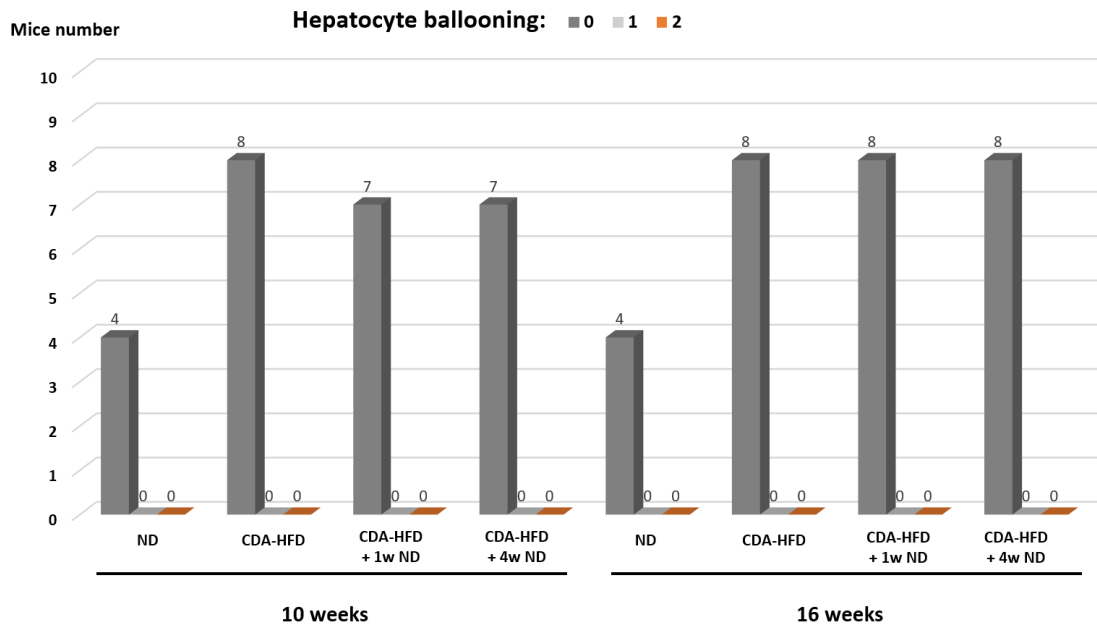


Figure 3.2. 4: Histological characterization of the CDA-HFD NASH mice model study displayed for each histological feature of NAFLD: a) steatosis, b) inflammation, c) hepatocyte ballooning and d) fibrosis, per group (CDA-HFD versus the reversed diet groups: CDA-HFD + 1 week of ND and CDA-HFD + 4 weeks of ND) at 10 weeks versus 16 weeks.

Table 3.2. 2: Histological results for the WD and the CDA-HFD mouse models.

WD			CDA-HFD	
Model induction duration	Results		Model induction duration	Results
	WD + oil	WD + CCL ₄		
12 weeks	Steatosis grade S2-S3, with no inflammation, no fibrosis and no ballooning	Steatosis grade S2-S3, inflammation grade I1-I2, fibrosis stage F1-F3 with no ballooning	10 weeks	Steatosis grade S3, inflammation grade I3, fibrosis stage F3 with no ballooning
			16 weeks	Steatosis grade S3, inflammation grade I3, fibrosis stage F3 with no ballooning
			10 weeks + 1 week of ND	Steatosis grade S0, inflammation grade I2-I3, fibrosis stage F1-F3
16 weeks	Steatosis grade S1-S3, inflammation grade I0-I2, fibrosis stage F0-F1 with no ballooning	Steatosis grade S3, inflammation grade I3, fibrosis stage F1-F3, ballooning grade B0-B1	16 weeks + 1 week of ND	Only steatosis decreased to grade S1
			10 weeks + 4 weeks of ND	Steatosis grade S0, inflammation grade I1-I3, fibrosis stage F2-F3
			16 weeks + 4 weeks of ND	Only steatosis decreased to grade S0

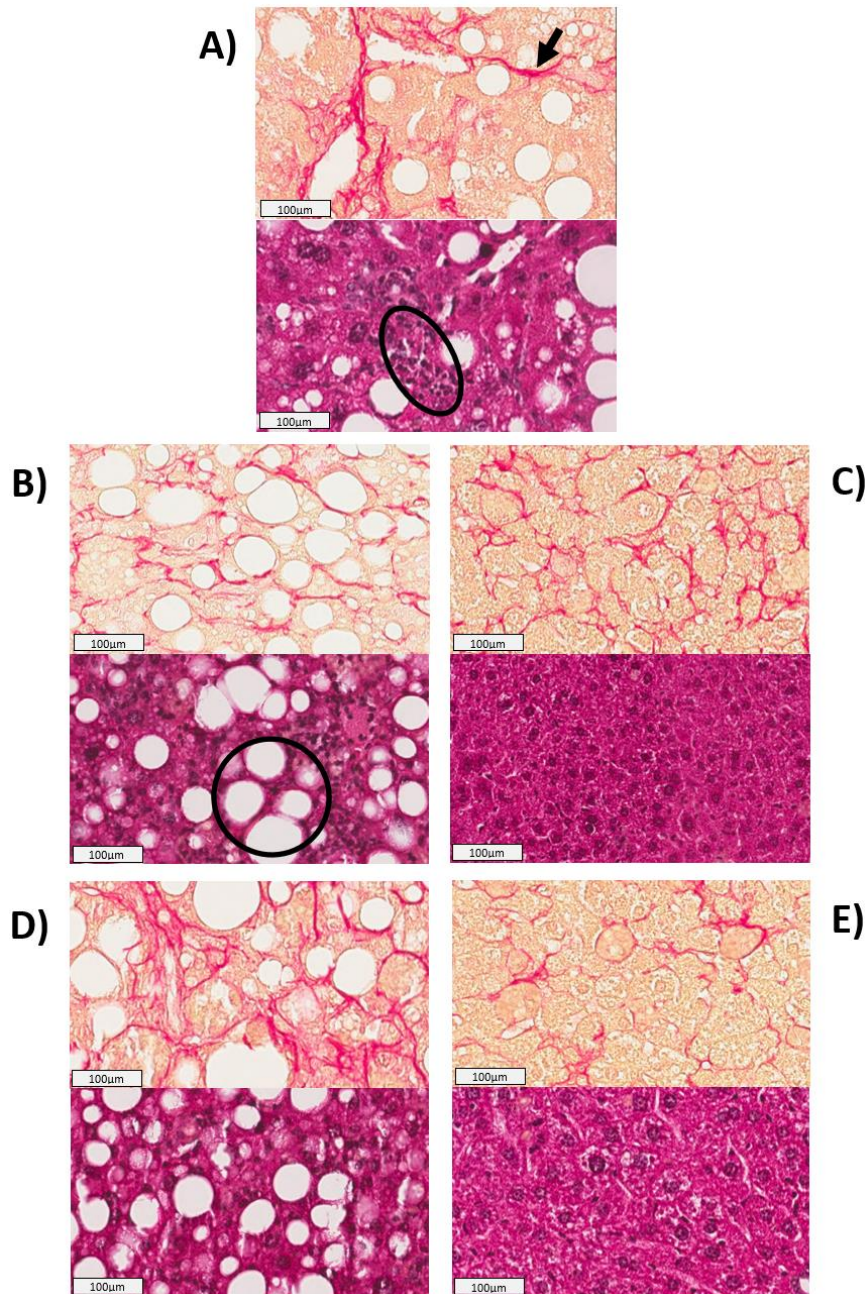


Figure 3.2. 5: Histological sections (upper row: picosirius red stained slices; second row: hematoxylin-eosin stained slices) with x20 image magnification. A) Mouse fed WD + CCL4 for 16 weeks (grade 3 for steatosis and inflammation (ellipse) without ballooning and with stage 2 for fibrosis (arrow)). B) Mouse fed CDA-HFD for 10 weeks (grade 3 for steatosis (circle) and inflammation without ballooning and with stage 3 for fibrosis). C) Mouse fed CDA-HFD for 10 weeks followed by ND for 4 weeks (grade 1 for inflammation with no steatosis nor ballooning and with stage 2 for fibrosis). D) Mouse fed CDA-HFD for 16 weeks (grade 3 for steatosis and inflammation with no ballooning and with stage 3 for fibrosis). E) Mouse fed CDA-HFD for 16 weeks followed by ND for 4 weeks (grade 3 for inflammation with no steatosis nor ballooning and with stage 3 for fibrosis).

3.2.3. Discussion

The weight of the WD mice groups increased (compared to the ND mice group) similarly before starting the CCl₄ or oil intraperitoneal injections because of the diet with high fat, sucrose, and cholesterol content in addition to glucose and fructose in the drinking water. However, once the injections started, the WD + oil mice weight continued to increase monotonously while the increase in the WD + CCl₄ mice weight was much less marked which confirms the effect of CCl₄ on the mice body weight and food intake observed in our first WD NASH mice model study.

For the CDA-HFD mice, their weight increased similarly during the 16 weeks of CDA-HFD diet, but the increase was lower than the ND mice weight increase which was because of the deficiency in choline in the CDA-HF diet. In fact, multiple studies have reported that animals with choline-deficient diet (CDAA) do not display a metabolic phenotype similar to human patients as they do not gain weight and do not display insulin resistance even when combined with a high fat diet (CDA-HFD) [54, 56, 73, 74]. This NASH mice model allows for a quick development of NASH with fibrosis (6–9 weeks of diet) but without metabolic syndrome features seen in human NAFLD such as obesity. Moreover, the results showed that once the diet was reversed and the mice were fed a normal diet their weight increased distinctly.

The histological results of the WD combined with a weekly low dose of CCl₄ model in this study were similar to those reported in the previous WD NASH model study even with the changes that have been adopted to improve the outcomes of the study, including starting the diet at four weeks, increasing the induction duration until 16 weeks, weighting and monitoring the mice, and improving animal housing conditions. As mentioned before this model was based on the NASH mice model induction of Tsuchida T. et al.,[10] which resulted in advanced bridging fibrosis and severe NASH (i.e. steatosis, inflammation and ballooning) development after only 12 weeks of induction. In our study in which the same diet with sugar in drinking water, the same weekly dose of CCl₄ mixed with oil and the same mice strain were used, we did not observe severe NAFLD even after 16 weeks of WD + CCl₄ induction. The mice in our study developed advanced steatosis and inflammation, moderate to advanced fibrosis but only few mice developed early stage ballooning (i.e. only few mice developed early NASH

stage). Thus, we did not reproduce the results of this NASH model and our study suggests that this model is not highly reproducible.

We used the CDA-HFD NASH model in another study (see section “Multi-parametric preclinical MRI of NAFLD”) with 4, 10 and 16 time points and most of the mice included have developed all the characteristics of NASH (some mice had severe NASH) with advanced bridging fibrosis. Here, using the CDA-HFD NASH model, mice developed severe stages of steatosis, inflammation and fibrosis after 10 weeks. However, no hepatocyte ballooning was detected after 10 or 16 weeks of induction. Hepatocyte ballooning is a crucial histological feature of NASH. Although, it is hard to detect [53].

Reversed diet was used in this study as treatment for NAFLD/NASH^[353]. Steatosis decreased after one week of reversed diet (ND) and disappeared after 4 weeks of ND in both 10w-CDA-HFD and 16w-CDAHFD groups. Inflammation and fibrosis decreased slightly for the 10w-CDA-HFD group, after both one week and four weeks of ND. However, these two last histological features did not regress within the 16w-CDA-HFD group. This suggests that when the disease is induced for a relatively long time, the inflammation and fibrosis development within the liver needs longer periods of ND to reduce the severity of these histological features of NASH. Longer reversed diet durations should be used in future studies.

To summarize, CDA-HFD NASH murine model allows for inducing more advanced stages of steatosis, inflammation and fibrosis than the WD combined with CCl₄ NASH mice model. Even though in our study early ballooning was observed in some mice with the WD+ CCl₄ model, the CDA-HFD model is more efficacious and reproducible and should be used in NASH imaging with long induction durations. However, this model should not be used when studying the metabolic syndrome of this disease.

4. Chapter II : Multi-parametric preclinical MRI of NAFLD

NAFLD encompasses a dynamic spectrum of histological lesions ranging from non-progressive or slowly progressive pure steatosis to a progressive form with active lesions of hepatocyte injury and inflammation leading to fibrosis and cirrhosis. Classically, NASH which associates steatosis, liver ballooning, and inflammation is considered to correspond to the progressive form of NAFLD associated with evolution to cirrhosis and its complications [11, 12, 354]. However, non-NASH is a heterogeneous group that includes not only simple steatosis or NAFL, but also borderline NASH forms, usually consisting of steatosis, inflammation, and appropriate fibrosis without ballooning [36, 355, 356]. These intermediate cases may represent more advanced disease than NAFL [36].

Fibrosis is the main prognostic factor in NAFLD [43-45]. The association of poorer prognosis with fibrosis has led to a shift for defining significant ($\geq F2$) fibrosis rather than NASH as progressive NAFLD that requires management [47, 48, 357, 358]. Several definitions of progressive NAFLD have been proposed. They include significant MLD defined as fibrosis stage ≥ 2 and/or activity (sum of inflammation and ballooning) grade ≥ 2 , NASH-related fibrosis identified by steatosis ≥ 1 (NAFLD) and significant fibrosis ($F \geq 2$), and fibro-NASH defined as NASH, $NAS \geq 4$, and advanced fibrosis ($F \geq 2$) [11, 42, 46, 359]. Significant MLD and NASH-related fibrosis can occur in both NASH and non-NASH cases.

Diagnosing progressive NASH still requires liver histology, and therefore presents all the drawbacks associated with liver biopsies. Hence, a noninvasive and accurate method for the characterization of NAFLD is needed.

This study covers two parts. The first part is applicative and concerns the diagnosis of progressive NAFLD with MRE while the second one is methodological and concerns PDFF and T1 mapping methods. The general elements presented first in the section below were used in both parts of the study.

4.1. General elements of the study

4.1.1. Study cohort

All animal experiments in this study were approved by the local ethics committee (Apafis n°19705). This study enrolled three groups of male C57/bl6 mice: a normal diet (ND) group (36 mice), a high fat diet (HFD; 60 kcal %, Research Diets/Brogaarden, D12492i, Lyngø, Denmark) group (36 mice) and a choline-deficient, L-amino acid-defined, high-fat diet (CDA-HFD; 60 kcal % fat and 0.1% methionine by weight, Research Diets/Brogaarden, A06071302i, Lyngø, Denmark) group (36 mice) [73, 346, 360]. The mice were housed in standard conditions for 4, 10 and 16 weeks (n = 12 mice per time point) (Figure 4.1.1). The group sizes were calculated to allow at least 90% power to detect at a 5% significance level, a significant difference between the AUC of NASH and a null hypothesis value of 0.50, considering the AUC of NASH being 0.8, and the ratio of mice without/with NASH being 2. Under these conditions, at least 39 mice were required in the study. Hence, a total number of 72 mice with NASH mouse models and 36 mice as control group (12 mice per study group and time point) was used to compensate for possible mice loss and for variable NAFLD occurrence.

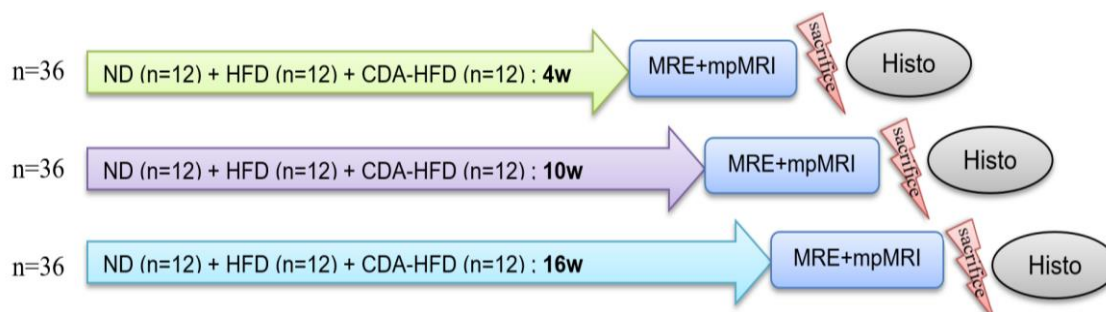


Figure 4.1. 1: Study timeline of groups and subgroups included

Mice excluded from the study

Of the 108 mice enrolled in the study, 7 (5 ND 16 weeks, 1 HFD 4 weeks and 1 CDA-HFD 4 weeks) were excluded because of lack of MRI data and histology (4 mice did not have histological analysis and 3 died during acquisitions).

4.1.2. MRI experiments

MRI experiments were performed with a horizontal-bore 7T 300 mT/m MRI system (Pharmascan - Bruker, Erlangen, Germany), using a radiofrequency volume coil for transmission, an actively decoupled 3 cm diameter surface coil for reception and ParaVision software (PV5, Bruker, Ettlingen, Germany).

The animals were anesthetized with isoflurane in a 70% air / 30% O₂ mixture at a concentration of 3%. To maintain the anesthesia during imaging, isoflurane at 1-2% concentration was used and constantly adjusted with real-time monitoring of the respiration using an abdominal pressure sensitive pad (SA instruments, New York, USA). The mice were scanned in prone position. Throughout the imaging sessions, a cooling/heating system was used to maintain the mice body during scanning.

4.1.3. Histological analysis

Following MRI, the mice were euthanized, and the hepatic histopathological features were assessed on the right medial lobe of the liver by a pathologist blinded to the dietary conditions and the MRI results. Based on the NASH CRN staging system [12, 361], the amount of steatosis (percentage of hepatocytes containing medium or large fat droplets) was scored as 0 (< 5%), 1 (5 – 33%), 2 (> 33 – 66%) and 3 (> 66%); hepatocyte ballooning was classified as 0 (none), 1 (few) or 2 (many cells/prominent ballooning); and foci of lobular inflammation were scored as 0 (no foci), 1 (\leq 2 foci per 20 \times field), 2 (> 2 foci per 20 \times field) or 3 (> 4 foci per 20 \times field). Fibrosis was staged as F0 (no fibrosis), stage F1a (mild, zone 3, perisinusoidal fibrosis), stage F1b (moderate, zone 3, perisinusoidal fibrosis), stage F1c (portal/periportal fibrosis), stage F2 (perisinusoidal and portal/ periportal fibrosis), stage F3 (bridging fibrosis) and stage F4 (cirrhosis) [12]. The 3 substages (1a, 1b, and 1c) were pooled into a single F1 score [362].

4.2. Diagnostic of NAFLD : Magnetic Resonance Elastography

Magnetic resonance elastography (MRE) has been reported to be a useful method for the diagnosis of hepatic fibrosis and inflammation in patients with NAFLD, even in the early stages of the disease [158, 209, 251, 253, 363]. Stiffness increase has been shown in patients with NASH and significant fibrosis [48, 49, 125, 364]. Moreover, it has been reported that viscosity-related parameters may be useful for assessing inflammation and disease activity in patients with NAFLD [171, 235, 365]. However, the diagnostic accuracy of MRE derived parameters in assessing the different definitions of the progressive form of NAFLD (i.e. NASH, significant MLD, NASH-related fibrosis and fibro-NASH) remains to be clarified. Therefore, the aim of this preclinical study was to investigate the role of MRE in detecting the histopathological features of NAFLD particularly inflammation, fibrosis and hepatocellular ballooning and in diagnosing the progressive forms of the disease, in mice with NAFLD.

4.2.1. Data acquisition

To perform MRE, the mechanical waves were generated by a uniaxial electrodynamic acoustic shaker (Bruel & Kjaer 4808, Mennecy, France) driven by an amplified function generator synchronized to the MRI system. The waves were transmitted to the piston via a carbon fiber rod and a flexible linkage converting the longitudinal motion of the rod into vertical motion of the piston as described previously [159]. The mice were scanned in the prone position and their liver was centered on the plastic piston.

Liver MRE was performed with a multi-slice multi-echo spin echo imaging sequence. Data were acquired sequentially in the three spatial directions of motion, with 4 time-offset samples per mechanical period. Three mechanical excitation frequencies of 200, 400, and 600 Hz were acquired sequentially with 1, 3 and 6 periods of a sinusoidal gradient waveform at the mechanical excitation frequency for motion encoding periods. Repetition and echo times were 1010 ms and 30 ms, respectively for all probed mechanical frequencies. Image acquisitions were obtained with 0.3 x 0.35 mm spatial resolution, 100 x 85 acquisition matrix, 30 mm x 30 mm field of view, 9 contiguous slices and 0.3 mm slice thickness. Scan time was 5 min 54 s per encoding direction for each of the three frequencies. An anatomic reference image was obtained with a T2-weighted RARE spin echo sequence acquired with respiratory

gating using the same geometry as the MRE sequence, with TR/TE = 3000 ms / 23 ms, RARE factor = 4 and 3 min 12 s scan time.

4.2.2. Data processing

Data processing was performed using in-house tools created with Root (CERN, Geneva, Switzerland) and MatLab (MathWorks, R2017a, Natick, Massachusetts, USA). Shear waves were extracted from the phase images by unwrapping and calculation of the curl, and the amplitude and phase of the shear wave displacement field at the main frequency were obtained via time-domain Fourier transform. The mechanical properties were analyzed in terms of the complex shear modulus, \mathbf{G}^* composed of a real part the storage modulus (G'), and an imaginary part the loss modulus (G''). Alternately, the shear modulus was also expressed as the shear stiffness ($G^* = \sqrt{G'^2 + G''^2}$) and the shear modulus phase angle ($\alpha = \text{atan}(G''/G')$). These quantities were retrieved for each pixel of the region of interest by inversion of the wave propagation equation in a viscoelastic medium, under assumptions of planar waves and tissue incompressibility:

$$-\rho\omega^2\mathbf{q} = G\Delta\mathbf{q} \quad (17)$$

with $q = A_q \cdot e^{i\varphi_q}$ the complex displacement field (with A_q the amplitude and φ_q the phase), ρ the tissue density (taken to be 1000 kg/m³), G the complex shear modulus and Δ the Laplacian operator, using a published algorithm [166]. To obtain the mechanical parameter maps for each animal, a region of interest was placed by an operator (with 3-year-expertise) on the wave amplitude map within the liver where the amplitude of the wave was at least 10 μm for the 200 Hz and 400 Hz images and 3 μm for the 600 Hz images. The slice on which each ROI was positioned was chosen with the aim of matching the histological slices performed on the right medial lobe of the liver and staying the closest possible to the piston generation the mechanical waves. Damping ratio (ζ) [166], shear modulus and phase angle were calculated locally based on the G' and G'' values obtained by the inversion process. For the multifrequency analysis, the frequency dispersion coefficient of the shear stiffness (γG^*) was assessed by assuming a power law (i.e. $|G^*(\omega)| \propto A \cdot \omega^\gamma$) with $|G^*(\omega)|$ being the frequency-dependent shear modulus, γ (gamma) the power law exponent or frequency dispersion coefficient, ω the angular frequency and A being a scaling parameter [190, 191].

The frequency dispersion coefficient (γ_{G^*}) was estimated by analytical regression (linear regression in log-log space) using $|G^*|$ average value of the ROI calculated at each frequency.

Data filtering

To examine whether or not wave amplitude and signal to SNR values within the region of interest had an effect on the estimation of the mechanical properties [366], mean values of wave amplitude were estimated and SNR values were measured by subtracting the magnitude images of the different encoding directions, two by two, and calculating the mean values of the standard deviation of this subtraction, adapted from Dietrich & al [367]. Based on the values obtained, for the monofrequency analysis we focused on the performance of the MRE parameters at 400 Hz as MRE wave amplitude and SNR values were the best at this frequency (see results below). Afterwards, a MatLab software was developed to exclude from the regions of interest, the pixels with values lower than a given arbitrary threshold. For convenience, the threshold was expressed as $(\mu - a \cdot \sigma)$ with μ the mean value of the entire cohort, σ the standard deviation and "a" a user-adjustable parameter. At high values of a, most pixels are retained and all mice are kept for analysis, but the data may present with artifacts arising from areas with weak waves or SNR. Conversely for low or even negative values of "a", data are effectively filtered from problematic pixels, but at the cost of excluding mice in which none of the pixels are above the threshold, and at the cost of generally smaller regions of interest, potentially limiting the statistical power of the estimated measurements and increasing the sensitivity of the measurements to the spatial heterogeneity arising from acquisition factors (surface coil sensitivity profile, wave penetration pattern) or from true physiologic heterogeneity. After multiple tests involving a range of values for "a" and different combination strategies between wave amplitude-based exclusion and SNR-based exclusion (either, both or thresholding on their product), a value of $a = 1$ for both SNR and wave amplitude was deemed satisfactory to enable data filtering while limiting the number of excluded mice. Final masks were obtained by only selecting pixels that satisfied both thresholding conditions (in terms of SNR and A_{tot}) with a threshold factor of $a = 1$. Then, storage and loss moduli and the shear stiffness were assessed for each animal using this pixel exclusion methodology. The data preserved were those for which both the wave amplitude

and the SNR were greater or equal to their thresholds. The resulting data were compared to the data obtained without filtering.

4.2.3. Statistical analysis

All statistical analysis were performed using MedCalc software version 19.4.1 (MedCalc Software Ltd, Ostend, Belgium). Comparisons of the mechanical parameters (shear stiffness and storage and loss moduli) without and with filtering versus the histological features of NAFLD were performed using Spearman's rank correlations and stepwise multiple regression with the mechanical parameters as the dependent variables and the histological features of NAFLD (i.e. steatosis, inflammation, ballooning and fibrosis) as the independent variables, while the evaluation of the diagnostic performance of these parameters in detecting NASH was performed using ROC curve analysis.

Once the suitable data to use were selected, the relationships between the MRE parameters and the histological features were assessed with Spearman's rank correlations and multiple regression analysis. Comparisons of the mechanical parameters between the different NAFLD classifications were performed with Mann Whitney statistical test. The diagnostic accuracy of the MRE parameters for NASH, significant MLD, NASH-related fibrosis and fibro-NASH was assessed with ROC curve analysis. All statistical analyses were performed in mice with NAFLD (steatosis ≥ 1). Mice with normal liver at histology were not included in this evaluation.

4.2.4. Results

Histological results

Of the 101 mice included in this study, 59 mice were classified as NAFLD (steatosis ≥ 1). Among the 59 mice with NAFLD, 21 (36%) mice had NASH (versus 38 (64%) non-NASH), 38 (64%) had significant MLD (versus 21 (36%) no significant MLD), 20 (34%) had NASH-related fibrosis (versus 39 (66%) no NASH-related fibrosis) and 12 (20%) had fibro-NASH (versus 47 (80%) no fibro-NASH). The 38 mice with significant MLD included 17 mice without NASH (Figure 4.2.1). The 20 mice with NASH related fibrosis included 8 mice without NASH. Steatosis, inflammation and ballooning grades, as well as fibrosis stages according to NASH, significant MLD, NASH-related fibrosis or fibro-NASH are shown in figures 4.2.2, 4.2.3, 4.2.4 and 4.2.5.

Representative images of the histologic analysis results are shown in Figure 4.2.6. Representative MRE images are shown in figure 4.2.7 and representative MRE parametric maps of the six mechanical parameters measured in this study are presented in appendix 8.1.

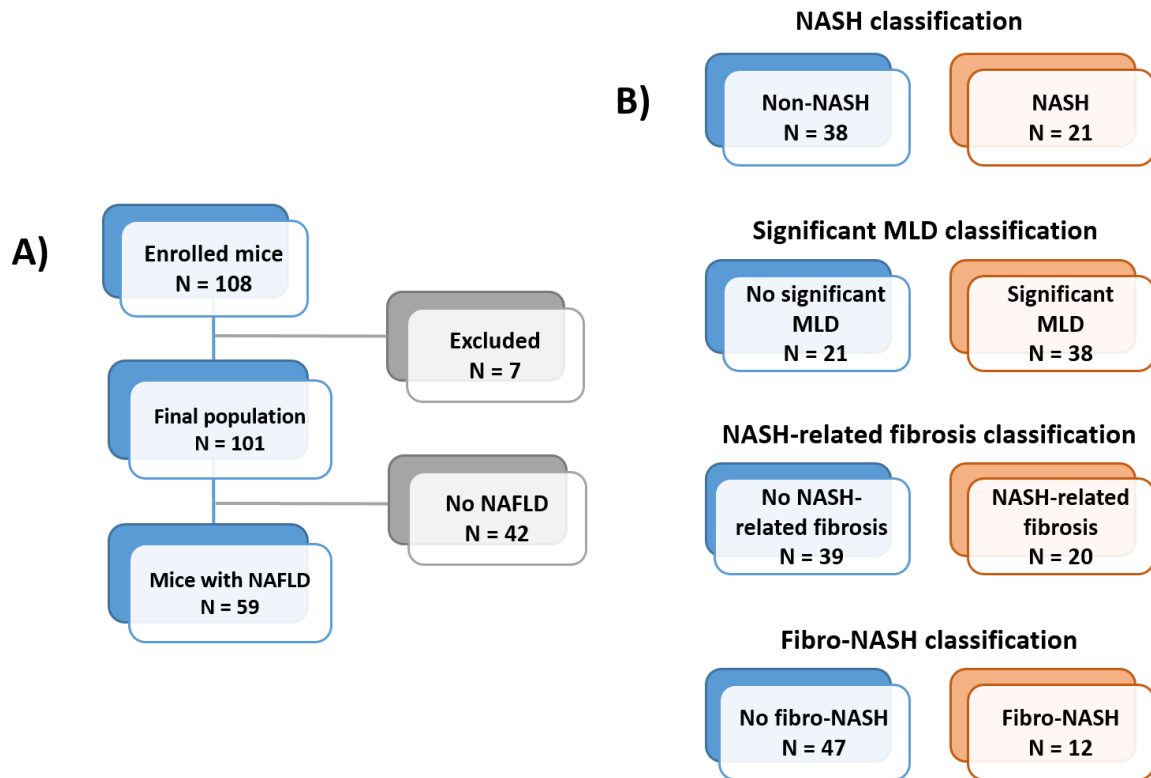


Figure 4.2. 1: A) flowchart of the mice included in the study. B) Mice number according to the different classification of the progressive form of NAFLD.

Steatosis grade ≥ 2 was observed in the 21 mice with NASH, in 37/38 (97%) mice with significant MLD, in 19/20 (95%) mice with NASH-related fibrosis and in the 12 mice with fibro-NASH (Figure 4.2.2). Inflammation grade ≥ 2 was observed in 12/21 (57%) mice with NASH, in 29/38 (76%) mice with significant MLD, in 15/20 (75%) mice with NASH-related fibrosis and in the 7/12 (58%) mice with fibro-NASH (Figure 4.2.3). Hepatocyte ballooning was observed in all the mice with NASH, in 21/38 (55%) mice with significant MLD, in 12/20 (60%) mice with NASH-related fibrosis and in all the mice with fibro-NASH (Figure 4.2.4). Fibrosis stage ≥ 2 was

observed in 12/21 (57%) mice with NASH, in 20/38 (53%) mice with significant MLD, and in all the mice with NASH-related fibrosis and fibro-NASH (Figure 4.2.5).

Inflammation was moderately correlated with fibrosis and steatosis with correlation coefficients and significance levels $r = 0.71$, $p < 0.0001$ and $r = 0.61$, $p < 0.0001$ respectively. Steatosis was also moderately correlated with fibrosis ($r = 0.54$, $p < 0.0001$). Hepatocyte ballooning had mild correlation with steatosis ($r = 0.38$, $p = 0.003$), fibrosis ($r = 0.34$, $p = 0.009$) and inflammation ($r = 0.32$, $p = 0.01$).

Data filtering results

The mean values of the wave amplitude and SNR measurements for the three frequencies are shown in Table 4.2.1. The best mean values of both MRE wave amplitude and SNR were at 400 Hz. Hence for the monofrequency analysis we focused on this frequency for the evaluation of the performance of the viscoelastic parameters.

The filtering thresholds used for the wave amplitude and SNR were fixed at $15.03 \mu\text{m}$ and 1.52 respectively. Using these thresholds, only one mouse was excluded. The mean value of the ROI size before and after filtering were 289 and 229 pixels respectively and the percentage of the pixels excluded by filtering was 21% (mean value).

Table 4.2. 1: Wave amplitude and SNR measurements mean values for each of the three frequencies.

Frequency	Wave amplitude (μm)	SNR
200 Hz	20.11 ± 7.68	2.09 ± 0.59
400 Hz	21.27 ± 6.24	2.31 ± 0.79
600 Hz	7.72 ± 3.67	2.06 ± 0.51

Steatosis

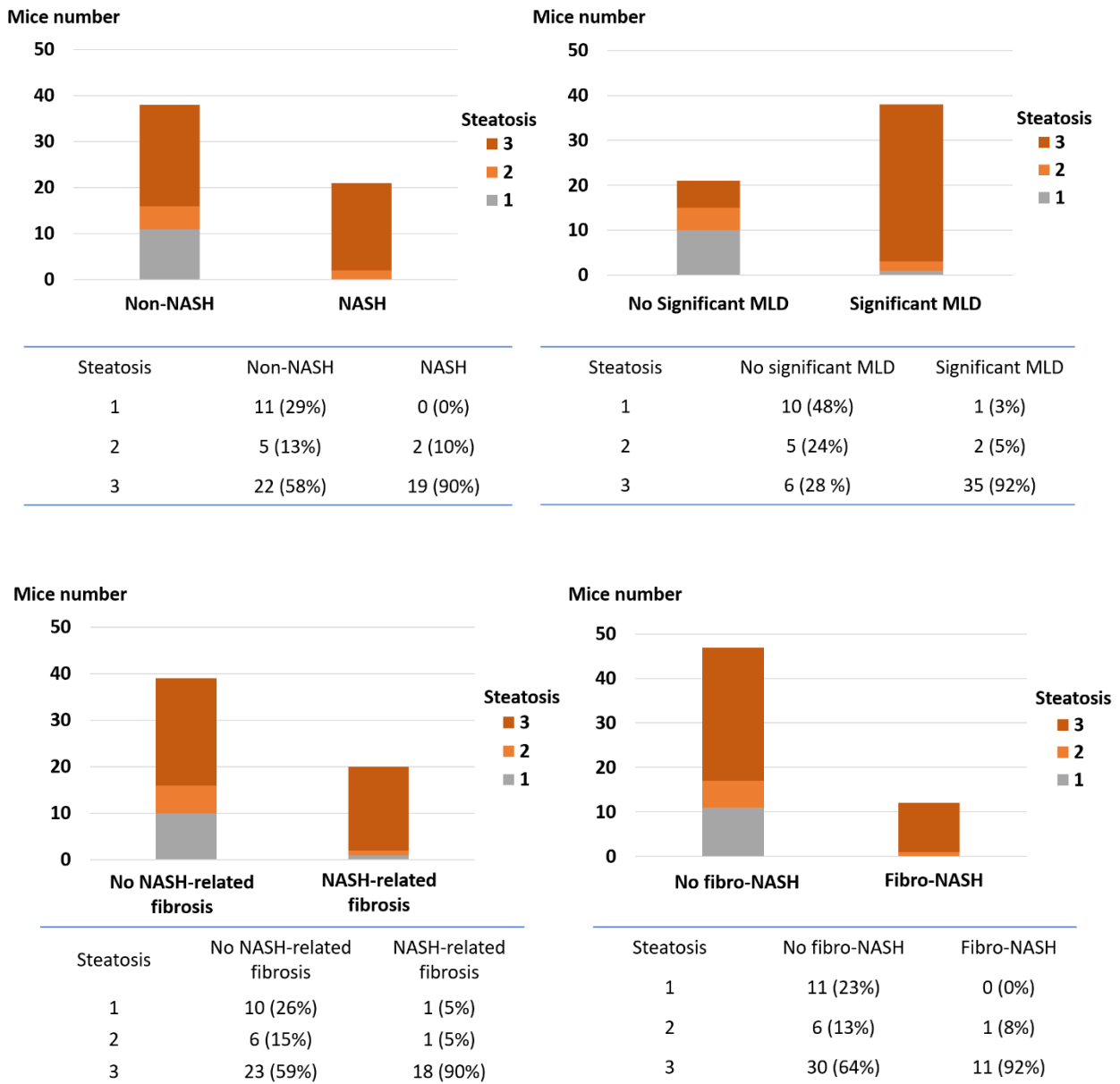
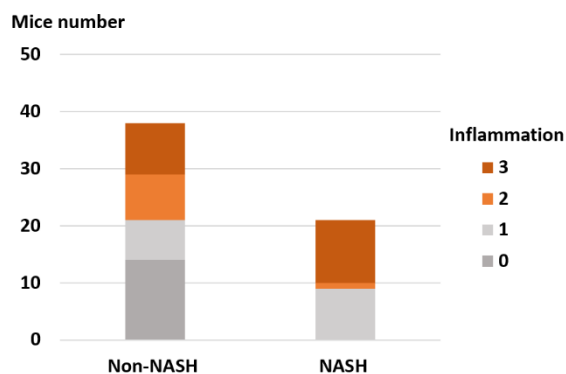
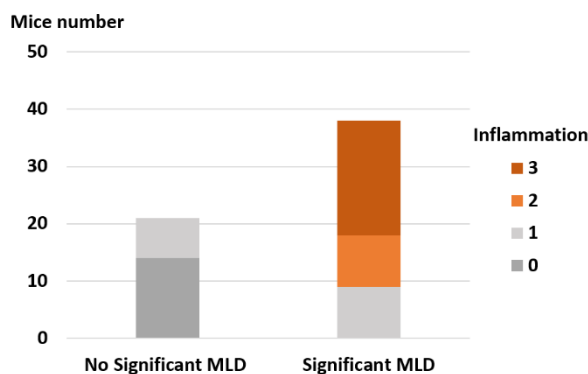


Figure 4.2. 2: Steatosis grades according to NASH, significant MLD, NASH-related fibrosis and fibro-NASH. Steatosis grade ≥ 2 is observed in the 21 mice with NASH, in 37/38 (97%) mice with significant MLD, in 19/20 (95%) mice with NASH-related fibrosis and in the 12 mice with fibro-NASH.

Inflammation

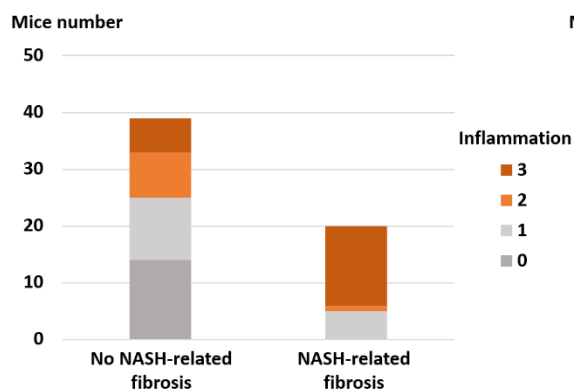


Inflammation	Non-NASH	NASH
0	14 (37%)	0 (0%)
1	7 (18%)	9 (43%)
2	8 (21%)	1 (5%)
3	9 (24%)	11 (52%)

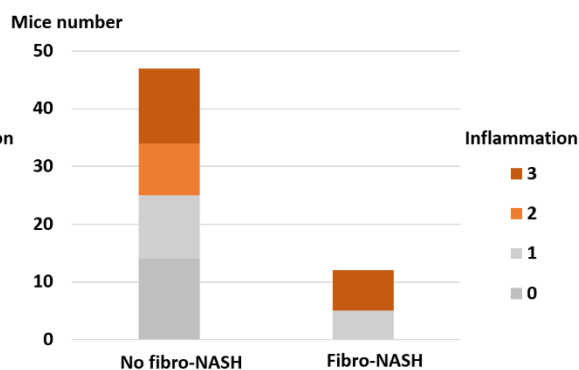


Inflammation	No significant MLD	Significant MLD
0	14 (67%)	0 (0%)
1	7 (33%)	9 (24%)
2	0 (0%)	9 (24%)
3	0 (0%)	20 (52%)

Inflammation



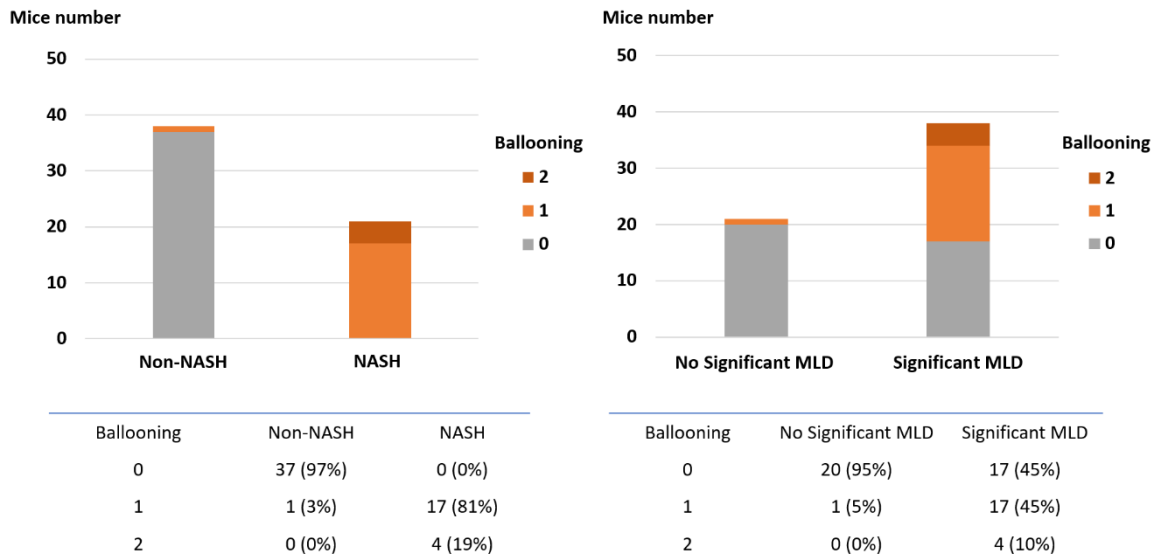
Inflammation	No NASH-related fibrosis	NASH-related fibrosis
0	14 (36%)	0 (0%)
1	11 (28%)	5 (25%)
2	8 (21%)	1 (5%)
3	6 (15%)	14 (70%)



Inflammation	No fibro-NASH	Fibro-NASH
0	14 (30%)	0 (0%)
1	11 (23%)	5 (42%)
2	9 (19%)	0 (0%)
3	13 (28%)	7 (58%)

Figure 4.2. 3: Inflammation grades according to NASH, significant MLD, NASH-related fibrosis and fibro-NASH. Inflammation grade ≥ 2 is observed in 12/21 (57%) mice with NASH, in 29/38 (76%) mice with significant MLD, in 15/20 (75%) mice with NASH-related fibrosis and in the 7/12 (58%) mice with fibro-NASH.

Ballooning



Ballooning

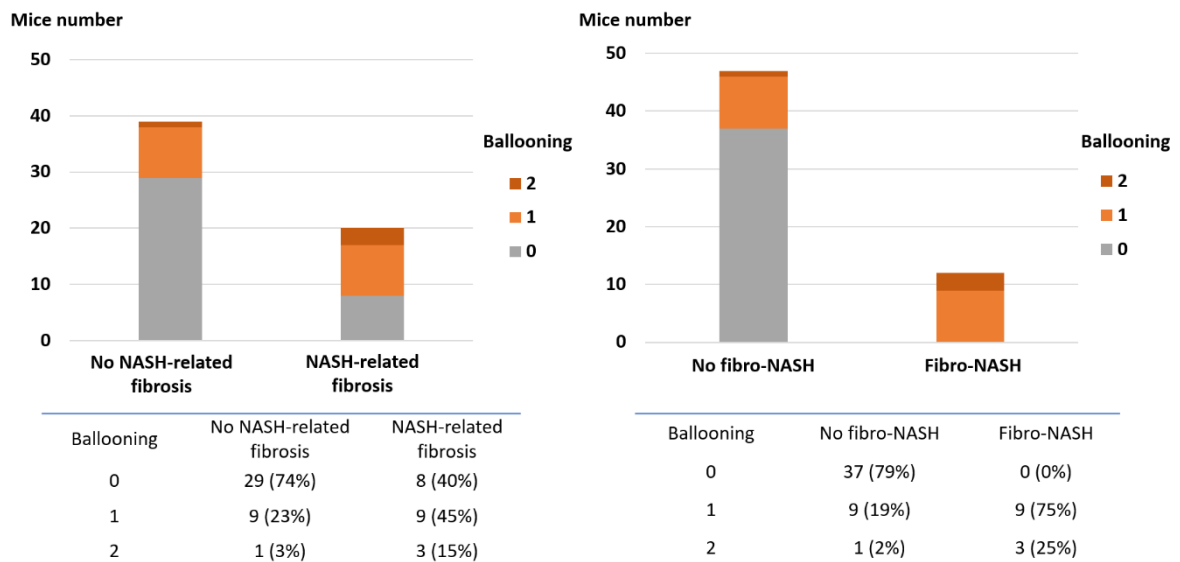
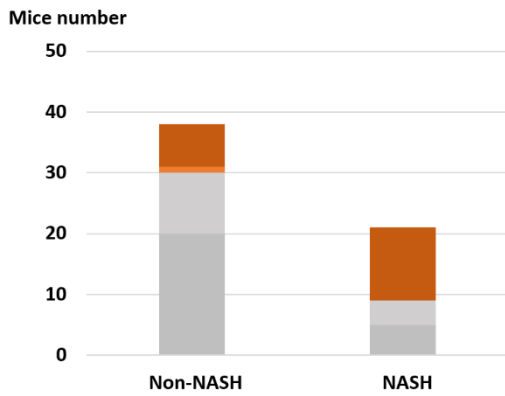
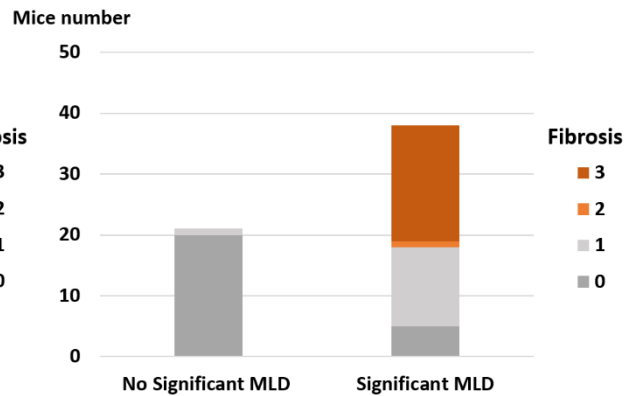


Figure 4.2. 4: Ballooning grades according to NASH, significant MLD, NASH-related fibrosis and fibro-NASH. Ballooning is observed in all the mice with NASH, in 21/38 (55%) mice with significant MLD, in 12/20 (60%) mice with NASH-related fibrosis and in all the mice with fibro-NASH.

Fibrosis

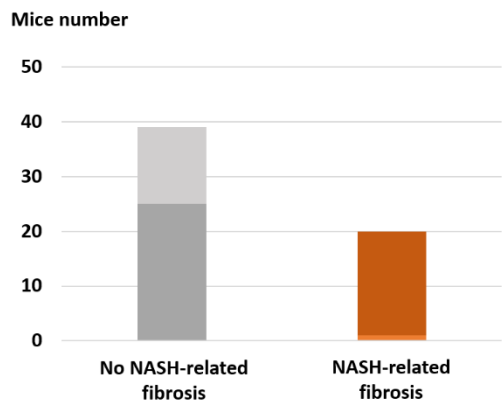


Fibrosis	Non-NASH	NASH
0	20 (53%)	5 (24%)
1	10 (26%)	4 (19%)
2	1 (3%)	0 (0%)
3	7 (18%)	12 (57%)

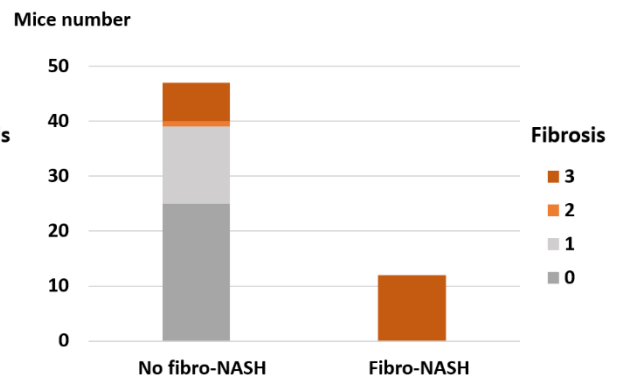


Fibrosis	No Significant MLD	Significant MLD
0	20 (95%)	5 (13%)
1	1 (5%)	13 (34%)
2	0 (0%)	1 (3%)
3	0 (0%)	19 (50%)

Fibrosis



Fibrosis	No NASH-related fibrosis	NASH-related fibrosis
0	25 (64%)	0 (0%)
1	14 (36%)	0 (0%)
2	0 (0%)	1 (5%)
3	0 (0%)	19 (95%)



Fibrosis	No fibro-NASH	Fibro-NASH
0	25 (53%)	0 (0%)
1	14 (30%)	0 (0%)
2	1 (2%)	0 (0%)
3	7 (15%)	12 (100%)

Figure 4.2. 5: Fibrosis stages according to NASH, significant MLD, NASH-related fibrosis and fibro-NASH. Fibrosis stage ≥ 2 is observed in 12/21 (57%) mice with NASH, in 20/38 (53%) mice with significant MLD, in all the mice with NASH-related fibrosis and fibro-NASH.

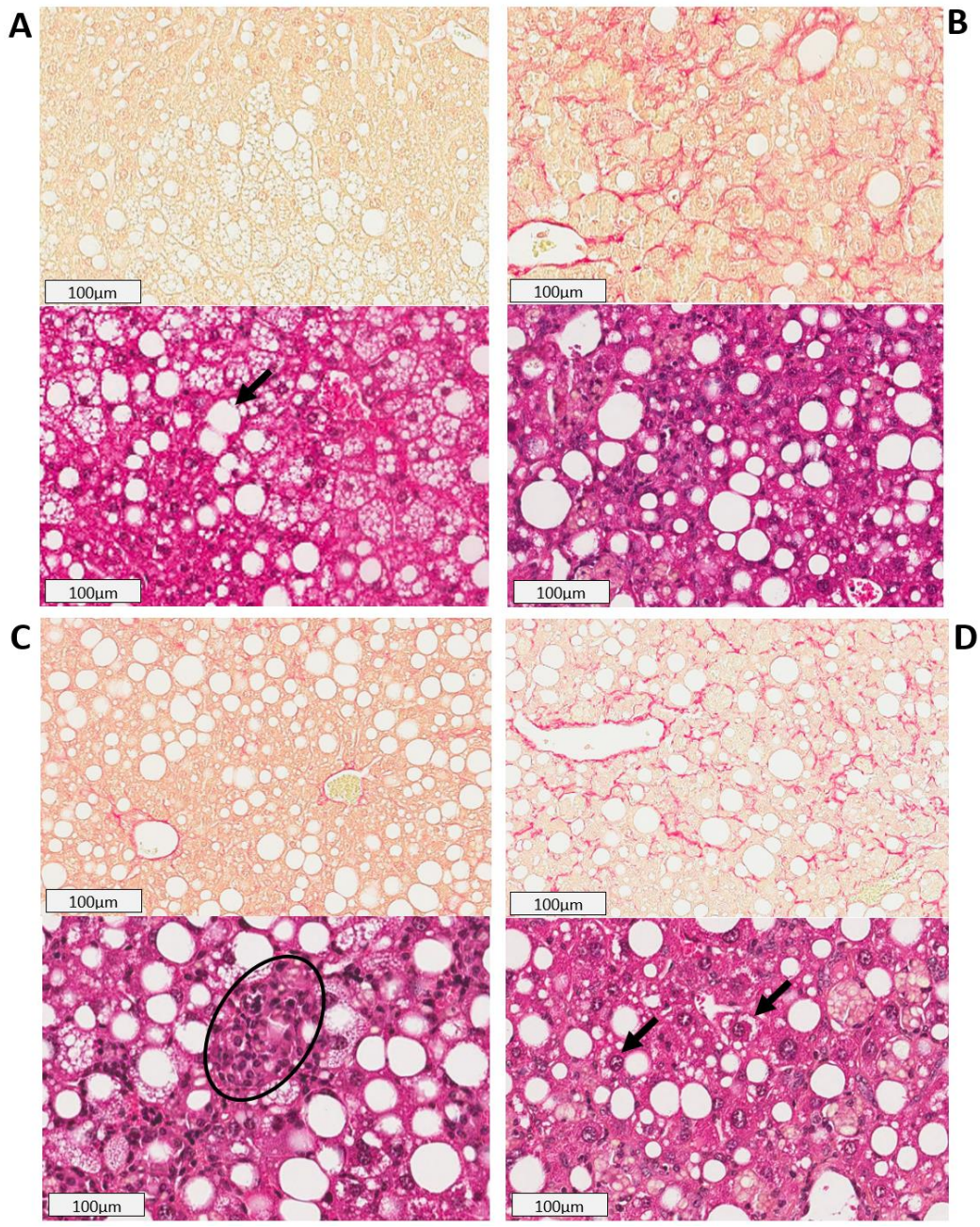


Figure 4.2. 6: Histological sections (upper row: picrosirius red stained slices; second row: hematoxylin-eosin stained slices) with x20 image magnification. (A) Mouse with NAFL (simple steatosis): fibrosis stage 0, steatosis grade 3 (arrow), and lobular inflammation and hepatocellular ballooning grade 0. (B) Mouse classified as both significant MLD and NASH-related fibrosis: fibrosis stage 3, inflammation and steatosis grade 3, and hepatocyte ballooning grade 0. (C) Mouse with NASH: fibrosis stage 0, steatosis and inflammation (circle) grade 3 and ballooning grade 1. (D) Mouse with fibro-NASH: fibrosis stage 3, steatosis and inflammation grade 3 and ballooning grade 2 (arrows).

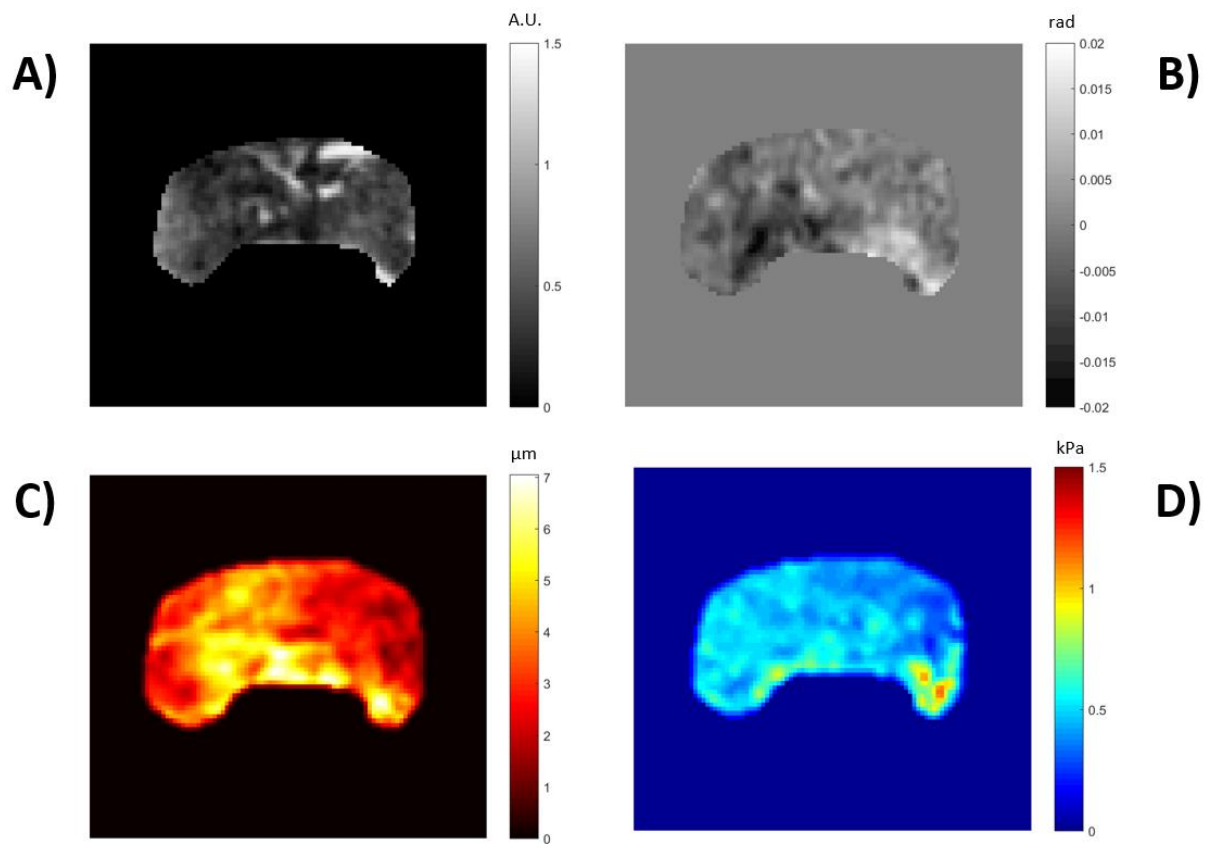


Figure 4.2. 7: Representative MRE images. A) magnitude image (A.U), B) phase image (rad), C) wave amplitude map and D) the mechanical property shear stiffness map (kPa).

The results of the evaluation of the relationship between the mechanical parameters and the histological features without and with data filtering using Spearman's rank correlations and multiple regression (stepwise) are shown in Table 4.2.2 and 4.2.3 respectively. Without filtering, the mechanical parameters were mainly determined by fibrosis with the highest effect of fibrosis on the loss modulus ($r = 0.54$, $p < 0.0001$) (Table 4.2.2). Similar results were observed with data filtering, although with the highest effect of fibrosis on the shear stiffness ($r = 0.41$, $p = 0.001$). Steatosis and inflammation were both moderately correlated with loss and storage moduli and with shear stiffness in both cases (i.e. without and with data filtering). Hepatocyte ballooning was not correlated with any of the mechanical parameters neither without nor with data filtering.

For fibrosis and inflammation, results both in terms of correlation coefficient and p-values were systematically better without filtering than with filtering.

These results agreed with those obtained with the multivariate analysis. Indeed, among the four studied histological features, the mechanical parameters were mostly affected by fibrosis with a better significance level p without data filtering (Table 4.2.3).

The mechanical parameters without data filtering had similar moderate accuracy for diagnosing NASH with AUC = 0.67 (with a significance level $p = 0.02$ and a confidence interval 95% CI = 0.53 – 0.79), AUC = 0.66 ($p = 0.03$, 95% CI = 0.52 – 0.78) and AUC = 0.68 ($p = 0.01$, 95% CI = 0.54 – 0.79) for loss modulus, storage modulus and shear stiffness, respectively. With data filtering, the three viscoelastic parameters had poor and statistically insignificant diagnostic accuracy for detecting NASH with AUC = 0.57 (with a significance level $p = 0.37$ and a confidence interval 95% CI = 0.44 – 0.70), AUC = 0.62 (with $p = 0.13$ and 95% CI = 0.48 – 0.74) and AUC = 0.53 (with $p = 0.71$ and 95% CI = 0.39 – 0.66) respectively.

Based on these results, for the rest of this study only the data without filtering were used.

Table 4.2. 2: Results of the analysis of the relationship between the mechanical parameters measured at 400Hz and the histological features of NAFLD with Spearman's Rank correlations. In gray, statistically non-significant values.

Spearman's rank correlations		Steatosis		Inflammation		Ballooning		Fibrosis	
		r	p	r	p	r	p	r	p
Without filtering	G' (kPa)	0.26	0.05	0.32	0.02	0.21	0.11	0.43	0.0007
	G'' (kPa)	0.28	0.03	0.35	0.01	0.21	0.11	0.54	<0.0001
	G* (kPa)	0.30	0.02	0.27	0.04	0.23	0.08	0.48	0.0001
With filtering	G' (kPa)	0.30	0.02	0.29	0.03	0.13	0.35	0.32	0.02
	G'' (kPa)	0.31	0.02	0.27	0.04	0.16	0.23	0.35	0.008
	G* (kPa)	0.28	0.03	0.26	0.05	-0.02	0.86	0.41	0.001

G', storage modulus (kPa); G'', loss modulus (kPa); |G*|, shear stiffness (kPa); r, the correlation coefficient and p the significance level.

Table 4.2. 3: Results of multivariate analysis using stepwise multiple regression the mechanical parameters as dependent variables and the histological features of NAFLD as independent variables.

Multiple regression (stepwise)		Steatosis		Inflammation		Ballooning		Fibrosis	
		r _{partial}	p	r _{partial}	p	r _{partial}	p	r _{partial}	p
Without filtering	G' (kPa)	NA	NA	NA	NA	NA	NA	0.36	0.005
	G'' (kPa)	NA	NA	NA	NA	NA	NA	0.53	<0.0001
	G* (kPa)	NA	NA	NA	NA	NA	NA	0.43	0.0006
With filtering	G' (kPa)	0.30	0.03	NA	NA	NA	NA	NA	NA
	G'' (kPa)	NA	NA	NA	NA	NA	NA	0.33	0.01
	G* (kPa)	NA	NA	NA	NA	NA	NA	0.28	0.03

G', storage modulus (kPa); G'', loss modulus (kPa); |G*|, shear stiffness (kPa); r_{partial}, the correlation coefficient; p, the significance level and NA, not assessed.

Relationship between mechanical parameters

Univariate analysis of the relationship between the mechanical parameters showed high correlation between the shear stiffness and storage and loss moduli ($r = 0.98$, $p < 0.0001$ et $r = 0.96$, $p < 0.0001$ respectively). The correlation was also elevated between loss and storage moduli ($r = 0.89$, $p < 0.0001$) and moderate between loss modulus and the shear stiffness phase angle ($r = 0.72$, $p < 0.0001$). The multifrequency dispersion coefficient showed negative moderate correlation with the storage and loss moduli ($r = -0.53$, $p < 0.0001$ and $r = -0.58$, $p < 0.0001$ respectively) and with shear stiffness and phase angle ($r = -0.57$, $p < 0.0001$ and $r = -0.57$, $p < 0.0001$ respectively). The damping ratio ζ was moderately correlated with the phase angle and weakly with the loss modulus ($r = 0.58$, $p < 0.0001$ and $r = 0.39$, $p = 0.002$ respectively) (Table 4.2.4).

Table 4.2. 4: Univariate analysis of the relationship between the mechanical parameters using Spearman's rank correlations. Correlation is considered high when $r \geq 0.9$. In gray, statistically non-significant values.

Rank correlations (Spearman's)	G''		$ G^* $		ζ		α		γ_{G^*}	
	r	p	r	p	r	p	r	p	r	p
G'	0.89	<0.0001	0.98	<0.0001	0.02	0.89	0.46	0.0002	-0.53	<0.0001
G''			0.96	<0.0001	0.39	0.002	0.72	<0.0001	-0.58	<0.0001
$ G^* $					0.16	0.22	0.57	<0.0001	-0.57	<0.0001
ζ							0.58	<0.0001	-0.21	0.11
α									-0.57	<0.0001

G' , storage modulus (kPa); G'' , loss modulus (kPa); $|G^*|$, shear stiffness (kPa); ζ , damping ratio (adim.); α , shear stiffness phase angle (rad) γ_{G^*} , the multifrequency dispersion coefficient (adim.). r, the correlation coefficient and p the significance level

Mechanical parameters versus histological characteristics

Fibrosis had mild correlation with all the mechanical parameters except with the loss modulus where the correlation was moderate ($r = 0.54$, $p < 0.0001$) (Table 4.2.5). Inflammation had mild correlation with loss and storage moduli ($r = 0.35$, $p = 0.008$; $r = 0.32$, $p = 0.02$ respectively) and with shear stiffness and multifrequency dispersion coefficient ($r = 0.27$, $p = 0.04$; $r = -0.30$, $p = 0.02$ respectively). Steatosis also had mild correlation with shear stiffness and loss and storage moduli ($r = 0.30$, $p = 0.02$; $r = 0.28$, $p = 0.03$ and $r = 0.26$, $p = 0.05$ respectively). Hepatocyte ballooning was not correlated with any of the mechanical parameters. With multivariate analysis, fibrosis was the only one affecting the mechanical parameters (Table 4.2.6).

Table 4.2. 5: Univariate analysis of the relationship between the mechanical parameters and the histological features of NAFLD using Spearman's rank correlations. In gray, statistically non-significant values.

Rank correlations (Spearman's)	Steatosis		Inflammation		Ballooning		Fibrosis	
	r	p	r	p	r	p	r	p
G'	0.26	0.05	0.32	0.02	0.21	0.11	0.43	0.0007
G''	0.28	0.03	0.35	0.01	0.21	0.11	0.54	<0.0001
$ G^* $	0.30	0.02	0.27	0.04	0.23	0.08	0.48	0.0001
ζ	0.17	0.20	0.16	0.24	-0.01	0.95	0.41	0.0011
α	-0.01	0.95	0.10	0.46	-0.15	0.27	0.40	0.0016
γ_{G^*}	-0.23	0.08	-0.30	0.02	-0.23	0.08	-0.48	0.0001

G' , storage modulus (kPa); G'' , loss modulus (kPa); $|G^*|$, shear stiffness (kPa); ζ , damping ratio (adim.); α , shear stiffness phase angle (rad); γ_{G^*} the multifrequency dispersion coefficient (adim.); r, the correlation coefficient and p the significance level.

Table 4.2. 6: Multivariate analysis using stepwise multiple regression with the mechanical parameters as the dependent variables and the histological features of NAFLD as the independent variables.

Multiple regression (Stepwise)	Steatosis		Inflammation		Ballooning		Fibrosis	
	r_{partial}	p	r_{partial}	p	r_{partial}	p	r_{partial}	p
G'	NA	NA	NA	NA	NA	NA	0.36	0.005
G''	NA	NA	NA	NA	NA	NA	0.53	<0.0001
$ G^* $	NA	NA	NA	NA	NA	NA	0.43	0.0006
ζ	NA	NA	NA	NA	NA	NA	0.41	0.001
α	NA	NA	NA	NA	NA	NA	0.27	0.03
γ_{G^*}	NA	NA	NA	NA	NA	NA	-0.46	0.0003

G' , storage modulus (kPa); G'' , loss modulus (kPa); $|G^*|$, shear stiffness (kPa); ζ , damping ratio (adim.); α , shear stiffness phase angle (rad); γ_{G^*} , the multifrequency dispersion coefficient (adim.); r_{partial} the correlation coefficient; p the significance level and NA: not assessed.

MRE variables as diagnostic markers in NASH, significant MLD, NASH-related fibrosis and fibro-NASH

The mechanical parameters graphs according to histological classification non-NASH versus NASH, no significant MLD versus significant MLD, no NASH-related fibrosis versus NASH-related fibrosis and “no fibro-NASH versus fibro-NASH are shown in figures 4.2.8, 4.2.9, 4.2.10 and 4.2.11, with the corresponding Mann-Whitney statistical results summarized in Table 4.2.7. The highest differences between non-NASH and NASH were similarly displayed with the storage modulus ($p = 0.03$), the shear stiffness ($p = 0.03$) and the multifrequency dispersion coefficient ($p = 0.03$). For no significant MLD versus significant MLD, the highest differences were shown with the loss modulus ($p = 0.001$). For no NASH-related fibrosis versus NASH-related fibrosis, the highest differences were also exhibited with the loss modulus ($p = 0.0001$). The highest differences between no fibro-NASH and fibro-NASH were similarly shown with loss modulus ($p = 0.01$) and shear stiffness ($p = 0.01$). The results of damping ratio and phase angle were only statistically significant when studying no NASH-related fibrosis versus NASH-related fibrosis ($p = 0.002$ and $p = 0.0009$ respectively).

Table 4.2. 7: Differences of MRE parameters between groups without/with NASH, significant MLD, NASH-related fibrosis and fibro-NASH.

Non-NASH (n = 38) vs. NASH (n = 21)		
Mechanical parameters	Median [CI95%]	Significance level p
G' (kPa)	0.49 [0.40 - 0.56] vs. 0.59 [0.55 - 0.66]	0.03
G'' (kPa)	0.31 [0.25 - 0.37] vs. 0.40 [0.33 - 0.50]	0.05
G* (kPa)	0.57 [0.51 - 0.70] vs. 0.73 [0.65 - 0.82]	0.03
ζ (adim.)	0.33 [0.31 - 0.36] vs. 0.34 [0.30 - 0.36]	0.94
α (rad)	0.56 [0.53 - 0.60] vs. 0.60 [0.55 - 0.63]	0.20
γ _{G*} (adim.)	3.26 [2.98 - 3.53] vs. 3.06 [2.95 - 3.20]	0.03
No significant MLD (n = 21) vs. Significant MLD (n = 38)		
Mechanical parameters	Median [CI95%]	Significance level p
G' (kPa)	0.43 [0.40 - 0.51] vs. 0.58 [0.53 - 0.64]	0.009
G'' (kPa)	0.26 [0.23 - 0.31] vs. 0.39 [0.34 - 0.47]	0.001
G* (kPa)	0.54 [0.48 - 0.59] vs. 0.73 [0.65 - 0.82]	0.003
ζ (adim.)	0.31 [0.29 - 0.34] vs. 0.34 [0.32 - 0.37]	0.06
α (rad)	0.54 [0.51 - 0.59] vs. 0.59 [0.55 - 0.63]	0.06
γ _{G*} (adim.)	3.40 [3.22 - 3.58] vs. 2.90 [2.72 - 3.17]	0.003
No NASH-related fibrosis (n = 39) vs. NASH-related fibrosis (n = 20)		
Mechanical parameters	Median [CI95%]	Significance level p
G' (kPa)	0.48 [0.42 - 0.56] vs. 0.63 [0.57 - 0.70]	0.004
G'' (kPa)	0.29 [0.25 - 0.34] vs. 0.46 [0.35 - 0.54]	0.0001
G* (kPa)	0.57 [0.51 - 0.66] vs. 0.82 [0.69 - 0.92]	0.001
ζ (adim.)	0.31 [0.30 - 0.33] vs. 0.37 [0.33 - 0.41]	0.002
α (rad)	0.54 [0.52 - 0.59] vs. 0.63 [0.59 - 0.67]	0.0009
γ _{G*} (adim.)	3.33 [3.17 - 3.54] vs. 2.77 [2.39 - 3.14]	0.002
No fibro-NASH (n = 47) vs. Fibro NASH (n = 12)		
Mechanical parameters	Median [CI95%]	Significance level p
G' (kPa)	0.50 [0.44 - 0.56] vs. 0.63 [0.57 - 0.78]	0.02
G'' (kPa)	0.31 [0.27 - 0.36] vs. 0.50 [0.35 - 0.56]	0.01
G* (kPa)	0.58 [0.54 - 0.68] vs. 0.82 [0.69 - 0.99]	0.01
ζ (adim.)	0.33 [0.31 - 0.35] vs. 0.35 [0.31 - 0.41]	0.16
α (rad)	0.55 [0.53 - 0.60] vs. 0.63 [0.57 - 0.67]	0.06
γ _{G*} (adim.)	3.25 [3.03 - 3.48] vs. 2.72 [2.38 - 3.14]	0.02

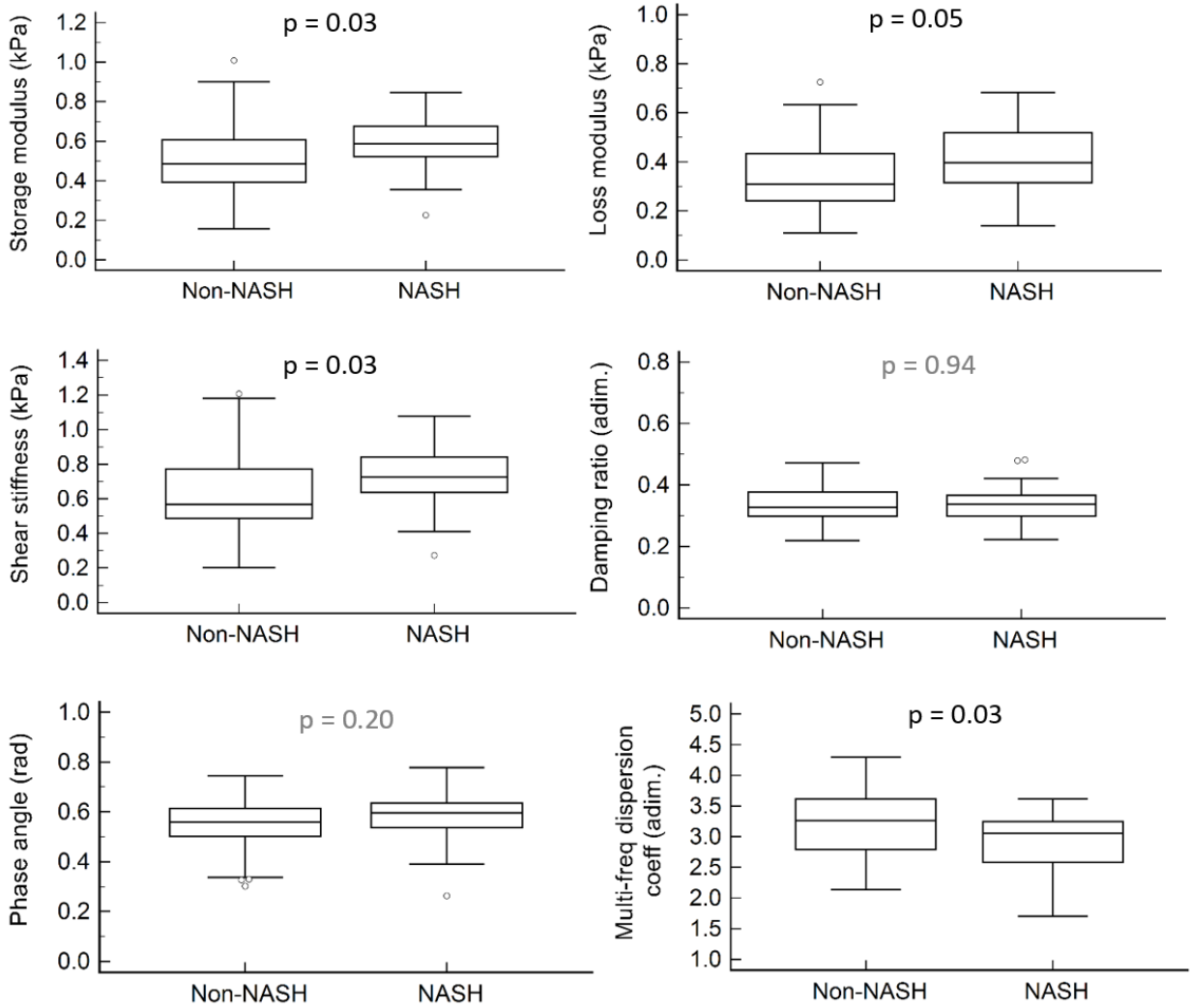


Figure 4.2. 8: Boxplots of the mechanical parameters in non-NASH versus NASH. The highest differences between groups are observed for the storage modulus, the shear stiffness and the multifrequency dispersion coefficient.

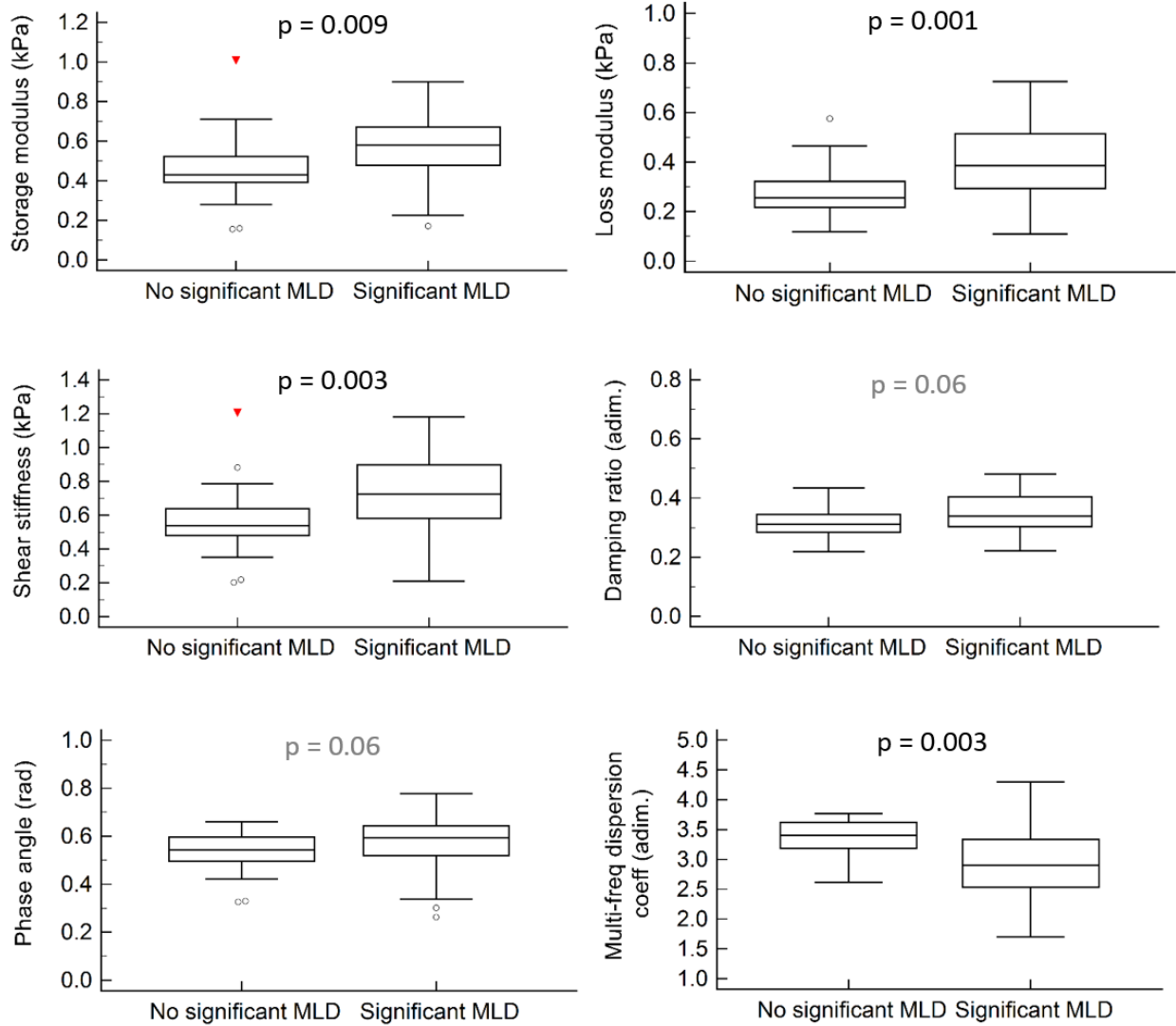


Figure 4.2. 9: Boxplots of the mechanical parameters in “no significant MLD versus significant MLD” classification. The highest differences between groups are seen for the loss modulus.

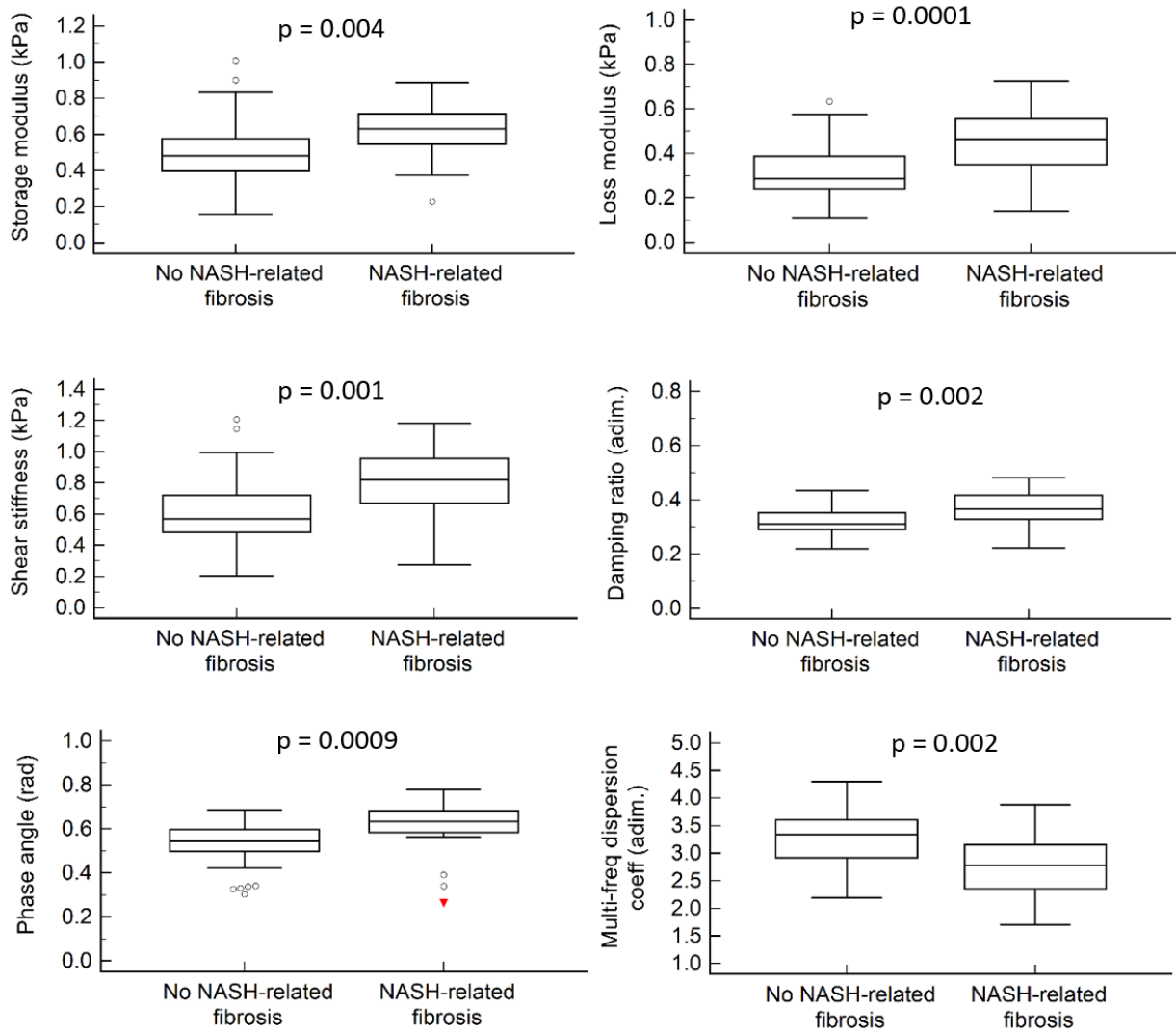


Figure 4.2. 10: Boxplots of the mechanical parameters in no NASH-related fibrosis versus NASH-related fibrosis. The highest differences between groups are observed with the loss modulus.

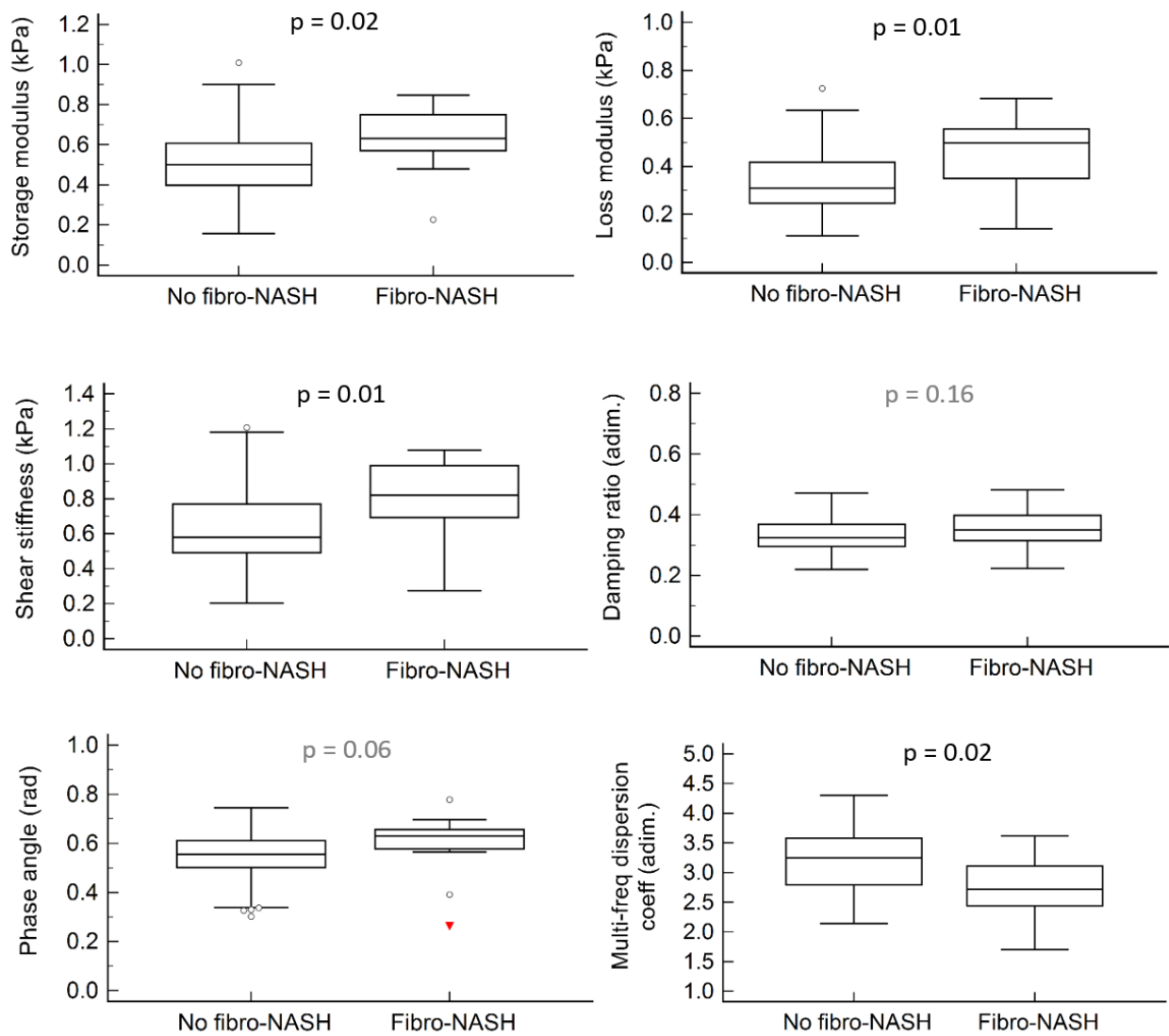


Figure 4.2. 11: Boxplots of the mechanical parameters in no fibro-NASH versus fibro-NASH. The highest differences between groups are seen for the loss modulus and the shear stiffness.

Diagnostic performance of MRE parameters

The diagnostic performance of loss and storage moduli, shear stiffness and multifrequency dispersion coefficient were all moderate for diagnosing NASH with AUC = 0.67 (with a significance level $p = 0.02$ and a confidence interval 95% CI = 0.53 – 0.79), AUC = 0.66 ($p = 0.03$, 95% CI = 0.52 – 0.78) and AUC = 0.68 ($p = 0.01$, 95% CI = 0.54 – 0.79) and AUC = 0.67 ($p = 0.01$, 95% CI = 0.54 – 0.79) respectively (Table 4.2.8).

The accuracy for diagnosing significant MLD was higher compared to NASH (AUC = 0.71 with $p = 0.004$ and 95% CI = 0.58 – 0.82 for storage modulus, AUC = 0.76 with $p = 0.0001$ and 95% CI = 0.63 – 0.86 for loss modulus, AUC = 0.74 with $p = 0.001$ and 95% CI = 0.61 – 0.84 for shear stiffness and AUC = 0.73 with $p = 0.0004$ and 95% CI = 0.60 – 0.84 for multifrequency dispersion coefficient) but similar to fibro-NASH (AUC = 0.72 with $p = 0.008$ and 95% CI = 0.59 – 0.83 for storage modulus, AUC = 0.74 with $p = 0.006$ and 95% CI = 0.61 – 0.85 for loss modulus, AUC = 0.74 with $p = 0.004$ and 95% CI = 0.61 – 0.85 for shear stiffness and AUC = 0.73 with $p = 0.006$ and 95% CI = 0.60 – 0.84 for multifrequency dispersion coefficient).

The highest AUC values were obtained when diagnosing NASH-related fibrosis (AUC = 0.73 with $p = 0.002$ and 95% CI = 0.60 – 0.84 for loss modulus, AUC = 0.81, $p < 0.0001$ and 95% CI = 0.68 – 0.90 for storage modulus, AUC = 0.76, $p = 0.0001$ and 95% CI = 0.63 – 0.86 for shear stiffness and AUC = 0.75, $p = 0.0004$ and 95% CI = 0.62 – 0.85 for multifrequency dispersion coefficient).

Both damping ratio and phase angle had non-significant diagnostic performance when determining NASH and fibro-NASH (AUC = 0.51 and 0.60, $p > 0.05$ for NASH and AUC = 0.63 and 0.68 $p > 0.05$ for fibro-NASH) and significant when diagnosing significant MLD and NASH-related fibrosis (AUC = 0.65 and 0.65, $p = 0.04$ for MLD; AUC = 0.75, $p = 0.0002$ and AUC = 0.77, $p = 0.0005$ for NASH-related fibrosis) (Table 4.2.8).

Table 4.2. 8: Results of ROC curve analysis of mechanical parameters (mono-frequency parameters at 400Hz and multi-frequency dispersion coefficient) for diagnosing NASH, significant MLD, NASH-related fibrosis and fibro-NASH. In gray, parameters with statistically non-significant p-values.

ROC Curve Analysis	Imaging parameters	AUC	P-value	CI95%	Associated criterion
Non-NASH (n = 38) vs. NASH (n = 21)	G'	0.67	0.02	0.53 to 0.79	> 0.52
	G''	0.66	0.03	0.52 to 0.78	> 0.27
	$ G^* $	0.68	0.01	0.54 to 0.79	> 0.57
	ζ	0.51	0.85	0.38 to 0.65	≤ 0.38
	α	0.60	0.20	0.47 to 0.73	≥ 0.59
	γ_{G^*}	0.67	0.01	0.54 to 0.79	≤ 3.18
No significant MLD (n = 21) vs. Significant MLD (n = 38)	G'	0.71	0.004	0.58 to 0.82	> 0.51
	G''	0.76	0.0001	0.63 to 0.86	> 0.34
	$ G^* $	0.74	0.001	0.61 to 0.84	>0.57
	ζ	0.65	0.04	0.52 to 0.77	> 0.33
	α	0.65	0.04	0.51 to 0.77	> 0.61
	γ_{G^*}	0.73	0.0004	0.60 to 0.84	≤ 3.18
Non NASH-related fibrosis (n = 39) vs. NASH-related fibrosis (n = 20)	G'	0.73	0.002	0.60 to 0.84	> 0.56
	G''	0.81	<0.0001	0.68 to 0.90	> 0.34
	$ G^* $	0.76	0.0001	0.63 to 0.86	> 0.69
	ζ	0.75	0.0002	0.62 to 0.86	> 0.33
	α	0.77	0.0005	0.64 to 0.87	> 0.61
	γ_{G^*}	0.75	0.0004	0.62 to 0.85	≤ 3.16
No fibro-NASH (n = 47) vs. Fibro-NASH (n = 12)	G'	0.72	0.008	0.59 to 0.83	> 0.56
	G''	0.74	0.006	0.61 to 0.85	> 0.35
	$ G^* $	0.74	0.004	0.61 to 0.85	>0.69
	ζ	0.63	0.16	0.50 to 0.75	> 0.34
	α	0.68	0.07	0.54 to 0.79	> 0.62
	γ_{G^*}	0.73	0.006	0.60 to 0.84	≤ 3.16

G' , storage modulus (kPa); G'' , loss modulus (kPa); $|G^*|$, shear stiffness (kPa); ζ , damping ratio (adim.); α , shear stiffness phase angle (rad) and γ_{G^*} , multi-frequency dispersion coefficient (adim.),

4.2.5. Discussion

In this preclinical mouse study, we performed MRE to evaluate the performance of the mechanical parameters as potential biomarkers of NAFLD progressive forms, namely NASH, significant MLD, NASH-related fibrosis and fibro-NASH. We also assessed the associations between the MRE parameters and the histological features of the disease (steatosis, inflammation, hepatocyte ballooning and fibrosis).

Understanding the pathophysiology of NAFLD and its advanced forms is still challenging and requires establishing preclinical models that can mimic all the pathogenic determinants of human NAFLD. So far, no current model can fully replicate all the characteristics of the disease. Here, using two mouse models of NAFLD allowed for generating the different variations of the disease along different progression paths, and resulted in sizeable groups of NAFL, NASH-related fibrosis, NASH without significant fibrosis and fibro-NASH. The results of the histological analysis performed on the right medial lobe of the liver showed that fibrosis, inflammation and steatosis were correlated which is expected as these histopathological features of NAFLD coexist and interactively affect each other during disease progression.

In this work, we only considered data at 400 Hz for monofrequency analysis as wave amplitude and SNR values were best at this frequency. MRE parameters were obtained with ROIs positioned on slices that were chosen with the aim of matching the histological slices and staying the closest possible to the piston generation the mechanical waves. However, the MRE chosen slice did not necessarily match the histological slice for all the mice of the study. Potentially, this did not affect our results since NAFLD is considered to be a diffuse disease.

Data filtering results showed that the mechanical parameters were mostly affected by fibrosis without or with the filtering process. However, the results were more statistically significant without than with data filtering. Our MRE data were pre-filtered during data processing. Indeed, the ROIs were placed on the wave amplitude maps within the liver where the amplitude of the wave was at least 10 μm for the 400 Hz images (at least 10 μm for the 200 Hz images as well and at least 3 μm for the 600 Hz images). That is probably why our post processing data filtering did not improve the mechanical parameter performance but rather, it worsens it. This might be explained by artifacts in some data arising from areas with weak

wave amplitude or SNR, or by spatial heterogeneity related to acquisition factors, including surface coil sensitivity profile and wave penetration pattern.

Studying the relationship between MRE parameters and histological features revealed that all the assessed mechanical parameters were primarily correlated with fibrosis. However, fibrosis was best associated with the viscosity related parameter loss modulus. High correlation between fibrosis and loss modulus has been reported in another murine study [158]. In some other studies, it has been reported that the association between fibrosis and storage modulus was stronger than between fibrosis and loss modulus has been shown in previous studies [160, 235]. The reasons explaining these various results are unclear. But probably the speed of fibrogenesis and the presence of associated edematous inflammation may play a role.

The results of our study showed that the shear stiffness phase angle and damping ratio had similar performance in detecting NAFLD histological features and in diagnosing the progressive forms of the disease. This is to be expected, because damping ratio ($G''/2G'$) is a rescaled version of the phase angle ($\alpha = \arctan(2\zeta)$). However, these two parameters were only moderately correlated which could be explained by the fact that the phase angle was obtained for each mouse with the data processing software where its value was measured for each pixel of the region of interest, while the damping ratio was calculated later, with the mean values of storage and loss modulus for each mouse. This difference in measuring the values of these parameters may have affected the accuracy of the measurements particularly for the damping ratio.

The multifrequency dispersion coefficient, related to a power law model that measures the changes of the shear modulus with frequency [190, 368], decreased with increasing fibrosis, and with a lesser degree, with inflammation. This decrease might be explained by the changes in tissue architecture related to edematous inflammation and fibrogenesis [187, 188, 190]. These results are in good agreement with observations of decreased dispersion coefficients in patients with inflammation and fibrosis caused by viral hepatitis [367]. In this previous patient study, however, inflammation seemed to have the strongest effect on the dispersion coefficient, whereas in our current study fibrosis but not inflammation had an influence on the dispersion coefficient. This difference may be explained by several factors, including the

range of assessed frequencies, the more severe histological lesions in viral hepatitis than in NAFLD, and the species differences. In the current study, frequencies ranging from 200 Hz to 600 Hz were used while in the clinical study the frequencies used ranged from 28 Hz to 84 Hz. This difference in the range of assessed frequencies is due to hardware limitations in clinical practice.

Moreover, our results showed that none of the mechanical parameters was correlated with hepatocyte ballooning suggesting that this histological characteristic of NASH does not affect the mechanical parameters. These results agree with those of Qu et al. in patients with early NASH [365]. However, correlations between liver stiffness, loss modulus or damping ratio and ballooning have been reported in some preclinical and clinical NAFLD studies [125, 171, 364, 369]. The reasons explaining the reported differences regarding the association or lack of association between the visco-elastic parameters and ballooning remain to be explored, but the high inter- and intra-observer variation in ballooning assessment even by expert hepatopathologists may be one reason explaining the heterogeneous results [53].

Our results showed that the hepatic mechanical parameters had better performance for diagnosing significant MLD, fibro NASH and even more NASH-related fibrosis, than for diagnosing NASH. This can be explained by the fact that significant MLD, fibro NASH and NASH-related fibrosis include mice with significant to severe fibrosis that alters the mechanical parameters at MRE. Moreover, damping ratio and phase angle were unable to help diagnosing NASH and fibro NASH (AUCs not significantly different from 0.5), but performed well for diagnosing significant MLD and NASH-related fibrosis. These results suggest that increased viscoelastic ratio may help diagnosing progressive NAFLD that includes fibro-NAFL, borderline NASH cases.

Similarly to what was reported in previous studies of our team [160, 222], mechanical parameters were mainly determined by fibrosis which may limit their value as biomarkers of NASH and indicate a larger potential for the diagnosis of the progressive forms of NAFLD that are associated with significant stages of fibrosis.

In this study, we have encountered several limitations. First, the limitation of the “gold-standard” histologic analysis as diagnosing hepatocellular ballooning is challenging [53].

Moreover, only semi-quantitative histological scores were available. However, the mechanical properties which depend on quantitative tissue features, are obtained on a continuous scale. Hence, the limited correlation coefficient may also be a consequence of grouping a range of quantitative tissue features having direct influence on the mechanical properties, into a few discrete histological classes.

Second, our study is related to the use of a mouse model of NAFLD with the known difficulty to reproduce all features of human NAFLD [346]. Particularly, the rapid development of fibrosis in the mouse NAFLD model that we used may differ from the course of chronic fibrogenesis in humans. We hypothesize that rapid inflammatory fibrogenesis in mice might preferentially influence the viscosity-related loss modulus parameter, explaining the high loss modulus observed here in the disease classification with significant fibrosis (significant MLD, NASH-related fibrosis and fibro-NASH). The value of the viscoelastic parameters for assessing NASH severity should thus be further studied in humans.

Third, for the multifrequency analysis, we used only three mechanical frequencies. A higher number of frequencies could allow for more precise measurements of the multifrequency dispersion coefficient.

Fourth, accurate matching between MRE images and histological slices can be hard to perform, limiting the comparison between MRE and histological features.

Fifth, the MRE data were not acquired with respiratory gating. Respiration related artifacts during MRE could lead to imprecise measurements of the viscoelastic parameters. This may also have played a role in the unexpected behavior of the SNR-based filtering step that we implemented. Indeed, motion artifacts may present as spurious high intensity signals smeared over the phase encoding direction. Particularly, subcutaneous fat signal may have been propagated throughout the hepatic ROIs, impairing the performance of the SNR-based filtering. No fat suppression was applied in this study because the presence of elevated fat levels in many mice would have translated into poor signal had fat suppression been implemented.

In conclusion, the results of our preclinical in vivo MRE study suggest that in mice with NAFLD, the diagnostic performance of MRE derived mechanical parameters was higher in NASH-

related fibrosis, significant MLD and fibro-NASH than in NASH, pointing to fibrosis as main driver of the MRE parameter changes in progressive NAFLD. Increased loss modulus and viscoelastic ratio were markers of NASH-related fibrosis. Hepatocyte ballooning did not significantly alter the MRE mechanical parameters, which weakened the viscoelastic parameter performance in diagnosing NASH.

4.3. Methodology

4.3.1. PDFF mapping

This study was performed to study the reproducibility and diagnostic accuracy of our PDFF sequence for liver steatosis imaging in the previous mice study.

4.3.1.1. Data acquisition

MRI-PDFF data acquisitions were performed with a multi-slice spoiled multi-gradient echo sequence with a radiofrequency volume transmit/receive coil and the ParaVision software (PV6, Bruker, Germany). Three echo trains (16 echoes per train) were used with initial echo times (TE_0) of 1.5, 2 and 2.5 ms and a separation time $\Delta TE = 0.75$ ms with no flipback. Data were acquired with respiratory gating. Acquisition parameters are detailed in Table 4.3.1.

4.3.1.2. Data processing

MRI-PDFF values were estimated with a MatLab in-house algorithm based on magnitude values [370] as:

$$S(TE) = abs \left(e^{-\frac{TE}{T_2^*}} \left[S_0^{wat} + S_0^{fat} \sum_{i=1}^N w_i e^{i \cdot 2\pi \cdot TE \cdot \Delta f_i} \right] \right) + \varepsilon(SNR) \quad (18)$$

Fitted values of PDFF, T_2^* and S_0^{wat} and S_0^{fat} were obtained with a model that considers SNR and a six-peak lipidic model (Δf , each peak having a relative signal weight of w). Images at increasing echo times and with matching readout gradient polarity were extracted and reordered from the three separate acquisitions with echo trains starting at offset TE_0 values. For this, ROIs covering the whole liver avoiding fat and vessels were used. PDFF values were obtained for each pixel of the ROI and a mean PDFF value was calculated for each mouse.

Data extraction (ROI positioning)

ROIs were positioned by two operators on the largest possible section of liver avoiding vessels and organ edges. Two separate sets of regions of interest were generated by each operator; the first one on slices chosen independently by each operator and the second one on slices

chosen independently by each operator but according to a common procedure defining the target slice as the second slice above the kidney dome. The choice of this slice location was an attempt to match the location of the MR analysis to the location of the histological analysis (performed on the right medial lobe of the mouse liver in this study).

Table 4.3. 1: PDFF data acquisitions parameters.

Parameters	PDFF mapping sequence
Repetition time (ms)	950 ms
Echo time (ms)	3 echo trains: TE ₀ =1.5, 2, 2.5 ms (ΔTE = 0.754ms, 16 echoes/train)
Bandwidth (kHz)	300 kHz
Flip angle	15°
flipback	No
Field of view (mm x mm)	45 x 35
Acquisition matrix	112 x 116
Number of slices	31
Slice thickness (mm)	1.5
Spatial resolution (mm x mm)	0.4 x 0.3
Acquisition time	3 m 40 s per echo train

4.3.1.3. Statistical analysis

Interoperator repeatability was obtained from Bland-Altman statistical testing (where differences are plotted in %) with coefficients of repeatability calculated as:

$$\text{Coefficient of repeatability} = \text{Standard deviation (\%)} \times 1.96 \quad (19)$$

where the standard deviation is the standard deviation of the percentage difference of both operators measurements (SD%). This coefficient of repeatability determines the threshold value below which the percentage difference between repeated measurements is expected to lie for 95% of pairs of repeated measurements [197].

Kruskal-Wallis and Mann–Whitney tests were used with PDFF as the studied variable and steatosis grade and NASH, respectively, as the reference values. Stepwise multivariate multiple regression analyses with a significance level $p < 0.05$ were carried out with PDFF values as the dependent variable and steatosis, inflammation, ballooning and fibrosis scores as independent parameters. Diagnostic performance of MRI-PDFF measurements for NASH was assessed with ROC curve analysis. All statistical analyses were performed with MedCalc software version 19.4.1 (MedCalc Software Ltd, Ostend, Belgium).

4.3.1.1. Results

The results of our study showed that our PDFF measurements had high interoperator repeatability coefficients of 54%. After standardization of the slice selection procedure, interoperator repeatability improved to a coefficient of repeatability of 32%. Representative images of the signal profile as function of the echo time and a PDFF parametric map are shown in figure 4.3.1.

Kruskal-Wallis statistical test results (figure 4.3.2) showed that PDFF is significantly different between steatosis grades with a significance level $p < 0.000001$ (median [IQR] in S0: 1.2 [0.8; 2.8]%, S1: 9.8 [8.1 ; 13.3]%, S2: 11.6 [7.3 ; 16.7]%, S3: 23.2 [19.2 ; 25.4]%). In multivariate analysis, PDFF was determined solely by steatosis with p -value = 0.0001 and $r_{\text{partial}} = 0.82$.

The results of diagnostic performance with ROC curve analysis showed that MRI-PDFF measurements had similar high accuracy for diagnosing both significant steatosis ($S \geq 2$) and advanced steatosis ($S \geq 3$) with AUC = 0.96 (with significance level $p < 0.0001$ and confidence interval 95% CI = 0.90 - 0.99) and AUC = 0.96 (with significance level $p < 0.0001$ and confidence interval 95% CI = 0.90 - 0.99) respectively.

PDFF displayed low performance in differentiating between NAFL and NASH with mean [IQR] values of 19% [15%; 23%] and 23% [20%; 24%], respectively (Mann-Whitney $p = 0.05$).

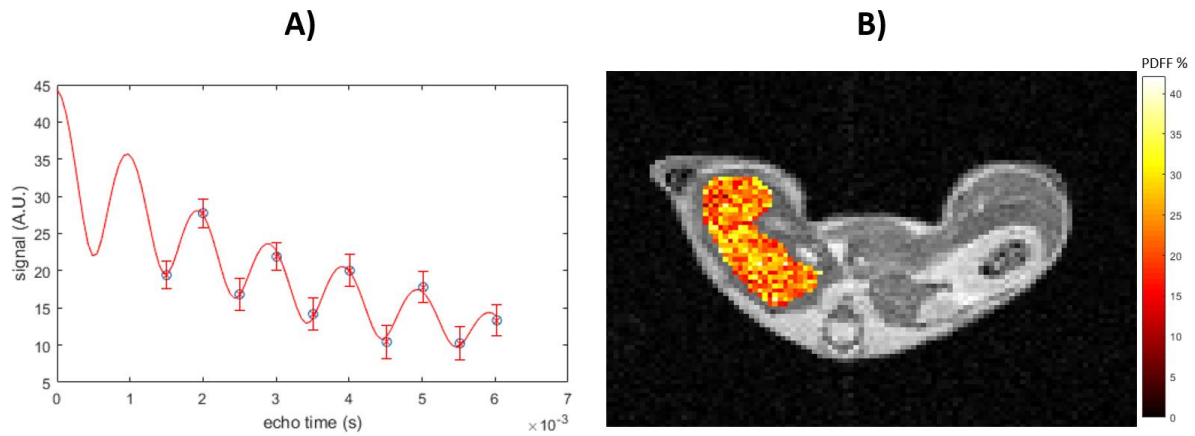


Figure 4.3. 1: Representative images of A) the signal profile as function of the echo time and B) PDFF parametric map of mouse with PDFF = 25.5% superpositioned on the magnitude image.

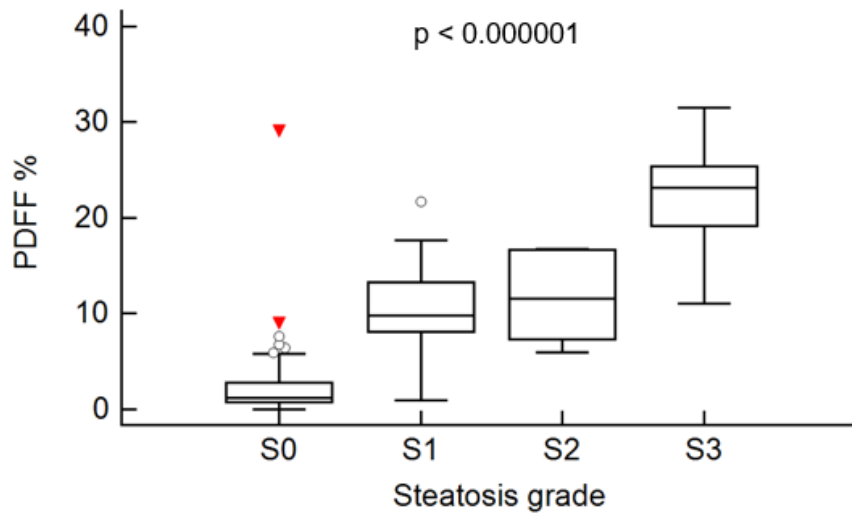


Figure 4.3. 2: Boxplots of PDFF measurements vs. steatosis grades. PDFF increases with steatosis grade. Kruskal-Wallis p value is indicated.

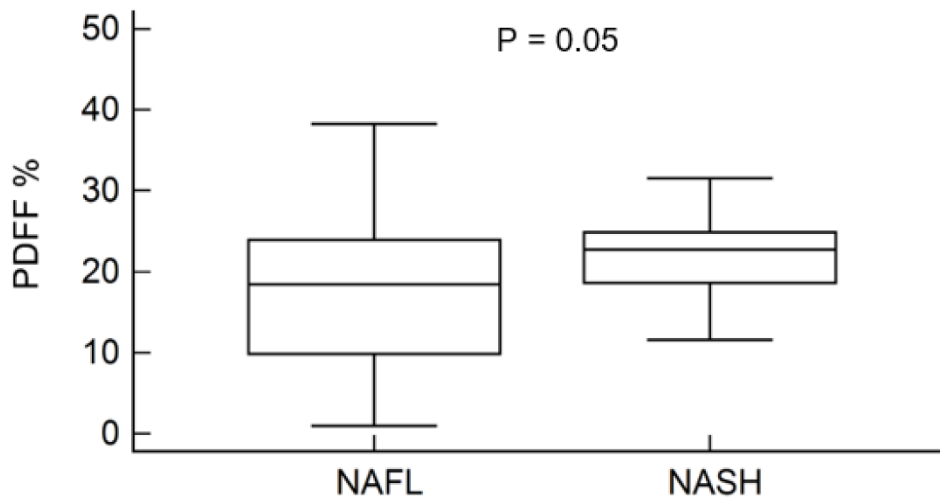


Figure 4.3. 3: Boxplots of PDFF measurements vs. NAFL/NASH classification according to NASH CRN scoring system. The Mann Whitney p value is indicated. PDFF was not significantly different between the NASH and NAFL groups.

4.3.1.2. Discussion

In this study we improved PDFF measurements reproducibility by adopting a standardizing step of slice selection prior to ROI positioning. The poor reproducibility may have been caused by heterogeneities in hepatic PDFF along the longitudinal axis, either because of true organ heterogeneity or because of artifactual modulations during acquisition or post-processing. Regardless, significant improvements in interoperator repeatability could be obtained merely by properly defining the ROI positioning procedure beforehand.

With respect to the diagnostic performance of PDFF for steatosis grades, our results agreed with preclinical and clinical literature results [94, 125, 128] confirming that standardized PDFF as calculated with our sequence and fitting procedure was an excellent biomarker of steatosis. Imajo N, et al. [125] reported higher accuracy of PDFF measurements (AUC = 0.90) in diagnosing significant steatosis (≥ 2) in patients with NAFLD and found PDFF to be better than transient elastography-based CAP measurements (AUC = 0.73).

PDFF displayed poor sensitivity to differentiate between NAFL and NASH. This can be explained by the advanced steatosis grades in both NAFL and NASH groups.

Even with our improved standardized procedure for ROIs selecting, accurately matching between imaging maps and histological slices can be challenging. Agreement on slice selection between pathologists and MRI operators before imaging and histology may help overcome this limitation.

To summarize, we confirmed that MRI-PDFF is an accurate and relatively precise biomarker for detecting and grading hepatic steatosis with histology as reference standard which makes it a good tool to accurately quantify hepatic steatosis in clinical research and NAFLD patient treatment.

4.3.2. T1 mapping

T1 relaxation time have been repeatedly associated with hepatic alterations caused by chronic liver diseases. Liver inflammation and fibrosis are believed to increase the T1 values because of the increase of extracellular water and proteins [240, 259, 267, 269-271]. Also, recent studies have reported significant rise in T1 relaxation time in chronically diseased livers as compared to healthy subjects in both animal models and human patients [124, 270, 272, 273]. NASH, the progressive form of NAFLD, is differentiated from NAFL, the early form of the disease, by both hepatic inflammation and hepatocyte ballooning. NASH, is also typically associated with liver fibrosis [11]. T1 mapping may be a useful method to diagnose NASH associated inflammation and fibrosis. However, fat has a confounding effect on T1 measurements that depends on the imaging sequence used to calculate T1. With conventional imaging methods, ie, spin echo inversion recovery, T1 decreases with high fat concentration, as shown by the short T1 of abdominal adipose tissue [371]. In contrast, elevated T1 is often measured in patients with fatty livers at 3T, when modified Look-Locker inversion recovery (MOLLI) is used. Indeed, the balanced steady-state free precession sequence used in MOLLI causes water and fat signals to have opposite phase when repetition time TR between 2.1 ms and 2.6 ms are used at 3T [275].

With these variable reported results, the confounding effect of steatosis on T1 measurements and the ways to correct this effect needs to be further studied. Recent studies have proposed methods to calculate a corrected T1 (cT1), a fat suppressed T1, to help eliminate the fat effect on T1 [276, 278].

In this preclinical study, first, we investigated whether T1 mapping measurements obtained with MRI across the whole liver are sensitive to hepatic inflammation and fibrosis obtained with liver histologic analysis in mice models of NAFLD/NASH and a confounding effect of steatosis on T1 values was observed. Subsequently, we studied this confounding effect using two two-compartment (fat-water) no-exchange models to eliminate this effect of fat on T1 values.

4.3.2.1. Methods

1) *Data acquisition*

T1 mapping acquisitions were performed with a single slice inversion recovery spin echo sequence with 21 inversion times (30, 230, 430, 630, 830, 1030, 1230, 1430, 1630, 1830, 2030, 2230, 2430, 2630, 2830, 3030, 3230, 3430, 3630, 3830, 4030 ms) and an inversion flip angle of 180° with a 90° excitation pulse and a 180° refocusing pulse. Data were acquired for a single slice adjusted on the largest axial cross-section of the liver, with TR/TE = 12 s/4.46 ms, RARE factor = 20, spatial resolution = 0.5 x 0.5 mm, acquisition matrix = 128 x 60, field of view = 64 mm x 30 mm, slice thickness = 1 mm and bandwidth = 100 kHz. The acquisition time was 11 min 41 s.

2) *Data processing*

T1 relaxation time maps were obtained with an in-house MatLab algorithm based on the inversion-recovery signal equation^[372] :

$$S = S_0 \left(1 - \beta e^{\left(-\frac{TI}{T1}\right)} \right) \quad (20)$$

with the wave inversion efficiency, β , total signal, S_0 and $T1$ as adjustable fit parameters. $T1$ values were calculated at each pixel of a region of interest (ROI) positioned manually covering the whole liver avoiding fat and vessels. Tissue $T1$ mean value was obtained by averaging the $T1$ values of all pixels of the region of interest.

3) *Statistical analysis*

All statistical analyses were performed with MedCalc software version 19.4.1 (MedCalc Software Ltd, Ostend, Belgium). To study the relationship between $T1$ relaxation time values and histological features of NAFLD, Spearman correlations, Kruskal-Wallis and multiple regression analyses were performed. To better match the clinically relevant problem of identifying subjects with NASH among a NAFLD population (rather than among a general population), mice with healthy liver at histology were not included in this analysis, leaving only mice with NAFLD in the study.

Repeatability study

To study the inter-operator repeatability of T1 measurements, regions of interest were obtained for a subgroup of 33 mice which were randomly selected by another operator. Bland-Altman statistical testing was applied to obtain standard deviation estimations and the coefficient of repeatability [197] was calculated the same way as in section (4.3.1.3.) with equation (19).

4.3.2.2. Results

The results of inter-operator repeatability of T1 measurements were good with coefficient of repeatability = 13.1%.

T1 was mainly correlated with steatosis (Spearman's rank correlation coefficient $r = -0.57$ with significance level $p < 0.0001$) and to a lesser degree to inflammation and hepatocyte ballooning ($r = -0.28$ with $p = 0.03$ and $r = -0.29$ with $p = 0.03$ respectively) but not with fibrosis ($r = -0.19$ with $p = 0.15$). Multivariate analysis using multiple stepwise regression with T1 as the dependent variable and steatosis, inflammation, ballooning and fibrosis scores as independent parameters confirmed that T1 is mainly affected by steatosis with $r_{\text{partial}} = -0.60$ and $p < 0.0001$. The other histological features were not included in the multiple regression model. Moreover, Kruskal-Wallis analysis with Conover post-hoc (figure 4.3.3) showed significant decrease of T1 with the increase in steatosis severity ($P < 0.0001$). T1 was significantly different according to inflammation grade ($P = 0.02$) and fibrosis stage ($P = 0.001$). T1 measurements tended to decrease between grade I0 and I2 and to increase between I2 and I3. Same for fibrosis, T1 tended to decrease between F0 and F1a and increase between F1a to F3. T1 was not significantly different between ballooning grades ($P = 0.08$).

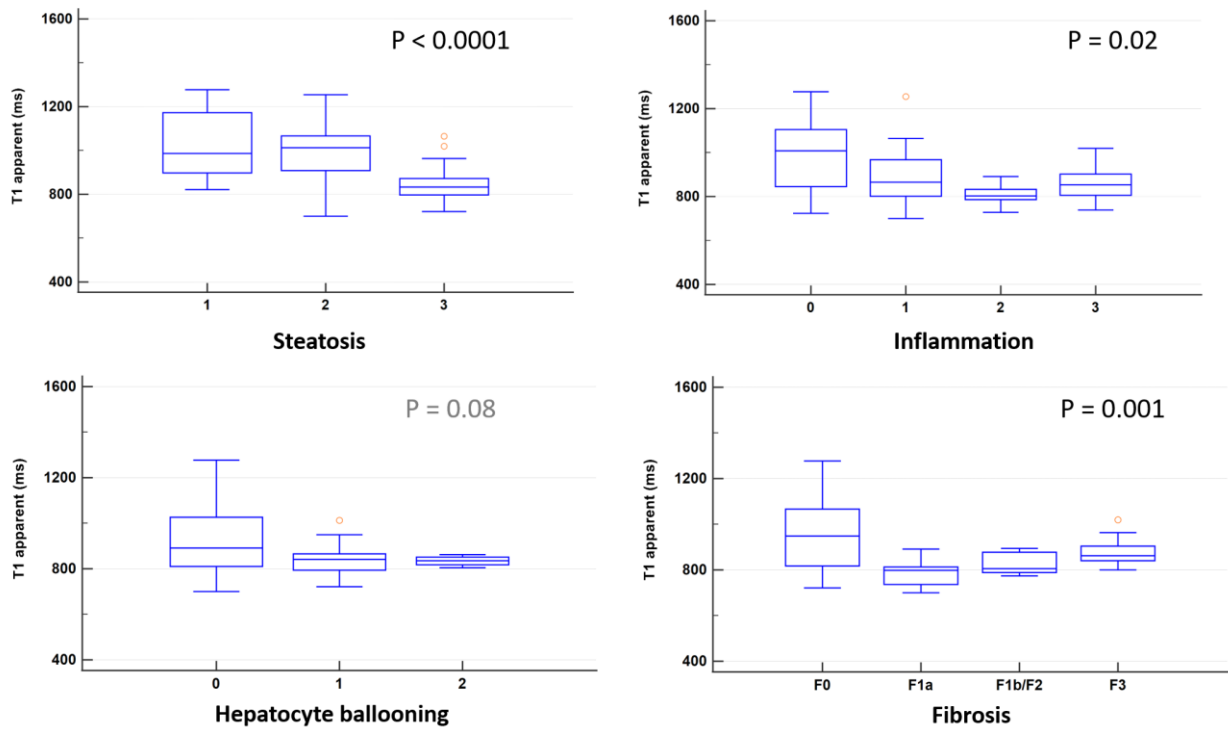


Figure 4.3. 4: Kruskal-Wallis statistical results: Boxplots of T1 relaxation time versus histological features of NAFLD. T1 differs significantly according to steatosis and inflammation grades and fibrosis stages. However, T1 was not significantly different according to ballooning grades.

4.3.2.3. Discussion

The aim of this study was to investigate the changes of T1 according to histological features of NAFLD. Increase in T1 with inflammation, fibrosis and cirrhosis has been reported. For example, Breit H. C. et al.,[373] showed that T1 was significantly lower in healthy subjects than in patients with fibrosis or cirrhosis or patients with acute liver disease.

With MOLLI sequences, Banerjee R et al. [267] and Eddowes PJ et al. [287] showed high T1 in liver with fibrosis, inflammation, and NASH.

In contrast, Wan Q. et al., [374] used water specific T1 (wT1, T1 of the water compartment of the tissue) measurements obtained with fat-water separation to evaluate liver inflammation in rats with methionine-choline-deficient diet induced NAFLD. Results showed a moderate but significant negative correlation between wT1 and histopathological inflammation grades

($r_s = - 0.42$). The wT1 of moderate-to-severe inflammation grades in this study was significantly lower than the wT1 of none-to-mild inflammation grades proving that wT1 could distinguish low from advanced inflammation in a NAFLD rat model.

In our study, the results showed that T1 measurements tended to decrease with early stages of inflammation and fibrosis rather than increase and increase with the progress of these two histological features to severe stages. These measurements were critically affected by the present of fat droplets within hepatocytes (i.e. steatosis). Steatosis is the first histological feature that occurs in NAFLD and with the progress of the disease inflammation and fibrosis progressively develop. Typically, early stages of fibrosis and inflammation coexist with advanced stages of steatosis which may explain the changes observed in our study.

T1 has been reported to have a strong correlation with fat content [275, 375, 376]. In our study, T1 decreased with the increase of steatosis grades. Our T1 mapping datasets were not fat-suppressed and in this type of data, steatosis may confound T1 measurements because of the decrease caused by the partial volume occupied by the fat compartment, since fat may present with short T1. Thus, the T1 measured in our study was an apparent T1 that was determined both by the T1 of the fat compartment and the T1 of the aqueous compartment. As the “real” T1 of the water compartment was masked by the fat content, a correction of this parameter with an adequate model based on both hepatic T1 and liver steatosis quantification is needed.

4.3.2.4. T1 data correction: correction model a posteriori on the R1

To eliminate the effect of the variable levels of fat in hepatocytes on the T1 relaxation time, a two compartment, no exchange model was used. The correction was performed on R1 measurements during post processing^[377]. R1 apparent ($R1_{app}$) was calculated from the T1 apparent ($T1_{app}$):

$$R1_{app} = \frac{1}{T1_{app}} \quad (21)$$

It has been demonstrated that when measuring the spin-lattice relaxation time $T1$ of a medium with multiple compartments that have different $T1$, the average relaxation rate can be estimated as^[377, 378] :

$$R1 = \frac{1}{T1} = \sum_i \frac{p_i}{T1_i} = \sum_i p_i \times R1_i \quad (22)$$

With $\sum_i p_i = 1$ and p_i : the relative population of protons in the i -th compartment. Here we used this expression to dissociate the measured apparent $R1$ ($R1_{app}$) with a two-compartment model consisting of 1) a fat compartment with fractional volume equal to the PDFF and the value of $R1_{fat}$, and 2) a water compartment occupying the remaining volume and characterized by a "corrected" $T1$, or $T1_c$:

$$R1_{app} = R1_{fat} \times PDFF + R1_c \times (1 - PDFF) \quad (23)$$

$R1_c$ was estimated as:

$$R1_c = \frac{R1_{app} - (PDFF \times R1_{fat})}{1 - PDFF} \quad (24)$$

$T1_c$ was retrieved:

$$T1_c = \frac{1}{R1_c} \quad (25)$$

With:

$$R1_{fat} = \frac{1}{T1_{fat}} \quad (26)$$

Where $T1_{fat}$ is $T1$ relaxation time of the fat compartment. To measure the $T1_{fat}$, with the assumption that subcutaneous fat has the same $T1$ as intra-tissue fat, a sub-group of 10 mice of the HFD mice group were randomly selected and ROIs were manually drawn on the acquired $T1$ maps in the subcutaneous fat area. Based on the measurements obtained from each mouse, a mean value of $T1_{fat}$ was estimated. With this procedure, we estimated $T1_{fat} = 588 \pm 20.4$ ms. Lower values of fat $T1$ have been reported in mice ($T1 = 304 \pm 4$ ms estimated in white adipose tissue) [379] and in healthy volunteers ($T1 = 382 \pm 13$ ms estimated in

subcutaneous fat) [371] however these measurements have been performed at 3T. The PDFF estimations used here were the ones measured individually for each animal as described in the previous section.

Statistical analyses with MedCalc software version 19.4.1 (MedCalc Software Ltd, Ostend, Belgium) were performed to evaluate the efficacy of the T1 correction model. For that, univariate (Spearman's rank correlation) and multivariate (stepwise - multiple regression) statistical tests were used to assess the relationship between the corrected T1 and histological features. Statistical analysis was performed only in mice with NAFLD. Mann-Whitney statistical test was performed to compare $T1_{app}$ and $T1_c$ at each steatosis grade (the S0 grade of steatosis was only included in this comparison to analyze the behavior of our model without fat).

Results

As expected by construction (equation 24), $T1_c$ was higher than apparent T1. The results of the comparison between T1 before and after correction at each steatosis grade showed that the effect of the PDFF correction was significant only at high steatosis grades (Mann-Whitney significant level $p < 0.0001$) (Table 4.3.2). The corrected T1 still showed a strong dependence on the degree of steatosis. Rank correlation analysis (Spearman's) showed that $T1_c$ measurements were still mainly correlated with steatosis with a correlation coefficient $r = -0.47$ with $p = 0.0002$. These corrected measurements were also negatively correlated to inflammation but with a lower degree ($r = -0.27$ with $p = 0.04$). No correlation with hepatocyte ballooning nor with fibrosis was detected ($r = -0.23$ with $p = 0.08$ and $r = -0.19$ with $p = 0.14$ respectively).

Multiple regression statistical test with $T1_c$ as the dependent variable and steatosis, inflammation, ballooning and fibrosis scores as independent parameters confirmed that T1 remained influenced by steatosis in the liver with $r_{\text{partial}} = -0.47$ and $p = 0.0002$. The other histological features were not included in the multiple regression model.

Even with the correction model, T1 still decreased with the increase of steatosis reflecting the persisting confounding effect of steatosis on T1. Another model more precise should be used to eliminate the effect of fat on T1 to provide an appropriate measurement of water only T1.

Table 4.3. 2: Mann-Whitney results comparing T1 before and after correction vs. steatosis grades.

Steatosis grade	$T1_{app}$ (median [C.I.])	$T1_c$ (median [C.I.])	Mann Whitney : p value
S0	1177 [1172 ; 1193]	1190 [1177 ; 1210]	P = 0.19
S1	987 [883 ; 1200]	1085 [1045 ; 1273]	P = 0.09
S2	1013 [802 ; 1165]	1140 [920 ; 1314]	P = 0.14
S3	833 [805 ; 857]	971 [956 ; 1003]	P < 0.0001

4.3.2.5. T1 data correction : correction model for the expression of the signal

For the correction of T1 measurements, another method operating at the level of the MRI signal model was proposed by injecting the PDFF in the expression for the MRI signal. This was done by decomposing the signal in two compartments, each with its own T1 relaxation time ($T1_c$ and $T1_{fat}$, respectively) and volume fraction ($1 - PDFF$ and $PDFF$, respectively):

$$S = S_0 \cdot \left\| (1 - PDFF) \cdot \left(1 - \beta \cdot \exp \left(- \frac{TI}{T1_c} \right) \right) + (PDFF) \cdot \left(1 - \beta \cdot \exp \left(- \frac{TI}{T1_{fat}} \right) \right) \right\| \quad (27)$$

where S_0 is the equilibrium magnetization, β is an inversion efficiency term, $T1_c$ is the T1 we are seeking to obtain (T1 corrected) corresponding to the T1 of the water compartment and $T1_{fat}$ is the T1 of the fat compartment. PDFF was measured independently for each mouse while for the $T1_{fat}$, a reference value was estimated ($T1_{fat} = 588 \pm 20.4$ ms) as described previously. All other parameters were kept free. The aqueous component was not subdivided in extracellular and intracellular sub-compartments as in Mozes et al^[278].

Phantom validation study

To validate this model, a biphasic phantom study was performed with a horizontal tube containing oil as the fatty compartment and a solution of gadoteric acid (0.13 mM) as the aqueous compartment. To imitate the steatotic liver environment, the fatty compartment was made up of sunflower oil (selected among four types of oils) based on its T1 value ($496 \pm$

6 ms) being the closest to that of the T1 of subcutaneous fat in mice (588 ± 5 ms), compared to olive oil: $T1_{olive} = 470 \pm 5.05$ ms, coconut oil: $T1_{coconut} = 458 \pm 6.55$ ms and colza oil: $T1_{colza} = 484 \pm 5.12$ ms. For the aqueous compartment, a solution of gadoteric acid was used, at a concentration of 0.13 mM to match the T1 of a healthy mouse liver ($T1_{Liver}$). $T1_{Liver}$ was calculated in a group of healthy mice ($T1_{Liver} = 1178 \pm 80.5$ ms, $n = 34$ mice) and gadolinium relaxivity at 7T was measured ($r(Gd) = 0.004 \text{ mM}^{-1} \cdot \text{ms}^{-1}$) to determine the appropriate concentration of Gd for $T1 = T1_{Liver} = 1178$ ms, which was $[Gd] = 0.13$ mM. The biphasic phantom was scanned with the imaging slice angulated across the horizontal water/fat interface to obtain a large linear transition between pure oil and water on opposed sides of the images. MRI acquisitions were performed with the same 7T imaging system (Pharmascan - Bruker, Erlangen, Germany), the same T1 mapping sequence (a single slice inversion recovery spin echo sequence) and the same acquisition parameters as for the T1 mapping of the preclinical study exhibited in the section above. PDFF was also assessed with the same sequence and parameters as the one used to quantify PDFF in mice (see section above). Afterwards, T1 phantom data were assessed with both our non-corrected T1 mapping fit to obtain the T1 apparent and the T1 fit with the correction model to obtain the corrected measurements of T1 ($T1_c$).

Correction model application in preclinical T1 data

All preclinical T1 mapping data were reprocessed to obtain new corrected $T1_c$ measurements. Mann-Whitney statistical test was performed to compare $T1_{app}$ and $T1_c$ and evaluate the efficiency of our model in mice liver T1 measurements.

Results

The phantom experiments demonstrated that the bicompartimental T1 relaxation model enabled to compensate for fat within 10% error (figure 4.3.4). The pixels at the interface between fat compartment and aqueous compartment contain both fat and water with different levels (transition zone with fat ranging from 0 to 1). At this interface the correction was effective even at high PDFF values.

In the mouse model of NASH, T1 of the second proposed corrective model was significantly higher than in the uncompensated model but only at steatosis grade 3 with $T1_{app}$ of 833 ms,

$T1_c$ of 922 ms and a significance level $p = 0.0001$ (figure 4.3.5, table 4.3.3). The correction by the PDFF term did not completely suppress the steatosis-induced decrease in $T1_c$.

Table 4.3. 3: Mann-Whitney results comparing $T1$ before and after correction vs. steatosis grades.

Steatosis grade	$T1_{app}$ (median [C.I.])	$T1_c$ (median [C.I.])	Mann Whitney : p value
S0	1177 [1172 ; 1193]	1182 [1154 ; 1203]	$P = 0.5976$
S1	987 [883 ; 1200]	1060 [969 ; 1240]	$P = 0.3410$
S2	1013 [802 ; 1165]	1064 [829 ; 1167]	$P = 0.6547$
S3	833 [805 ; 857]	922 [897 ; 940]	$P = 0.0001$

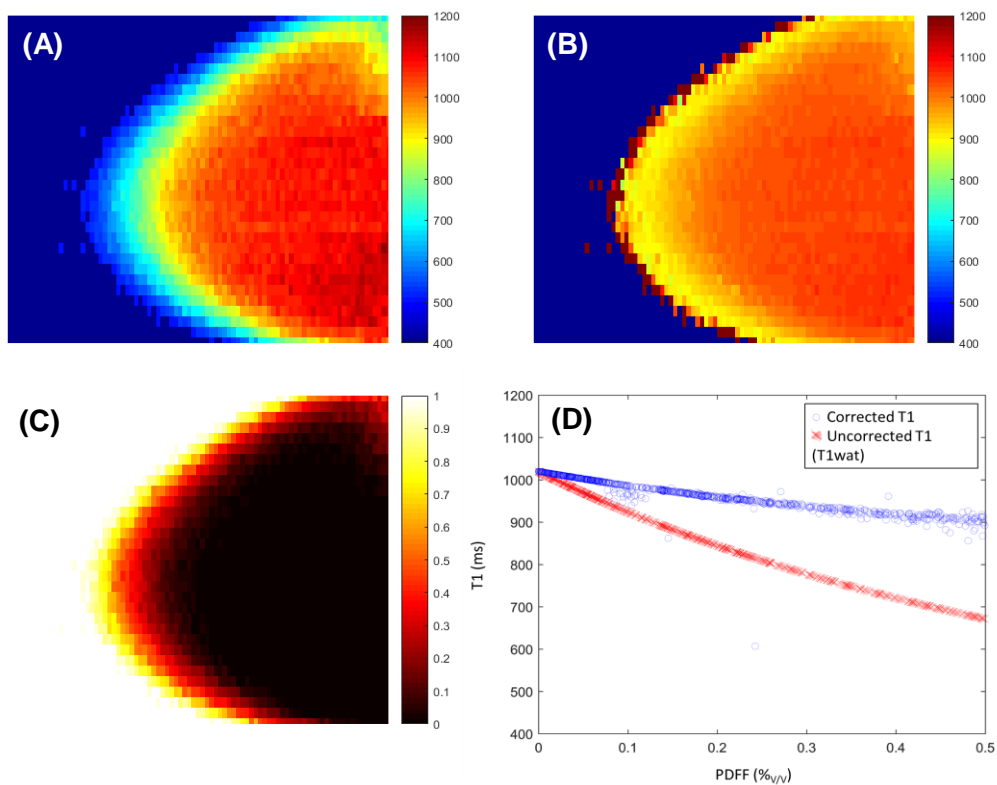


Figure 4.3. 5: Phantom maps of $T1$ (A: uncorrected, B: corrected) and PDFF (C). D: scatter plot between PDFF and $T1$ (blue circles: PDFF-corrected $T1$; red crosses: uncorrected $T1$).

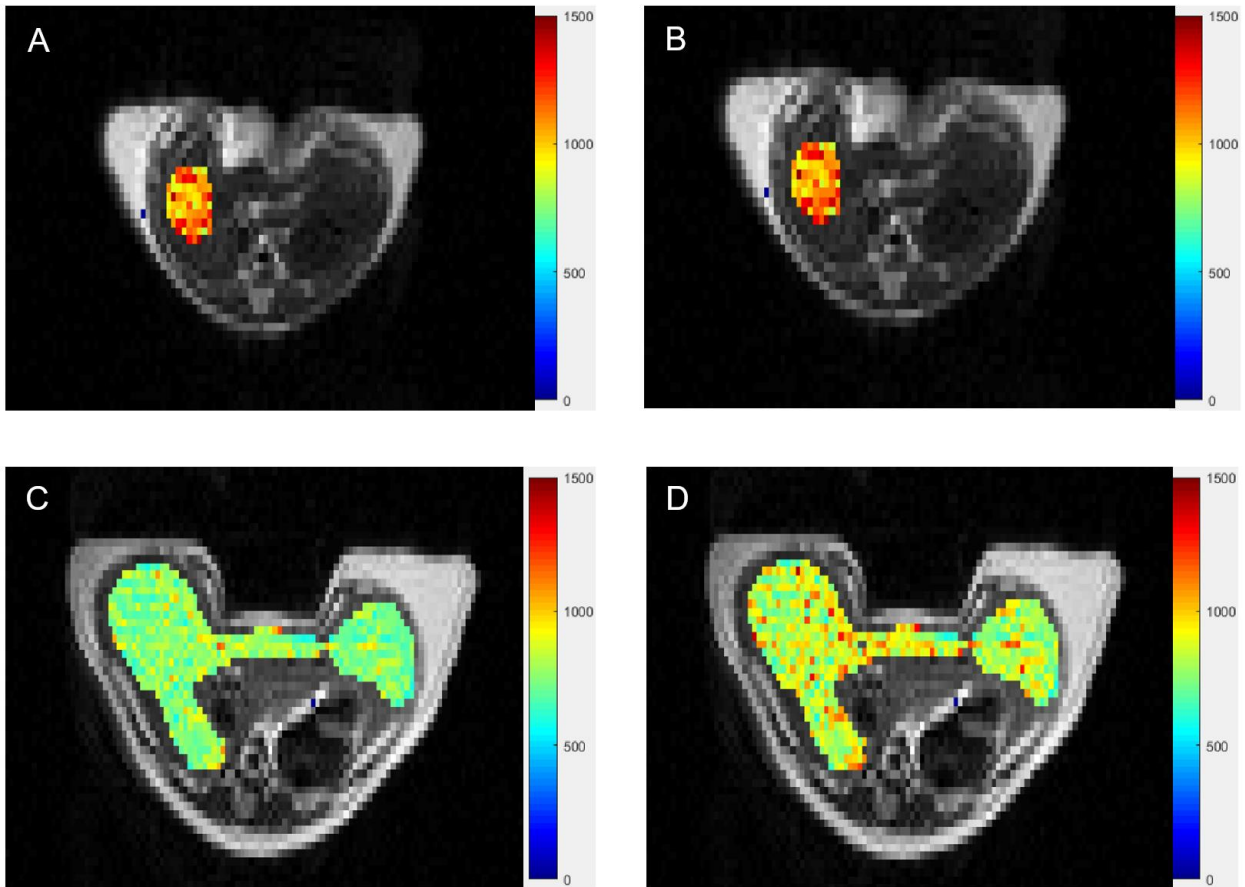


Figure 4.3. 6: T1 maps in mice with steatosis grade S0 (PDFF = 2%) : A) without PDFF correction ($T_{1_{app}} = 1139 \pm 152$ ms), B) with PDFF correction ($T_{1_c} = 1100 \pm 157$ ms), and with steatosis grade S3 (PDFF = 30%): C) without PDFF correction ($T_{1_{app}} = 762 \pm 88$ ms), D) with PDFF correction ($T_{1_c} = 858 \pm 136$ ms). The PDFF correction factor increases the measured T_{1_c} only in the mouse with high steatosis.

4.3.2.6. Discussion

This study was performed with the purpose of correcting the effect of fat on T1 measured in vivo in mice models of NAFLD. We used two correction models. In first one, the correction was performed a posteriori while in the second one PDFF was injected in the MRI signal model used for the T1 fit to suppress the fat effect. In both cases, our results showed that the corrected T1 still showed a strong dependence on the degree of steatosis. The effect of the

fat correction was significant only at high steatosis grades (S3). Even with the application of the correction models, T1 decreased with the increase of steatosis grades.

The phantom experiments demonstrated that the second T1 correction model enabled to compensate for fat within 10% error. When applied to the preclinical data, T1 was significantly higher than in the uncompensated model (T1 apparent), and that the model correction had, as expected, only an effect at high levels of fat (steatosis grade 3). The amount of compensation, however, was not sufficient to observe the T1 increase reported by Mozes et al [278] with shMOLLI and by Hoad et al [276] with fat-suppressed inversion recovery. Multiple reasons could be behind this variability including the scanner field strength, the imaging sequence used for T1 mapping, the type of study (animal or human study), the fitting model used and the difference in fat fraction of the assessed tissues [274]. It has been shown that the chemical shift of fat at 3T is larger than that at 1.5T [380, 381]. Mozes et al [278] performed T1 measurements with shMOLLI (multiple-echo spoiled gradient-recalled echo) sequence at 3T with an algorithm for fat suppression in phantoms and patients with different liver diseases while Hoad C. et al. [276] used fat suppressed inversion recovery (single shot EPI) sequence at 1.5T for T1 mapping to obtain water T1 measurements in patients with liver fibrosis and cirrhosis.

The discrepancy between phantom and in vivo models may be attributed to the different subvoxel distribution of fat and water in the biphasic phantom and in the lipid droplets of hepatocytes. The relationship between fat and water in the tissue is more complex than in a simple oil/water model. Fat droplets in hepatocytes are not of homogeneous size or shape, there are two types of lipid vesicles, namely micro- and macro-vesicles. Moreover, this accumulation of lipids differs between hepatocytes. However, the phantom used in our study is made of homogenous compartments of sunflower oil and water, and the fat fraction is achieved via partial volume within the voxels intersecting the water / fat interface. Thus, we need to use correction models that take into consideration the complexity of living tissue. Further validation of our results will be obtained by comparing them with fat suppressed sequences results that will be obtained in a future study. Also using lipid emulsion phantoms may be useful for further validation of our correction models.

This study has several limitations. First, the reference used to evaluate our Imaging biomarker performance is histologic analysis which is an invasive subjective procedure which may have some inaccuracies as diagnosing Inflammation and hepatocellular ballooning could be challenging particularly in early stages of the disease. This histology related limitation could partially lead to the performance lack of the studied biomarkers. Another limitation that should be taken into consideration is the challenge of accurate matching between single slice T1 maps and histological slices which can be hard to accomplish. Furthermore, our T1 mapping sequence was not performed with respiratory gating. Thus, artifacts caused by respiratory movement during acquisitions may lead to imprecise T1 measurements. Moreover, T1 maps were acquired for one slice.

To summarize, T1 relaxation time measured with a non-fat suppressed imaging sequence can be highly affected by liver fat. Two bi-compartmental no exchange models have been used to correct the effect of fat. As expected, these models were only effective at high steatosis levels, but other models that take into consideration the complexity of living tissue should be used. We think that with a fat suppressed imaging sequence to measure T1 may further improve the results for diagnosing fibrosis and inflammation.

5. Chapter III : Temporal Diffusion Spectroscopy with oscillating gradients echoplanar imaging

5.1. Introduction

Apparent diffusion coefficients (ADC) noninvasively provide information on diffusion properties of tissue water molecules that are affected by restrictions to free movement, reflecting the microstructural properties of biological tissues [327, 329, 382]. Conventionally, ADC is obtained with pulsed gradient spin echo (PGSE) sequences. But with this method, ADC lack specificity as it is influenced by several spatial scales. Temporal diffusion spectroscopy (TDS) with oscillating gradient spin echo (OGSE) has been proposed as an alternative DWI approach where the ADC is considered as having a frequency (ω) content, corresponding to different spatial scales. This frequency content is based on the fact that the diffusion coefficient (D) translates the autocorrelation function of the particle velocities (v), which emerges from spatial obstructions hindering diffusion:

$$D_{i,j} = \int_0^{\infty} dt' \exp(i\omega t') \langle v_i(t') v_j(0) \rangle \quad (28)$$

This autocorrelation function ($\langle v_i(t') v_j(0) \rangle$) can be interrogated at a range of time intervals τ . Correspondingly, the diffusion encoding gradients $g(t)$ in any diffusion weighted sequences are endowed with a certain frequency content, $F(\omega)$:

$$F(\omega) = \int_{-\infty}^{\infty} dt \exp(i\omega t) \int_0^t dt' \gamma g(t') \quad (29)$$

where γ is the gyromagnetic ratio. Thereby, the application of such diffusion-encoding gradient with a specific frequency content, results in the measurement of an ADC integrated over this range of frequencies. To exploit this mechanism, the OGSE technique relies on the application of carefully designed encoding gradient shapes that select a narrow frequency range. Therefore, the MR signal is encoded with a specific ADC value at the requested frequency:

$$S = S_0 \exp\left(-\frac{1}{\pi} \int_0^\infty F(\omega)D(\omega)F(-\omega)d\omega\right) \quad (30)$$

where S_0 is the signal magnitude in the absence of the diffusion gradient. The frequency (or equivalently the time scale t) at which the ADC is sampled determines the root mean square diffusion length r for a given diffusion rate as per Einstein's relation:

$$\langle \vec{r}^2 \rangle = 2dDt \quad (31)$$

where D is the self-diffusion coefficient (i.e. free diffusivity) and d is the dimensionality considered. Hence the user-selectable frequency in an OGSE sequence enables to arbitrarily select a spatial scale r of interest. Under typical hardware constraints, tissue microstructure at scales smaller than the diameter of a single cell can be interrogated, allowing a more comprehensive assessment of diseases [327-329, 382-385].

OGSE methods have been used in various studies, for estimating nuclear size changes after anticancer therapy[338, 386, 387], measuring cell size in human breast cancer [388], probing water diffusion in the gray matter of ischemic rat brain[327], and characterizing hepatocellular nodules in liver cirrhosis in in a rat model [337]. More recently, OGSE with EPI readout was used to characterize hepatocyte size [389].

Moreover, it has been reported in several studies with conventional DWI that steatosis [390], inflammation [390, 391], fibrosis [391] and some combination [392] thereof, may affect ADC measurements. Hence, with the possibility to detect diffusion restrictions at a subcellular spatial scale, OGSE-EPI may be an useful tool for characterizing NASH and particularly the changes in hepatocyte size caused by hepatocellular ballooning, hallmark of disease. To the best of our knowledge, this technique has not been applied before to explore ADC changes in vivo in mice with NAFLD. The aim of this study was to implement an OGSE method in an echoplanar imaging (OGSE-EPI) sequence, study the feasibility and robustness of this technique and apply it to assess NAFLD, NASH and its histopathological features in vivo in mice models of NAFLD.

In the absence of a true reference measure for the diffusion coefficient, validating the implementation of a diffusion sequence may prove challenging. In this context, the validation

of a sequence can instead come from the observation of expected behaviors in carefully controlled systems. Packed beads can be used in the study of OGSE because such beads can be manufactured with very tightly controlled size distributions, allowing the diffusion of water molecules to be observed in the space between these packed beads. This space represents a restricted medium which characteristic size is proportional to the beads size. Multiple samples with different bead size can be used to study the diffusion of water molecules in restricted media of different, well characterized and controlled sizes.

In vivo, reference measurements for newly implemented diffusion sequences are also not available. Variations in observed values between experimental disease model groups can be interpreted by having experimentally assessed the repeatability of the measurement. Particularly, the reproducibility of the OGSE method has been recently investigated in vivo in the brain of a healthy mice at 9.4T for multiple diffusion metrics including linear diffusion kurtosis, isotropic diffusion kurtosis, and the diffusion dispersion rate, but not the ADC, with 4 frequencies ranging from 50 Hz to 190 Hz. In these conditions, coefficients of variation showed high repeatability (CVs < 15%) [393].

To the best of our knowledge, no reproducibility studies have been conducted for the OGSE-EPI sequence in vivo in mice liver. Experimental conditions such as the choice of radiofrequency coil and the use of respiratory gating may significantly impact the repeatability coefficient and the SNR available from the diffusion-weighted images. Hence, we also studied the repeatability in several experimental conditions to determine an optimal imaging protocol.

Here, we implemented the OGSE sequence, tested it in phantoms, healthy mice and in a NAFLD mouse model with disease regression.

Chronologically, the repeatability study was acquired first, while the available system had gradients of 300 mT/m, while the phantom and disease model acquisitions were realized later, after the imaging platform had been equipped with a higher performance gradient system of 660 mT/m. This explains some variations in the acquisition parameters, which were adapted to benefit from the performance of the new gradient system.

5.2. Methods

5.2.1. Sequence programming

A TDS sequence was developed based on OGSE in an EPI sequence, with the objective of shortening the acquisition time. Sequence programming was performed on ParaVision software (PV6, Bruker, Ettlingen, Germany). For the OGSE-EPI sequence, we altered the EPI sequence of the manufacturer by inserting oscillating gradients symmetrically on either side of the refocusing pulse. Two oscillating gradients waveforms were used. First, the double-sine waveform was implemented, followed by the trapezoidal waveform.

5.2.1.1. Double-sine wave form implementation

A double sinusoidal oscillating gradient waveform was first implemented:

$$g(t) = G \sin(2\omega_0 t) \operatorname{sgn}[\sin(\omega_0 t)] \quad (32)$$

Where G is the gradients amplitude, ω_0 is the oscillation frequency ($\omega_0 = 2\pi N/T$, with N the number of oscillation periods and T the waveform duration) and sgn is the signum function. With the mathematical expression relating the amount of diffusion-weighting known as the b-value to the gradient waveform $g(t)$ described by Stejskal and Tanner [394]:

$$b = \gamma^2 \int_0^T dt \left[\int_0^t dt' g(t') \right]^2 \quad (33)$$

The b-value (s/mm^2) formula corresponding to our double-sinusoid gradient waveform is:

$$b = \frac{3}{32} \left(\frac{\gamma \gamma}{\pi N} \right)^2 T^3 \quad (34)$$

Where γ is the gyromagnetic ratio. The corresponding diffusion time is calculated here by comparison to the b-value formula as done by Does et al [327]:

$$\Delta_{eff} = \frac{3}{32 f} \quad (35)$$

With f being the frequency. On the spectral level, the double-sine gradient waveform contains spectral components at $(1+2k)\omega_0/2$ with $k = 1 \dots N$. However, the first one at $\omega_0/2$ contains most of the spectral energy while the second and subsequent components represent at most 4% of the energy and are thus safely neglected [327]. The double-sinusoid waveform and its corresponding power spectrum are illustrated in Figure 5.1.

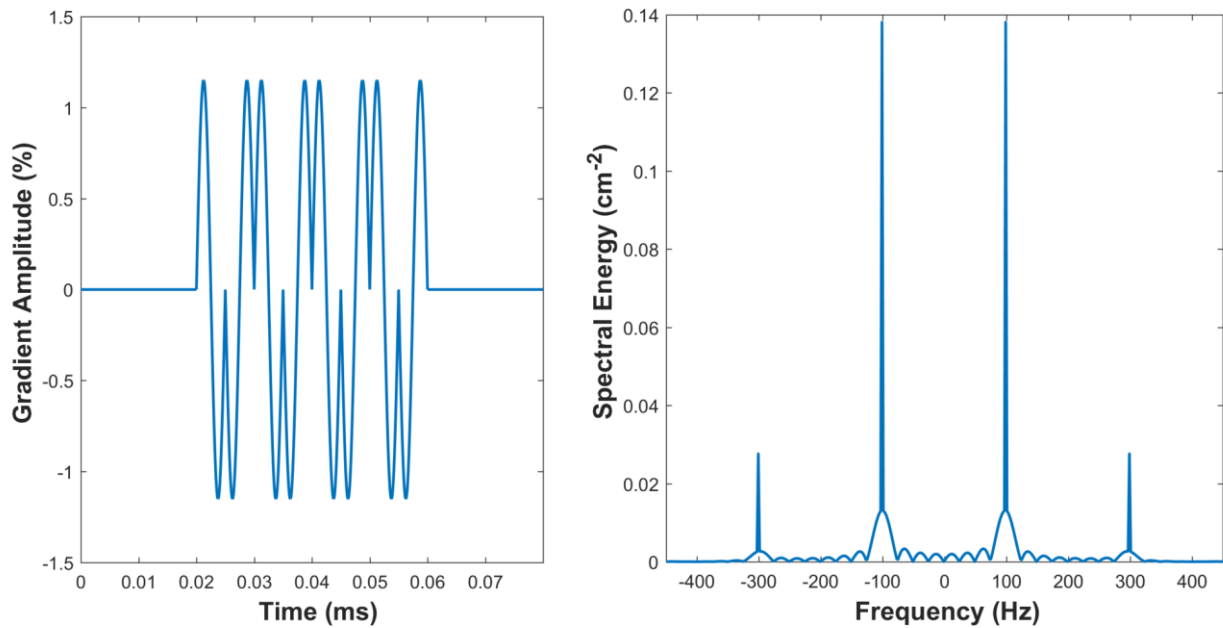


Figure 5. 1: Illustration of the double-sinusoid gradient waveform and its corresponding power spectrum with the gradient oscillation frequency $f = 100$ Hz and the number of gradient oscillation periods $N = 4$ (as of 2 on each side of the refocusing pulse).

5.2.1.2. Sequence optimization : Trapezoidal waveform

To improve our sequence a trapezoidal gradient waveform was implemented[388]. This waveform provides increased maximum b-value (through markedly lowered duty cycle requirements) with minimal degradation to the encoding spectrum [340]. The formula of the trapezoidal waveform as implemented on our system is:

$$g(t) = \begin{cases} \frac{A}{t_r} \times t & \text{if } 0 \leq t < t_r \\ A & \text{if } t_r \leq t < t_r + \tau_1 \\ A \left(\frac{2t}{\tau_1 - \tau_2} + \frac{\tau_1 + \tau_2}{\tau_2 - \tau_1} \right) & \text{if } t_r + \tau_1 \leq t < t_r + \tau_2 \\ -A & \text{if } t_r + \tau_2 \leq t < t_r + \tau_3 \\ A \left(\frac{2t}{\tau_4 - \tau_3} + \frac{\tau_3 + \tau_4}{\tau_3 - \tau_4} \right) & \text{if } t_r + \tau_3 \leq t < t_r + \tau_4 \\ A & \text{if } t_r + \tau_4 \leq t < t_r + \tau \\ -\frac{A}{t_r} \times t & \text{if } T - t_r \leq t < T \end{cases} \quad (36)$$

With A: the amplitude of the gradient in percentage, t_r : the gradient ramp time from zero gradient to the maximum gradient value (in our system $t_r = 140 \mu\text{s}$), τ : the period of the waveform ($\tau = 1/f$). $T = 2 * t_r + N * \tau$ with N the number of periods and τ_1, τ_2 and τ_3 represent :

$$\tau_1 = \frac{(\tau - 4t_r)}{4} \quad (37)$$

$$\tau_2 = \tau_1 + 2t_r \quad (38)$$

$$\tau_3 = 3\tau_1 + 2t_r \quad (39)$$

The diagram of the waveform is represented in figure 5.2. A Matlab software based on numerical integration of the waveform (equation (33)) [327] was programmed to compute the effective b-value for a given waveform and a user-selectable amplitude scaling parameter ranging from 0 to 100% of the available system gradient strength. The b-values were later confirmed with the b-value expression corresponding to the trapezoid gradient waveform as calculated by Baron C. A. et al., [330]:

$$b = 2N\gamma^2 G^2 \left(\frac{1}{4f} - \frac{t_r}{2} \right)^2 \Delta_{eff} \quad (40)$$

Where the effective diffusion time Δ_{eff} formula is [330]:

$$\Delta_{eff} = \frac{1}{6f} + \frac{2}{3}(t_r - (t_r^2 * f)) \quad (41)$$

Indeed, for specific values of G of e.g. 50% and 100% of the maximum gradient strength of 660 mT/m available on the FRIM MRI system, the b-values achieved with the trapezoidal waveform at 250 Hz with 2 gradient waveform periods on each side of the refocusing pulse are 83 and 337 s/mm², respectively, whereas with the double sinusoidal waveform, these same gradient amplitudes only yield b-values of 38 and 152 s/mm². Thus b value gains on the order of x2.2 (as expected by estimating the ratio of expressions 40 and 34) can be achieved merely by changing the waveform at nearly no cost in terms of frequency content.

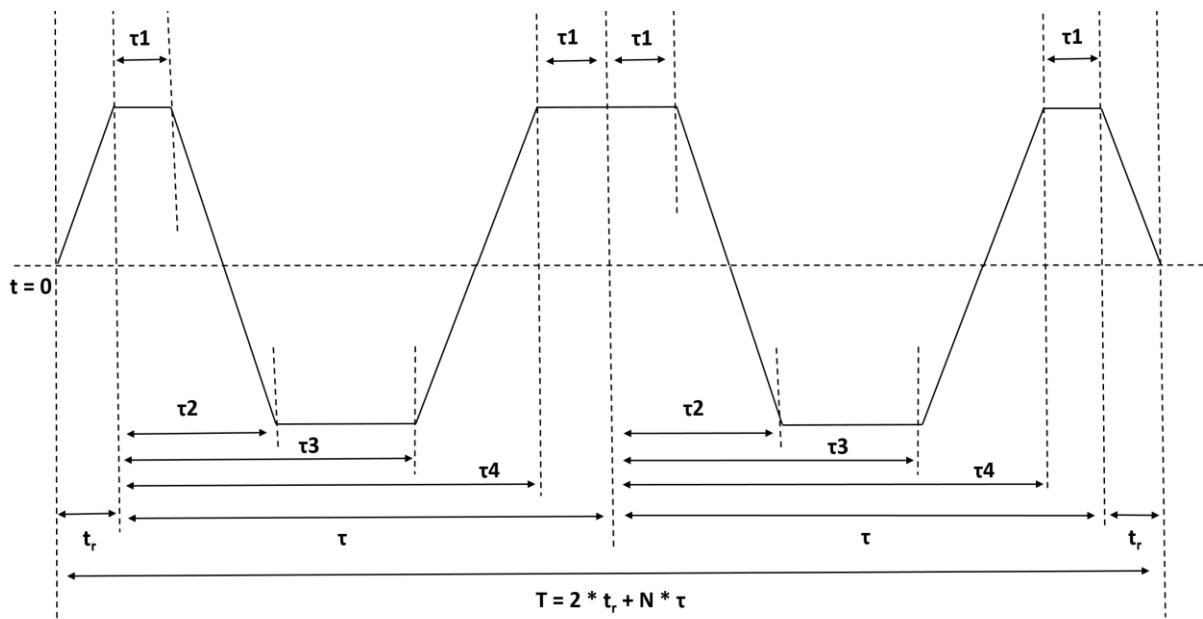


Figure 5. 2: Illustration of the diagram of the trapezoidal waveform with t_r : the gradient ramp time (in our system $t_r = 140 \mu s$), τ : the period of the waveform ($\tau = 1/f$). Here the number of the periods $N = 2$.

The trapezoidal waveform and its corresponding power spectrum are illustrated in Figure 5.3.

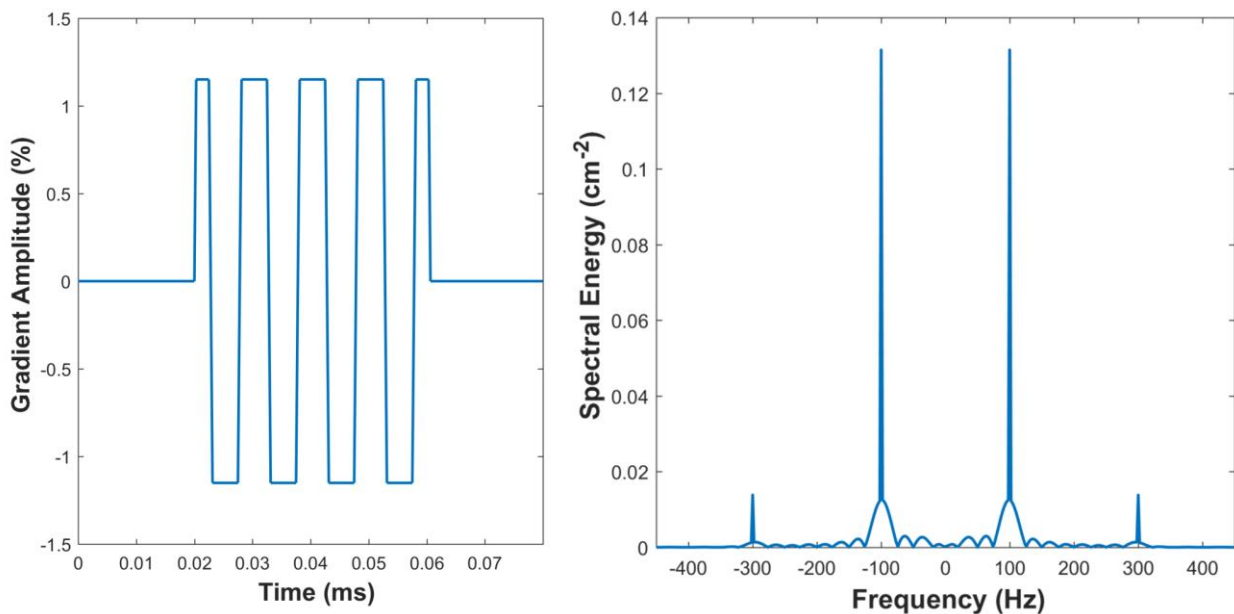


Figure 5. 3: Illustration of the trapezoidal gradient waveform and its corresponding power spectrum with the gradient oscillation frequency $f = 100$ Hz and the number of gradient oscillation periods $N = 4$ (as of 2 on each side of the refocusing pulse).

We also implemented the ability of using encoding gradients simultaneously in several encoding directions to enhance the total available effective gradient strength by a factor of up to $\sqrt{3}$. Crosstalk terms between the slice selection gradient and the encoding gradients limited this strategy to the phase and readout directions, enhancing gradient strength by a maximum factor of $\sqrt{2}$.

5.2.2. Materials and subjects

5.2.2.1. Phantom study

The phantom based study was performed with polystyrene latex microspheres (Polysciences, Eppelheim, Germany) of the following average diameters: 3, 7, 15, 30 and 150 μm with a density of 1.05 g/cm^3 , suspended in deionized water [329]. The samples were placed in 1.5 ml plastic tubes (height ~ 4 cm) and centrifuged at a relative centrifugal force of 10000 G for 5 minutes to induce close packing. The supernatant water was removed and replaced with a mixture of pure water and gadolinium with T1 relaxation time equivalent to the T1 of healthy

mouse liver (~ 1180 ms). The average sample volume was 0.5 ml. The samples were well mixed, re-centrifuged and the supernatant of water + Gd was carefully replaced with olive oil to maintain the induced close packing as olive oil density ($\rho = 0.917$ kg/L) is lower than both the density of water ($\rho = 1$ kg/L) and of beads (1.05 kg/L), thus preventing beads from spontaneously resuspending in the residual supernatant volume. The bead tubes were then embedded in agarose gel for support and rf impedance matching.

5.2.2.2. In vivo repeatability study

The repeatability study was conducted in a group of 5 healthy C57BL/6JRj male mice (Janvier Labs, Genest-Saint-Isle, France) housed and fed with standard conditions in accordance with local ethical regulations (Apafis: #15218-2018052410286448v4).

5.2.2.3. NAFLD mouse models

The NAFLD preclinical mouse model study was done in accordance with local ethical regulations (CEEA-121, Apafis: #19705 and #32302). A cohort of 132 C57BL/6JRj, (Janvier Labs, Genest-Saint-Isle, France) male mice was fed with three dietary models: a normal diet (ND, 1324 IRR, Altromin, Lage, Allemagne) (36 mice), a high fat diet with 60 kcal% fat (HFD, D12492i, Research Diets/Brogaarden, Lyngø, Danemark) (36 mice), and a CDA-HFD with 60 kcal% fat, no choline and 0.1% methionine (A06071302i, Research Diets/Brogaarden Lyngø, Danemark) (60 mice). Forty-eight of the CDA-HFD-fed mice were subjected to two diet reversal therapy approaches that started at 10 weeks after induction. The two reversals lasted 4 to 8 weeks. The first was a reversal to HFD and the second to ND. The animals were housed in standard conditions for 10, 14 and 18 weeks (n = 12 mice per time point subgroup) (Figure 5.4).

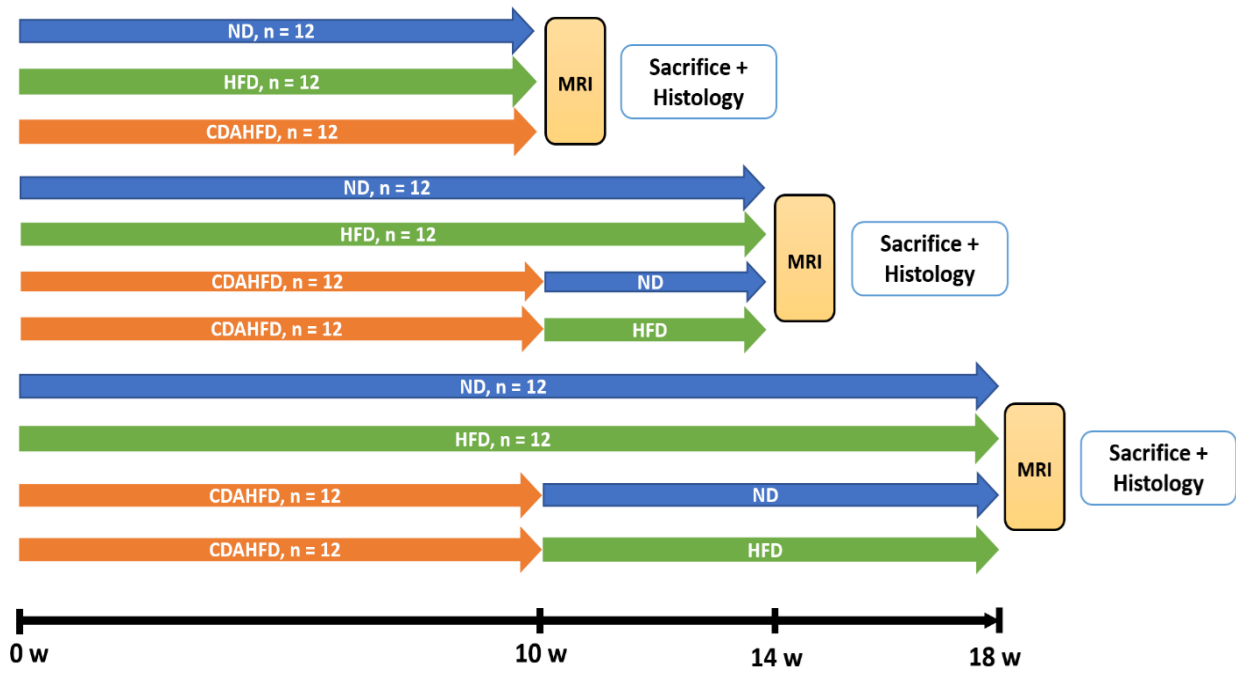


Figure 5. 4: Study timeline and the groups and subgroups included.

After imaging, mice were sacrificed and their livers were analyzed by an expert liver pathologist blinded to the dietary condition, to diagnose steatosis, inflammation, ballooning and fibrosis based on the NASH CRN staging system [361, 395].

5.2.2.4. Animal procedures

All animal in this study were only handled by staff with the appropriate training and authorizations. They were anesthetized with isoflurane in a 70% air / 30% O₂ mixture at a concentration of 3% for induction and scanned in the prone position. To maintain the animals anesthetized during scanning, 1-2% concentration of isoflurane was used and constantly adjusted with real-time monitoring of the respiration rate with a pressure sensitive pad placed on the abdomen (SA instruments, Stony Brook, NY). During scanning, mice body temperature was maintained with a cooling/heating water system placed on the mouse.

5.2.3. Acquisition parameters

5.2.3.1. MRI system

MRI examinations were performed with a 7T imaging system (7TBiospec - Bruker, Erlangen, Germany). For the repeatability study, MRI gradients BGA20S HP (300 mT/m, 280 μ s rise time) were used. For the phantom study and sequence application in NAFLD mouse models, new and more powerful MRI gradients BGA12S HP (660 mT/m, 140 μ s rise time) were used with the actively decoupled, 4-channel surface coil array for reception and a volume transmit coil.

5.2.3.2. Conditions assessed in the repeatability study

For the repeatability study, eight combinations of acquisition factors were tested. MRI acquisitions were performed with either a volume coil or a combination of a volume transmit coil and an actively decoupled, 4-channel surface coil array for reception, with and without respiratory gating. Two frequencies were tested 100 and 150 Hz with effective diffusion times of approximately 0.94 ms and 0.63 ms respectively which corresponds to characteristic diffusion lengths of 1.94 μ m and 1.58 μ m respectively.

5.2.3.3. Sequence parameters used in the three studies

4) *Phantom study*

MRI acquisitions were performed with 4 OGSE-EPI frequencies (130, 170, 230 and 250 Hz) and a PGSE at 47 Hz. The corresponding effective diffusion times and characteristic diffusion lengths were as presented in table 5.1.

Table 5. 1: The effective diffusion times and characteristic diffusion lengths for the OGSE and PGSE acquisitions

Frequency (Hz)		Effective diffusion time Δ_{eff} (ms)	the characteristic diffusion length L (μ m)
PGSE	47	22	9.38
OGSE	130	1.38	2.35
	170	1.07	2.07
	230	0.82	1.81
	250	0.76	1.74

Four b-values ($b = 0, 150, 300$ and 500 s/mm^2) were obtained by modulating the gradient amplitude according to expression (35). At 230 Hz and 250 Hz, the 4th b-value (500 s/mm^2) was degraded to $b = 429 \text{ s/mm}^2$ and $b = 337 \text{ s/mm}^2$ respectively, corresponding to the values achieved at 100% of system gradient strength. Throughout all b-values and frequencies, echo time was maintained at a constant minimal value of 29.52ms. Acquisition parameters are detailed in Table 5.2.

5) *In vivo* repeatability study

MRI acquisitions were performed with four b-values 0, 75, 113 and 150 s/mm^2 because of limitations of the gradient system available at the time. These b-values were obtained by varying the gradient amplitude at a constant echo time, which on the system available at the time was minimally 51.8 ms. In all tested conditions, MRI acquisitions were repeated twice during a single anesthesia. Scan time per b-value was 1 min 20 s and 3 min 40 s without and with respiratory gating, respectively. The other sequence parameters are detailed in Table 5.2.

6) *NAFLD mouse models*

The TDS data were acquired with the same conventional PGSE at 47 Hz and trapezoid-modulated OGSE-EPI sequences as those used in the phantom study (Table 5.2). In this animal study, to accommodate a multi-contrast acquisition protocol while staying under limited duration of anesthesia, only the 130 Hz and 250 Hz OGSE frequencies were acquired (corresponding effective diffusion times of 1.38 ms and 0.76 ms and spatial scales of $2.35 \mu\text{m}$ and $1.74 \mu\text{m}$ respectively). Acquisitions were performed with spectral-selective fat suppression and respiratory gating and with the 4-channel parallel receive surface coil, in accordance with the optimized setup as determined from the repeatability study. B-values identical to those used in the phantom study were used (table 5.2).

For PDFF and $R2^*$ determination, a multislice spoiled multi gradient echo sequence was used. Data acquisition was performed with TR of 800 ms, two echo trains (12 echoes/train) with $TE_0 = 1.5$ and 2 ms ($\Delta TE = 0.5$ ms) acquired in two sequential acquisitions, 15° flip angle and 326 kHz bandwidth. The other acquisition parameters were: field of view = 0.45×0.35 (mm x mm),

acquisition matrix = 64 x 100, spatial resolution = 0.7 x 0.35 (mm x mm), slice thickness = 1.05 with 31 slices. Acquisition time was 2 min 40 s per TE.

5.2.4. Data processing

Data processing was performed with an in-house software (Matlab, (MathWorks, R2017a (version 9.2), Natick, MA) for the data and user interface and microsoft visual studio (Microsoft, Redmond, Washington, USA)-compiled C++ code running Immin (Forschungszentrum Juelich, Germany) for computation.

ADC measurements were calculated based on the standard Stejskal and Tanner diffusion signal attenuation equation [394]:

$$S = S_0 e^{-b \cdot \text{ADC}} \quad (44)$$

Where b is the b -value, S the signal at b value b , S_0 the signal at $b = 0$ and ADC the apparent diffusion coefficient. ADC was retrieved by linear regression of signal logs versus b -values (monoexponential fit).

Specifically for animal studies, the repetitions were examined separately. Repetitions were kept for averaging or discarded based on the visible amount of respiratory artifacts. For the vast majority of datasets, the three repetitions were averaged.

SNR at $b = 150 \text{ s/mm}^2$ were estimated with the standard deviation of the subtraction of the two available image averages as noise estimation to remove the effect of the surface coil sensitivity profile [367].

PDFF was measured the same way as in section "4.2.1. PDFF mapping - data processing".

5.2.1. Statistical analysis

Repeatability was estimated based on Bland-Altman statistical tests plotted in percentage (%) with coefficient of repeatability [197, 396] calculated the same way as in section (4.3.1.3.) with equation (19).

Table 5. 2: Acquisition parameters for the OGSE and the PGSE sequences for phantom and mouse NAFLD studies.

Parameters	Double-sine OGSE-EPI sequence		Trapezoidal OGSE-EPI sequence				PGSE
Repetition time (ms)	5000		2500				2500
Echo time (ms)	51.84		29.52				29.52
Bandwidth (kHz)	200		200				200
Field of view (mm x mm)	40 x 40		40 x 50 (phantom) 30 x 30 (animal)				40 x 50 (phantom) 30 x 30 (animal)
Acquisition matrix	96 x 64		96 x 64				96 x 64
Number of slices	5		9				9
Slice thickness (mm)	1.00		1.05				1.05
Spatial resolution (mm x mm)	0.42 x 0.63		0.42 x 0.78 (phantom) 0.31 x 0.47 (animal)				0.42 x 0.78 (phantom) 0.31 x 0.47 (animal)
diffusion encoding b values (s / mm ²)	100 Hz (1.94 μm)	150 Hz (1.58 μm)	130 Hz (2.4 μm)	170 Hz (2.1 μm)	230 Hz (1.8 μm)	250 Hz (1.7 μm)	47 Hz (9.47 μm)
	animal		phantom, animal	phantom only	phantom only	phantom, animal	phantom, animal
	0		0	0	0	0	0
	75		150	150	150	150	150
	113		300	300	300	300	300
	150		500	500	429	337	500
Number of diffusion encoding directions	3		2				1
Number of EPI shots	8		6				6
Number of averages	2		1				1
Number of repetitions	2		3				3
Scan time (without and with respiratory gating respectively)	1 min 20 s and 3 min 40 s / b-value / frequency		40 s and 120 s / b-value / frequency				3 min and 9 min 30 s / frequency

Univariate (Spearman rank correlations) and multivariate (multiple regression (stepwise)) statistical analysis were performed with MedCalc software version 19.4.1 (MedCalc Software Ltd, Ostend, Belgium). The diagnostic accuracy of the MRI parameters was assessed with ROC curve analysis. In these analyses, all mice included in the study were evaluated, regardless of their experimental groups.

To analyze the differences in ADC measurements between the CDA-HFD group (mice with NAFLD/NASH) and the 4 mice groups which had diet reversal, Mann-Whitney statistical tests were used.

5.2.2. Results

5.2.2.1. ADC behavior at multiple frequencies in samples with calibrated characteristic lengths

ADC measurements for each polystyrene latex microsphere size at each frequency are represented in table 5.3. Representative ADC maps are shown in figure 5.5. The ADC increased with microsphere size increase in most of the cases (Figure 5.6). Moreover, at each sample size, the ADC increased with frequency increase (Figure 5.7). The self-diffusion coefficient D_0 was measured at the laboratory temperature with a mixture of pure water and gadolinium for a T1 relaxation time equivalent to the T1 of a healthy mouse liver (~ 1180 ms) and was estimated to be $2.03 \times 10^{-3} \pm 6.34 \times 10^{-5}$ mm²/s.

Table 5. 3: ADC measurements(mean (standard deviation)) in mm²/s for the different tested bead sizes and frequencies

Frequency (Hz)	Bead size: 3µm	Bead size: 7µm	Bead size: 15µm	Bead size: 30µm	Bead size: 150µm
47	1.20x10 ⁻³ (5.82x10 ⁻⁵)	1.21x10 ⁻³ (4.38x10 ⁻⁵)	1.22x10 ⁻³ (4.30x10 ⁻⁵)	1.21x10 ⁻³ (4.35x10 ⁻⁵)	1.59x10 ⁻³ (3.58x10 ⁻⁵)
130	1.25x10 ⁻³ (5.49x10 ⁻⁵)	1.30x10 ⁻³ (5.42x10 ⁻⁵)	1.36x10 ⁻³ (6.84x10 ⁻⁵)	1.66x10 ⁻³ (6.74x10 ⁻⁵)	1.65x10 ⁻³ (5.41x10 ⁻⁵)
170	1.37x10 ⁻³ (3.90x10 ⁻⁵)	1.29x10 ⁻³ (3.72x10 ⁻⁵)	1.44x10 ⁻³ (3.62x10 ⁻⁵)	1.55x10 ⁻³ (0.10x10 ⁻⁵)	1.68x10 ⁻³ (4.17x10 ⁻⁵)
230	1.38x10 ⁻³ (5.94x10 ⁻⁵)	1.36x10 ⁻³ (0.11x10 ⁻⁵)	1.49x10 ⁻³ (6.62x10 ⁻⁵)	1.59x10 ⁻³ (0.12x10 ⁻⁵)	1.72x10 ⁻³ (4.01x10 ⁻⁵)
250	1.28x10 ⁻³ (7.00x10 ⁻⁵)	1.38x10 ⁻³ (8.62x10 ⁻⁵)	1.56x10 ⁻³ (6.21x10 ⁻⁵)	1.67x10 ⁻³ (7.17x10 ⁻⁵)	1.77x10 ⁻³ (5.26x10 ⁻⁵)

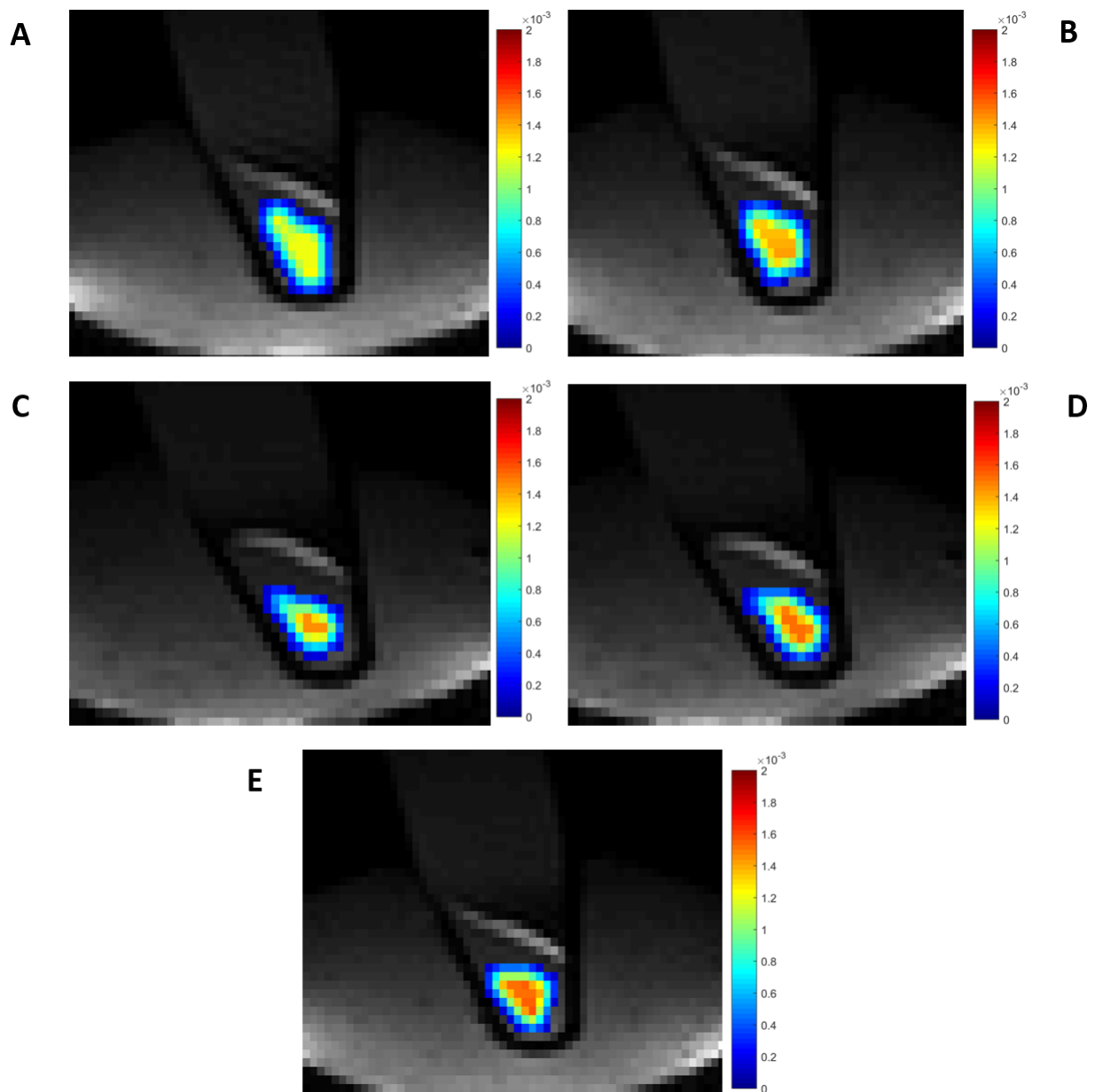
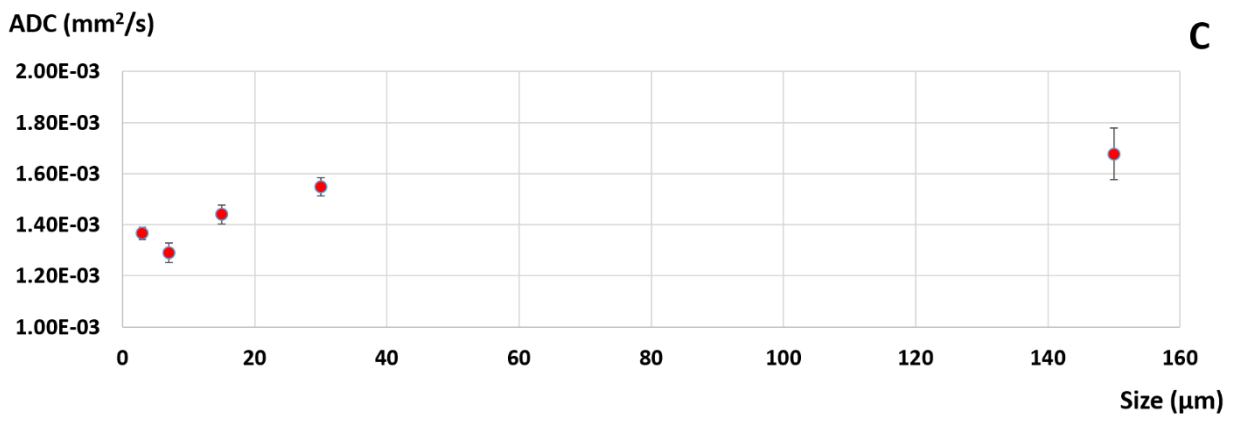
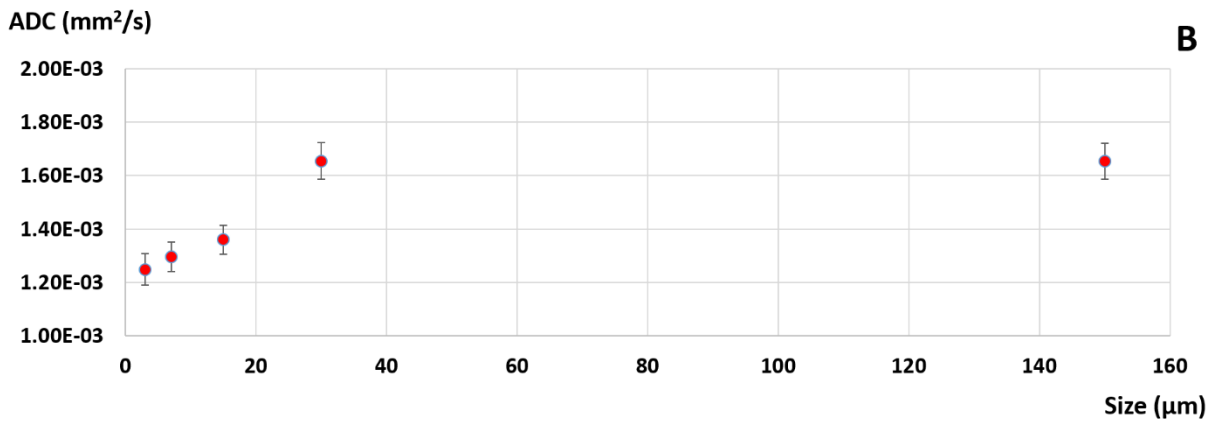
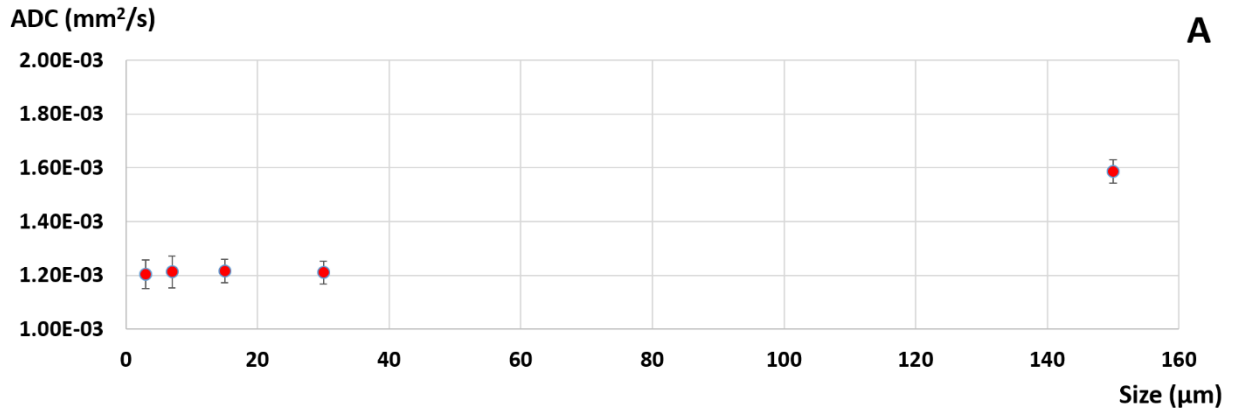


Figure 5. 5: Representative ADC maps (mm^2/s) measured in a sample of $15 \mu\text{m}$ at A) 47Hz, B) 130Hz, C) 170Hz, D) 230Hz and E) 250Hz



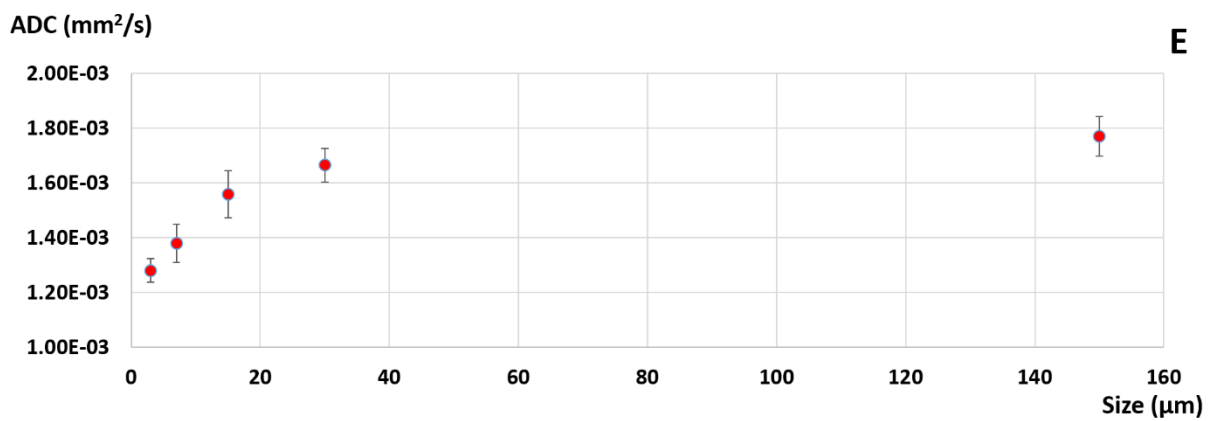
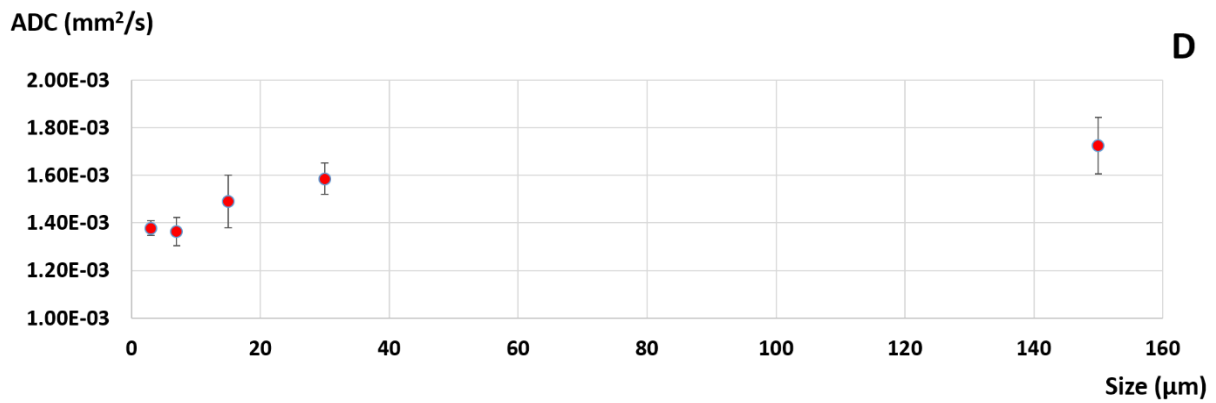
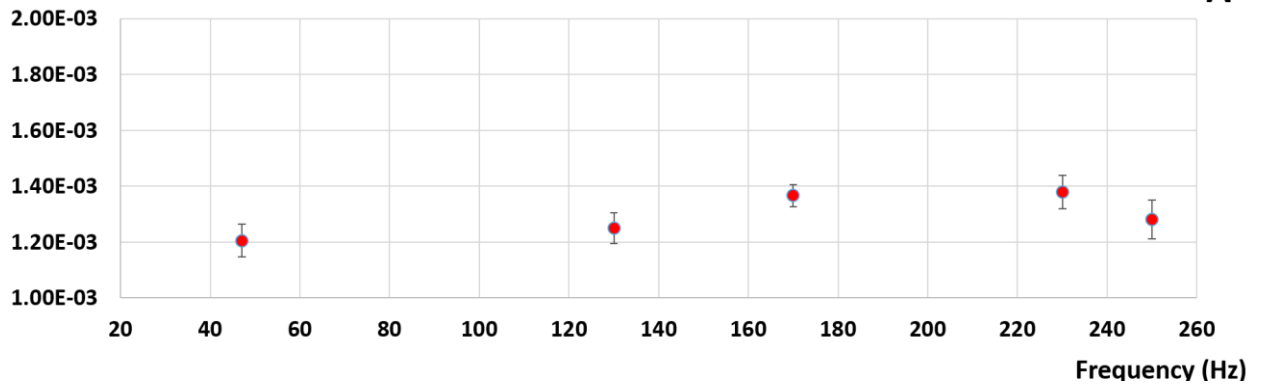
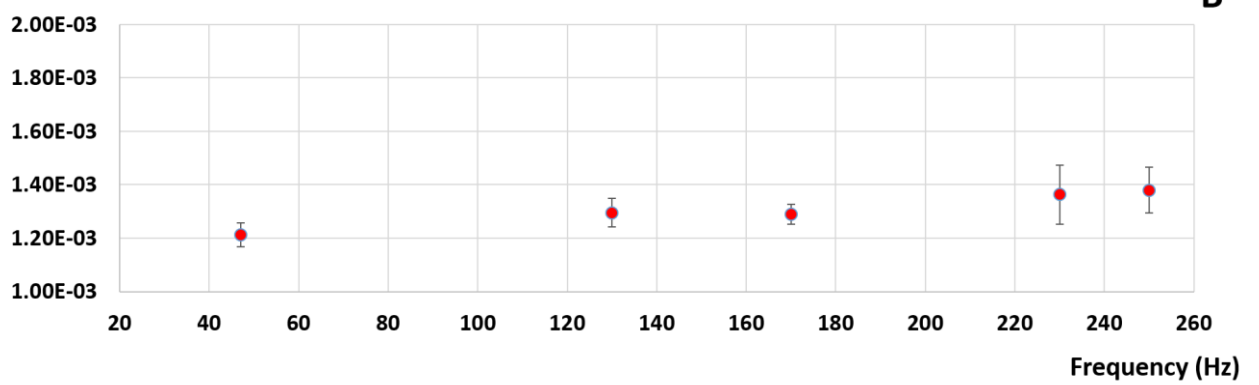


Figure 5. 6: Scatter plot of phantom ADC measurements (mm²/s) versus microsphere sizes (3, 7, 15, 30 and 150 µm) at A: 47Hz (PGSE sequence frequency), B: 130Hz, C: 170Hz, D: 230Hz and E: 250Hz (the four OGSE sequence frequencies). ADC increases with microsphere size increase

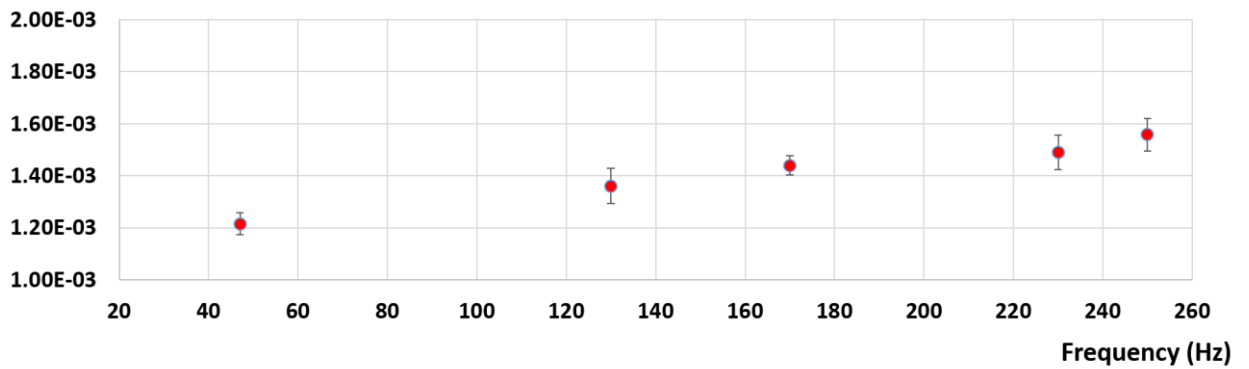
ADC (mm²/s)



ADC (mm²/s)



ADC (mm²/s)



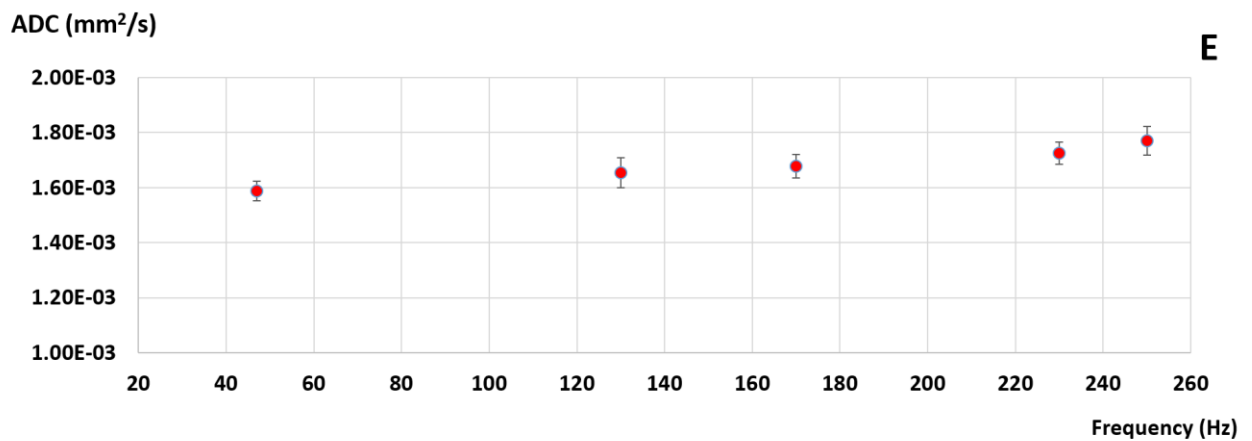
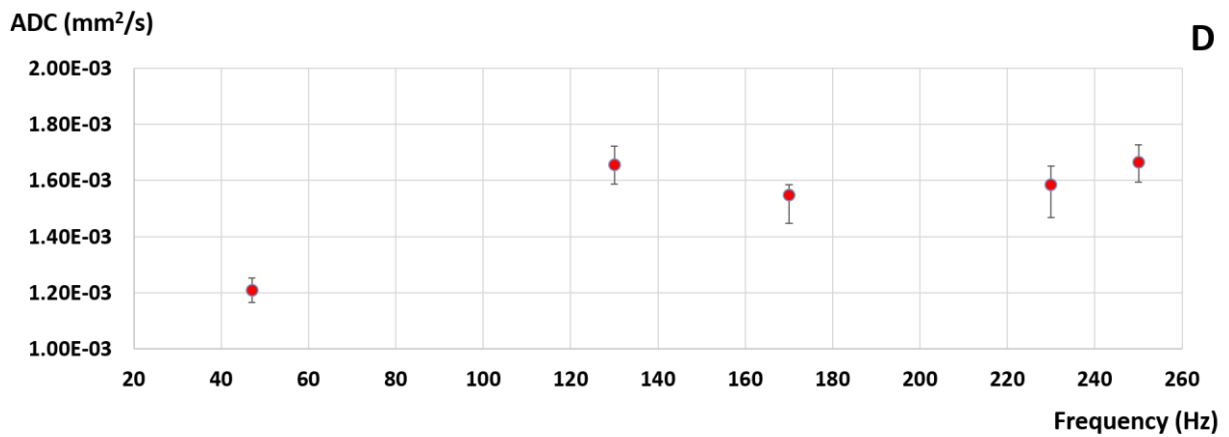


Figure 5. 7: Scatter plots of phantom-based ADC measurements (mm²/s) versus acquisition frequency (47 Hz (PGSE sequence frequency), 130 Hz, 170 Hz, 230 Hz and 250 Hz (the four OGSE sequence frequencies)) for each of the microsphere sizes; A: 3 µm, B: 7 µm, C: 15 µm, D: 30 µm and E: 150 µm. ADC measurements increase with frequency increase.

5.2.2.2. In vivo repeatability study

ADC as well as repeatability and SNR estimations are represented in Table 5.4. The ADC ranged from $0.78 \pm 0.49 \mu\text{m}^2/\text{ms}$ to $1.02 \pm 0.54 \mu\text{m}^2/\text{ms}$. Also, these coefficients were similar at 100 Hz and 150 Hz. The standard deviation of the ADC estimations were relatively high. However, standard deviation were lower with respiratory gating than without respiratory gating.

Moreover, our results showed that repeatability coefficients and SNR measurements were better (i.e smaller repeatability coefficient and higher SNR) with the 4-channel surface coil than with the volume coil in 7 of 8 tested combinations. Volume coil images had larger sensitivity area while surface coil images had higher signal magnitudes but the signal vanished with the distance to the surface coil elements (figure 5.8). Also, repeatability coefficient and SNR measurements were better with respiratory gating in 6 of 8 and 8 of 8 tested combinations respectively. Visually, respiratory gating had an important effect on image quality. The images acquired with respiratory gating had much less motion artifacts than the images acquired without respiratory gating (figure 5.8).

SNR was slightly higher at 150 Hz in 8 of 8 tested combinations, and ADC did not vary significantly between these two frequencies (figure 5.9). The optimal repeatability coefficient was 28% obtained with the 4-channel surface coil and respiratory gating when measuring ADC at 100 Hz while the best SNR value was measured with the same conditions but at 150 Hz.

Table 5. 4: ADCs, repeatability, and SNR according to the different conditions used in our study.

Coil	Respiratory gating	Frequency (Hz)	ADC ($\mu\text{m}^2/\text{ms}$) Mean $\times 10^{-3} \pm \text{SD} \times 10^{-3}$	Repeatability coefficient (%)	SNR (n = 5) Mean $\pm \text{SD}$
Volume coil	Without respiratory gating	100	0.85 \pm 0.50	126%	7 \pm 1.3
		150	0.90 \pm 0.57	80 %	9 \pm 3.4
	With respiratory gating	100	0.95 \pm 0.50	142 %	11 \pm 2.2
		150	0.96 \pm 0.53	66%	11 \pm 2.0
4-channel surface coil	Without respiratory gating	100	0.88 \pm 0.52	119 %	8 \pm 2.4
		150	1.06 \pm 0.46	143 %	12 \pm 2.4
	With respiratory gating	100	1.04 \pm 0.48	32 %	14 \pm 3.1
		150	0.82 \pm 0.38	44 %	18 \pm 6.6

Note: In bold, the optimal repeatability coefficient and SNR value

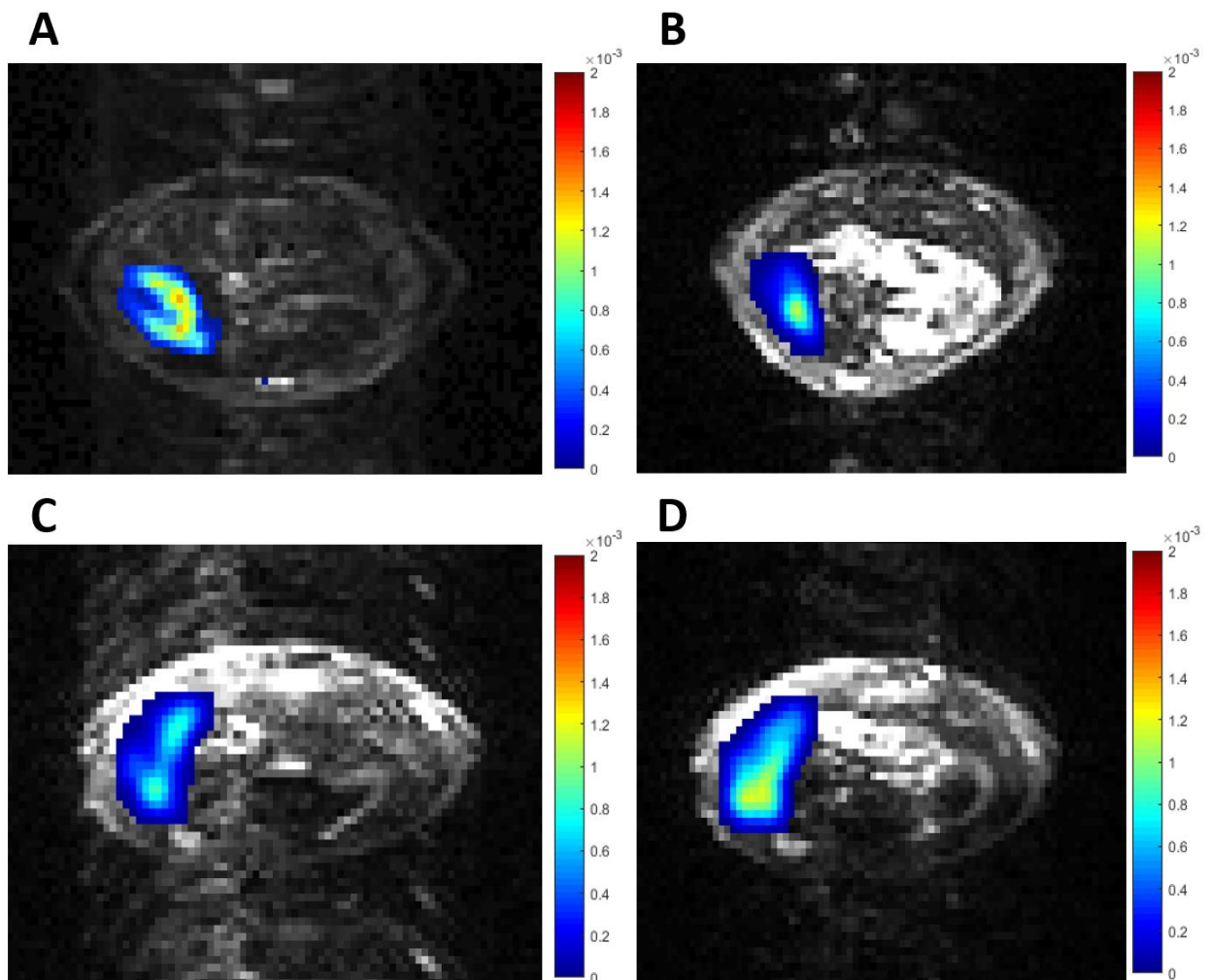


Figure 5. 8: ADC maps at 100Hz, superimposed on magnitude images at $b\text{-value} = 0 \text{ s/mm}^2$. A) with volume coil, without respiratory gating, B) with volume coil and respiratory gating, C) with 4-channel parallel coil, without respiratory gating, D) with 4-channel parallel coil and respiratory gating. Volume coil images had more homogeneous sensitivity area but with lower overall signal, while surface coil images had higher signal magnitude but with spatial modulation according to the distance to the coil elements. Respiratory gating visually reduces signal artifacts.

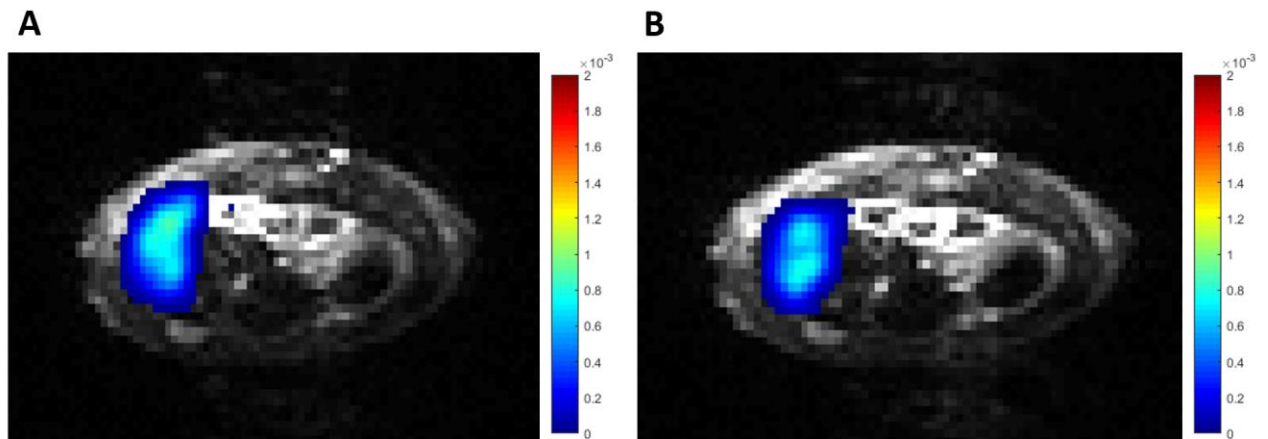


Figure 5. 9: ADC maps with 4-channel surface coil and respiratory gating at A) 100 Hz and B) 150Hz. Maps are superimposed on magnitude images at $b\text{-value} = 0 \text{ s/mm}^2$.

5.2.2.3. Sequence application in mouse models of NAFLD

Histological results

Among the 132 mice enrolled in this study, 14 and 13 mice were excluded for the 130 Hz and 250 Hz OGSE-EPI acquisitions respectively (8 ND mice were excluded from MRI scanning because of lack of time and the others were erroneously scanned without respiratory gating and with different b -values). Moreover, 45 mice were excluded for the 47Hz PGSE acquisitions because of motion artifacts. The final number of mice included in the study and the mean values of ADC measurements per group for each frequency are summarized in tables 5.5 and 5.6 respectively. Representative ADC maps and histologic images are shown in figure 5.10 and 5.11.

In the diseased mice group (without diet reversal) of 48 mice, NAFLD was observed in 42 mice among which 15 (36%) had NASH.

After exclusion because PGSE imaging failure, the diseased mice group included 28 animals, of which 26 had NAFLD (15 NAFL and 11 NASH), while after exclusion because of OGSE imaging failure, the diseased mice group included 45 animals, of which 40 had NAFLD (28 NAFL and 12 NASH).

For the mice that underwent diet reversal (n = 48), 34 did not have steatosis nor ballooning but still had some inflammation and/or fibrosis, while 14 had NAFLD; 11 had NAFL (steatosis and inflammation, with stage 2 fibrosis) and 3 had NASH (ballooning stage 1). After exclusion because of PGSE imaging failure, this diet reversal mice group yielded a cohort of 40 animals, of which 27 mice did not have nor ballooning but still had some inflammation and/or fibrosis and 13 had NAFLD (11 had NAFL and 3 had NASH). For the OGSE sequence, no mice were excluded in the diet reversal group. Of the 48 mice included in this group, 34 had no steatosis nor ballooning but some inflammation and/or fibrosis and 14 had NAFLD (11 had NAFL and 3 had NASH).

Histological features grades for the CDA-HFD 10w group versus the 4 diet reversal groups for both PGSE and OGSE cohorts are represented in figure 5.12 and 5.13.

Relationship between histological features

Fibrosis was highly correlated with inflammation (Spearman's rank correlation coefficient $r = 0.77$, significance level $p < 0.0001$) and moderately correlated with hepatocyte ballooning ($r = 0.38$, $p < 0.0001$) but was not correlated with steatosis ($r = 0.03$, $p = 0.79$). Hepatocyte ballooning had moderate correlation with inflammation ($r = 0.45$, $p < 0.0001$) and steatosis ($r = 0.49$, $p < 0.0001$). Similarly, inflammation and steatosis had moderate correlation ($r = 0.33$, $p = 0.0003$).

Diet reversal mice presented with lesser steatosis and showed evidence of regressing inflammation grade. Diet reversal did drastically decrease the proportion of mice with ballooning. The effect of diet reversal on fibrosis evolution was less marked, most mice in the reversal groups still having stage 2 fibrosis, although none of them had stage 3 fibrosis that was observed in the diseased groups.

Table 5. 5: Mice groups included in this study

Mice groups included in the study		Mice number		
		47 Hz	130 Hz	250 Hz
ND	ND 10 w	8	10	10
	ND 14 w	5	7	8
	ND 18 w	6	8	8
NAFLD diet induction	HFD 10 w	4	10	10
	HFD 14 w	5	12	12
	HFD 18 w	9	12	12
	CDA-HFD 10 w	10	11	11
Diet reversal	CDA-HFD 10w + ND 4w	9	12	12
	CDA-HFD 10w + ND 8w	10	12	12
	CDA-HFD 10w + HFD 4w	10	12	12
	CDA-HFD 10w + HFD 8w	11	12	12
Total mice number	ND	19	25	26
	NAFLD diet induction	28	45	45
	Diet reversal cohort	40	48	48

Relationship between MRI parameters

ADC at 47 Hz had modest correlation with ADC at 130 Hz ($r = 0.30$, $p = 0.005$) and ADC at 250 Hz ($r = 0.31$, $p = 0.004$). ADC measurements at 130 Hz and 250 Hz were moderately correlated ($r = 0.56$, $p < 0.0001$). Moreover, PDFF had elevated correlation with ADC measurements at 130 Hz ($r = -0.67$, $p < 0.0001$) and moderate correlation with ADC at 250 Hz ($r = -0.51$, $p < 0.0001$) but was not correlated with ADC at 47 Hz ($r = -0.17$, $p = 0.11$).

Table 5. 6: Mean ADC according to frequency and diet

Groups		ADC : mean \pm SD ($\times 10^{-3}$ mm ² /s)		
		47 Hz	130 Hz	250 Hz
Control group	ND 10w	0.69 \pm 0.06	0.97 \pm 0.08	1.13 \pm 0.20
	ND 14w	0.70 \pm 0.20	1.05 \pm 0.19	1.14 \pm 0.16
	ND 18w	1.04 \pm 0.21	1.09 \pm 0.10	1.18 \pm 0.13
NAFLD diet induction	HFD 10w	0.67 \pm 0.19	0.82 \pm 0.19	0.93 \pm 0.24
	HFD 14w	0.69 \pm 0.37	0.78 \pm 0.29	0.90 \pm 0.21
	HFD 18w	0.81 \pm 0.21	0.73 \pm 0.26	0.84 \pm 0.23
	CDA-HFD 10w	0.74 \pm 0.13	0.68 \pm 0.04	0.98 \pm 0.13
Diet reversal	CDA-HFD 10w + ND 4w	0.87 \pm 0.21	0.97 \pm 0.19	1.16 \pm 0.15
	CDA-HFD 10w + ND 8w	1.03 \pm 0.10	1.10 \pm 0.07	1.14 \pm 0.14
	CDA-HFD 10w + HFD 4w	0.97 \pm 0.26	0.99 \pm 0.14	1.12 \pm 0.19
	CDA-HFD 10w + HFD 8w	0.95 \pm 0.24	1.09 \pm 0.17	1.10 \pm 0.22

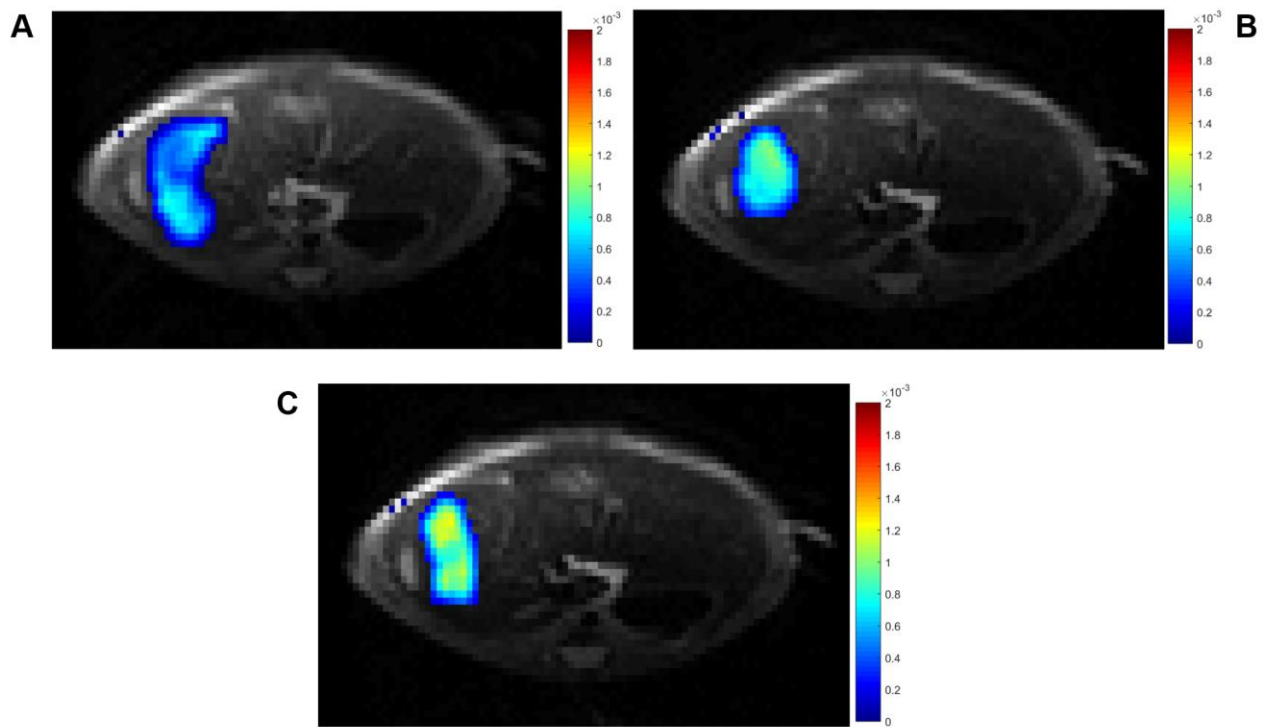


Figure 5. 10: ADC maps measured at A) 47 Hz ($ADC = 0.62 \pm 0.20 \times 10^{-3} \text{ mm}^2/\text{s}$), B) 130 Hz ($ADC = 0.70 \pm 0.24 \times 10^{-3} \text{ mm}^2/\text{s}$) and C) 250 Hz ($ADC = 0.95 \pm 0.29 \times 10^{-3} \text{ mm}^2/\text{s}$) in “CDA-HFD 10w” mouse with inflammation grade 3, steatosis grade 3, ballooning grade 1 and fibrosis stage 3.

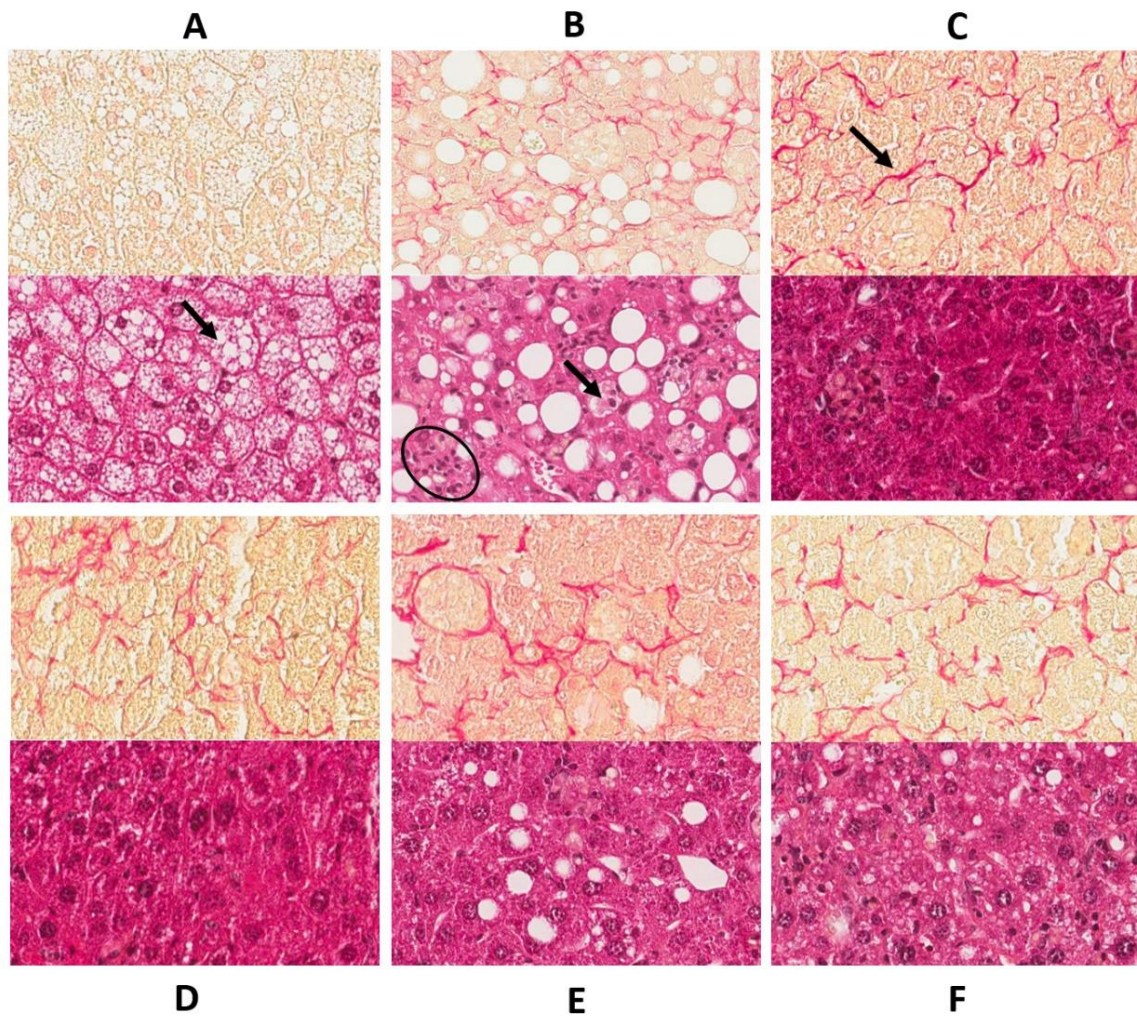


Figure 5. 11: Histological sections (upper row: picrosirius red stained slices; second row: hematoxylin-eosin stained slices). From the NAFLD induction groups: (A) Mouse with NAFL (HFD 14w group): fibrosis stage 0, steatosis grade 3 (arrow), and lobular inflammation and hepatocellular ballooning grade 0. (B) Mouse with NASH (CDA-HFD 10w group): fibrosis stage 3, inflammation (circle) and steatosis grade 3, and hepatocyte ballooning (arrow) grade 1. From the diet reversal groups: (C) Mouse of the group “CDA-HFD 10w + ND 4w”: fibrosis (arrow) stage 2, steatosis and ballooning grade 0, inflammation grade 1. (D) Mouse of the group “CDA-HFD 10w + ND 8w”: fibrosis stage 2, steatosis and inflammation and ballooning grade 0. (E) Mouse of the group “CDA-HFD 10w + HFD 4w”: fibrosis stage 2, steatosis grade 1, inflammation grade 1 and ballooning grade 0. (F) Mouse of the group “CDA-HFD 10w + HFD 8w”: fibrosis stage 2, steatosis and ballooning grade 0 and inflammation grade 2.

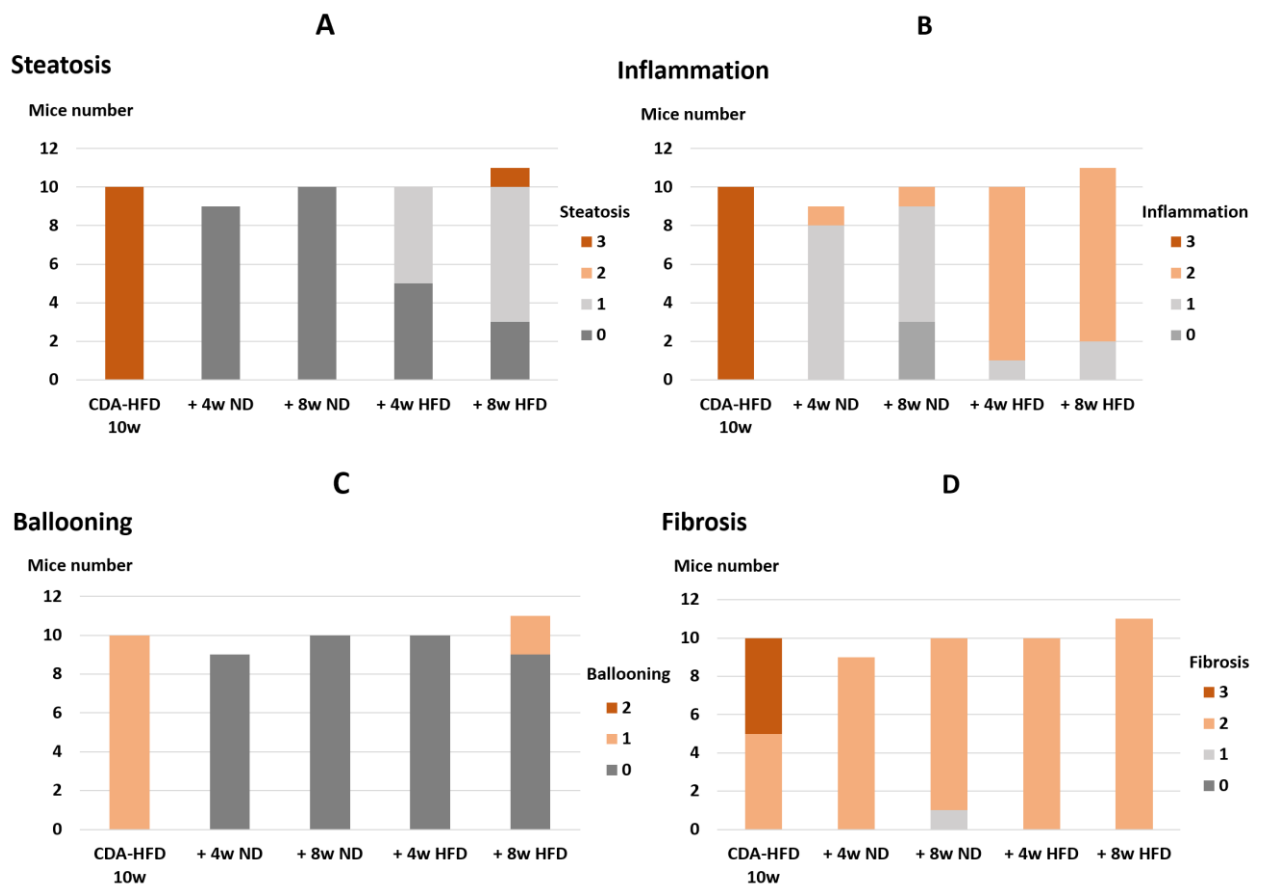


Figure 5. 12: (A) Steatosis, (B) inflammation, (C) hepatocyte ballooning grades and (D) fibrosis stages in the CDA-HFD 10w group (n = 10) vs. the 4 diet reversal groups: CDA-HFD 10w followed by 4 weeks of ND (“+ 4w ND”, n = 9), CDA-HFD 10w followed by 8 weeks of ND (“+ 8w ND”, n = 10), CDA-HFD 10w followed by 4 weeks of HFD (“+ 4w HFD”, n = 10) and CDA-HFD 10w followed by 8 weeks of HFD (“+ 8w HFD”, n = 11) for the 47 Hz-PGSE mice cohort.

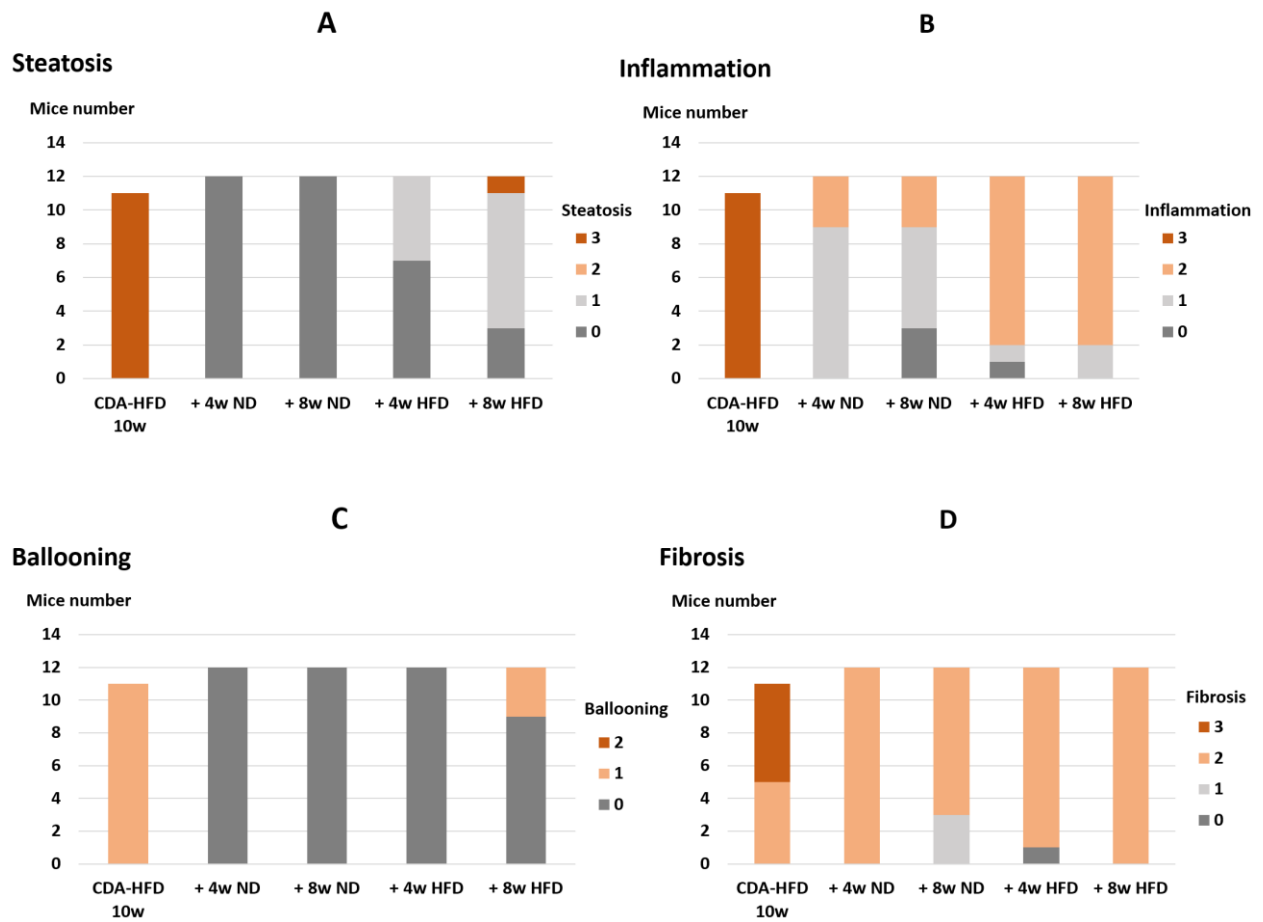


Figure 5. 13: (A) Steatosis, (B) inflammation, (C) hepatocyte ballooning grades and (D) fibrosis stages in the CDA-HFD 10w group (n = 11) vs. the 4 diet reversal groups: CDA-HFD 10w followed by 4 weeks of ND (“+ 4w ND”, n = 12), CDA-HFD 10w followed by 8 weeks of ND (“+ 8w ND”, n = 12), CDA-HFD 10w followed by 4 weeks of HFD (“+ 4w HFD”, n = 12) and CDA-HFD 10w followed by 8 weeks of HFD (“+ 8w HFD”, n = 12) for the OGSE mice cohort.

MRI measurements versus histological features

Univariate analysis of MRI parameters versus histological features showed that fibrosis was only correlated with ADC at 47 Hz ($r = 0.26$, $p = 0.02$) (Table 5.7). Ballooning and inflammation were only correlated to ADC at the intermediate frequency of 130 Hz ($r = -0.35$, $p = 0.0001$ and $r = -0.28$, $p = 0.0001$ respectively). Steatosis was correlated with the ADC at the intermediate (130 Hz) and high (250 Hz) frequencies only ($r = -0.73$, $p < 0.0001$ and $r = -0.59$, $p < 0.0001$ respectively). PDFF was highly correlated with steatosis ($r = -0.86$, $p < 0.0001$) and moderately correlated with ballooning and inflammation ($r = 0.36$, $p = 0.0001$ and $r = 0.26$, $p = 0.005$ respectively).

Multivariate analysis showed that at 47 Hz, ADC was influenced by fibrosis ($r_{\text{partial}} = 0.30$, $p = 0.005$) but also to a lesser degree by steatosis ($r_{\text{partial}} = -0.26$, $p = 0.02$). At 130 Hz, they were influenced by steatosis only ($r_{\text{partial}} = -0.72$, $p < 0.0001$). At 250 Hz, they were influenced by steatosis ($r_{\text{partial}} = -0.59$, $p < 0.0001$) and to a lesser degree by fibrosis ($r_{\text{partial}} = -0.25$, $p = 0.006$).

Table 5. 7: Spearman rank correlations between MRI parameters and histological features of NAFLD.

Spearman rank correlations	Steatosis		Inflammation		Ballooning		Fibrosis	
	r	p	r	p	r	p	r	p
ADC at 47Hz	-0.18	0.09	0.09	0.39	-0.12	0.28	0.26	0.02
ADC at 130Hz	-0.73	< 0.0001	-0.28	0.002	-0.35	0.0001	-0.04	0.71
ADC at 250Hz	-0.59	< 0.0001	-0.06	0.50	-0.14	0.13	0.17	0.06
PDFF	0.86	< 0.0001	0.26	0.005	0.36	0.0001	-0.06	0.53

Note: In gray, statistically non-significant results

Diagnostic performance of MRI parameters

ROC curve analysis showed that ADC measurements at 250 Hz had good diagnostic accuracy in differentiating between NASH and NAFL with AUC of 0.71 (significance level $p = 0.003$ and 95% CI = [0.57 – 0.82]), while ADC measurements at 130 Hz and 47 Hz had poor diagnostic performance with AUC of 0.59 ($p = 0.27$ and 95% CI = [0.45 – 0.72]) and 0.54 ($p = 0.65$ and 95% CI = [0.38 – 0.70]). PDFF had poor diagnostic performance with AUC of 0.53 ($p = 0.76$ and 95% CI = [0.38 – 0.66]).

Comparison of ADC without / with diet reversal

ADCs at 47Hz (Figure 5.14 A) were significantly higher only in the group of mice fed CDA-HFD for 10 weeks followed by 8 weeks of ND (CDA-HFD 10w + ND 4w) and in the group of mice fed CDA-HFD for 10 weeks followed by 4 weeks of HFD (CDA-HFD 10w + HFD 4w) compared to the mice fed CDA-HFD for 10 weeks ($p = 0.0002$ and $p = 0.03$ respectively). At 130 Hz (Figure 5.14 B), ADCs were significant higher in all the 4 groups of diet reversal when compared to the “CDA-HFD 10w” group with the highest difference observed between this group and the “CDA-HFD 10w + ND 8w” ($p < 0.0001$). At 250 Hz (Figure 5.14 C), ADC measurements were significantly higher in the “CDA-HFD 10w + ND 4w” and the “CDA-HFD 10w + ND 8w” groups compared to the “CDA-HFD + 10w” group ($p = 0.006$ and $p = 0.01$ respectively).

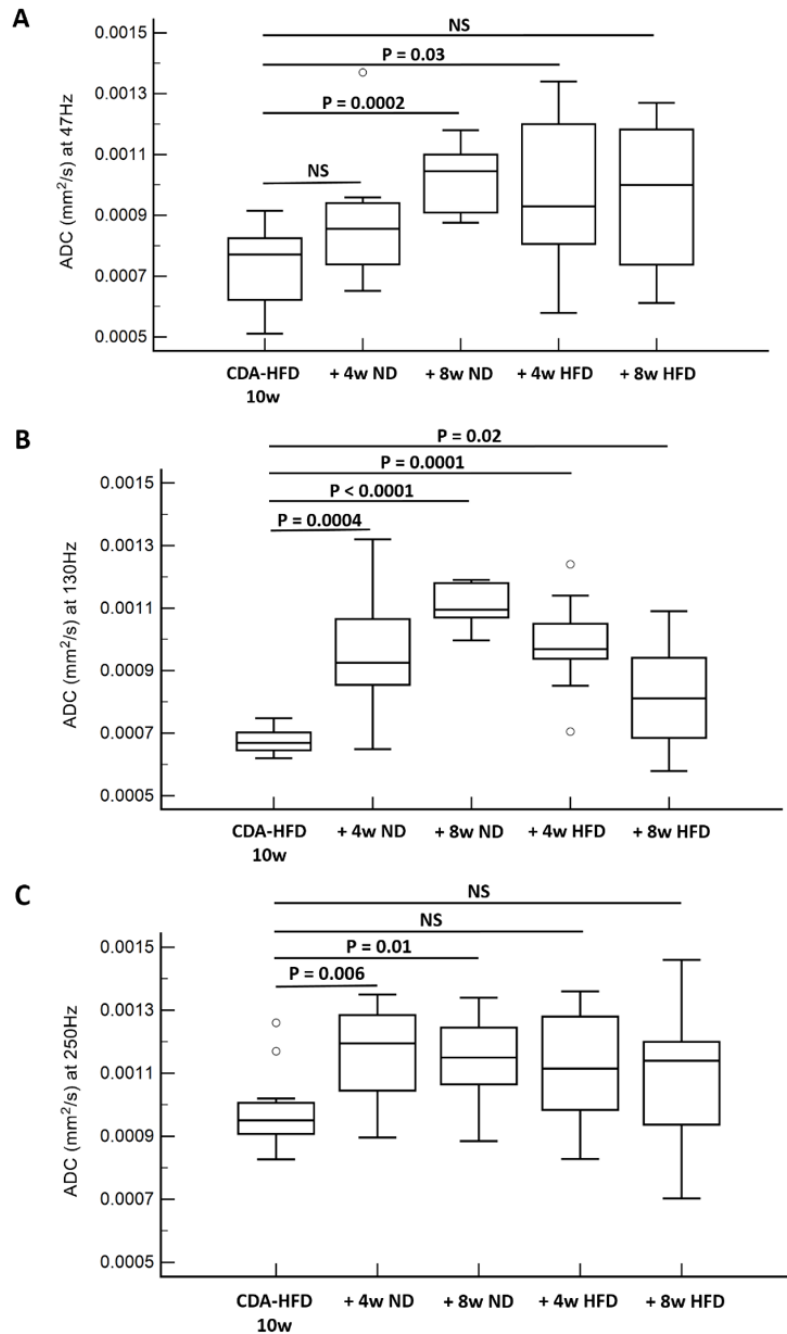


Figure 5. 14: Box plots of ADC measurements in the “CDA-HFD 10w” group compared to the ADCs of the 4 diet reversal groups at A) 47 Hz, B) 130 Hz and C) 250 Hz. “+ 4w ND”: CDA-HFD 10w followed by 4 weeks of ND, “+ 8w ND”: CDA-HFD 10w followed by 8 weeks of ND, “+ 4w HFD”: CDA-HFD 10w followed by 4 weeks of HFD and “+ 8w HFD”: CDA-HFD 10w followed by 8 weeks of HFD. P values refer to the results of the Mann-Whitney tests between the diseased group and the different diet reversal groups. NS: non-significant.

5.2.3. Discussion

A TDS technique was implemented with an OGSE-EPI sequence with double-sinusoid and trapezoidal encoding gradient waveforms. The aim was to implement an OGSE-EPI sequence for studying the changes in ADC measurements in mice liver with NAFLD.

A validation study was performed in phantoms of microspheres of polystyrene at multiple sizes as was done by Parsons E. C. et al., [329] to explore the changes in ADC values in restricted systems of different sizes. The results of our validation study showed that the ADC increased with the increase of the microsphere size which corresponds to an increase in the space (i.e. spatial scale) in which the water molecules can move. This result is in accordance with the previously reported findings [329]. This result also agrees with the OGSE-diffusion imaging theory that states that ADC increases according spatial scale increase up to the boundary value of the self-diffusion coefficient (the diffusion coefficient measured at the same temperature in the fluid under consideration in the absence of barriers) [327-329]. The self-diffusion coefficient in our study was estimated to be $2 \times 10^{-3} \text{ mm}^2/\text{s}$ which is similar to the estimation of $2.06 \times 10^{-3} \text{ mm}^2/\text{s}$ done by Parsons E. C. et al. [329]. Moreover, our results showed that, at each sample size, the ADC increased according to frequency. This also is consistent with the theory of OGSE-TDS imaging [329] indicating that the effective diffusion time and thus also the observed spatial scale are smaller at higher frequency. ADC behavior was not perfectly monotonous, particularly for the beads of $3 \mu\text{m}$ and $7 \mu\text{m}$, and at 170Hz and 230Hz. Moreover, ADC of the $30 \mu\text{m}$ beads at 130 Hz was unexpectedly similar to the one at 250 Hz.

Our results could have been more eloquent if more bead sizes had been used. Unfortunately, we were limited by the available bead size samples provided by the manufacturer. Other bead sizes, particularly between $30 \mu\text{m}$ and $150 \mu\text{m}$ should be added to provide better understanding of the ADC behavior. Also, investigating ADC at more frequencies may allow for better sampling and may provide more reliable information on ADC changes with frequency.

Moreover, in our study the self-diffusion coefficient was only approached but not reached even at the smallest spatial scale (i.e. highest OGSE frequency) and at the highest bead size.

This could be explained by the fact that the diffusion mechanism was observed in the pores between the polystyrene beads which were smaller than the bead size. The results presented in this study were only descriptive. The development of a fitting model [397, 398] for objective interpretation of frequency/time dependent ADC measurement changes with objective biophysical parameters is ongoing. Future directions will attempt to clarify if the frequency dispersion of ADC is best described in NAFLD regression models by the short time regime characterized by $\omega^{-3/2}$ dependency and tortuosity-limited ADC at low frequency (D_∞), or by the short time regime characterized by $-\omega^{-1/2}$ dependency and asymptotically limited diffusion at high frequencies (D_0) [399].

In the living mouse liver, the repeatability of the sequence was improved by increasing the image SNR with a 4-channel surface coil. Despite the slight TR variability introduced by respiratory gating, we obtained better repeatability with respiratory gating than without gating, where the TR is strictly defined by the MRI sequence, but where physiologic respiratory motion perturbs the acquisitions. No marked differences in repeatability were found with respect to frequency. The SNRs were similar at 100 Hz and at 150 Hz, which is to be expected since for a given b-value, the factors driving the SNR (echo time, repetition time, voxel volume, bandwidth) were all kept constant. Of note, SNR was slightly but systematically higher at 150 Hz. The diffusion coefficients were similar at 100 Hz and 150 Hz where the effective diffusion times and characteristic diffusion lengths were approximately 0.98 ms / 1.98 μm and 0.63 ms / 1.59 μm respectively. This might be explained by the fact that the magnitude of the frequency dispersion of ADC was not sufficiently resolved by these two relatively similar frequencies considering the variance of the ADC measurement. Therefore, interrogating the frequency dispersion over a larger range of frequencies or improving measurement variance should be pursued to obtain measurable differences between the diffusion coefficients. In subsequent acquisitions in phantoms and in small animals, higher frequencies were included in the acquisition protocol.

With the hardware constraints available at the time of the experiments, our results were limited by the combination of desired b-values and frequencies, yielding an echo time of 52 ms. In Jiang and al. [389], a similar sequence with respiratory gating was proposed and yielded good results despite a higher TE (70 ms). Furthermore, our work was performed in a group of

5 healthy mice only. Better repeatability and SNR estimations might be obtained with a larger mice group.

Our study suggests that the OGSE sequence with EPI readout and double-sine encoding gradient waveform is usable at 7T in vivo in mice. High frequencies and b-values could be achieved with a stronger hardware. Among the acquisition conditions, 4-channel parallel coil, respiratory gating and 4 b-values enabled to optimize the repeatability of the measurement.

Furthermore, our OGSE-EPI sequence was used to study the ADC changes according to the histopathological alterations in NAFLD mouse models. OGSE-EPI with trapezoidal encoding gradient waveform was recently used to evaluate mean cell size in human breast tumors in silico, in animal models, and in breast cancer patients [388], to assess mean cell size and cellularity in vivo in three types of human colon cancers [400], to diagnose malignant head and neck tumors in phantoms and in patients [342] and to quantify hepatocyte size in vivo in human healthy subjects [332]. To the best of our knowledge, this is the first study to apply this technique to explore ADC changes in vivo in mice with NAFLD. In this study, we combined a PGSE frequency with 2 OGSE frequencies to obtain ADC at longer and shorter effective diffusion times and ensure the observation at larger and smaller spatial scales.

The results of this preclinical study suggest that ADC was mainly affected by steatosis at 250 Hz (small spatial scale), by steatosis but also hepatocyte ballooning and inflammation at 130 Hz (intermediate scale), and mainly by fibrosis at 47 Hz. Steatosis and hepatocyte ballooning may change the intracellular diffusion and cell size, whereas fibrosis concerns large-scale networks of fibers spanning multicellular assemblies. The results we observed could be the consequence of higher frequencies showing more marked sensitivity to small spatial scale features, and decreasing the frequency introduces a sensitivity to progressively larger features.

Steatosis has been reported to influence conventional ADC measurements. In a study performed by Manning P. et al. [401] on sixty four children with NAFLD, ADC decreased with the increase in hepatic steatosis as evaluated by histology. In a study we performed in phantoms and patients with hepatic steatosis [402], conventional ADC also decreased with the increase in histological grades of steatosis. This estimation was higher with fat

suppression. Our acquisitions were performed with fat suppression, but the effect of steatosis still showed a strong effect on our ADC measurements. The non-monotonous influence of inflammation with respect to probed spatial scale (absence of correlation at the small and large spatial scales, but correlation at the intermediate spatial scale), remains to be understood. The presence of multiple inflammatory cells may be one factor limiting the diffusion at intermediate scales.

The diagnostic performance analysis showed that only ADC measurements at small spatial scale (250 Hz) had significant moderate performance for distinguishing between NASH and NAFL. The only histopathological factor that differentiates NASH from NAFL is hepatocyte ballooning. This suggests that hepatocyte ballooning may affect ADC measurements even at small spatial scales, although this effect may be partially masked by the accompanying lipid accumulation. Further studies will evaluate whether mice that are matched for steatosis levels but have varying degrees of ballooning, do differ in their ADC frequency behavior.

Moreover, diet reversal as therapy for NAFLD/NASH increased ADC measurements. The only histopathological feature that almost completely disappeared with diet reversal, particularly when adopting a normal diet, was steatosis. Hepatocyte ballooning and inflammation also decreased with diet reversal but did not completely disappear. Fibrosis did not decrease much even after 8 weeks of normal diet. Longer periods of diet reversal are needed to reverse inflammation, hepatocyte ballooning and particularly fibrosis.

In this study, the intravoxel incoherent motion (IVIM) effects were not taken into consideration because we wanted to simplify our analysis by focusing on the ADC behavior. Future investigations will include evaluating the IVIM effect on the ADC measurements obtained by PGSE and OGSE methods.

PDFF measurements had the highest correlation coefficient with steatosis. Here again, our results confirm that PDFF is the best MRI biomarker of steatosis.

In conclusion, in this study we implemented, validated [403] and improved TDS by implementing trapezoid-modulated encoding gradient waveforms on a 7T preclinical scanner. TDS might be a promising tool for detecting hepatocellular ballooning at specific spatial scales (i.e. frequencies) with additional fat suppression tools, and therefore, for diagnosing NASH. A

study in phantoms was conducted to validate TDS and agreed with the expected behaviors for ADC in function of frequency and spatial scale. However, the diffusion coefficient in free water was only approached but not reached even at the lowest time scale and at the highest bead size. In a mouse model with high clinical relevance, despite a measurable effect of steatosis on ADC, the method shows promise for NASH diagnosis through an effect mediated by hepatocyte ballooning. TDS also enabled us to detect changes occurring during therapy, which might be of interest for pharmaceutical applications. Furthermore, the ADC was shown to vary with probed spatial scale in the liver. Further understanding of the relations between histologic features at various scales in diseased tissue and their frequency-selective ADCs should come from future iterations of the research that was initiated here.

6. Discussion and perspectives

6.1. Discussion

In this PhD project, multiple MRI-based quantitative markers including MRE derived mechanical parameters, PDFF measurements, T1 relaxation times, and ADCs were investigated as potential biomarkers of NAFLD, its histopathologic features and its progressive forms in vivo using mouse models of the disease with histologic analysis as the standard reference.

Animal models have a role in understanding the pathophysiology of NAFLD and are important for developing novel diagnostic and therapeutic approaches. Over the last decades, many animal models of NAFLD have been proposed. So far, no current model can fully replicate all the features associated with the disease. Hence, enrolling more than one model in a NAFLD study could be useful to include different variations of the disease along different progression paths. In our study of mouse models of NAFLD, we investigated the reproducibility and efficacy of two models, the Western diet combined with weekly injections of low doses of CCl₄ (WD+CCl₄) and the choline deficient L-amino acid - high fat diet (CDA-HFD) mice models. Our results with the WD+CCl₄ model, which has histopathological and metabolic features close to human NAFLD, did not fully duplicate the results from the literature, even after improving the study factors. These factors included starting diet feeding at an early age (4 weeks), increasing the induction duration (16 weeks), regular monitoring of the animals and improving animal housing conditions.

The CDA-HFD model appeared more reproducible and efficacious because stages of NAFLD with advanced fibrosis could be obtained. More studies should be conducted to establish an effective reproducible animal model that closely mimics human NAFLD/NASH with all the histopathologic and metabolic features. Among the three mouse models of NAFLD in this work, the HFD should be considered when investigating hepatic steatosis is the main focus, whereas when studying NAFLD with significant inflammation and fibrosis, the CDA-HFD mouse model should be used.

When investigating the value of MRE derived parameters as biomarkers of NAFLD, we observed that these parameters were mainly affected by fibrosis and had better performance in diagnosing progressive forms of NAFLD associated with significant fibrosis (i.e. significant MLD, NASH-related fibrosis and fibro-NASH) rather than diagnosing NASH.

Stiffness increase is known to be correlated with fibrosis, as observed in our study. However, we also observed that the viscosity related loss modulus was the parameter with the best association with fibrosis. This might be partially explained by the fact that fibrosis and inflammation were highly correlated. Moreover, the CDA-HFD mouse model induces rapid inflammatory fibrogenesis which might have affected the viscosity related parameters. The accelerated development of fibrosis in mouse models may differ from the course of chronic fibrogenesis observed in humans. Therefore, the value of the mechanical parameters for assessing NAFLD severity should be further studied in humans.

In our MRE study, none of the mechanical parameters was correlated with hepatocyte ballooning showing that MRE had poor performance in detecting this important histologic feature of NASH. This might be explained by at least two reasons. First, hepatocyte ballooning might cause limited viscoelastic changes. This hypothesis should be further explored with cell rheometry. Second, hepatocyte ballooning is difficult to diagnose with histopathology. This second factor is well known and poor interrater reliability of ballooning grading has been reported in patients [404-406]. Moreover, hepatocyte ballooning is even more difficult to diagnose in small animal NAFLD models than in humans [346].

MRI-PDFF has been proposed as non-invasive method for assessing steatosis in the liver. Several studies have shown the high performance of this parameter. Our results of PDFF measurements have confirmed that this method has excellent performance in detecting and grading hepatic steatosis. Moreover, a standardized ROI positioning protocol improved the reproducibility of our measurements.

Liver T1 relaxation times have been reported to increase with the increase of inflammation and fibrosis. Our measurements of T1 were influenced by hepatic inflammation and fibrosis. However, this influence was marginal because T1 values were also highly affected by hepatic steatosis which masked the effect of inflammation or fibrosis on T1. We used two bi-

compartment no exchange models to eliminate the confounding effect of fat on T1 values. The first one was used a posteriori on R1 values determined with a single compartment model, while the second one was performed by using an MRI signal model which explicitly involved two compartments in the T1 fitting procedure. In both cases, corrected T1 still showed strong dependence on the degree of steatosis. The effect of fat correction was substantial at high steatosis grades (S3), but ultimately did not totally remove the potential confounding effect of steatosis. Further analysis to ameliorate our understanding of the mechanisms underlying the influence of lipid and water compartments on T1 values in the liver and the exchange between these two compartments is needed.

Another MRI-based method that we investigated was TDS OGSE to probe diffusion at several spatial scales (i.e. frequencies). We implemented and validated [403] a TDS OGSE-EPI sequence, and further improved it by implementing trapezoid-modulated encoding gradient waveforms on a 7T preclinical scanner. We assessed the ADC values in phantoms and our results agreed with expected ADCs in terms of frequency and spatial scale. The use of the method in a mouse model yielded promising results for the diagnosis of NASH through hepatocyte ballooning characterization despite the confounding effect of steatosis on ADC values. This confounding effect was observed even with the use of a fat saturation pulse and may be explained by the complex fat spectra. Moreover, with TDS we detected some changes occurring during therapy, which may be of interest for pharmaceutical applications.

Further studies in animals and humans will be needed to elucidate the mechanisms by which NAFLD histopathological features affect MRE mechanical parameters, T1 values and ADC measurements.

6.2. Perspectives

There are several studies that we envision to perform for further validating MRI-based NAFLD biomarkers:

First, the MRE data at 200 Hz and 600 Hz should be analyzed and the results compared to those at 400 Hz presented in this work. In our study of multiparametric MRI of NAFLD, the MRE data were acquired at three frequencies. However, we focused our analysis on 400 Hz because the wave amplitude and SNR were the best at this frequency. The next step will be to investigate the performance of the monofrequency mechanical parameters at the two other acquired frequencies to improve our understanding of the viscoelastic frequency dispersion.

Second, to better understand the decrease in T1 values associated with the increase in steatosis grades, a more effective correction model that takes into consideration the complexity of hepatic lipid accumulation and the interactions at the interface between the lipid compartment and the aqueous compartment within hepatocytes need to be used. In addition, hepatic iron overload has been shown to reduce T1 values [407]. The correction of T1 measurements to eliminate the effect of iron overload has been recently proposed [269] and should be investigated. Fat suppression schemes during MRI acquisition should also be assessed.

Third, for TDS, the results of the validation study with microspheres of polystyrene at multiple sizes presented in this work were only descriptive. The next step of our work will be to develop a fitting model [397, 398] that enables an objective interpretation of frequency/time dependent ADC measurements changes with biophysical parameters to interpret ADC changes in diseased tissues. More precisely, we will study whether the frequency dispersion of ADC is best described in NAFLD regression models by the short time regime in the long time regime characterized by $\omega^{-3/2}$ dependency and tortuosity-limited ADC at low frequency (D_∞), or by the short time regime characterized by $-\omega^{-1/2}$ dependency and asymptotically limited diffusion at high frequencies (D_0) [399]. We also will further analyze our data for the beads of 3 μm and 7 μm , and at 170 Hz and 230 Hz to better understand the non-monotonous behavior of ADC, spot the causes of this behavior and if relevant re-acquire the data at these sizes and

frequencies. Adding other samples with different bead sizes, particularly between 30 μm and 150 μm , and using other sampling frequencies may provide better insights into the ADC behavior and enhance our fitting model.

Furthermore, we performed TDS in mouse with NAFLD and obtained some interesting results. However, our ADC measurements were affected by hepatic steatosis which may have masked or diminished an effect of the other histologic factors on the imaging marker. An additional model to remove this undesirable effect is needed. Also, further investigation of our data is necessary to provide a better understanding of the relations between histologic features of various characteristic scales in the diseased tissue and the frequency-selective ADC.

The effect of blood microcirculation on the diffusion measurements as translated by the intravoxel incoherent motion (IVIM) theory has been neglected in this study because we considered that the b -values were relatively high to observe the IVIM effect. Here we focused on measuring an effective ADC which may be influenced both by diffusion of water molecules and by microcirculation. According to IVIM principles, the choice of b values determines the degree to which the measured ADC is influenced by tissue perfusion, with low b values being dominated by perfusion and high b -values being dominated with true apparent diffusion [332, 408]. Because of the form of the IVIM model, in which there is a cross term between pure diffusion and perfusion, the perfusion effect, although vanishing with increasing b values, cannot be said to be absent from data at high b -values. The threshold of b -value separating both regimes is itself not fixed and may depend on the tissue under consideration. The IVIM approach has been used in several liver diseases including fibrosis, cirrhosis, NAFLD, and focal liver lesions [409-411]. It has been reported that IVIM effects are dependent on the effective diffusion time in both animal and human livers [332], in mouse brain [412] and in the human liver and pancreas [413]. As PGSE measurements use relatively long diffusion times, they are significantly affected by blood perfusion. However, in the OGSE method, measurements at frequencies ≥ 50 Hz are affected mostly by microcirculatory flow that stays in the same vessel segment during the effective diffusion time [332, 412, 413]. The randomness of the orientation of the vessel segments within the voxel may still induce a sensitivity to circulatory motion even without invoking particles undergoing directional changes at the end of vessel segments during the time of encoding. Furthermore, the bipolar properties of the motion

encoding gradients are endowed with velocity-compensation characteristics. The evaluation of this effect on ADC measurements obtained by PGSE and OGSE methods is planned for future investigations.

Moreover, in both the “Multiparametric preclinical MRI of NAFLD” and “Temporal diffusion spectroscopy with oscillating gradient echoplanar imaging” studies, T2* values were acquired with PDFF measurements. However, T2* was not assessed as a biomarker of NAFLD because of lack of time. This MRI parameter has been reported to decrease with the increase in iron levels in patients with NAFLD [414-416] and has been used for the evaluation of hepatic fat fraction [417]. Future perspectives include analysis of the T2* mapping method as biomarker of NAFLD.

Finally, the diagnostic value of the various MRI biomarkers of NAFLD should be further assessed in patients to provide a virtual biopsy with better characterization of disease severity and response to treatment.

7. References

1. Younossi, Z.M., et al., *Global epidemiology of nonalcoholic fatty liver disease-Meta-analytic assessment of prevalence, incidence, and outcomes*. *Hepatology*, 2016. **64**(1): p. 73-84.
2. Hagstrom, H., et al., *SAF score and mortality in NAFLD after up to 41 years of follow-up*. *Scand J Gastroenterol*, 2017. **52**(1): p. 87-91.
3. Chalasani, N., et al., *The diagnosis and management of non-alcoholic fatty liver disease: practice Guideline by the American Association for the Study of Liver Diseases, American College of Gastroenterology, and the American Gastroenterological Association*. *Hepatology*, 2012. **55**(6): p. 2005-23.
4. Chalasani, N., et al., *The diagnosis and management of nonalcoholic fatty liver disease: Practice guidance from the American Association for the Study of Liver Diseases*. *Hepatology*, 2018. **67**(1): p. 328-357.
5. Li, Z., et al., *Prevalence of nonalcoholic fatty liver disease in mainland of China: a meta-analysis of published studies*. *J Gastroenterol Hepatol*, 2014. **29**(1): p. 42-51.
6. Vernon, G., A. Baranova, and Z.M. Younossi, *Systematic review: the epidemiology and natural history of non-alcoholic fatty liver disease and non-alcoholic steatohepatitis in adults*. *Aliment Pharmacol Ther*, 2011. **34**(3): p. 274-85.
7. Portillo Sanchez, P., et al., *High Prevalence of Nonalcoholic Fatty Liver Disease in Patients with Type 2 Diabetes Mellitus and Normal Plasma Aminotransferase Levels*. *J Clin Endocrinol Metab*, 2014. **100**(5).
8. Kasturiratne, A., et al., *Influence of non-alcoholic fatty liver disease on the development of diabetes mellitus*. *J Gastroenterol Hepatol*, 2013. **28**(1): p. 142-7.
9. Yamazaki, H., et al., *Independent Association Between Improvement of Nonalcoholic Fatty Liver Disease and Reduced Incidence of Type 2 Diabetes*. *Diabetes Care*, 2015. **38**(9): p. 1673-9.
10. Tsuchida, T., et al., *A simple diet- and chemical-induced murine NASH model with rapid progression of steatohepatitis, fibrosis and liver cancer*. *J Hepatol*, 2018. **69**(2): p. 385-395.
11. Bedossa, P., et al., *Histopathological algorithm and scoring system for evaluation of liver lesions in morbidly obese patients*. *Hepatology*, 2012. **56**(5): p. 1751-9.
12. Kleiner, D.E., et al., *Design and validation of a histological scoring system for nonalcoholic fatty liver disease*. *Hepatology*, 2005. **41**(6): p. 1313-21.
13. Arab, J.P., M. Arrese, and M. Trauner, *Recent Insights into the Pathogenesis of Nonalcoholic Fatty Liver Disease*. *Annu Rev Pathol*, 2018. **13**: p. 321-350.
14. World health statistics 2022: monitoring health for the SDGs, s.d.g., *Geneva: World Health Organization; 2022. Licence: CC BY-NC-SA 3.0 IGO*.
15. Gonzalez-Muniesa, P., et al., *Obesity*. *Nat Rev Dis Primers*, 2017. **3**: p. 17034.
16. Ross, R., et al., *Waist circumference as a vital sign in clinical practice: a Consensus Statement from the IAS and ICCR Working Group on Visceral Obesity*. *Nat Rev Endocrinol*, 2020. **16**(3): p. 177-189.
17. Despres, J.P., *Body fat distribution and risk of cardiovascular disease: an update*. *Circulation*, 2012. **126**(10): p. 1301-13.

18. Lambert, J.E., et al., *Increased de novo lipogenesis is a distinct characteristic of individuals with nonalcoholic fatty liver disease*. *Gastroenterology*, 2014. **146**(3): p. 726-35.
19. Softic, S., D.E. Cohen, and C.R. Kahn, *Role of Dietary Fructose and Hepatic De Novo Lipogenesis in Fatty Liver Disease*. *Dig Dis Sci*, 2016. **61**(5): p. 1282-93.
20. Donnelly, K.L., et al., *Sources of fatty acids stored in liver and secreted via lipoproteins in patients with nonalcoholic fatty liver disease*. *J Clin Invest*, 2005. **115**(5): p. 1343-51.
21. Mendez-Sanchez, N., et al., *Current concepts in the pathogenesis of nonalcoholic fatty liver disease*. *Liver Int*, 2007. **27**(4): p. 423-33.
22. Sayiner, M., et al., *Epidemiology of Nonalcoholic Fatty Liver Disease and Nonalcoholic Steatohepatitis in the United States and the Rest of the World*. *Clin Liver Dis*, 2016. **20**(2): p. 205-14.
23. Tsuchida, T. and S.L. Friedman, *Mechanisms of hepatic stellate cell activation*. *Nat Rev Gastroenterol Hepatol*, 2017. **14**(7): p. 397-411.
24. Koyama, Y. and D.A. Brenner, *Liver inflammation and fibrosis*. *J Clin Invest*, 2017. **127**(1): p. 55-64.
25. Tsochatzis, E.A., J. Bosch, and A.K. Burroughs, *Liver cirrhosis*. *Lancet*, 2014. **383**(9930): p. 1749-61.
26. Singh, S., et al., *Fibrosis progression in nonalcoholic fatty liver vs nonalcoholic steatohepatitis: a systematic review and meta-analysis of paired-biopsy studies*. *Clin Gastroenterol Hepatol*, 2015. **13**(4): p. 643-54 e1-9; quiz e39-40.
27. Huang, D.Q., H.B. El-Serag, and R. Loomba, *Global epidemiology of NAFLD-related HCC: trends, predictions, risk factors and prevention*. *Nat Rev Gastroenterol Hepatol*, 2021. **18**(4): p. 223-238.
28. Jemal, A., et al., *Global cancer statistics*. *CA Cancer J Clin*, 2011. **61**(2): p. 69-90.
29. Sanyal, A.J., *Past, present and future perspectives in nonalcoholic fatty liver disease*. *Nat Rev Gastroenterol Hepatol*, 2019. **16**(6): p. 377-386.
30. Estes, C., et al., *Modeling the epidemic of nonalcoholic fatty liver disease demonstrates an exponential increase in burden of disease*. *Hepatology*, 2018. **67**(1): p. 123-133.
31. Bedossa, P., *Pathology of non-alcoholic fatty liver disease*. *Liver Int*, 2017. **37** **Suppl 1**: p. 85-89.
32. Bedossa, P., *Histological Assessment of NAFLD*. *Dig Dis Sci*, 2016. **61**(5): p. 1348-55.
33. Papatheodoridi, M. and E. Cholongitas, *Diagnosis of Non-alcoholic Fatty Liver Disease (NAFLD): Current Concepts*. *Curr Pharm Des*, 2018. **24**(38): p. 4574-4586.
34. Itoh, M., et al., *Hepatic crown-like structure: a unique histological feature in non-alcoholic steatohepatitis in mice and humans*. *PLoS One*, 2013. **8**(12): p. e82163.
35. Abe, N., et al., *Longitudinal characterization of diet-induced genetic murine models of non-alcoholic steatohepatitis with metabolic, histological, and transcriptomic hallmarks of human patients*. *Biol Open*, 2019. **8**(5).
36. Siddiqui, M.S., et al., *Case definitions for inclusion and analysis of endpoints in clinical trials for nonalcoholic steatohepatitis through the lens of regulatory science*. *Hepatology*, 2018. **67**(5): p. 2001-2012.
37. Brunt, E.M., et al., *Nonalcoholic fatty liver disease (NAFLD) activity score and the histopathologic diagnosis in NAFLD: distinct clinicopathologic meanings*. *Hepatology*, 2011. **53**(3): p. 810-20.

38. Dixon, J.B., P.S. Bhathal, and P.E. O'Brien, *Nonalcoholic fatty liver disease: predictors of nonalcoholic steatohepatitis and liver fibrosis in the severely obese*. *Gastroenterology*, 2001. **121**(1): p. 91-100.
39. Campos, G.M., et al., *A clinical scoring system for predicting nonalcoholic steatohepatitis in morbidly obese patients*. *Hepatology*, 2008. **47**(6): p. 1916-23.
40. Yamaguchi, K., et al., *Inhibiting triglyceride synthesis improves hepatic steatosis but exacerbates liver damage and fibrosis in obese mice with nonalcoholic steatohepatitis*. *Hepatology*, 2007. **45**(6): p. 1366-74.
41. Belfort, R., et al., *A placebo-controlled trial of pioglitazone in subjects with nonalcoholic steatohepatitis*. *N Engl J Med*, 2006. **355**(22): p. 2297-307.
42. Bedossa, P. and F.P. Consortium, *Utility and appropriateness of the fatty liver inhibition of progression (FLIP) algorithm and steatosis, activity, and fibrosis (SAF) score in the evaluation of biopsies of nonalcoholic fatty liver disease*. *Hepatology*, 2014. **60**(2): p. 565-75.
43. Angulo, P., et al., *Liver Fibrosis, but No Other Histologic Features, Is Associated With Long-term Outcomes of Patients With Nonalcoholic Fatty Liver Disease*. *Gastroenterology*, 2015. **149**(2): p. 389-97 e10.
44. Ekstedt, M., et al., *Fibrosis stage is the strongest predictor for disease-specific mortality in NAFLD after up to 33 years of follow-up*. *Hepatology*, 2015. **61**(5): p. 1547-54.
45. Dulai, P.S., et al., *Increased risk of mortality by fibrosis stage in nonalcoholic fatty liver disease: Systematic review and meta-analysis*. *Hepatology*, 2017. **65**(5): p. 1557-1565.
46. Poynard, T., et al., *Diagnostic performance of a new noninvasive test for nonalcoholic steatohepatitis using a simplified histological reference*. *Eur J Gastroenterol Hepatol*, 2018. **30**(5): p. 569-577.
47. Kim, B.K., et al., *Head-to-head comparison between MEFIB, MAST, and FAST for detecting stage 2 fibrosis or higher among patients with NAFLD*. *J Hepatol*, 2022.
48. Jung, J., et al., *MRE combined with FIB-4 (MEFIB) index in detection of candidates for pharmacological treatment of NASH-related fibrosis*. *Gut*, 2021. **70**(10): p. 1946-1953.
49. Tamaki, N., et al., *Magnetic resonance elastography plus Fibrosis-4 versus FibroScan-aspartate aminotransferase in detection of candidates for pharmacological treatment of NASH-related fibrosis*. *Hepatology*, 2022. **75**(3): p. 661-672.
50. Newsome, P.N., et al., *FibroScan-AST (FAST) score for the non-invasive identification of patients with non-alcoholic steatohepatitis with significant activity and fibrosis: a prospective derivation and global validation study*. *Lancet Gastroenterol Hepatol*, 2020. **5**(4): p. 362-373.
51. Loomba, R., et al., *Expert Panel Review to Compare FDA and EMA Guidance on Drug Development and Endpoints in Nonalcoholic Steatohepatitis*. *Gastroenterology*, 2022. **162**(3): p. 680-688.
52. Nouredin, M., et al., *MRI-based (MAST) score accurately identifies patients with NASH and significant fibrosis*. *J Hepatol*, 2022. **76**(4): p. 781-787.
53. Brunt, E.M., et al., *Complexity of ballooned hepatocyte feature recognition: Defining a training atlas for artificial intelligence-based imaging in NAFLD*. *J Hepatol*, 2022. **76**(5): p. 1030-1041.
54. Santhekadur, P.K., D.P. Kumar, and A.J. Sanyal, *Preclinical models of non-alcoholic fatty liver disease*. *J Hepatol*, 2018. **68**(2): p. 230-237.

55. Jahn, D., et al., *Animal models of NAFLD from a hepatologist's point of view*. *Biochim Biophys Acta Mol Basis Dis*, 2019. **1865**(5): p. 943-953.
56. Van Herck, M.A., L. Vonghia, and S.M. Francque, *Animal Models of Nonalcoholic Fatty Liver Disease-A Starter's Guide*. *Nutrients*, 2017. **9**(10).
57. Machado, M.V., et al., *Mouse models of diet-induced nonalcoholic steatohepatitis reproduce the heterogeneity of the human disease*. *PLoS One*, 2015. **10**(5): p. e0127991.
58. Charlton, M., et al., *Fast food diet mouse: novel small animal model of NASH with ballooning, progressive fibrosis, and high physiological fidelity to the human condition*. *Am J Physiol Gastrointest Liver Physiol*, 2011. **301**(5): p. G825-34.
59. Kirsch, R., et al., *Rodent nutritional model of non-alcoholic steatohepatitis: species, strain and sex difference studies*. *J Gastroenterol Hepatol*, 2003. **18**(11): p. 1272-82.
60. Hewitt, K.N., et al., *Estrogen replacement reverses the hepatic steatosis phenotype in the male aromatase knockout mouse*. *Endocrinology*, 2004. **145**(4): p. 1842-8.
61. Ibrahim, S.H., et al., *Animal Models of Nonalcoholic Steatohepatitis: Eat, Delete, and Inflammation*. *Dig Dis Sci*, 2016. **61**(5): p. 1325-36.
62. Pregoica, I., et al., *Diet-induced rodent models of obesity-related metabolic disorders-A guide to a translational perspective*. *Obes Rev*, 2020. **21**(12): p. e13081.
63. Newberry, E.P., et al., *Phenotypic divergence in two lines of L-Fabp^{-/-} mice reflects substrain differences and environmental modifiers*. *Am J Physiol Gastrointest Liver Physiol*, 2015. **309**(8): p. G648-61.
64. Nakamura, A. and Y. Terauchi, *Lessons from mouse models of high-fat diet-induced NAFLD*. *Int J Mol Sci*, 2013. **14**(11): p. 21240-57.
65. Asgharpour, A., et al., *A diet-induced animal model of non-alcoholic fatty liver disease and hepatocellular cancer*. *J Hepatol*, 2016. **65**(3): p. 579-88.
66. Lieber, C.S., et al., *Model of nonalcoholic steatohepatitis*. *Am J Clin Nutr*, 2004. **79**(3): p. 502-9.
67. Eccleston, H.B., et al., *Chronic exposure to a high-fat diet induces hepatic steatosis, impairs nitric oxide bioavailability, and modifies the mitochondrial proteome in mice*. *Antioxid Redox Signal*, 2011. **15**(2): p. 447-59.
68. Kodama, Y., et al., *c-Jun N-terminal kinase-1 from hematopoietic cells mediates progression from hepatic steatosis to steatohepatitis and fibrosis in mice*. *Gastroenterology*, 2009. **137**(4): p. 1467-1477 e5.
69. Nakae, D., et al., *High incidence of hepatocellular carcinomas induced by a choline deficient L-amino acid defined diet in rats*. *Cancer Res*, 1992. **52**(18): p. 5042-5.
70. Nakae, D., et al., *Production of both 8-hydroxydeoxyguanosine in liver DNA and gamma-glutamyltransferase-positive hepatocellular lesions in rats given a choline-deficient, L-amino acid-defined diet*. *Jpn J Cancer Res*, 1990. **81**(11): p. 1081-4.
71. Nakae, D., et al., *Comparative changes in the liver of female Fischer-344 rats after short-term feeding of a semipurified or a semisynthetic L-amino acid-defined choline-deficient diet*. *Toxicol Pathol*, 1995. **23**(5): p. 583-90.
72. Miura, K., et al., *Toll-like receptor 9 promotes steatohepatitis by induction of interleukin-1beta in mice*. *Gastroenterology*, 2010. **139**(1): p. 323-34 e7.
73. Matsumoto, M., et al., *An improved mouse model that rapidly develops fibrosis in non-alcoholic steatohepatitis*. *Int J Exp Pathol*, 2013. **94**(2): p. 93-103.
74. Kamada, Y., et al., *Hypoadiponectinemia accelerates hepatic tumor formation in a nonalcoholic steatohepatitis mouse model*. *J Hepatol*, 2007. **47**(4): p. 556-64.

75. Chiba, T., et al., *Evaluation of Methionine Content in a High-Fat and Choline-Deficient Diet on Body Weight Gain and the Development of Non-Alcoholic Steatohepatitis in Mice*. PLoS One, 2016. **11**(10): p. e0164191.
76. Ikawa-Yoshida, A., et al., *Hepatocellular carcinoma in a mouse model fed a choline-deficient, L-amino acid-defined, high-fat diet*. Int J Exp Pathol, 2017. **98**(4): p. 221-233.
77. Yasuda, D., et al., *Reduced Serum Cholesterol and Triglyceride Levels in a Choline-Deficient L-Amino Acid-Defined High-Fat Diet (CDAHFD)-Induced Mouse Model of Non-alcoholic Steatohepatitis (NASH)*. Biol Pharm Bull, 2020. **43**(4): p. 616-618.
78. Suzuki-Kemuriyama, N., et al., *Nonobese mice with nonalcoholic steatohepatitis fed on a choline-deficient, l-amino acid-defined, high-fat diet exhibit alterations in signaling pathways*. FEBS Open Bio, 2021. **11**(11): p. 2950-2965.
79. Park, S., et al., *Korean Pine Nut Oil Attenuated Hepatic Triacylglycerol Accumulation in High-Fat Diet-Induced Obese Mice*. Nutrients, 2016. **8**(1).
80. Tetri, L.H., et al., *Severe NAFLD with hepatic necroinflammatory changes in mice fed trans fats and a high-fructose corn syrup equivalent*. Am J Physiol Gastrointest Liver Physiol, 2008. **295**(5): p. G987-95.
81. Nakamura, A., et al., *Protection from non-alcoholic steatohepatitis and liver tumorigenesis in high fat-fed insulin receptor substrate-1-knockout mice despite insulin resistance*. Diabetologia, 2012. **55**(12): p. 3382-91.
82. Merat, S., et al., *Western-type diets induce insulin resistance and hyperinsulinemia in LDL receptor-deficient mice but do not increase aortic atherosclerosis compared with normoinsulinemic mice in which similar plasma cholesterol levels are achieved by a fructose-rich diet*. Arterioscler Thromb Vasc Biol, 1999. **19**(5): p. 1223-30.
83. DeLeve, L.D., et al., *Prevention of hepatic fibrosis in a murine model of metabolic syndrome with nonalcoholic steatohepatitis*. Am J Pathol, 2008. **173**(4): p. 993-1001.
84. Ishimoto, T., et al., *High-fat and high-sucrose (western) diet induces steatohepatitis that is dependent on fructokinase*. Hepatology, 2013. **58**(5): p. 1632-43.
85. Younossi, Z.M., et al., *Nonalcoholic fatty liver disease: assessment of variability in pathologic interpretations*. Mod Pathol, 1998. **11**(6): p. 560-5.
86. Younossi, Z.M., et al., *Pathologic criteria for nonalcoholic steatohepatitis: interprotocol agreement and ability to predict liver-related mortality*. Hepatology, 2011. **53**(6): p. 1874-82.
87. Ratziu, V., et al., *Sampling variability of liver biopsy in nonalcoholic fatty liver disease*. Gastroenterology, 2005. **128**(7): p. 1898-906.
88. Ooi, G.J., et al., *Evaluation of the histological variability of core and wedge biopsies in nonalcoholic fatty liver disease in bariatric surgical patients*. Surg Endosc, 2021. **35**(3): p. 1210-1218.
89. Vuppalanchi, R., et al., *Effects of liver biopsy sample length and number of readings on sampling variability in nonalcoholic Fatty liver disease*. Clin Gastroenterol Hepatol, 2009. **7**(4): p. 481-6.
90. Jung, E.S., et al., *Interobserver Agreement on Pathologic Features of Liver Biopsy Tissue in Patients with Nonalcoholic Fatty Liver Disease*. J Pathol Transl Med, 2016. **50**(3): p. 190-6.
91. Mehta, S.R., et al., *Non-invasive means of measuring hepatic fat content*. World J Gastroenterol, 2008. **14**(22): p. 3476-83.

92. Peng, X.G., et al., *Comparison of brown and white adipose tissue fat fractions in ob, seipin, and Fsp27 gene knockout mice by chemical shift-selective imaging and (1)H-MR spectroscopy*. *Am J Physiol Endocrinol Metab*, 2013. **304**(2): p. E160-7.
93. Reeder, S.B., et al., *Quantitative Assessment of Liver Fat with Magnetic Resonance Imaging and Spectroscopy*. *J Magn Reson Imaging*, 2011. **34**(4): p. 729-749.
94. Caussy, C., et al., *Noninvasive, Quantitative Assessment of Liver Fat by MRI-PDFF as an Endpoint in NASH Trials*. *Hepatology*, 2018. **68**(2): p. 763-772.
95. Lee, S.S. and S.H. Park, *Radiologic evaluation of nonalcoholic fatty liver disease*. *World J Gastroenterol*, 2014. **20**(23): p. 7392-402.
96. Thomsen, C., et al., *Quantification of liver fat using magnetic resonance spectroscopy*. *Magn Reson Imaging*, 1994. **12**(3): p. 487-95.
97. Kim, H.J., et al., *Accuracy and precision of proton density fat fraction measurement across field strengths and scan intervals: A phantom and human study*. *J Magn Reson Imaging*, 2019. **50**(1): p. 305-314.
98. Zhou, J.H., et al., *Noninvasive evaluation of nonalcoholic fatty liver disease: Current evidence and practice*. *World J Gastroenterol*, 2019. **25**(11): p. 1307-1326.
99. Schaapman, J.J., et al., *Multiparametric MRI in Patients With Nonalcoholic Fatty Liver Disease*. *J Magn Reson Imaging*, 2021. **53**(6): p. 1623-1631.
100. Nouredin, M., et al., *Utility of magnetic resonance imaging versus histology for quantifying changes in liver fat in nonalcoholic fatty liver disease trials*. *Hepatology*, 2013. **58**(6): p. 1930-40.
101. Hines, C.D., et al., *T1 independent, T2* corrected MRI with accurate spectral modeling for quantification of fat: validation in a fat-water-SPIO phantom*. *J Magn Reson Imaging*, 2009. **30**(5): p. 1215-22.
102. Hernando, D., et al., *Multisite, multivendor validation of the accuracy and reproducibility of proton-density fat-fraction quantification at 1.5T and 3T using a fat-water phantom*. *Magn Reson Med*, 2017. **77**(4): p. 1516-1524.
103. Hines, C.D., et al., *Quantification of hepatic steatosis with 3-T MR imaging: validation in ob/ob mice*. *Radiology*, 2010. **254**(1): p. 119-28.
104. Hines, C.D., et al., *Validation of MRI biomarkers of hepatic steatosis in the presence of iron overload in the ob/ob mouse*. *J Magn Reson Imaging*, 2012. **35**(4): p. 844-51.
105. Bannas, P., et al., *Quantitative magnetic resonance imaging of hepatic steatosis: Validation in ex vivo human livers*. *Hepatology*, 2015. **62**(5): p. 1444-55.
106. Artz, N.S., et al., *Reproducibility of MR-based liver fat quantification across field strength: Same-day comparison between 1.5T and 3T in obese subjects*. *J Magn Reson Imaging*, 2015. **42**(3): p. 811-7.
107. Bashir, M.R., et al., *Quantification of hepatic steatosis with a multistep adaptive fitting MRI approach: prospective validation against MR spectroscopy*. *AJR Am J Roentgenol*, 2015. **204**(2): p. 297-306.
108. Meisamy, S., et al., *Quantification of hepatic steatosis with T1-independent, T2-corrected MR imaging with spectral modeling of fat: blinded comparison with MR spectroscopy*. *Radiology*, 2011. **258**(3): p. 767-75.
109. Tyagi, A., et al., *Intra- and inter-examination repeatability of magnetic resonance spectroscopy, magnitude-based MRI, and complex-based MRI for estimation of hepatic proton density fat fraction in overweight and obese children and adults*. *Abdom Imaging*, 2015. **40**(8): p. 3070-7.

110. Idilman, I.S., et al., *Hepatic steatosis: quantification by proton density fat fraction with MR imaging versus liver biopsy*. Radiology, 2013. **267**(3): p. 767-75.
111. Starekova, J. and S.B. Reeder, *Liver fat quantification: where do we stand?* Abdom Radiol (NY), 2020. **45**(11): p. 3386-3399.
112. Middleton, M.S., et al., *Agreement Between Magnetic Resonance Imaging Proton Density Fat Fraction Measurements and Pathologist-Assigned Steatosis Grades of Liver Biopsies From Adults With Nonalcoholic Steatohepatitis*. Gastroenterology, 2017. **153**(3): p. 753-761.
113. Castera, L., M. Friedrich-Rust, and R. Loomba, *Noninvasive Assessment of Liver Disease in Patients With Nonalcoholic Fatty Liver Disease*. Gastroenterology, 2019. **156**(5): p. 1264-1281 e4.
114. Bonekamp, S., et al., *Spatial distribution of MRI-Determined hepatic proton density fat fraction in adults with nonalcoholic fatty liver disease*. J Magn Reson Imaging, 2014. **39**(6): p. 1525-32.
115. Negrete, L.M., et al., *Inter-examination precision of magnitude-based MRI for estimation of segmental hepatic proton density fat fraction in obese subjects*. J Magn Reson Imaging, 2014. **39**(5): p. 1265-71.
116. Kang, G.H., et al., *Reproducibility of MRI-determined proton density fat fraction across two different MR scanner platforms*. J Magn Reson Imaging, 2011. **34**(4): p. 928-34.
117. Permutt, Z., et al., *Correlation between liver histology and novel magnetic resonance imaging in adult patients with non-alcoholic fatty liver disease - MRI accurately quantifies hepatic steatosis in NAFLD*. Aliment Pharmacol Ther, 2012. **36**(1): p. 22-9.
118. Tang, A., et al., *Accuracy of MR imaging-estimated proton density fat fraction for classification of dichotomized histologic steatosis grades in nonalcoholic fatty liver disease*. Radiology, 2015. **274**(2): p. 416-25.
119. Schwimmer, J.B., et al., *A phase 2 clinical trial of metformin as a treatment for non-diabetic paediatric non-alcoholic steatohepatitis*. Aliment Pharmacol Ther, 2005. **21**(7): p. 871-9.
120. Reeder, S.B., H.H. Hu, and C.B. Sirlin, *Proton density fat-fraction: a standardized MR-based biomarker of tissue fat concentration*. J Magn Reson Imaging, 2012. **36**(5): p. 1011-4.
121. Reeder, S.B., *Emerging quantitative magnetic resonance imaging biomarkers of hepatic steatosis*. Hepatology, 2013. **58**(6): p. 1877-80.
122. Le, T.A., et al., *Effect of colesvelam on liver fat quantified by magnetic resonance in nonalcoholic steatohepatitis: a randomized controlled trial*. Hepatology, 2012. **56**(3): p. 922-32.
123. Tang, A., et al., *Nonalcoholic fatty liver disease: MR imaging of liver proton density fat fraction to assess hepatic steatosis*. Radiology, 2013. **267**(2): p. 422-31.
124. McDonald, N., et al., *Multiparametric magnetic resonance imaging for quantitation of liver disease: a two-centre cross-sectional observational study*. Sci Rep, 2018. **8**(1): p. 9189.
125. Imajo, K., et al., *Magnetic Resonance Imaging More Accurately Classifies Steatosis and Fibrosis in Patients With Nonalcoholic Fatty Liver Disease Than Transient Elastography*. Gastroenterology, 2016. **150**(3): p. 626-637 e7.
126. Garteiser, P., et al., *Prospective comparison of transient elastography, MRI and serum scores for grading steatosis and detecting non-alcoholic steatohepatitis in bariatric surgery candidates*. JHEP Rep, 2021. **3**(6): p. 100381.

127. Qu, Y., et al., *Diagnostic accuracy of hepatic proton density fat fraction measured by magnetic resonance imaging for the evaluation of liver steatosis with histology as reference standard: a meta-analysis*. Eur Radiol, 2019. **29**(10): p. 5180-5189.
128. Gu, J., et al., *Diagnostic value of MRI-PDFF for hepatic steatosis in patients with non-alcoholic fatty liver disease: a meta-analysis*. Eur Radiol, 2019. **29**(7): p. 3564-3573.
129. Kim, M., B.K. Kang, and D.W. Jun, *Comparison of conventional sonographic signs and magnetic resonance imaging proton density fat fraction for assessment of hepatic steatosis*. Sci Rep, 2018. **8**(1): p. 7759.
130. Loomba, R., et al., *GS-0976 Reduces Hepatic Steatosis and Fibrosis Markers in Patients With Nonalcoholic Fatty Liver Disease*. Gastroenterology, 2018. **155**(5): p. 1463-1473 e6.
131. Runge, J.H., et al., *Measuring liver triglyceride content in mice: non-invasive magnetic resonance methods as an alternative to histopathology*. MAGMA, 2014. **27**(4): p. 317-27.
132. Ryu, J.E., et al., *Evaluation of Nonalcoholic Fatty Liver Disease in C57BL/6J Mice by Using MRI and Histopathologic Analyses*. Comp Med, 2015. **65**(5): p. 409-15.
133. Liu, C.Y., et al., *Fat quantification with IDEAL gradient echo imaging: correction of bias from T(1) and noise*. Magn Reson Med, 2007. **58**(2): p. 354-64.
134. Bydder, M., et al., *Relaxation effects in the quantification of fat using gradient echo imaging*. Magn Reson Imaging, 2008. **26**(3): p. 347-59.
135. Yu, H., et al., *Multiecho reconstruction for simultaneous water-fat decomposition and T2* estimation*. J Magn Reson Imaging, 2007. **26**(4): p. 1153-61.
136. Datz, C., E. Muller, and E. Aigner, *Iron overload and non-alcoholic fatty liver disease*. Minerva Endocrinol, 2017. **42**(2): p. 173-183.
137. Yu, H., et al., *Multiecho water-fat separation and simultaneous R2* estimation with multifrequency fat spectrum modeling*. Magn Reson Med, 2008. **60**(5): p. 1122-34.
138. Hernando, D., et al., *Addressing phase errors in fat-water imaging using a mixed magnitude/complex fitting method*. Magn Reson Med, 2012. **67**(3): p. 638-44.
139. Hutton, C., et al., *Validation of a standardized MRI method for liver fat and T2* quantification*. PLoS One, 2018. **13**(9): p. e0204175.
140. Yu, H., et al., *Combination of complex-based and magnitude-based multiecho water-fat separation for accurate quantification of fat-fraction*. Magn Reson Med, 2011. **66**(1): p. 199-206.
141. Cui, J., et al., *Sitagliptin vs. placebo for non-alcoholic fatty liver disease: A randomized controlled trial*. J Hepatol, 2016. **65**(2): p. 369-76.
142. Loomba, R., et al., *Ezetimibe for the treatment of nonalcoholic steatohepatitis: assessment by novel magnetic resonance imaging and magnetic resonance elastography in a randomized trial (MOZART trial)*. Hepatology, 2015. **61**(4): p. 1239-50.
143. Loporq, B., et al., *Hepatic fat fraction and visceral adipose tissue fatty acid composition in mice: Quantification with 7.0T MRI*. Magn Reson Med, 2016. **76**(2): p. 510-8.
144. Peng, X.G., et al., *Quantification of liver fat in mice: comparing dual-echo Dixon imaging, chemical shift imaging, and 1H-MR spectroscopy*. J Lipid Res, 2011. **52**(10): p. 1847-55.
145. Manduca, A., et al., *MR elastography: Principles, guidelines, and terminology*. Magn Reson Med, 2021. **85**(5): p. 2377-2390.

146. Huwart, L. and B.E. van Beers, *MR elastography*. *Gastroenterol Clin Biol*, 2008. **32**(6 Suppl 1): p. 68-72.
147. Venkatesh, S.K., M. Yin, and R.L. Ehman, *Magnetic resonance elastography of liver: technique, analysis, and clinical applications*. *J Magn Reson Imaging*, 2013. **37**(3): p. 544-55.
148. Muthupillai, R., et al., *Magnetic resonance elastography by direct visualization of propagating acoustic strain waves*. *Science*, 1995. **269**(5232): p. 1854-7.
149. Campos-Murguia, A., et al., *Clinical assessment and management of liver fibrosis in non-alcoholic fatty liver disease*. *World J Gastroenterol*, 2020. **26**(39): p. 5919-5943.
150. Selvaraj, E.A., et al., *Diagnostic accuracy of elastography and magnetic resonance imaging in patients with NAFLD: A systematic review and meta-analysis*. *J Hepatol*, 2021. **75**(4): p. 770-785.
151. Glaser, K.J., A. Manduca, and R.L. Ehman, *Review of MR elastography applications and recent developments*. *J Magn Reson Imaging*, 2012. **36**(4): p. 757-74.
152. Mariappan, Y.K., K.J. Glaser, and R.L. Ehman, *Magnetic resonance elastography: a review*. *Clin Anat*, 2010. **23**(5): p. 497-511.
153. Dong, H., R.D. White, and A. Kolipaka, *Advances and Future Direction of Magnetic Resonance Elastography*. *Top Magn Reson Imaging*, 2018. **27**(5): p. 363-384.
154. Latta, P., et al., *Convertible pneumatic actuator for magnetic resonance elastography of the brain*. *Magn Reson Imaging*, 2011. **29**(1): p. 147-52.
155. Braun, J., K. Braun, and I. Sack, *Electromagnetic actuator for generating variably oriented shear waves in MR elastography*. *Magn Reson Med*, 2003. **50**(1): p. 220-2.
156. Uffmann, K. and M.E. Ladd, *Actuation systems for MR elastography: design and applications*. *IEEE Eng Med Biol Mag*, 2008. **27**(3): p. 28-34.
157. Venkatesh, S.K., et al., *Magnetic resonance elastography for the detection and staging of liver fibrosis in chronic hepatitis B*. *Eur Radiol*, 2014. **24**(1): p. 70-8.
158. Salameh, N., et al., *Early detection of steatohepatitis in fatty rat liver by using MR elastography*. *Radiology*, 2009. **253**(1): p. 90-7.
159. Chatelin, S., et al., *Cannabinoid receptor activation in the juvenile rat brain results in rapid biomechanical alterations: Neurovascular mechanism as a putative confounding factor*. *Journal of Cerebral Blood Flow & Metabolism*, 2016. **36**(5): p. 954-964.
160. Ronot, M., et al., *Viscoelastic parameters for quantifying liver fibrosis: three-dimensional multifrequency MR elastography study on thin liver rat slices*. *PLoS One*, 2014. **9**(4): p. e94679.
161. Dioguardi Burgio, M., *Ultrasound quantification of hepatic steatosis and multiparametric MRI evaluation of nonalcoholic fatty liver disease*. *PhD thesis*. 2019, Université Paris Cité.
162. Venkatesh, S.K., et al., *MR elastography of liver tumors: preliminary results*. *AJR Am J Roentgenol*, 2008. **190**(6): p. 1534-40.
163. Hines, C.D., et al., *Repeatability of magnetic resonance elastography for quantification of hepatic stiffness*. *J Magn Reson Imaging*, 2010. **31**(3): p. 725-31.
164. Rouviere, O., et al., *MR elastography of the liver: preliminary results*. *Radiology*, 2006. **240**(2): p. 440-8.
165. Garteiser, P., et al., *Rapid acquisition of multifrequency, multislice and multidirectional MR elastography data with a fractionally encoded gradient echo sequence*. *NMR Biomed*, 2013. **26**(10): p. 1326-35.

166. Sinkus, R., et al., *Imaging anisotropic and viscous properties of breast tissue by magnetic resonance-elastography*. *Magnetic Resonance in Medicine*, 2005. **53**(2): p. 372-387.
167. Huwart, L., et al., *Liver fibrosis: noninvasive assessment with MR elastography versus aspartate aminotransferase-to-platelet ratio index*. *Radiology*, 2007. **245**(2): p. 458-66.
168. Asbach, P., et al., *Viscoelasticity-based staging of hepatic fibrosis with multifrequency MR elastography*. *Radiology*, 2010. **257**(1): p. 80-6.
169. Asbach, P., et al., *Assessment of liver viscoelasticity using multifrequency MR elastography*. *Magn Reson Med*, 2008. **60**(2): p. 373-9.
170. Huwart, L., et al., *MR elastography of liver fibrosis: preliminary results comparing spin-echo and echo-planar imaging*. *Eur Radiol*, 2008. **18**(11): p. 2535-41.
171. Yin, Z., et al., *Prediction of nonalcoholic fatty liver disease (NAFLD) activity score (NAS) with multiparametric hepatic magnetic resonance imaging and elastography*. *Eur Radiol*, 2019. **29**(11): p. 5823-5831.
172. Rump, J., et al., *Fractional encoding of harmonic motions in MR elastography*. *Magn Reson Med*, 2007. **57**(2): p. 388-95.
173. Tang, A., et al., *Ultrasound Elastography and MR Elastography for Assessing Liver Fibrosis: Part 1, Principles and Techniques*. *AJR Am J Roentgenol*, 2015. **205**(1): p. 22-32.
174. Sinkus, R., et al., *High-resolution tensor MR elastography for breast tumour detection*. *Phys Med Biol*, 2000. **45**(6): p. 1649-64.
175. Wagner, M., et al., *Technical Failure of MR Elastography Examinations of the Liver: Experience from a Large Single-Center Study*. *Radiology*, 2017. **284**(2): p. 401-412.
176. Kim, D.W., et al., *Comparison of technical failure of MR elastography for measuring liver stiffness between gradient-recalled echo and spin-echo echo-planar imaging: A systematic review and meta-analysis*. *J Magn Reson Imaging*, 2020. **51**(4): p. 1086-1102.
177. Manduca, A., et al., *Magnetic resonance elastography: non-invasive mapping of tissue elasticity*. *Med Image Anal*, 2001. **5**(4): p. 237-54.
178. Sinkus, R., et al., *Viscoelastic shear properties of in vivo breast lesions measured by MR elastography*. *Magn Reson Imaging*, 2005. **23**(2): p. 159-65.
179. Oliphant, T.E., et al., *Complex-valued stiffness reconstruction for magnetic resonance elastography by algebraic inversion of the differential equation*. *Magn Reson Med*, 2001. **45**(2): p. 299-310.
180. Romano, A.J., J.J. Shirron, and J.A. Bucaro, *On the noninvasive determination of material parameters from a knowledge of elastic displacements theory and numerical simulation*. *IEEE Trans Ultrason Ferroelectr Freq Control*, 1998. **45**(3): p. 751-9.
181. Romano, A.J., et al., *Evaluation of a material parameter extraction algorithm using MRI-based displacement measurements*. *IEEE Trans Ultrason Ferroelectr Freq Control*, 2000. **47**(6): p. 1575-81.
182. Serai, S.D. and M. Yin, *MR Elastography of the Abdomen: Basic Concepts*. *Methods Mol Biol*, 2021. **2216**: p. 301-323.
183. Fovargue, D., D. Nordsletten, and R. Sinkus, *Stiffness reconstruction methods for MR elastography*. *NMR Biomed*, 2018. **31**(10): p. e3935.

184. Klatt, D., et al., *Noninvasive assessment of the rheological behavior of human organs using multifrequency MR elastography: a study of brain and liver viscoelasticity*. Phys Med Biol, 2007. **52**(24): p. 7281-94.
185. Okamoto, R.J., E.H. Clayton, and P.V. Bayly, *Viscoelastic properties of soft gels: comparison of magnetic resonance elastography and dynamic shear testing in the shear wave regime*. Phys Med Biol, 2011. **56**(19): p. 6379-400.
186. Yasar, T.K., et al., *Selective spectral displacement projection for multifrequency MRE*. Phys Med Biol, 2013. **58**(16): p. 5771-81.
187. Sack, I., et al., *Structure-sensitive elastography: on the viscoelastic powerlaw behavior of in vivo human tissue in health and disease*. Soft Matter, 2013. **9**(24): p. 5672-5680.
188. Reiter, R., et al., *Wideband MRE and static mechanical indentation of human liver specimen: sensitivity of viscoelastic constants to the alteration of tissue structure in hepatic fibrosis*. J Biomech, 2014. **47**(7): p. 1665-74.
189. Posnansky, O., et al., *Fractal network dimension and viscoelastic powerlaw behavior: I. A modeling approach based on a coarse-graining procedure combined with shear oscillatory rheometry*. Phys Med Biol, 2012. **57**(12): p. 4023-40.
190. Sinkus, R., et al., *MR elastography of breast lesions: understanding the solid/liquid duality can improve the specificity of contrast-enhanced MR mammography*. Magn Reson Med, 2007. **58**(6): p. 1135-44.
191. Garteiser, P., et al., *Necro-inflammatory activity grading in chronic viral hepatitis with three-dimensional multifrequency MR elastography*. Sci Rep, 2021. **11**(1): p. 19386.
192. Kiss, M.Z., T. Varghese, and T.J. Hall, *Viscoelastic characterization of in vitro canine tissue*. Phys Med Biol, 2004. **49**(18): p. 4207-18.
193. Trout, A.T., et al., *Liver Stiffness Measurements with MR Elastography: Agreement and Repeatability across Imaging Systems, Field Strengths, and Pulse Sequences*. Radiology, 2016. **281**(3): p. 793-804.
194. Shire, N.J., et al., *Test-retest repeatability of MR elastography for noninvasive liver fibrosis assessment in hepatitis C*. J Magn Reson Imaging, 2011. **34**(4): p. 947-55.
195. Venkatesh, S.K., et al., *Magnetic resonance elastography of liver in healthy Asians: normal liver stiffness quantification and reproducibility assessment*. J Magn Reson Imaging, 2014. **39**(1): p. 1-8.
196. Jajamovich, G.H., et al., *Quantitative liver MRI combining phase contrast imaging, elastography, and DWI: assessment of reproducibility and postprandial effect at 3.0 T*. PLoS One, 2014. **9**(5): p. e97355.
197. Bohte, A.E., et al., *MR elastography of the liver: defining thresholds for detecting viscoelastic changes*. Radiology, 2013. **269**(3): p. 768-76.
198. Lee, Y., et al., *MR elastography for noninvasive assessment of hepatic fibrosis: reproducibility of the examination and reproducibility and repeatability of the liver stiffness value measurement*. J Magn Reson Imaging, 2014. **39**(2): p. 326-31.
199. Hines, C.D., et al., *Effects of postprandial state and mesenteric blood flow on the repeatability of MR elastography in asymptomatic subjects*. J Magn Reson Imaging, 2011. **33**(1): p. 239-44.
200. Lee, D.H., et al., *MR elastography of healthy liver parenchyma: Normal value and reliability of the liver stiffness value measurement*. J Magn Reson Imaging, 2013. **38**(5): p. 1215-23.
201. Shi, Y., et al., *Short- and midterm repeatability of magnetic resonance elastography in healthy volunteers at 3.0 T*. Magn Reson Imaging, 2014. **32**(6): p. 665-70.

202. Forsgren, M.F., et al., *Comparing hepatic 2D and 3D magnetic resonance elastography methods in a clinical setting - Initial experiences*. Eur J Radiol Open, 2015. **2**: p. 66-70.
203. Serai, S.D., et al., *Cross-vendor validation of liver magnetic resonance elastography*. Abdom Imaging, 2015. **40**(4): p. 789-94.
204. Yasar, T.K., et al., *Interplatform reproducibility of liver and spleen stiffness measured with MR elastography*. J Magn Reson Imaging, 2016. **43**(5): p. 1064-72.
205. Runge, J.H., et al., *Comparison of interobserver agreement of magnetic resonance elastography with histopathological staging of liver fibrosis*. Abdom Imaging, 2014. **39**(2): p. 283-90.
206. Motosugi, U., et al., *Magnetic resonance elastography of the liver: preliminary results and estimation of inter-rater reliability*. Jpn J Radiol, 2010. **28**(8): p. 623-7.
207. Page, G., et al., *Assessing Tumor Mechanics by MR Elastography at Different Strain Levels*. J Magn Reson Imaging, 2019. **50**(6): p. 1982-1989.
208. Yin, M., et al., *Assessment of hepatic fibrosis with magnetic resonance elastography*. Clin Gastroenterol Hepatol, 2007. **5**(10): p. 1207-1213 e2.
209. Huwart, L., et al., *Magnetic resonance elastography for the noninvasive staging of liver fibrosis*. Gastroenterology, 2008. **135**(1): p. 32-40.
210. Huwart, L., et al., *Liver fibrosis: non-invasive assessment with MR elastography*. NMR Biomed, 2006. **19**(2): p. 173-9.
211. Wells, R.G., *Tissue mechanics and fibrosis*. Biochim Biophys Acta, 2013. **1832**(7): p. 884-90.
212. Wang, Y., et al., *Assessment of chronic hepatitis and fibrosis: comparison of MR elastography and diffusion-weighted imaging*. AJR Am J Roentgenol, 2011. **196**(3): p. 553-61.
213. Ajmera, V.H., et al., *Clinical Utility of an Increase in Magnetic Resonance Elastography in Predicting Fibrosis Progression in Nonalcoholic Fatty Liver Disease*. Hepatology, 2020. **71**(3): p. 849-860.
214. Xanthakos, S.A., A.T. Trout, and J.R. Dillman, *Magnetic resonance elastography assessment of fibrosis in children with NAFLD: Promising but not perfect*. Hepatology, 2017. **66**(5): p. 1373-1376.
215. Tamaki, N., et al., *Two-Step Strategy, FIB-4 Followed by Magnetic Resonance Elastography, for Detecting Advanced Fibrosis in NAFLD*. Clin Gastroenterol Hepatol, 2022.
216. Loomba, R., et al., *Novel 3D Magnetic Resonance Elastography for the Noninvasive Diagnosis of Advanced Fibrosis in NAFLD: A Prospective Study*. Am J Gastroenterol, 2016. **111**(7): p. 986-94.
217. Torres, L., et al., *New FIB-4 and NFS cutoffs to guide sequential non-invasive assessment of liver fibrosis by magnetic resonance elastography in NAFLD*. Ann Hepatol, 2022. **28**(1): p. 100774.
218. Kim, S.W., et al., *Diagnostic Performance of Spin-Echo Echo-Planar Imaging Magnetic Resonance Elastography in 3T System for Noninvasive Assessment of Hepatic Fibrosis*. Korean J Radiol, 2022. **23**(2): p. 180-188.
219. Venkatesh, S.K., et al., *Non-invasive detection of liver fibrosis: MR imaging features vs. MR elastography*. Abdom Imaging, 2015. **40**(4): p. 766-75.
220. Rustogi, R., et al., *Accuracy of MR elastography and anatomic MR imaging features in the diagnosis of severe hepatic fibrosis and cirrhosis*. J Magn Reson Imaging, 2012. **35**(6): p. 1356-64.

221. Choi, Y.R., et al., *Comparison of magnetic resonance elastography and gadoxetate disodium-enhanced magnetic resonance imaging for the evaluation of hepatic fibrosis*. Invest Radiol, 2013. **48**(8): p. 607-13.
222. Leitao, H.S., et al., *Hepatic Fibrosis, Inflammation, and Steatosis: Influence on the MR Viscoelastic and Diffusion Parameters in Patients with Chronic Liver Disease*. Radiology, 2017. **283**(1): p. 98-107.
223. Park, H.S., et al., *Three-Tesla magnetic resonance elastography for hepatic fibrosis: comparison with diffusion-weighted imaging and gadoxetic acid-enhanced magnetic resonance imaging*. World J Gastroenterol, 2014. **20**(46): p. 17558-67.
224. Dyvorne, H.A., et al., *Prospective comparison of magnetic resonance imaging to transient elastography and serum markers for liver fibrosis detection*. Liver Int, 2016. **36**(5): p. 659-66.
225. Wang, Q.B., et al., *Performance of magnetic resonance elastography and diffusion-weighted imaging for the staging of hepatic fibrosis: A meta-analysis*. Hepatology, 2012. **56**(1): p. 239-47.
226. Zou, L.Q., et al., *Comparison of magnetic resonance elastography and diffusion-weighted imaging for staging hepatic fibrosis*. Chin Med J (Engl), 2015. **128**(5): p. 620-5.
227. Ichikawa, S., et al., *Magnetic resonance elastography for staging liver fibrosis in chronic hepatitis C*. Magn Reson Med Sci, 2012. **11**(4): p. 291-7.
228. Godfrey, E.M., et al., *A comparison of MR elastography and 31P MR spectroscopy with histological staging of liver fibrosis*. Eur Radiol, 2012. **22**(12): p. 2790-7.
229. Bensamoun, S.F., et al., *Measurement of liver stiffness with two imaging techniques: magnetic resonance elastography and ultrasound elastometry*. J Magn Reson Imaging, 2008. **28**(5): p. 1287-92.
230. Hsu, C., et al., *Magnetic Resonance vs Transient Elastography Analysis of Patients With Nonalcoholic Fatty Liver Disease: A Systematic Review and Pooled Analysis of Individual Participants*. Clin Gastroenterol Hepatol, 2019. **17**(4): p. 630-637 e8.
231. Cui, J., et al., *Magnetic resonance elastography is superior to acoustic radiation force impulse for the Diagnosis of fibrosis in patients with biopsy-proven nonalcoholic fatty liver disease: A prospective study*. Hepatology, 2016. **63**(2): p. 453-61.
232. Chou, C.T., et al., *Prospective Comparison of the Diagnostic Performance of Magnetic Resonance Elastography with Acoustic Radiation Force Impulse Elastography for Pre-operative Staging of Hepatic Fibrosis in Patients with Hepatocellular Carcinoma*. Ultrasound Med Biol, 2017. **43**(12): p. 2783-2790.
233. Guo, Y., et al., *Magnetic resonance elastography and acoustic radiation force impulse for staging hepatic fibrosis: a meta-analysis*. Abdom Imaging, 2015. **40**(4): p. 818-34.
234. Kamphues, C., et al., *Viscoelasticity-based magnetic resonance elastography for the assessment of liver fibrosis in hepatitis C patients after liver transplantation*. Rofo, 2012. **184**(11): p. 1013-9.
235. Yin, M., et al., *Distinguishing between Hepatic Inflammation and Fibrosis with MR Elastography*. Radiology, 2017. **284**(3): p. 694-705.
236. Zhu, B., et al., *Combined magnetic resonance elastography and collagen molecular magnetic resonance imaging accurately stage liver fibrosis in a rat model*. Hepatology, 2017. **65**(3): p. 1015-1025.
237. Yin, M., et al., *Quantitative assessment of hepatic fibrosis in an animal model with magnetic resonance elastography*. Magn Reson Med, 2007. **58**(2): p. 346-53.

238. Salameh, N., et al., *Hepatic viscoelastic parameters measured with MR elastography: correlations with quantitative analysis of liver fibrosis in the rat.* J Magn Reson Imaging, 2007. **26**(4): p. 956-62.
239. Klatt, D., et al., *Viscoelastic properties of liver measured by oscillatory rheometry and multifrequency magnetic resonance elastography.* Biorheology, 2010. **47**(2): p. 133-41.
240. Zhou, I.Y., et al., *Advanced MRI of Liver Fibrosis and Treatment Response in a Rat Model of Nonalcoholic Steatohepatitis.* Radiology, 2020. **296**(1): p. 67-75.
241. Kostallari, E., et al., *Stiffness is associated with hepatic stellate cell heterogeneity during liver fibrosis.* Am J Physiol Gastrointest Liver Physiol, 2022. **322**(2): p. G234-G246.
242. Chen, J., et al., *Multiparametric magnetic resonance imaging/magnetic resonance elastography assesses progression and regression of steatosis, inflammation, and fibrosis in alcohol-associated liver disease.* Alcohol Clin Exp Res, 2021. **45**(10): p. 2103-2117.
243. Li, J., et al., *Quantitative assessment of portal hypertension with bi-parametric dual-frequency hepatic MR elastography in mouse models.* Eur Radiol, 2021. **31**(4): p. 2303-2311.
244. Tang, H., et al., *Evaluation of a PEGylated Fibroblast Growth Factor 21 Variant Using Novel Preclinical Magnetic Resonance Imaging and Magnetic Resonance Elastography in a Mouse Model of Nonalcoholic Steatohepatitis.* J Magn Reson Imaging, 2022. **56**(3): p. 712-724.
245. Singh, S., et al., *Diagnostic accuracy of magnetic resonance elastography in liver transplant recipients: A pooled analysis.* Ann Hepatol, 2016. **15**(3): p. 363-76.
246. Crespo, S., et al., *Non-invasive assessment of liver fibrosis using magnetic resonance elastography in liver transplant recipients with hepatitis C.* Clin Transplant, 2013. **27**(5): p. 652-8.
247. Garteiser, P., S. Doblas, and B.E. Van Beers, *Magnetic resonance elastography of liver and spleen: Methods and applications.* NMR Biomed, 2018. **31**(10): p. e3891.
248. Yoshimitsu, K., et al., *MR elastography of the liver at 3.0 T in diagnosing liver fibrosis grades; preliminary clinical experience.* Eur Radiol, 2016. **26**(3): p. 656-63.
249. Ichikawa, S., et al., *Hepatitis activity should be considered a confounder of liver stiffness measured with MR elastography.* J Magn Reson Imaging, 2015. **41**(5): p. 1203-8.
250. Shi, Y., et al., *MR elastography for the assessment of hepatic fibrosis in patients with chronic hepatitis B infection: does histologic necroinflammation influence the measurement of hepatic stiffness?* Radiology, 2014. **273**(1): p. 88-98.
251. Loomba, R., et al., *Magnetic resonance elastography predicts advanced fibrosis in patients with nonalcoholic fatty liver disease: a prospective study.* Hepatology, 2014. **60**(6): p. 1920-8.
252. Park, C.C., et al., *Magnetic Resonance Elastography vs Transient Elastography in Detection of Fibrosis and Noninvasive Measurement of Steatosis in Patients With Biopsy-Proven Nonalcoholic Fatty Liver Disease.* Gastroenterology, 2017. **152**(3): p. 598-607 e2.
253. Chen, J., et al., *Early detection of nonalcoholic steatohepatitis in patients with nonalcoholic fatty liver disease by using MR elastography.* Radiology, 2011. **259**(3): p. 749-56.

254. Fernandes, J.L. and C.E. Rochitte, *T1 mapping: technique and applications*. Magn Reson Imaging Clin N Am, 2015. **23**(1): p. 25-34.
255. Taylor, A.J., et al., *T1 Mapping: Basic Techniques and Clinical Applications*. JACC Cardiovasc Imaging, 2016. **9**(1): p. 67-81.
256. *Magnetic resonance imaging of parenchymal liver disease: a comparison with ultrasound, radionuclide scintigraphy and X-ray computed tomography*. The Clinical NMR Group. Clin Radiol, 1987. **38**(5): p. 495-502.
257. Thomsen, C., et al., *Prolonged T1 in patients with liver cirrhosis: an in vivo MRI study*. Magn Reson Imaging, 1990. **8**(5): p. 599-604.
258. Radenkovic, D., et al., *T1 mapping in cardiac MRI*. Heart Fail Rev, 2017. **22**(4): p. 415-430.
259. Li, Z., et al., *Assessment of liver fibrosis by variable flip angle T1 mapping at 3.0T*. J Magn Reson Imaging, 2016. **43**(3): p. 698-703.
260. Hoffman, D.H., et al., *T1 mapping, T2 mapping and MR elastography of the liver for detection and staging of liver fibrosis*. Abdom Radiol (NY), 2020. **45**(3): p. 692-700.
261. Kellman, P. and M.S. Hansen, *T1-mapping in the heart: accuracy and precision*. J Cardiovasc Magn Reson, 2014. **16**: p. 2.
262. Zhu, D.C. and R.D. Penn, *Full-brain T1 mapping through inversion recovery fast spin echo imaging with time-efficient slice ordering*. Magn Reson Med, 2005. **54**(3): p. 725-31.
263. Gowland, P.A. and M.O. Leach, *A simple method for the restoration of signal polarity in multi-image inversion recovery sequences for measuring T1*. Magn Reson Med, 1991. **18**(1): p. 224-31.
264. Cheng, H.L., et al., *Practical medical applications of quantitative MR relaxometry*. J Magn Reson Imaging, 2012. **36**(4): p. 805-24.
265. Mitschelen, M., et al., *Basal and hypercapnia-altered cerebrovascular perfusion predict mild cognitive impairment in aging rodents*. Neuroscience, 2009. **164**(3): p. 918-28.
266. Kim, S.G., *Quantification of relative cerebral blood flow change by flow-sensitive alternating inversion recovery (FAIR) technique: application to functional mapping*. Magn Reson Med, 1995. **34**(3): p. 293-301.
267. Banerjee, R., et al., *Multiparametric magnetic resonance for the non-invasive diagnosis of liver disease*. J Hepatol, 2014. **60**(1): p. 69-77.
268. Harrison, S.A., et al., *Utility and variability of three non-invasive liver fibrosis imaging modalities to evaluate efficacy of GR-MD-02 in subjects with NASH and bridging fibrosis during a phase-2 randomized clinical trial*. PLoS One, 2018. **13**(9): p. e0203054.
269. Tunnicliffe, E.M., et al., *A model for hepatic fibrosis: the competing effects of cell loss and iron on shortened modified Look-Locker inversion recovery T1 (shMOLLI-T1) in the liver*. J Magn Reson Imaging, 2017. **45**(2): p. 450-462.
270. Hoy, A.M., et al., *Non-invasive assessment of liver disease in rats using multiparametric magnetic resonance imaging: a feasibility study*. Biol Open, 2018. **7**(7).
271. Dennis, A., et al., *A composite biomarker using multiparametric magnetic resonance imaging and blood analytes accurately identifies patients with non-alcoholic steatohepatitis and significant fibrosis*. Sci Rep, 2020. **10**(1): p. 15308.
272. Luetkens, J.A., et al., *Quantification of Liver Fibrosis at T1 and T2 Mapping with Extracellular Volume Fraction MRI: Preclinical Results*. Radiology, 2018. **288**(3): p. 748-754.

273. Muller, A., et al., *Effects of Liver Fibrosis Progression on Tissue Relaxation Times in Different Mouse Models Assessed by Ultrahigh Field Magnetic Resonance Imaging*. Biomed Res Int, 2017. **2017**: p. 8720367.
274. Ahn, J.H., et al., *Effect of hepatic steatosis on native T1 mapping of 3T magnetic resonance imaging in the assessment of T1 values for patients with non-alcoholic fatty liver disease*. Magn Reson Imaging, 2021. **80**: p. 1-8.
275. Mozes, F.E., et al., *Influence of fat on liver T1 measurements using modified Look-Locker inversion recovery (MOLLI) methods at 3T*. J Magn Reson Imaging, 2016. **44**(1): p. 105-11.
276. Hoad, C.L., et al., *A study of T(1) relaxation time as a measure of liver fibrosis and the influence of confounding histological factors*. NMR Biomed, 2015. **28**(6): p. 706-14.
277. Kellman, P., et al., *Characterization of myocardial T1-mapping bias caused by intramyocardial fat in inversion recovery and saturation recovery techniques*. J Cardiovasc Magn Reson, 2015. **17**(1): p. 33.
278. Mozes, F.E., et al., *Mapping tissue water T1 in the liver using the MOLLI T1 method in the presence of fat, iron and B0 inhomogeneity*. NMR Biomed, 2019. **32**(2): p. e4030.
279. Garrison, L.D., et al., *Water-Only Look-Locker Inversion recovery (WOLLI) T1 mapping*. bioRxiv, 2022.
280. Feng, L., et al., *Magnetization-prepared GRASP MRI for rapid 3D T1 mapping and fat/water-separated T1 mapping*. Magn Reson Med, 2021. **86**(1): p. 97-114.
281. Li, Z., et al., *Rapid fat-water separated T₁ mapping using a single-shot radial inversion-recovery spoiled gradient recalled pulse sequence*. NMR Biomed, 2022. **35**(12): p. e4803.
282. Henninger, B., et al., *Evaluation of MR imaging with T1 and T2* mapping for the determination of hepatic iron overload*. Eur Radiol, 2012. **22**(11): p. 2478-86.
283. Zou, L.Q., et al., *Effect of Iron Deposition on Native T1 Mapping and Blood Oxygen Level Dependent for the Assessment of Liver Fibrosis in Rabbits With Carbon Tetrachloride Intoxication*. Acad Radiol, 2022.
284. Mojtahed, A., et al., *Reference range of liver corrected T1 values in a population at low risk for fatty liver disease-a UK Biobank sub-study, with an appendix of interesting cases*. Abdom Radiol (NY), 2019. **44**(1): p. 72-84.
285. Dillman, J.R., et al., *Diagnostic performance of quantitative magnetic resonance imaging biomarkers for predicting portal hypertension in children and young adults with autoimmune liver disease*. Pediatr Radiol, 2019. **49**(3): p. 332-341.
286. Harrison, S.A., et al., *NGM282 Improves Liver Fibrosis and Histology in 12 Weeks in Patients With Nonalcoholic Steatohepatitis*. Hepatology, 2020. **71**(4): p. 1198-1212.
287. Eddowes, P.J., et al., *Utility and cost evaluation of multiparametric magnetic resonance imaging for the assessment of non-alcoholic fatty liver disease*. Aliment Pharmacol Ther, 2018. **47**(5): p. 631-644.
288. Pavlides, M., et al., *Multiparametric magnetic resonance imaging predicts clinical outcomes in patients with chronic liver disease*. J Hepatol, 2016. **64**(2): p. 308-315.
289. Kele, P.G. and E.J. van der Jagt, *Diffusion weighted imaging in the liver*. World J Gastroenterol, 2010. **16**(13): p. 1567-76.
290. Taouli, B. and D.M. Koh, *Diffusion-weighted MR imaging of the liver*. Radiology, 2010. **254**(1): p. 47-66.
291. Mannelli, L., et al., *Advances in diffusion-weighted imaging*. Radiol Clin North Am, 2015. **53**(3): p. 569-81.

292. Chavhan, G.B., Z. Alsabban, and P.S. Babyn, *Diffusion-weighted imaging in pediatric body MR imaging: principles, technique, and emerging applications*. Radiographics, 2014. **34**(3): p. E73-88.
293. Lewis, S., et al., *Diffusion-weighted imaging of the liver: techniques and applications*. Magn Reson Imaging Clin N Am, 2014. **22**(3): p. 373-95.
294. Bammer, R., *Basic principles of diffusion-weighted imaging*. Eur J Radiol, 2003. **45**(3): p. 169-84.
295. Charles-Edwards, E.M. and N.M. deSouza, *Diffusion-weighted magnetic resonance imaging and its application to cancer*. Cancer Imaging, 2006. **6**: p. 135-43.
296. Thoeny, H.C. and F. De Keyser, *Extracranial applications of diffusion-weighted magnetic resonance imaging*. Eur Radiol, 2007. **17**(6): p. 1385-93.
297. Kwee, T.C., et al., *Diffusion-weighted whole-body imaging with background body signal suppression (DWIBS): features and potential applications in oncology*. Eur Radiol, 2008. **18**(9): p. 1937-52.
298. Sandrasegaran, K., et al., *The value of diffusion-weighted imaging in characterizing focal liver masses*. Acad Radiol, 2009. **16**(10): p. 1208-14.
299. Koh, D.M. and D.J. Collins, *Diffusion-weighted MRI in the body: applications and challenges in oncology*. AJR Am J Roentgenol, 2007. **188**(6): p. 1622-35.
300. Culverwell, A.D., et al., *Diffusion-weighted MRI of the liver-Interpretative pearls and pitfalls*. Clin Radiol, 2013. **68**(4): p. 406-14.
301. Stejskal, E.O. and J.E. Tanner, *Spin diffusion measurements: spin echoes in the presence of a time-dependent field gradient*. The journal of chemical physics, 1965. **42**(1): p. 288-292.
302. Serai, S.D., *Basics of magnetic resonance imaging and quantitative parameters T1, T2, T2*, T1rho and diffusion-weighted imaging*. Pediatr Radiol, 2022. **52**(2): p. 217-227.
303. Cercignani, M. and M.A. Horsfield, *The physical basis of diffusion-weighted MRI*. J Neurol Sci, 2001. **186 Suppl 1**: p. S11-4.
304. Naganawa, S., et al., *Diffusion-weighted imaging of the liver: technical challenges and prospects for the future*. Magn Reson Med Sci, 2005. **4**(4): p. 175-86.
305. Koh, D.M., et al., *Practical aspects of assessing tumors using clinical diffusion-weighted imaging in the body*. Magn Reson Med Sci, 2007. **6**(4): p. 211-24.
306. Le Bihan, D., et al., *Artifacts and pitfalls in diffusion MRI*. J Magn Reson Imaging, 2006. **24**(3): p. 478-88.
307. Kwee, T.C., et al., *Whole-body diffusion-weighted magnetic resonance imaging*. Eur J Radiol, 2009. **70**(3): p. 409-17.
308. Ivancevic, M.K., et al., *Diffusion-weighted MR imaging of the liver at 3.0 Tesla using TRacking Only Navigator echo (TRON): a feasibility study*. J Magn Reson Imaging, 2009. **30**(5): p. 1027-33.
309. Taouli, B., et al., *Diffusion-weighted imaging of the liver: comparison of navigator triggered and breathhold acquisitions*. J Magn Reson Imaging, 2009. **30**(3): p. 561-8.
310. Yoshikawa, T., et al., *Abdominal apparent diffusion coefficient measurements: effect of diffusion-weighted image quality and usefulness of anisotropic images*. Magn Reson Imaging, 2008. **26**(10): p. 1415-20.
311. Kwee, T.C., et al., *Influence of cardiac motion on diffusion-weighted magnetic resonance imaging of the liver*. MAGMA, 2009. **22**(5): p. 319-25.
312. Hori, M., K. Kamiya, and K. Murata, *Technical Basics of Diffusion-Weighted Imaging*. Magn Reson Imaging Clin N Am, 2021. **29**(2): p. 129-136.

313. Taouli, B., et al., *Diffusion-weighted MRI for quantification of liver fibrosis: preliminary experience*. AJR Am J Roentgenol, 2007. **189**(4): p. 799-806.
314. Lewin, M., et al., *Diffusion-weighted magnetic resonance imaging for the assessment of fibrosis in chronic hepatitis C*. Hepatology, 2007. **46**(3): p. 658-65.
315. Goyal, A., et al., *Diffusion-weighted MRI in inflammatory renal lesions: all that glitters is not RCC!* Eur Radiol, 2013. **23**(1): p. 272-9.
316. Kiryu, S., et al., *Free-breathing diffusion-weighted imaging for the assessment of inflammatory activity in Crohn's disease*. J Magn Reson Imaging, 2009. **29**(4): p. 880-6.
317. Taouli, B., et al., *Chronic hepatitis: role of diffusion-weighted imaging and diffusion tensor imaging for the diagnosis of liver fibrosis and inflammation*. J Magn Reson Imaging, 2008. **28**(1): p. 89-95.
318. Poyraz, A.K., et al., *Diffusion-weighted MRI of fatty liver*. J Magn Reson Imaging, 2012. **35**(5): p. 1108-11.
319. Murphy, P., et al., *Associations between histologic features of nonalcoholic fatty liver disease (NAFLD) and quantitative diffusion-weighted MRI measurements in adults*. J Magn Reson Imaging, 2015. **41**(6): p. 1629-38.
320. Anderson, S.W., et al., *Effect of disease progression on liver apparent diffusion coefficient values in a murine model of NASH at 11.7 Tesla MRI*. J Magn Reson Imaging, 2011. **33**(4): p. 882-8.
321. Annet, L., et al., *Assessment of diffusion-weighted MR imaging in liver fibrosis*. J Magn Reson Imaging, 2007. **25**(1): p. 122-8.
322. Guan, S., et al., *Magnetic resonance diffusion-weighted imaging in the diagnosis of diffuse liver diseases in rats*. Chin Med J (Engl), 2005. **118**(8): p. 639-44.
323. Deng, J., et al., *In vivo diffusion-weighted imaging of liver tumor necrosis in the VX2 rabbit model at 1.5 Tesla*. Invest Radiol, 2006. **41**(4): p. 410-4.
324. Vossen, J.A., et al., *Diffusion-weighted and Gd-EOB-DTPA-contrast-enhanced magnetic resonance imaging for characterization of tumor necrosis in an animal model*. J Comput Assist Tomogr, 2009. **33**(4): p. 626-30.
325. Anderson, S.W., et al., *Quantifying hepatic fibrosis using a biexponential model of diffusion weighted imaging in ex vivo liver specimens*. Magn Reson Imaging, 2012. **30**(10): p. 1475-82.
326. Chung, Y.H., et al., *Diffusion-weighted MRI and (18)F-FDG PET correlation with immunity in early radiotherapy response in BNL hepatocellular carcinoma mouse model: timeline validation*. Eur J Nucl Med Mol Imaging, 2019. **46**(8): p. 1733-1744.
327. Does, M.D., E.C. Parsons, and J.C. Gore, *Oscillating gradient measurements of water diffusion in normal and globally ischemic rat brain*. Magn Reson Med, 2003. **49**(2): p. 206-15.
328. Parsons, E.C., M.D. Does, and J.C. Gore, *Modified oscillating gradient pulses for direct sampling of the diffusion spectrum suitable for imaging sequences*. Magn Reson Imaging, 2003. **21**(3-4): p. 279-85.
329. Parsons, E.C., Jr., M.D. Does, and J.C. Gore, *Temporal diffusion spectroscopy: theory and implementation in restricted systems using oscillating gradients*. Magn Reson Med, 2006. **55**(1): p. 75-84.
330. Baron, C.A. and C. Beaulieu, *Oscillating gradient spin-echo (OGSE) diffusion tensor imaging of the human brain*. Magn Reson Med, 2014. **72**(3): p. 726-36.

331. Arbabi, A., et al., *Diffusion dispersion imaging: Mapping oscillating gradient spin-echo frequency dependence in the human brain*. Magn Reson Med, 2020. **83**(6): p. 2197-2208.
332. Jiang, X., J. Xu, and J.C. Gore, *Mapping hepatocyte size in vivo using temporal diffusion spectroscopy MRI*. Magn Reson Med, 2020. **84**(5): p. 2671-2683.
333. Colvin, D.C., et al., *New insights into tumor microstructure using temporal diffusion spectroscopy*. Cancer Res, 2008. **68**(14): p. 5941-7.
334. Colvin, D.C., et al., *Effects of intracellular organelles on the apparent diffusion coefficient of water molecules in cultured human embryonic kidney cells*. Magn Reson Med, 2011. **65**(3): p. 796-801.
335. Xu, J., et al., *Influence of cell cycle phase on apparent diffusion coefficient in synchronized cells detected using temporal diffusion spectroscopy*. Magn Reson Med, 2011. **65**(4): p. 920-6.
336. Colvin, D.C., et al., *Earlier detection of tumor treatment response using magnetic resonance diffusion imaging with oscillating gradients*. Magn Reson Imaging, 2011. **29**(3): p. 315-23.
337. Mathilde Wagner, e.a., *Comparison of Pulsed and Oscillating Gradient Diffusion-Weighted MRI for Characterizing Hepatocellular Nodules in Liver Cirrhosis: ex vivo Study in a Rat Model*. J. MAGN. RESON. IMAGING, 2019.
338. Junzhong Xu, e.a., *Characterizing Tumor Response to Chemotherapy at Various Length Scales Using Temporal Diffusion Spectroscopy*. PlosOne, 2012.
339. Xiaoyu Jiang, e.a., *In vivo imaging of cancer cell size and cellularity using temporal diffusion spectroscopy*. Magnetic Resonance in Medicine, 2017.
340. Van, A.T., S.J. Holdsworth, and R. Bammer, *In vivo investigation of restricted diffusion in the human brain with optimized oscillating diffusion gradient encoding*. Magn Reson Med, 2014. **71**(1): p. 83-94.
341. Ianus, A., et al., *Gaussian phase distribution approximations for oscillating gradient spin echo diffusion MRI*. J Magn Reson, 2013. **227**: p. 25-34.
342. Lima, M., et al., *Time-dependent diffusion MRI to distinguish malignant from benign head and neck tumors*. J Magn Reson Imaging, 2019. **50**(1): p. 88-95.
343. Jiang, X., et al., *In vivo magnetic resonance imaging of treatment-induced apoptosis*. Sci Rep, 2019. **9**(1): p. 9540.
344. Jiang, X., J. Xu, and J.C. Gore, *Quantitative temporal diffusion spectroscopy as an early imaging biomarker of radiation therapeutic response in gliomas: A preclinical proof of concept*. Adv Radiat Oncol, 2019. **4**(2): p. 367-376.
345. Wagner, M., et al., *Comparison of pulsed and oscillating gradient diffusion-weighted MRI for characterizing hepatocellular nodules in liver cirrhosis: ex vivo study in a rat model*. J Magn Reson Imaging, 2020. **51**(4): p. 1065-1074.
346. Farrell, G., et al., *Mouse Models of Nonalcoholic Steatohepatitis: Toward Optimization of Their Relevance to Human Nonalcoholic Steatohepatitis*. Hepatology, 2019. **69**(5): p. 2241-2257.
347. Hansen, H.H., et al., *Mouse models of nonalcoholic steatohepatitis in preclinical drug development*. Drug Discov Today, 2017. **22**(11): p. 1707-1718.
348. Itagaki, H., et al., *Morphological and functional characterization of non-alcoholic fatty liver disease induced by a methionine-choline-deficient diet in C57BL/6 mice*. Int J Clin Exp Pathol, 2013. **6**(12): p. 2683-96.

349. Clapper, J.R., et al., *Diet-induced mouse model of fatty liver disease and nonalcoholic steatohepatitis reflecting clinical disease progression and methods of assessment*. Am J Physiol Gastrointest Liver Physiol, 2013. **305**(7): p. G483-95.
350. Dowman, J.K., et al., *Development of hepatocellular carcinoma in a murine model of nonalcoholic steatohepatitis induced by use of a high-fat/fructose diet and sedentary lifestyle*. Am J Pathol, 2014. **184**(5): p. 1550-61.
351. Scholten, D., et al., *The carbon tetrachloride model in mice*. Lab Anim, 2015. **49**(1 Suppl): p. 4-11.
352. Urtasun, R., et al., *Osteopontin, an oxidant stress sensitive cytokine, up-regulates collagen-I via integrin alpha(V)beta(3) engagement and PI3K/pAkt/NFkappaB signaling*. Hepatology, 2012. **55**(2): p. 594-608.
353. Waghorn, P.A., et al., *Quantitative, noninvasive MRI characterization of disease progression in a mouse model of non-alcoholic steatohepatitis*. Sci Rep, 2021. **11**(1): p. 6105.
354. European Association for the Study of the Liver, D. European Association for the Study of, and O. European Association for the Study of, *EASL-EASD-EASO Clinical Practice Guidelines for the management of non-alcoholic fatty liver disease*. J Hepatol, 2016. **64**(6): p. 1388-402.
355. Kleiner, D.E. and P. Bedossa, *Liver histology and clinical trials for nonalcoholic steatohepatitis-perspectives from 2 pathologists*. Gastroenterology, 2015. **149**(6): p. 1305-8.
356. Kleiner, D.E., et al., *Association of Histologic Disease Activity With Progression of Nonalcoholic Fatty Liver Disease*. JAMA Netw Open, 2019. **2**(10): p. e1912565.
357. Nouredin, N., et al., *Noninvasive Testing Using Magnetic Resonance Imaging Techniques as Outcomes in Nonalcoholic Steatohepatitis Clinical Trials: How Full Is the Glass?* Hepatol Commun, 2020. **4**(2): p. 141-144.
358. Kanwal, F., et al., *Clinical Care Pathway for the Risk Stratification and Management of Patients With Nonalcoholic Fatty Liver Disease*. Gastroenterology, 2021. **161**(5): p. 1657-1669.
359. Poynard, T., et al., *Impact of steatosis and inflammation definitions on the performance of NASH tests*. Eur J Gastroenterol Hepatol, 2018. **30**(4): p. 384-391.
360. Ito, M., et al., *Longitudinal analysis of murine steatohepatitis model induced by chronic exposure to high-fat diet*. Hepatol Res, 2007. **37**(1): p. 50-7.
361. Rinella, M.E., et al., *Report on the AASLD/EASL joint workshop on clinical trial endpoints in NAFLD*. J Hepatol, 2019. **71**(4): p. 823-833.
362. Nascimbeni, F., et al., *Clinical validation of the FLIP algorithm and the SAF score in patients with non-alcoholic fatty liver disease*. J Hepatol, 2020. **72**(5): p. 828-838.
363. Kim, D., et al., *Advanced Fibrosis in Nonalcoholic Fatty Liver Disease: Noninvasive Assessment with MR Elastography*. Radiology, 2013. **268**(2): p. 411-9.
364. Allen, A.M., et al., *The Role of Three-Dimensional Magnetic Resonance Elastography in the Diagnosis of Nonalcoholic Steatohepatitis in Obese Patients Undergoing Bariatric Surgery*. Hepatology, 2020. **71**(2): p. 510-521.
365. Qu, Y., et al., *Magnetic resonance elastography biomarkers for detection of histologic alterations in nonalcoholic fatty liver disease in the absence of fibrosis*. Eur Radiol, 2021. **31**(11): p. 8408-8419.
366. Yue, J.L., et al., *Acquisition and reconstruction conditions in silico for accurate and precise magnetic resonance elastography*. Phys Med Biol, 2017. **62**(22): p. 8655-8670.

367. Dietrich, O., et al., *Measurement of signal-to-noise ratios in MR images: influence of multichannel coils, parallel imaging, and reconstruction filters*. J Magn Reson Imaging, 2007. **26**(2): p. 375-85.
368. Testu, J., et al., *Viscoelastic power law parameters of in vivo human brain estimated by MR elastography*. J Mech Behav Biomed Mater, 2017. **74**: p. 333-341.
369. Komiyama, Y., et al., *Early diagnosis of hepatic inflammation in Japanese NAFLD patients using 3D MR elastography*. Hepatol Res, 2022.
370. Leporq, B., et al., *Quantification of the triglyceride fatty acid composition with 3.0 T MRI*. NMR Biomed, 2014. **27**(10): p. 1211-21.
371. de Bazelaire, C.M., et al., *MR imaging relaxation times of abdominal and pelvic tissues measured in vivo at 3.0 T: preliminary results*. Radiology, 2004. **230**(3): p. 652-9.
372. Messroghli, D.R., et al., *Modified Look-Locker inversion recovery (MOLLI) for high-resolution T1 mapping of the heart*. Magn Reson Med, 2004. **52**(1): p. 141-6.
373. Breit, H.C., et al., *Evaluation of liver fibrosis and cirrhosis on the basis of quantitative T1 mapping: Are acute inflammation, age and liver volume confounding factors?* Eur J Radiol, 2021. **141**: p. 109789.
374. Wan, Q., et al., *Water Specific MRI T1 Mapping for Evaluating Liver Inflammation Activity Grades in Rats With Methionine-Choline-Deficient Diet-Induced Nonalcoholic Fatty Liver Disease*. J Magn Reson Imaging, 2022.
375. Erden, A., et al., *MRI quantification techniques in fatty liver: the diagnostic performance of hepatic T1, T2, and stiffness measurements in relation to the proton density fat fraction*. Diagn Interv Radiol, 2021. **27**(1): p. 7-14.
376. Eylem Levelt, e.a., *Ectopic and Visceral Fat Deposition in Lean and Obese Patients With Type 2 Diabetes*. JO U RNAL OF THE AME R I CAN COLLEGE O F CARDIOLOGY, 2016.
377. Calucci, L. and C. Forte, *Proton longitudinal relaxation coupling in dynamically heterogeneous soft systems*. Progress in Nuclear Magnetic Resonance Spectroscopy, 2009. **55**: p. 296-323.
378. Zimmerman, J. and W.E. Brittin, *Nuclear magnetic resonance studies in multiple phase systems: lifetime of a water molecule in an adsorbing phase on silica gel*. The Journal of Physical Chemistry, 1957. **61**(10): p. 1328-1333.
379. Huo, M., et al., *Quantification of brown adipose tissue in vivo using synthetic magnetic resonance imaging: an experimental study with mice model*. Quant Imaging Med Surg, 2022. **12**(1): p. 526-538.
380. Lufkin, R., et al., *Magnetic field strength dependence of chemical shift artifacts*. Computerized medical imaging and graphics, 1988. **12**(2): p. 89-96.
381. Soher, B.J., B.M. Dale, and E.M. Merkle, *A review of MR physics: 3T versus 1.5 T*. Magnetic resonance imaging clinics of North America, 2007. **15**(3): p. 277-290.
382. Xiaoyu Jiang, e.a., *In vivo magnetic resonance imaging of treatment-induced apoptosis*. Scientific Reports, 2019.
383. Junzhong Xu, e.a., *Quantitative Characterization of Tissue Microstructure with Temporal Diffusion Spectroscopy*. J Magn Reson Imaging, 2009.
384. Gore, J.C., et al., *Characterization of tissue structure at varying length scales using temporal diffusion spectroscopy*. NMR Biomed, 2010. **23**(7): p. 745-56.
385. Xu, J., M.D. Does, and J.C. Gore, *Quantitative characterization of tissue microstructure with temporal diffusion spectroscopy*. J Magn Reson, 2009. **200**(2): p. 189-97.
386. Xiaoyu Jiang, e.a., *Quantification of Cell Size Using Temporal Diffusion Spectroscopy*. Magnetic Resonance in Medicine, 2016.

387. Colvin, e.a., *Earlier detection of tumor treatment response using magnetic resonance diffusion imaging with oscillating gradients*. Magn Reson Imaging, 2011.
388. Xu, J., et al., *Magnetic resonance imaging of mean cell size in human breast tumors*. Magn Reson Med, 2020. **83**(6): p. 2002-2014.
389. Xiaoyu Jiang, e.a., *Mapping hepatocyte size in vivo using temporal diffusion spectroscopy MRI*. Magnetic Resonance in Medicine, 2020.
390. Ijin Joo, e.a., *Nonalcoholic Fatty Liver Disease: Intravoxel Incoherent Motion Diffusion-weighted MR Imaging - An Experimental Study in a Rabbit Model*. Radiology, 2014.
391. Bachir Taouli , e.a., *Chronic hepatitis: role of diffusion-weighted imaging and diffusion tensor imaging for the diagnosis of liver fibrosis and inflammation* J Magn Reson Imaging, 2008.
392. Helena S. Leitão, e.a., *Hepatic Fibrosis, Inflammation, and Steatosis: Influence on the MR Viscoelastic and Diffusion Parameters in Patients with Chronic Liver Disease*. Radiology, 2016.
393. Rahman, N., et al., *Test-retest reproducibility of in vivo oscillating gradient and microscopic anisotropy diffusion MRI in mice at 9.4 Tesla*. PLoS One, 2021. **16**(11): p. e0255711.
394. Stejskal, E.O. and J.E. Tanner, *Spin Diffusion Measurements: Spin Echoes in the Presence of a Time-Dependent Field Gradient*. Journal of Chemical Physics, 1965. **42**: p. 288-292.
395. David E. Kleiner, e.a., *Design and Validation of a Histological Scoring System for Nonalcoholic Fatty Liver Disease*. HEPATOLOGY, 2005.
396. Anneloes E. Bohte, e.a., *MR Elastography of the Liver: Defining Thresholds for Detecting Viscoelastic Changes*. Radiology, 2013.
397. Reynaud, O., et al., *Surface-to-volume ratio mapping of tumor microstructure using oscillating gradient diffusion weighted imaging*. Magn Reson Med, 2016. **76**(1): p. 237-47.
398. Novikov, D.S. and V.G. Kiselev, *Surface-to-volume ratio with oscillating gradients*. J Magn Reson, 2011. **210**(1): p. 141-5.
399. Reynaud, O., *Time-dependent diffusion MRI in cancer: tissue modeling and applications*. Frontiers in Physics, 2017. **5**: p. 58.
400. Jiang, X., et al., *MR cell size imaging with temporal diffusion spectroscopy*. Magn Reson Imaging, 2021. **77**: p. 109-123.
401. Manning, P., et al., *Liver histology and diffusion-weighted MRI in children with nonalcoholic fatty liver disease: A MAGNET study*. Journal of Magnetic Resonance Imaging, 2017. **46**(4): p. 1149-1158.
402. Leitao, H.S., et al., *Fat deposition decreases diffusion parameters at MRI: a study in phantoms and patients with liver steatosis*. Eur Radiol, 2013. **23**(2): p. 461-7.
403. Khalfallah, M., et al. *Abstract 2135 : Temporal diffusion spectroscopy with oscillating gradient echoplanar MRI : signal to noise and ADC repeatability in mice liver. in Proceedings of the 2021 joint International Society for Magnetic Resonance in Medicine conference. 2021.*
404. Davison, B.A., et al., *Suboptimal reliability of liver biopsy evaluation has implications for randomized clinical trials*. J Hepatol, 2020. **73**(6): p. 1322-1332.
405. Gawrieh, S., et al., *Effects of interventions on intra- and interobserver agreement on interpretation of nonalcoholic fatty liver disease histology*. Ann Diagn Pathol, 2011. **15**(1): p. 19-24.

406. Kuwashiro, T., et al., *Discordant pathological diagnosis of non-alcoholic fatty liver disease: A prospective multicenter study*. JGH Open, 2020. **4**(3): p. 497-502.
407. Krittayaphong, R., et al., *Detection of cardiac iron overload with native magnetic resonance T1 and T2 mapping in patients with thalassemia*. International journal of cardiology, 2017. **248**: p. 421-426.
408. Le Bihan, D., et al., *MR imaging of intravoxel incoherent motions: application to diffusion and perfusion in neurologic disorders*. Radiology, 1986. **161**(2): p. 401-7.
409. Yamada, I., et al., *Diffusion coefficients in abdominal organs and hepatic lesions: evaluation with intravoxel incoherent motion echo-planar MR imaging*. Radiology, 1999. **210**(3): p. 617-23.
410. Luciani, A., et al., *Liver cirrhosis: intravoxel incoherent motion MR imaging--pilot study*. Radiology, 2008. **249**(3): p. 891-9.
411. Patel, J., et al., *Diagnosis of cirrhosis with intravoxel incoherent motion diffusion MRI and dynamic contrast-enhanced MRI alone and in combination: preliminary experience*. J Magn Reson Imaging, 2010. **31**(3): p. 589-600.
412. Wu, D. and J. Zhang, *The Effect of Microcirculatory Flow on Oscillating Gradient Diffusion MRI and Diffusion Encoding with Dual-Frequency Orthogonal Gradients (DEFOG)*. Magn Reson Med, 2017. **77**(4): p. 1583-1592.
413. Wetscherek, A., B. Stieltjes, and F.B. Laun, *Flow-compensated intravoxel incoherent motion diffusion imaging*. Magn Reson Med, 2015. **74**(2): p. 410-9.
414. Ryan, J.D., et al., *Hepatic iron is the major determinant of serum ferritin in NAFLD patients*. Liver Int, 2018. **38**(1): p. 164-173.
415. Radmard, A.R., et al., *Liver enzyme levels and hepatic iron content in Fatty liver: a noninvasive assessment in general population by T2* mapping*. Acad Radiol, 2015. **22**(6): p. 714-21.
416. Hui, S.C.N., et al., *Validation of water-fat MRI and proton MRS in assessment of hepatic fat and the heterogeneous distribution of hepatic fat and iron in subjects with non-alcoholic fatty liver disease*. Eur J Radiol, 2018. **107**: p. 7-13.
417. Deng, J., et al., *Quantitative MRI for hepatic fat fraction and T2* measurement in pediatric patients with non-alcoholic fatty liver disease*. Pediatr Radiol, 2014. **44**(11): p. 1379-87.
418. Reeder, S.B., et al., *Quantification of hepatic steatosis with MRI: the effects of accurate fat spectral modeling*. J Magn Reson Imaging, 2009. **29**(6): p. 1332-9.
419. Joo, I., et al., *Nonalcoholic fatty liver disease: intravoxel incoherent motion diffusion-weighted MR imaging-an experimental study in a rabbit model*. Radiology, 2014. **270**(1): p. 131-40.
420. Tamaki, N., V. Ajmera, and R. Loomba, *Non-invasive methods for imaging hepatic steatosis and their clinical importance in NAFLD*. Nat Rev Endocrinol, 2022. **18**(1): p. 55-66.
421. Jiang, X., et al., *Quantification of cell size using temporal diffusion spectroscopy*. Magn Reson Med, 2016. **75**(3): p. 1076-85.
422. Xu, J., et al., *Characterizing tumor response to chemotherapy at various length scales using temporal diffusion spectroscopy*. PLoS One, 2012. **7**(7): p. e41714.

8. Appendix

8.1. MRE parametric maps

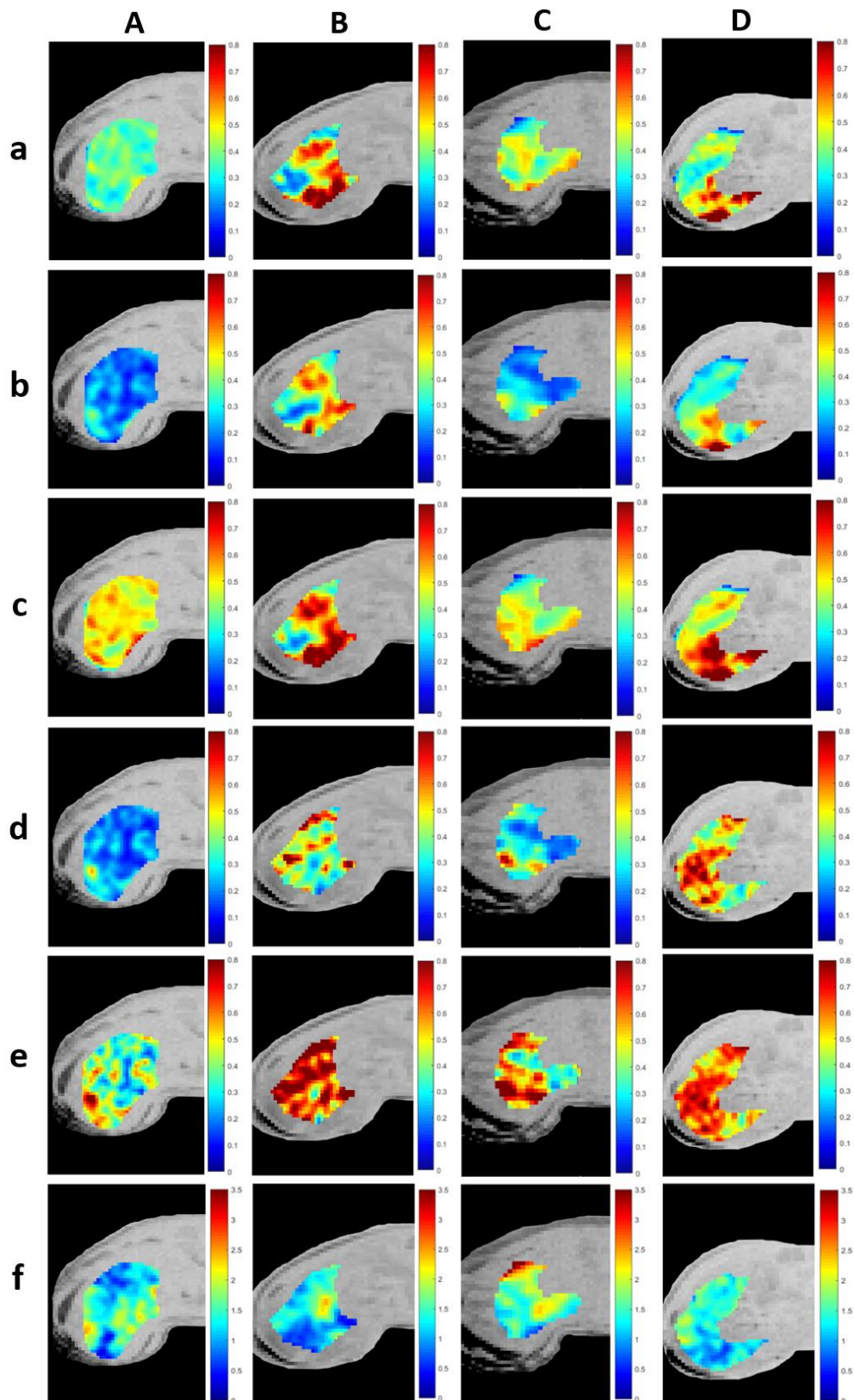


Figure 8.1. 1: Representative MRE visco-elastic parameter maps of a) storage modulus (color scale in kPa); b) loss modulus (color scale in kPa), c) shear stiffness (color scale in kPa), d) damping ratio (color scale is adimensional), e) shear stiffness phase angle (colorscale in radians) and f) mmultifrequency dispersion coefficient (colorscale is adimensional) for A) mouse with NAFL, B) mouse with fibro-NAFL, C) mouse with early NASH and D) mouse with fibro-NASH. The mean value of each parameter for each mouse are presented in the table below:

Visco-elastic parameters	Mouse with NAFL	Mouse with Fibro-NAFL	Mouse with Early NASH	Mouse with Fibro-NASH
Storage modulus (kPa)	0.50 ± 0.12	0.65 ± 0.29	0.48 ± 0.19	0.75 ± 0.39
Loss modulus (kPa)	0.24 ± 0.09	0.58 ± 0.28	0.28 ± 0.15	0.59 ± 0.29
Shear stiffness (kPa)	0.57 ± 0.14	0.80 ± 0.40	0.58 ± 0.25	0.79 ± 0.40
Damping ratio (adim.)	0.24 ± 0.36	0.45 ± 0.48	0.30 ± 0.39	0.36 ± 0.37
Shear stiffness phase angle (rad)	0.45 ± 0.14	0.73 ± 0.14	0.55 ± 0.36	0.63 ± 0.16
Multifrequency dispersion coefficient (adim.)	3.00 ± 0.79	2.80 ± 1.01	3.09 ± 1.78	2.60 ± 1.42

8.2. Résumé

Introduction

L'hépatopathie stéatosique non alcoolique (non alcoholic fatty liver disease, NAFLD) est l'une des principales causes de lésions hépatiques chroniques affectant environ 25 % de la population adulte dans le monde [1, 3]. Il s'agit d'une cause croissante de maladie hépatique, entraînant une morbidité et une mortalité hépatiques élevées [3]. La NAFLD englobe un spectre dynamique de lésions histologiques allant de la simple stéatose à une forme progressive avec des lésions actives de ballonnisation hépatocytaire et d'inflammation hépatique conduisant à la fibrose et à la cirrhose. Il existe plusieurs définitions de formes progressives de la NAFLD. En effet, outre la stéatohépatite non alcoolique (non alcoholic steatohepatitis, NASH), les formes progressives peuvent être basées sur la présence de fibrose, incluant la maladie hépatique métabolique significative (metabolic liver disease, MLD), la fibrose liée à la NASH et la fibro-NASH [11, 42, 46, 359]. Le diagnostic de ces formes progressives de NAFLD de la maladie nécessite une analyse histologique du foie. L'histologie étant souvent réalisée sur une biopsie hépatique, cette méthode présente donc des inconvénients liés au caractère invasif de la biopsie, au biais de prélèvement et à la reproductibilité inter et intra-opérateur imparfaite de l'analyse histologique.

Par conséquent, une méthode non invasive et précise pour diagnostiquer et caractériser la NAFLD est souhaitable [12, 113]. L'imagerie par résonance magnétique (IRM) est une approche multiparamétrique non invasive bien adaptée à la caractérisation de l'ensemble du foie. Plusieurs marqueurs quantitatifs issus de l'IRM ont été associés aux caractéristiques de la NAFLD. On citera notamment la fraction de graisse (proton density fat fraction, PDFF) utilisée pour estimer la quantité de stéatose hépatique [100, 112, 418]. Les propriétés mécaniques du foie, que l'on peut mesurer avec l'élastographie par résonance magnétique (ERM) [247] permet de diagnostiquer la fibrose et l'inflammation hépatique chez les patients atteints de NAFLD [158, 209, 251, 253, 363]. Le temps de relaxation T1, obtenu avec les méthodes IRM de relaxométrie T1, croît avec l'augmentation du liquide extracellulaire dans la fibrose et l'inflammation [267]. Finalement, le coefficient de diffusion apparent (apparent diffusion coefficient, ADC) qui reflète les propriétés microstructurales des tissus biologiques

sur une échelle spatiale plus petite que le diamètre d'une cellule, peut être étudié au moyen de la spectroscopie temporelle de diffusion utilisant l'imagerie par écho de spin à gradient oscillant (oscillating gradient spin echo, OGSE). L'OGSE est une approche alternative d'imagerie pondérée en diffusion, utilisant des gradients d'encodage de diffusion oscillants. Plusieurs études ont rapporté que la stéatose [419], l'inflammation [317, 419] et la fibrose [222, 317] peuvent affecter les mesures de l'ADC.

L'objectif de notre étude préclinique est de développer et d'évaluer l'apport de ces méthodes d'IRM quantitatives pour le diagnostic des formes progressives de NAFLD et de ses caractéristiques histopathologiques, en utilisant des modèles murins de la maladie.

Nous avons utilisé deux modèles alimentaires murins, d'une part un modèle obésogène riche en graisses "High Fat Diet" (HFD) qui reproduit la stéatose hépatique simple (non alcoholic fatty liver disease, NAFL) et d'autre part le modèle déficient en choline et défini en acides aminés L ("choline deficient with defined L-amino acids - high fat diet", CDA-HFD) qui reproduit des caractéristiques de la NASH [346, 347]. Une étude histologique de la NAFLD a en outre été réalisée dans un modèle de régime alimentaire occidental (Western Diet, WD) qui a été rapporté reproduire les stades progressifs de NAFLD, de la stéatose simple à l'inflammation, la fibrose et la NASH [10].

Chapitre I: Modèles animaux de NAFLD/NASH

Comprendre la physiopathologie de la NASH reste un défi. Par conséquent, des modèles précliniques de cette maladie sont nécessaires. Plusieurs modèles murins de NASH ont été décrits [336, 346], mais aucun modèle peut reproduire entièrement tous les déterminants lésionnels de la NASH humaine. Le modèle WD consiste en un régime riche en graisses, en fructose et en cholestérol et peut être associé à une faible dose hebdomadaire de tétrachlorure de carbone (CCl₄) intrapéritonéal, dont les propriétés pro-inflammatoires servent à accélérer l'évolution de la maladie. Il a été montré que ce modèle peut entraîner une progression vers la fibrose avancée (F3) et la NASH sévère en 12 semaines d'induction et vers un cancer hépatique en 24 semaines. De plus, ce modèle présente des caractéristiques histologiques, immunologiques et transcriptomiques similaires à la NASH humaine [10].

Nous avons réalisé une étude histologique de la NAFLD en utilisant un WD combiné à une faible dose de CCl₄, chez la souris, pour une durée de 6, 12 et 16 semaines.

Seule une stéatose hépatique avec inflammation et fibrose modérées a été observée. Aucune ballonnisation hépatocellulaire n'a été détectée. Plusieurs raisons expliquer ces résultats, notamment la température ambiante et le microbiote de l'animalerie, les souris ayant subi un changement de régime alimentaire (d'un régime normal à un WD) à 8 semaines et le stress causé par les injections intrapéritonéales de CCl₄. De plus, 16 semaines de régime auraient pu être insuffisantes pour obtenir une NASH.

Ensuite, une deuxième étude a été réalisée dans de meilleures conditions d'hébergement des animaux en utilisant un modèle CDA-HFD avec inversion de régime comme traitement de la NASH [559] (souris âgées de 8 semaines avec 10 et 16 semaines de régime CDA-HFD suivi de 0, 1 ou 4 semaines de régime inversé (régime normal, ND))

Dans ce modèle, les souris ont développé des scores avancés de stéatose, d'inflammation et de fibrose dès 10 semaines de régime. Cependant, aucune ballonnisation hépatocytaire n'a été détectée (et en conséquence pas de NASH).

La stéatose a diminué après une semaine et a disparu après 4 semaines de diète normale. L'inflammation et la fibrose ont légèrement diminué mais n'ont pas totalement disparu, ce qui suggère que l'inflammation et surtout la fibrose hépatique nécessitent des périodes plus longues avec une alimentation saine pour disparaître.

Pour conclure, le modèle murin de NASH « CDA-HFD » permet d'induire des stades plus avancés de stéatose, d'inflammation et de fibrose que le modèle de souris WD combiné au modèle CCl₄.

Chapitre II : IRM préclinique multiparamétrique de la NAFLD

Cette étude préclinique d'IRM multiparamétrique de la NAFLD comporte deux parties. La première partie est applicative et concerne le diagnostic de la NAFLD par ERM tandis que la seconde est méthodologique et concerne les méthodes de cartographie PDFF et T1.

Trois groupes de souris ont été inclus dans cette étude : un groupe ND, un groupe HFD et un groupe CDA-HFD avec 4, 10 et 16 semaines comme durées des régimes. Toutes les souris ont été sacrifiées après imagerie, leurs foies ont été analysés par un anatomopathologiste hépatique pour évaluer la stéatose, l'inflammation, la ballonnisation hépatocytaire et la fibrose en se basant sur le système de classification NASH Clinical Research Network [12, 361].

Les acquisitions IRM ont été réalisées à l'aide d'un système d'imagerie 7T (Pharmascan - Bruker, Erlangen, Allemagne). Les animaux ont été anesthésiés à l'isoflurane. Les données en IRM ont consisté en une élastographie multifréquence (à 200 Hz, 400 Hz, et 600 Hz), une détermination de PDFF et $R2^*$ et une détermination du temps de relaxation $T1$.

1) Diagnostic de la NAFLD : Élastographie par résonance magnétique (ERM)

Les paramètres mécaniques obtenus par EMR sont utiles pour le diagnostic de la fibrose hépatique et de l'inflammation chez les patients atteints de NAFLD, y compris à des stades précoces de la maladie [48, 49, 125, 158, 171, 209, 235, 251, 253, 363-365]. Cependant, la performance diagnostique des paramètres ERM dans l'évaluation des formes progressives de la NAFLD (c'est-à-dire NASH, MLD significative, fibrose liée à la NASH et fibro-NASH) reste à clarifier. Par conséquent, le but de cette étude préclinique est d'étudier le rôle des paramètres mécaniques obtenus par ERM dans la détection des caractéristiques histopathologiques de la NAFLD, en particulier l'inflammation, la fibrose et la ballonnisation hépatocellulaire, et dans le diagnostic des formes progressives de la maladie, chez les souris atteintes de NAFLD.

Les paramètres mécaniques monofréquences (le module de cisaillement/paramètre lié à la rigidité du tissu ($|G^*| = \sqrt{G'^2 + G''^2}$), le module de stockage/paramètre lié à l'élasticité du tissu G' , le module de perte/paramètre lié à la viscosité du tissu G'' , le taux d'amortissement ($\zeta = G''/(2G')$) [235], l'angle de phase du module de cisaillement ($\alpha = \text{atan}(G''/G')$) et le coefficient de dispersion multifréquence (γ_{G^*}) [191]) ont été calculés. Pour les paramètres monofréquentiels, nous nous sommes concentrés sur les résultats à 400 Hz dans cette étude car l'amplitude de l'onde et les valeurs du rapport signal à bruit étaient les meilleures à cette fréquence. De plus, les souris avec un foie sain à l'histologie n'ont pas été incluses dans cette évaluation.

L'évaluation de la relation entre les paramètres ERM et les caractéristiques histologiques a montré que les modules de stockage, de perte et de cisaillement étaient corrélés avec la fibrose et dans une moindre mesure avec l'inflammation et la stéatose. Le coefficient de dispersion fréquentielle était corrélé à la fibrose et dans une moindre mesure à l'inflammation. Le taux d'amortissement et l'angle de phase étaient corrélés à la fibrose. Cependant, aucun des paramètres biomécaniques n'était corrélé à la ballonnisation hépatocytaire. Ces résultats ont été confirmés par les résultats de l'analyse multivariée où il a été mis en évidence que la fibrose avait une influence significative sur tous les biomarqueurs biomécaniques, en particulier sur le module de perte. De plus les paramètres biomécaniques avaient une meilleure performance pour le diagnostic de la MLD significative, de la fibrose liée à la NASH et du fibro-NASH que pour le diagnostic de NASH.

Ces résultats suggèrent que les paramètres mécaniques hépatiques obtenus par ERM sont plus performants pour diagnostiquer la MLD significative, la fibro-NASH et la fibrose liée à la NASH, que pour diagnostiquer la NASH. Cela peut s'expliquer par le fait que des souris sans NASH peuvent présenter une fibrose significative, qui altère les paramètres mécaniques à l'ERM. De plus, les définitions histologiques de la MLD significative et de la fibrose liée à la NASH ne dépendent pas de la ballonnisation hépatocellulaire qui est une caractéristique importante dans la définition de la NASH. Nos résultats suggèrent que l'ERM a de faibles performances dans la détection de la ballonnisation hépatocytaire et donc dans le diagnostic de la NASH.

2) Développements méthodologiques pour la mesure de la PDFF et du T1 dans les modèles murins de la NAFLD

a) PDFF

La mesure de la PDFF en IRM est actuellement reconnue comme une méthode robuste pour quantifier de manière non invasive la concentration de triglycérides dans le tissu hépatique. Cette mesure a été utilisée dans de multiples études précliniques et cliniques [94, 100, 102, 105, 112, 118, 125, 418, 420]. Notre étude a été réalisée dans le but d'évaluer la reproductibilité de notre séquence PDFF, de définir une procédure standardisée optimisée pour le positionnement de la région d'intérêt, et d'analyser les performances diagnostiques

de la PDFF dans des modèles murins de NAFLD pour détermination des grades de stéatose et de la présence de NASH.

Pour cela les régions d'intérêt ont été positionnées par deux opérateurs sur la plus grande section possible du foie en évitant les vaisseaux et les bords des organes. Deux ensembles distincts de régions d'intérêt ont été générés par chaque opérateur ; le premier sur des coupes choisies indépendamment par chaque opérateur et le second sur des coupes choisies indépendamment par chaque opérateur mais selon une procédure commune définissant la coupe cible comme la seconde coupe au-dessus du dôme rénal. Cet emplacement a été choisi pour faire correspondre l'emplacement de l'analyse IRM à celui de l'analyse histologique, celle-ci ayant été faite sur le lobe hépatique médial droit.

La répétabilité inter-opérateur de la PDFF était meilleure avec la procédure standardisée (coefficients de répétabilité de 32% et de 54% avant standardisation). En accord avec les résultats de la littérature, nous avons également montré que la PDFF ainsi standardisée, était un bon marqueur de la stéatose. Cependant, la PDFF montrait une faible sensibilité à la présence de NASH parmi une population de stéatose simple, ce qui peut s'expliquer par la présence de niveaux avancés de stéatose dans les deux groupes stéatose simple et NASH.

Nous avons confirmé que la PDFF obtenue par IRM après standardisation des régions d'intérêt était un biomarqueur précis pour détecter la stéatose hépatique avec l'histologie comme référence.

b) Cartographie du temps de relaxation T1

Le temps de relaxation T1 est associé aux altérations hépatiques dues aux maladies chroniques du foie. En effet, l'inflammation et la fibrose hépatiques augmentent les valeurs de T1 en raison de l'augmentation de la concentration d'eau et de protéines extracellulaires [240, 259, 267, 269-271]. La mesure du T1 peut ainsi être utile pour diagnostiquer l'inflammation et la fibrose associées à la NASH. Cependant, des études ont rapporté que la graisse a un effet confondant sur les mesures de T1 [274, 275]. Dans cette étude préclinique, nous avons étudié si les mesures de T1 du foie sont sensibles à l'inflammation et à la fibrose hépatiques chez des souris ayant une NAFLD et nous avons étudié l'effet confondant de la stéatose.

Nos résultats ont montré que les valeurs de T1 étaient influencées par l'inflammation et la fibrose hépatique mais que cette influence était moindre que celle de la stéatose. Pour éliminer cet effet de la graisse dans les hépatocytes sur le T1, un modèle à deux compartiments (graisse/eau) sans échanges et tenant compte de la fraction volumique de graisse déterminée par PDFF, a été utilisé soit sur les valeurs de R1 obtenues avec une expression du signal mono-compartimentale, soit en implémentant le modèle bicompartimental directement au niveau de l'expression du signal utilisée pour l'étape d'ajustement des données. Pour valider ce modèle, une étude sur fantôme biphasique a été réalisée avec un tube horizontal contenant de l'huile de tournesol comme compartiment gras et une solution d'acide gadotérique (0,13 mM) comme compartiment aqueux. Dans le fantôme, le modèle de relaxation bicompartimental T1 permettait de compenser la présence de graisse avec une erreur de 10%. Dans le modèle murin de la NASH, le T1 corrigé pour la graisse était significativement plus élevé que le T1 non corrigé lorsque la fraction de graisse était importante. Au contraire, lorsque la fraction de graisse était faible, les T1 corrigés et non corrigés étaient similaires.

Chapitre III: Spectroscopie temporelle de diffusion avec imagerie écho-planaire à gradients oscillants

En IRM de diffusion, on utilise habituellement des séquences PGSE (pulse gradient spin echo) qui ne permettent d'observer la diffusion que sur des temps longs. Au contraire, les méthodes de spectroscopie temporelle de diffusion avec OGSE permettent d'interroger spécifiquement une échelle spatiale donnée en vertu du contenu fréquentiel des gradients d'encodage de diffusion. La spectroscopie temporelle de diffusion a été utilisée pour estimer les changements de taille nucléaire après un traitement anticancéreux [336, 421, 422], pour mesurer la taille des cellules dans le cancer du sein [388], pour sonder la diffusion de l'eau dans la matière grise du rat ischémique [327] ou pour caractériser les nodules hépatocellulaires dans la cirrhose chez le rat [345]. Plus récemment, l'OGSE avec lecture EPI (echo planar imaging) a été utilisée pour caractériser la taille des hépatocytes[332]. De plus, plusieurs études utilisant la PGSE (séquence conventionnelle de diffusion) ont montré que la stéatose [419], l'inflammation [317, 419], la fibrose [317] et certaines combinaisons [222] de ces caractéristiques pouvaient affecter les mesures de l'ADC.

Le but de cette étude a été de développer et de valider une méthode de spectroscopie temporelle de diffusion pour l'évaluation des caractéristiques histologiques, en particulier la ballonisation hépatocytaire dans la NASH.

Dans cette étude, une séquence de spectroscopie temporelle de diffusion utilisant un encodage par gradients oscillants (OGSE) a été créée avec un train de lecture EPI afin de raccourcir le temps d'acquisition. Cette nouvelle séquence « OGSE-EPI » a été obtenue en insérant des gradients oscillants symétriquement de part et d'autre de l'impulsion de refocalisation de la séquence EPI. Tout d'abord, une forme d'onde modulée à double sinus a été implémentée car son contenu en fréquence est important à la fréquence principale et nul à fréquence nulle, tout en ne requérant que peu de puissance de la part des gradients [329]. Cette séquence a été validée, et sa répétabilité a été étudiée chez des souris saines avec différentes configurations matérielles, plusieurs fréquences et valeurs de b , avec ou sans synchronisation respiratoire. Les résultats ont montré que les coefficients de répétabilité et le rapport signal à bruit étaient meilleurs avec l'utilisation de l'antenne de surface à 4 canaux et que la synchronisation respiratoire était cruciale pour les mesures.

Pour améliorer la séquence d'acquisition, une forme trapézoïdale de gradients d'encodage a été implémentée [388]. En effet, cette forme d'encodage fournit une valeur de b maximale plus élevée (grâce à des exigences nettement réduites sur la puissance des gradients) tout en permettant de maintenir un spectre d'encodage similaire à celui du double sinus [329].

Après programmation de la séquence, une étude de validation sur fantômes a été réalisée en utilisant des culots de centrifugation de microsphères de latex et polystyrène (Polysciences) de plusieurs diamètres compris entre 3 et 150 μm . Ces microsphères ont été utilisées pour obtenir des canaux de diffusion inter-billes dont la taille caractéristique était uniforme et contrôlée par le diamètre des billes [329]. Ces échantillons ont été imagés à plusieurs fréquences (i.e. échelles spatiales) et plusieurs valeurs de b . Nous avons observé que les valeurs d'ADC augmentaient avec la taille des microsphères (i.e. l'augmentation de l'échelle spatiale caractéristique de l'échantillon). Ces résultats sont en conformité avec la théorie de l'imagerie de diffusion OGSE, selon laquelle plus l'échelle spatiale augmente, plus les valeurs d'ADC augmentent jusqu'à la valeur limite supérieure du coefficient d'autodiffusion du fluide considéré [327-329]. De plus, nos résultats ont montré que, à chaque taille d'échantillon, les

valeurs d'ADC augmentaient avec la fréquence, ce qui est également cohérent avec la théorie de l'imagerie OGSE [329].

Application dans des modèles murins de NAFLD

Après validation de la séquence, une étude préclinique a été réalisée pour déterminer si l'ADC à différentes fréquences était un biomarqueur de la NAFLD ou d'une de ses caractéristiques histologiques. Cette hypothèse a été testée chez des souris avec deux modèles alimentaires (HFD et CDA-HFD) et deux approches thérapeutiques par arrêt du régime obésogène. Les examens IRM ont compris une séquence PGSE-EPI (fréquence centrale 47 Hz), une séquence OGSE-EPI avec encodage trapézoïdal à 130 Hz et 250 Hz et une séquence en écho de gradients à échos multiples pour déterminer la PDFF et le $R2^*$. Après imagerie, les souris ont été sacrifiées et leurs foies ont été analysés à l'aveugle par un pathologiste pour diagnostiquer la présence et la sévérité de la stéatose, de l'inflammation, de la ballonnisation et de la fibrose.

Les résultats de cette étude ont montré que la fibrose n'était corrélée qu'avec l'ADC_{PGSE}. La ballonnisation et l'inflammation étaient corrélés à l'ADC à la fréquence intermédiaire de 130 Hz. La stéatose était corrélée à l'ADC aux fréquences intermédiaires (130 Hz) et hautes (250 Hz). La PDFF était fortement corrélée à la stéatose et modérément corrélée à la ballonnisation et à l'inflammation. Les mesures d'ADC à 250 Hz avaient une bonne performance pour le diagnostic de la NASH, tandis que les mesures ADC à 130 Hz et l'ADC_{PGSE} ainsi que la mesure de la PDFF avaient de mauvaises performances diagnostiques pour la NASH.

Le groupe de souris ayant reçu un régime riche en graisse (CDA-HFD) pendant 10 semaines avait une ADC_{PGSE} significativement plus bas que le groupe contrôle, et cette baisse était inversée par l'arrêt de la diète obésogène. L'ADC à 130 Hz était significativement plus élevé dans les 4 groupes d'inversion de régime par rapport au groupe ayant une diète obésogène. À 250 Hz, les mesures ADC n'étaient significativement plus élevées que dans les groupes de 4 et de 8 semaines de diète normale par rapport au groupe ayant une diète obésogène.

Ces résultats suggèrent que la stéatose affecte principalement les valeurs d'ADC interrogées à de petites échelles spatiales, que l'inflammation et la ballonnisation ont un impact sur l'ADC à des échelles spatiales intermédiaires et que la fibrose a un impact sur l'ADC à de plus grandes échelles spatiales. L'analyse des performances de diagnostic montrait que seules les

mesures d'ADC à petite échelle spatiale (250 Hz) avaient des performances significatives pour le diagnostic de la NASH. Comme le seul facteur histopathologique qui différencie la NASH de la stéatose simple est la ballonisation, cela suggère que la ballonisation peut avoir un effet sur les mesures de l'ADC même à de petites échelles spatiales, bien que cet effet puisse être partiellement masqué par l'accumulation de lipides qui l'accompagne. De plus, l'application de l'inversion du régime alimentaire comme thérapie pour la NAFLD entraînait une ré-augmentation des valeurs de l'ADC. Cette variation bidirectionnelle du marqueur d'imagerie (une diminution lors du développement de la pathologie, et une augmentation lors de sa résorption), pourrait rendre ce biomarqueur utile pour interroger l'efficacité de traitements de la NASH.

CONCLUSION GÉNÉRALE

Dans notre étude de NAFLD avec IRM multiparamétrique chez des souris, des résultats intéressants ont été obtenus en ERM et en IRM PDFF et T1. En particulier, nous avons montré la performance diagnostique supérieure des paramètres viscoélastiques en ERM pour le diagnostic de formes progressives fibrosantes de NAFLD que pour le diagnostic de NASH.

De plus, un meilleur modèle de correction de l'effet de la stéatose sur les valeurs de T1 est nécessaire pour une évaluation du rôle de ce paramètre dans le diagnostic de la NAFLD.

Enfin, la spectroscopie temporelle de diffusion avec la séquence OGSE pourrait être un outil prometteur pour détecter la ballonisation hépatocellulaire et, par conséquent, diagnostiquer la NASH.

8.3. List of tables

Table 1.1. 1: Scoring systems for evaluating the different histological features of NAFLD based on liver biopsy in NAFLD patients.	18
Table 1.2. 1: Examples of high fat diets used to induce NAFLD/NASH with diet composition and the resulting NAFLD histological features, displayed according to diet duration.	27
Table 1.2. 2: Examples of CDA-HFD models used to induce NAFLD/NASH with diet composition and the resulting NAFLD histological features, displayed according to diet duration.	29
Table 1.2. 3: Examples of Western diets used to induce NAFLD/NASH with diet composition and the resulting NAFLD histological features, displayed according to diet duration.	30
Table 3.1. 1: Mice number per group after 6 and 12 weeks of induction.....	64
Table 3.2. 1: The final mice cohort included in this study.	73
Table 3.2. 2: Histological results for the WD and the CDA-HFD mouse models.	80
Table 4.2. 1: Wave amplitude and SNR measurements mean values for each of the three frequencies.	92
Table 4.2. 2: Results of the analysis of the relationship between the mechanical parameters measured at 400Hz and the histological features of NAFLD with Spearman’s Rank correlations. In gray, statistically non-significant values.	100
Table 4.2. 3: Results of multivariate analysis using stepwise multiple regression the mechanical parameters as dependent variables and the histological features of NAFLD as independent variables.	100
Table 4.2. 4: Univariate analysis of the relationship between the mechanical parameters using Spearman’s rank correlations. Correlation is considered high when $r \geq 0.9$. In gray, statistically non-significant values.	101
Table 4.2. 5: Univariate analysis of the relationship between the mechanical parameters and the histological features of NAFLD using Spearman’s rank correlations. In gray, statistically non-significant values.	102
Table 4.2. 6: Multivariate analysis using stepwise multiple regression with the mechanical parameters as the dependent variables and the histological features of NAFLD as the independent variables.	103

Table 4.2. 7: Differences of MRE parameters between groups without/with NASH, significant MLD, NASH-related fibrosis and fibro-NASH.	104
Table 4.2. 8: Results of ROC curve analysis of mechanical parameters (mono-frequency parameters at 400Hz and multi-frequency dispersion coefficient) for diagnosing NASH, significant MLD, NASH-related fibrosis and fibro-NASH. In gray, parameters with statistically non-significant p-values.	110
Table 4.3. 1: PDFF data acquisitions parameters.....	117
Table 4.3. 2: Mann-Whitney results comparing T1 before and after correction vs. steatosis grades.....	129
Table 4.3. 3: Mann-Whitney results comparing T1 before and after correction vs. steatosis grades.....	131
Table 5. 1: The effective diffusion times and characteristic diffusion lengths for the OGSE and PGSE acquisitions.....	145
Table 5. 2: Acquisition parameters for the OGSE and the PGSE sequences for phantom and mouse NAFLD studies.	148
Table 5. 3: ADC measurements(mean (standard deviation)) in mm ² /s for the different tested bead sizes and frequencies.....	149
Table 5. 4: ADCs, repeatability, and SNR according to the different conditions used in our study.....	156
Table 5. 5: Mice groups included in this study	160
Table 5. 6: Mean ADC according to frequency and diet.....	161
Table 5. 7: Spearman rank correlations between MRI parameters and histological features of NAFLD.....	166

8.4. List of figures

Figure 1.1. 1: Representative histological sections: A) picrosirius red stained slice and B) hematoxylin-eosin stained slice. On A), the black circle indicates steatosis, the accumulation of lipids within hepatocytes, the yellow circle indicates ballooned hepatocytes which exhibit a clear, flocculent, non-vacuolar cytoplasm and a balloon-like shape described as the loss of sharp angles in the liver cell, while the blue ellipse shows lobular inflammation which includes small foci of inflammatory cells (lymphocytes and macrophages, sometimes associated with hepatocyte dropout or apoptotic bodies) within the hepatic lobules. On B), the purple ellipse indicates fibrosis described as hepatic tissue scarring caused by a relatively long wound-healing process which involves progressive accumulation of extracellular matrix proteins, mainly collagen.19

Figure 1.1. 2 : The FLIP algorithm used for diagnosing NAFLD and NASH. This algorithm is only a classification method and does not necessarily denote the order in which the lesions appear in the course of disease progression. (from: *Bedossa P. et al., HEPATOLOGY, 2012[11]*)22

Figure 1.3. 1: Illustration of the pneumatic driver design used in clinical hepatic MRE. Mechanical waves are transmitted from the active driver system placed outside the scanner room to the passive driver placed on the liver via a flexible plastic tube. (Venkatesh S. K., et al., *J Magn Reson Imaging 2014 [157]*)37

Figure 1.3. 2: Illustration of the external electromechanical acoustic transducer (this type of transducers has been used in MRE experiments in this PhD project). Mechanical waves are transmitted by a carbon fiber rod from a remote vibration generator to a piston in contact to the liver of the animal placed in the prone position.38

Figure 1.3. 3: Representation of A) a single period sine waveform similar to a standard PGSE approach B) sine-, C) cosine- D) double-sine- and E) trapezoid modulated oscillating gradient waveforms and their corresponding gradient modulation power spectra. The spectra were numerically determined which explains the truncation/apodisation effects that broaden the components from their ideal spectral form.57

Figure 3.1. 1: Study timeline with the groups and subgroups included62

Figure 3.1. 2: Mice mean weight per group measured weekly for the 12 weeks of model induction.64

Figure 3.1. 3: Histological results of our NASH mice model study presented per group (ND + oil, ND + CCl₄, WD + oil and WD + CCl₄) at 6 weeks versus 12 weeks for each histological feature of NAFLD; a) steatosis, b) inflammation, c) hepatocyte ballooning and d) fibrosis.67

Figure 3.1. 4: Histological sections (upper row: picosirius red stained slices; second row: hematoxylin-eosin stained slices) with x20 image magnification. A) Mouse fed WD for 6 weeks (grade 1 for steatosis with no inflammation, ballooning nor fibrosis). B) Mouse fed WD for 12 weeks (grade 1 for steatosis (circle) and inflammation with no ballooning nor fibrosis). C) Mouse fed WD + CCl₄ for 6 weeks (grade 3 for steatosis with no inflammation nor ballooning and with stage 1 for fibrosis). D) Mouse fed WD + CCl₄ for 12 weeks (grade 3 for steatosis, grade 1 for inflammation with no ballooning and with stage 3 for fibrosis (arrow)).68

Figure 3.2. 1: Study timeline with the groups and subgroups included. a) the WD combined with a low dose CCl₄ mice model of NASH (12 or 16 weeks of induction). b) the CDA-HFD mice model (10 or 16 weeks of diet) with diet reversal (normal diet) as treatment of NASH (0, 1 or 4 weeks of reversed diet, i.e. normal diet). C) Control groups (normal diet, n = 4 mice per group) with 10, 12 and 16 weeks as time points.71

Figure 3.2. 2: Mice mean weight per group measured weekly for a) WD NASH mice model from 4 weeks until 20 weeks and b) CDA-HFD NASH mice model (the results presented here are those of the 16 weeks of diet, 16 weeks of diet + 1 weeks of reversed diet (ND) and 16 weeks of diet + 4 weeks of reversed diet (ND) in addition to the control group (16 weeks of ND)).74

Figure 3.2. 3: Histological analysis of our WD NASH mice model study presented for each histological feature of NAFLD; a) steatosis, b) inflammation, c) hepatocyte ballooning and d) fibrosis, per group (WD + oil and WD + CCl₄ groups versus the control group (ND)) at 12 weeks versus 16 weeks.77

Figure 3.2. 4: Histological characterization of the CDA-HFD NASH mice model study displayed for each histological feature of NAFLD: a) steatosis, b) inflammation, c) hepatocyte ballooning and d) fibrosis, per group (CDA-HFD versus the reversed diet groups: CDA-HFD + 1 week of ND and CDA-HFD + 4 weeks of ND) at 10 weeks versus 16 weeks..... 79

Figure 3.2. 5: Histological sections (upper row: picrosirius red stained slices; second row: hematoxylin-eosin stained slices) with x20 image magnification. A) Mouse fed WD + CCL4 for 16 weeks (grade 3 for steatosis and inflammation (ellipse) without ballooning and with stage 2 for fibrosis (arrow)). B) Mouse fed CDA-HFD for 10 weeks (grade 3 for steatosis (circle) and inflammation without ballooning and with stage 3 for fibrosis). C) Mouse fed CDA-HFD for 10 weeks followed by ND for 4 weeks (grade 1 for inflammation with no steatosis nor ballooning and with stage 2 for fibrosis). D) Mouse fed CDA-HFD for 16 weeks (grade 3 for steatosis and inflammation with no ballooning and with stage 3 for fibrosis). E) Mouse fed CDA-HFD for 16 weeks followed by ND for 4 weeks (grade 3 for inflammation with no steatosis nor ballooning and with stage 3 for fibrosis). 81

Figure 4.1. 1: Study timeline of groups and subgroups included 85

Figure 4.2. 1: A) flowchart of the mice included in the study. B) Mice number according to the different classification of the progressive form of NAFLD..... 91

Figure 4.2. 2: Steatosis grades according to NASH, significant MLD, NASH-related fibrosis and fibro-NASH. Steatosis grade ≥ 2 is observed in the 21 mice with NASH, in 37/38 (97%) mice with significant MLD, in 19/20 (95%) mice with NASH-related fibrosis and in the 12 mice with fibro-NASH. 93

Figure 4.2. 3: Inflammation grades according to NASH, significant MLD, NASH-related fibrosis and fibro-NASH. Inflammation grade ≥ 2 is observed in 12/21 (57%) mice with NASH, in 29/38 (76%) mice with significant MLD, in 15/20 (75%) mice with NASH-related fibrosis and in the 7/12 (58%) mice with fibro-NASH..... 94

Figure 4.2. 4: Ballooning grades according to NASH, significant MLD, NASH-related fibrosis and fibro-NASH. Ballooning is observed in all the mice with NASH, in 21/38 (55%) mice with

significant MLD, in 12/20 (60%) mice with NASH-related fibrosis and in all the mice with fibro-NASH.95

Figure 4.2. 5: Fibrosis stages according to NASH, significant MLD, NASH-related fibrosis and fibro-NASH. Fibrosis stage ≥ 2 is observed in 12/21 (57%) mice with NASH, in 20/38 (53%) mice with significant MLD, in all the mice with NASH-related fibrosis and fibro-NASH.....96

Figure 4.2. 6: Histological sections (upper row: picrosirius red stained slices; second row: hematoxylin-eosin stained slices) with x20 image magnification. (A) Mouse with NAFL (simple steatosis): fibrosis stage 0, steatosis grade 3 (arrow), and lobular inflammation and hepatocellular ballooning grade 0. (B) Mouse classified as both significant MLD and NASH-related fibrosis: fibrosis stage 3, inflammation and steatosis grade 3, and hepatocyte ballooning grade 0. (C) Mouse with NASH: fibrosis stage 0, steatosis and inflammation (circle) grade 3 and ballooning grade 1. (D) Mouse with fibro-NASH: fibrosis stage 3, steatosis and inflammation grade 3 and ballooning grade 2 (arrows).....97

Figure 4.2. 7: Representative MRE images. A) magnitude image (A.U), B) phase image (rad), C) wave amplitude map and D) the mechanical property shear stiffness map (kPa).98

Figure 4.2. 8: Boxplots of the mechanical parameters in non-NASH versus NASH. The highest differences between groups are observed for the storage modulus, the shear stiffness and the multifrequency dispersion coefficient.....105

Figure 4.2. 9: Boxplots of the mechanical parameters in “no significant MLD versus significant MLD” classification. The highest differences between groups are seen for the loss modulus.106

Figure 4.2. 10: Boxplots of the mechanical parameters in no NASH-related fibrosis versus NASH-related fibrosis. The highest differences between groups are observed with the loss modulus.107

Figure 4.2. 11: Boxplots of the mechanical parameters in no fibro-NASH versus fibro-NASH. The highest differences between groups are seen for the loss modulus and the shear stiffness.108

Figure 4.3. 1: Representative images of A) the signal profile as function of the echo time and B) PDFF parametric map of mouse with PDFF = 25.5% superpositioned on the magnitude image.....	119
Figure 4.3. 2: Boxplots of PDFF measurements vs. steatosis grades. PDFF increases with steatosis grade. Kruskal-Wallis p value is indicated.	119
Figure 4.3. 3: Boxplots of PDFF measurements vs. NAFL/NASH classification according to NASH CRN scoring system. The Mann Whitney p value is indicated. PDFF was not significantly different between the NASH and NAFL groups.	120
Figure 4.3. 4: Kruskal-Wallis statistical results: Boxplots of T1 relaxation time versus histological features of NAFLD. T1 differs significantly according to steatosis and inflammation grades and fibrosis stages. However, T1 was not significantly different according to ballooning grades.....	125
Figure 4.3. 5: Phantom maps of T1 (A: uncorrected, B: corrected) and PDFF (C). D: scatter plot between PDFF and T1 (blue circles: PDFF-corrected T1; red crosses: uncorrected T1).....	131
Figure 4.3. 6: T1 maps in mice with steatosis grade S0 (PDFF = 2%) : A) without PDFF correction ($T_{1app} = 1139 \pm 152$ ms), B) with PDFF correction ($T_{1c} = 1100 \pm 157$ ms), and with steatosis grade S3 (PDFF = 30%): C) without PDFF correction ($T_{1app} = 762 \pm 88$ ms), D) with PDFF correction ($T_{1c} = 858 \pm 136$ ms). The PDFF correction factor increases the measured T_{1c} only in the mouse with high steatosis.	132
Figure 5. 1: Illustration of the double-sinusoid gradient waveform and its corresponding power spectrum with the gradient oscillation frequency $f = 100$ Hz and the number of gradient oscillation periods $N = 4$ (as of 2 on each side of the refocusing pulse).	139
Figure 5. 2: Illustration of the diagram of the trapezoidal waveform with t_r : the gradient ramp time (in our system $t_r = 140 \mu s$), τ : the period of the waveform ($\tau = 1/f$). Here the number of the periods $N = 2$	141
Figure 5. 3: Illustration of the trapezoidal gradient waveform and its corresponding power spectrum with the gradient oscillation frequency $f = 100$ Hz and the number of gradient oscillation periods $N = 4$ (as of 2 on each side of the refocusing pulse).	142

Figure 5. 4: Study timeline and the groups and subgroups included.	144
Figure 5. 5: Representative ADC maps (mm ² /s) measured in a sample of 15 μm at A) 47Hz, B) 130Hz, C) 170Hz, D) 230Hz and E) 250Hz	150
Figure 5. 6: Scatter plot of phantom ADC measurements (mm ² /s) versus microsphere sizes (3, 7, 15, 30 and 150 μm) at A: 47Hz (PGSE sequence frequency), B: 130Hz, C: 170Hz, D: 230Hz and E: 250Hz (the four OGSE sequence frequencies). ADC increases with microsphere size increase	152
Figure 5. 7: Scatter plots of phantom-based ADC measurements (mm ² /s) versus acquisition frequency (47 Hz (PGSE sequence frequency), 130 Hz, 170 Hz, 230 Hz and 250 Hz (the four OGSE sequence frequencies)) for each of the microsphere sizes; A: 3 μm, B: 7 μm, C: 15 μm, D: 30 μm and E: 150 μm. ADC measurements increase with frequency increase.	154
Figure 5. 8: ADC maps at 100Hz, superimposed on magnitude images at b-value = 0 s/mm ² . A) with volume coil, without respiratory gating, B) with volume coil and respiratory gating, C) with 4-channel parallel coil, without respiratory gating, D) with 4-channel parallel coil and respiratory gating. Volume coil images had more homogeneous sensitivity area but with lower overall signal, while surface coil images had higher signal magnitude but with spatial modulation according to the distance to the coil elements. Respiratory gating visually reduces signal artifacts.	157
Figure 5. 9: ADC maps with 4-channel surface coil and respiratory gating at A) 100 Hz and B) 150Hz. Maps are superimposed on magnitude images at b-value = 0 s/mm ²	158
Figure 5. 10: ADC maps measured at A) 47 Hz (ADC = 0.62 ± 0.20 x 10 ⁻³ mm ² /s), B) 130 Hz (ADC = 0.70 ± 0.24 x 10 ⁻³ mm ² /s) and C) 250 Hz (ADC = 0.95 ± 0.29 x 10 ⁻³ mm ² /s) in “CDA-HFD 10w” mouse with inflammation grade 3, steatosis grade 3, ballooning grade 1 and fibrosis stage 3.	162
Figure 5. 11: Histological sections (upper row: picrosirius red stained slices; second row: hematoxylin-eosin stained slices). From the NAFLD induction groups: (A) Mouse with NAFL (HFD 14w group): fibrosis stage 0, steatosis grade 3 (arrow), and lobular inflammation and hepatocellular ballooning grade 0. (B) Mouse with NASH (CDA-HFD 10w group): fibrosis stage 3, inflammation (circle) and steatosis grade 3, and hepatocyte ballooning (arrow) grade 1. From the diet reversal groups: (C) Mouse of the group “CDA-HFD 10w + ND 4w”:	222

(arrow) stage 2, steatosis and ballooning grade 0, inflammation grade 1. (D) Mouse of the group “CDA-HFD 10w + ND 8w”: fibrosis stage 2, steatosis and inflammation and ballooning grade 0. (E) Mouse of the group “CDA-HFD 10w + HFD 4w”: fibrosis stage 2, steatosis grade 1, inflammation grade 1 and ballooning grade 0. (F) Mouse of the group “CDA-HFD 10w + HFD 8w”: fibrosis stage 2, steatosis and ballooning grade 0 and inflammation grade 2.163

Figure 5. 12: (A) Steatosis, (B) inflammation, (C) hepatocyte ballooning grades and (D) fibrosis stages in the CDA-HFD 10w group (n = 10) vs. the 4 diet reversal groups: CDA-HFD 10w followed by 4 weeks of ND (“+ 4w ND”, n = 9), CDA-HFD 10w followed by 8 weeks of ND (“+ 8w ND”, n = 10), CDA-HFD 10w followed by 4 weeks of HFD (“+ 4w HFD”, n = 10) and CDA-HFD 10w followed by 8 weeks of HFD (“+ 8w HFD”, n = 11) for the 47 Hz-PGSE mice cohort.164

Figure 5. 13: (A) Steatosis, (B) inflammation, (C) hepatocyte ballooning grades and (D) fibrosis stages in the CDA-HFD 10w group (n = 11) vs. the 4 diet reversal groups: CDA-HFD 10w followed by 4 weeks of ND (“+ 4w ND”, n = 12), CDA-HFD 10w followed by 8 weeks of ND (“+ 8w ND”, n = 12), CDA-HFD 10w followed by 4 weeks of HFD (“+ 4w HFD”, n = 12) and CDA-HFD 10w followed by 8 weeks of HFD (“+ 8w HFD”, n = 12) for the OGSE mice cohort.....165

Figure 5. 14: Box plots of ADC measurements in the “CDA-HFD 10w” group compared to the ADCs of the 4 diet reversal groups at A) 47 Hz, B) 130 Hz and C) 250 Hz. “+ 4w ND”: CDA-HFD 10w followed by 4 weeks of ND, “+ 8w ND”: CDA-HFD 10w followed by 8 weeks of ND, “+ 4w HFD”: CDA-HFD 10w followed by 4 weeks of HFD and “+ 8w HFD”: CDA-HFD 10w followed by 8 weeks of HFD. P values refer to the results of the Mann-Whitney tests between the diseased group and the different diet reversal groups. NS: non-significant.....168

Figure 8.1. 1: Representative MRE visco-elastic parameter maps of a) storage modulus (color scale in kPa); b) loss modulus (color scale in kPa), c) shear stiffness (color scale in kPa), d) damping ratio (color scale is adimensional), e) shear stiffness phase angle (colorscale in radians) and f) mmultifrequency dispersion coefficient (colorscale is adimensional) for A) mouse with NAFL, B) mouse with fibro-NAFL, C) mouse with early NASH and D) mouse with fibro-NASH. The mean value of each parameter for each mouse are presented in the table below:204

